

Deciphering the Multifaceted Role of MIC13 in Cristae Formation and Mitochondrial Hepato-Encephalopathy

Inaugural dissertation

for the attainment of the title of doctor
in the Faculty of Mathematics and Natural Sciences
at the Heinrich Heine University Düsseldorf

presented by

Ritam Naha

from Kolkata, India

Düsseldorf, April 2024

from the Institute of Biochemistry and Molecular Biology I, Medical faculty,
at the Heinrich Heine University Düsseldorf

Published by permission of the
Faculty of Mathematics and Natural Sciences at
Heinrich Heine University Düsseldorf

Supervisor: Prof. Dr. Andreas Reichert
Co-supervisor: Prof. Dr. Felix Distelmaier

Date of the oral examination: 24.06.2024

In the Middle of Difficulty Lies Opportunity. -
Albert Einstein.

Table of Contents

1	SUMMARY	V
2	ABBREVIATIONS	1
3	INTRODUCTION	3
3.1.	MITOCHONDRIA: A SEMI-AUTONOMOUS ORGANELLE	3
3.2.	MITOCHONDRIA: A FUNCTIONAL PERSPECTIVE	4
3.3.	THE DYNAMIC NATURE OF MITOCHONDRIA	5
3.4.	MITOCHONDRIAL ULTRASTRUCTURE	7
3.4.1.	<i>Mitochondrial outer membrane</i>	7
3.4.2.	<i>Mitochondrial inner membrane</i>	8
3.4.3.	<i>Cristae: An architectural marvel of mitochondria</i>	10
3.5.	PROTEINS SHAPING IM	11
3.5.1.	<i>MICOS complex: the sentinel of crista junctions</i>	11
3.5.2.	<i>Regulation of IM by OPA1 and F₁F₀ ATP Synthase</i>	13
3.6.	SLP2: A MITOCHONDRIAL SCAFFOLD	15
3.7.	MITOCHONDRIAL PROTEASES: GUARDIANS OF QUALITY CONTROL IN ASSOCIATION WITH SLP2 ...	16
3.8.	MITOCHONDRIAL ULTRASTRUCTURE: DECODING LINKS TO HUMAN DISEASES	18
4	AIM OF THE PROJECT	22
5	RESULTS	23
5.1.	CONSERVED GXXXG AND WN MOTIFS OF MIC13 ARE ESSENTIAL FOR BRIDGING TWO MICOS SUBCOMPLEXES	24
5.2.	MITOCHONDRIAL APOLIPOPROTEIN MIC26 IS A METABOLIC RHEOSTAT REGULATING CENTRAL CELLULAR FUEL PATHWAYS	40
5.3.	MIC13 AND SLP2 SEED THE ASSEMBLY OF MIC60-SUBCOMPLEX TO FACILITATE CRISTA JUNCTION FORMATION	102
6	DISCUSSION	149
6.1.	MIC13 STABILIZES MIC10 SUBCOMPLEX WITH ITS CONSERVED WN AND GXXXG MOTIF	150
6.2.	MIC13 IS STABILIZES MIC10 SUBCOMPLEX FROM YME1L MEDIATED PROTEOLYSIS	150
6.3.	SLP2 IS A NOVEL INTERACTOR OF MIC13 REGULATING MIC26 STABILITY AND CRISTAE ARCHITECTURE	151
6.4.	SLP2 MEDIATED MIC26 STABILIZATION IS CRUCIAL FOR MAINTAINING CELLULAR METABOLIC DEMANDS	152
6.5.	MIC13-SLP2 SYNERGISTICALLY REGULATE MIC60-SUBCOMPLEX ASSEMBLY	154
4.4.	SLP2 REGULATES ASSEMBLY KINETICS OF MIC60 IN PRESENCE OF MIC10 SUBCOMPLEX	155
6.6.	'SEEDER MODEL' OF MICOS ASSEMBLY AND CRISTAE JUNCTION FORMATION	156
7	OUTLOOK	159
7.1.	DEEPER INVESTIGATION INTO MIC13'S REGULATORY MECHANISMS	159
7.2.	THERAPEUTIC IMPLICATIONS OF MIC10 STABILIZATION	159
7.3.	INVESTIGATING THE ROLE OF SLP2 MEDIATED YME1L REGULATION IN CRISTA SWELLING	160
7.4.	MECHANISTIC INSIGHTS INTO MIB COMPLEX REGULATION BY MICOS COMPONENTS	160
7.5.	MECHANISTIC INSIGHTS INTO MIB COMPLEX REGULATION BY IM QUALITY CONTROL PATHWAYS ..	161
8	CONCLUSION	162
9	REFERENCES	163
10	PUBLICATIONS	174
11	ACKNOWLEDGEMENTS	175
12	EIDESSTÄTTLICHE VERSICHERUNG	178

1 Summary

The Mitochondrial Contact Site and Cristae Organizing System (MICOS) is a key regulator of mitochondrial ultrastructure, consisting of seven core proteins which are divided into two subcomplexes: MIC60-subcomplex including MIC60/MIC19/MIC25 and MIC10-subcomplex including MIC10/MIC26/MIC27, with MIC13 previously known to bridge the two subcomplexes. Mutation in MIC13 induces loss of the MIC10 subcomplex and a mitochondrial ultrastructure abnormality with a dominant pronounced onion-like crista arrangement. Patient mutations in Qil1/MIC13 cause mitochondrial hepato-encephalopathy, a condition with severe hepatic and neurodegenerative implications, leading to early onset lethality. Crucialness of MIC13 for mitochondrial function as well as patient survival underscores the relevance of a detailed study to unravel the underlying molecular mechanism of MIC13 in formation of crista junctions (CJs). It is reported while deficiency in MIC13 triggers a destabilization of the MIC10-subcomplex, leading to pronounced abnormalities in cristae formation, the MIC60-subcomplex remains relatively unaltered in protein levels, yet MIC13 modulates its assembly as indicated by variations in molecular weight migration patterns. Consistent with the conclusion as MIC60 being the master regulator of MICOS complex assembly. Central to MIC13's functionality are the conserved WN and GxxxG motifs- key structural motifs necessary for maintaining the stability of MIC13 and its interaction within the MICOS complex.

In this thesis, I aimed to significantly advance the understanding of MIC13 beyond its presumed structural role. A significant discovery from this thesis describes a regulatory role of MIC13 on the mitochondrial protease YME1L. This rewrites the hypothesis of MIC13 being a bridging protein, by revealing its critical function in maintaining the stability of the MIC10-subcomplex by regulating YME1L activity. We demonstrate that depleting YME1L in MIC13 deficient cells effectively restores the MIC10 subcomplex assembly, its interaction with MIC60 and significantly rescues CJs. This marks a fundamental shift in the current understanding of MICOS assembly. Furthermore, elucidating the interactome of MIC13, we identified stomatin-like protein 2 (SLP2) as a novel player in cristae morphogenesis, which extends its functional spectrum beyond the previously identified role of regulating mitochondrial hyperfusion in cellular stress condition. SLP2 emerged as a stabilizer for the MICOS subunit MIC26 via regulating YME1L activity, and depletion resulting in crista swelling and significant loss in CJs. The synergistic interplay between MIC13 and SLP2 is critical for the assembly of the MIC60-subcomplex and subsequently the integration of mitochondrial membrane bridging (MIB) proteins such as SAM50 and MTX1, adding a new layer of understanding of MICOS assembly. The assembly kinetics of MIC60 into the MICOS complex was found to be dependent on SLP2 upon partially assembled MIC10-subcomplex. While MIC13 is essential for MIC10 stability, the presence of SLP2 is instrumental in the assembly kinetics of the MIC60-subcomplex in conjugation with a pre-assembled MIC10-subcomplex, leading to a hypothesis that MIC10-subcomplex and SLP2 provides a 'seeding' ground for efficient assembly of MIC60-subcomplex and MIB complex. In conclusion our 'seeder model' posits that the MIC10-subcomplex, together with SLP2, promotes the efficient assembly of the MIC60 subcomplex and MIB complex. Validation of this model is achieved through YME1L knockdown in cells deficient in both MIC13 and SLP2, which leads to the restoration of the MIC10-subcomplex and consequently facilitates a more effective assembly of the MIC60-subcomplex without any conclusive alterations in their steady-state levels, as well as the MIB proteins SAM50 and MTX1. This 'seeder complex' of MIC10 and SLP2 underscores a novel paradigm within the MICOS assembly process, vital for the formation of crista junctions. These insights not only propel our understanding of mitochondrial dynamics but also to the molecular mechanism involved in the development mitochondrial hepato-encephalopathy.

2 Abbreviations

ATP - Adenosine Triphosphate

mtDNA - Mitochondrial DNA

OXPPOS - Oxidative Phosphorylation

IMM - Inner Mitochondrial Membrane

ETC - Electron Transport Chain

ADP - Adenosine Diphosphate

Pi - Inorganic Phosphate

NADH - Nicotinamide Adenine Dinucleotide (reduced form)

FADH₂ - Flavin Adenine Dinucleotide (reduced form)

ROS - Reactive Oxygen Species

SOD - Superoxide Dismutase

Ca²⁺ - Calcium Ion

PD - Parkinson's Disease

OM - Outer Membrane (contextually, Mitochondrial Outer Membrane)

VDACs - Voltage-Dependent Anion Channels

TOM - Translocase of the Outer Membrane

Bcl-2 - B-cell lymphoma 2

MAMs - Mitochondria-Associated ER Membranes

ER - Endoplasmic Reticulum

PC - Phosphatidylcholine

PE - Phosphatidylethanolamine

TIM - Translocase of the Inner Membrane

AAC (or ANT) - ADP/ATP Carrier (Adenine Nucleotide Translocase)

PiC - Phosphate Carrier

MCU - Mitochondrial Calcium Uniporter

MPC - Mitochondrial Pyruvate Carrier

PHB - Prohibitins

SLC25 - Solute Carrier Family 25

LS - Leigh Syndrome

TAZ - Tafazzin

CL - Cardiolipin

SLP2 - Stomatin-Like Protein 2

OMA1 - a mitochondrial metallopeptidase

PARL - Presenilin-Associated Rhomboid-Like Protein

PINK1 - PTEN Induced Putative Kinase 1

PGAM5 - Phosphoglycerate Mutase Family Member 5

HIF1 α - Hypoxia-Inducible Factor 1-alpha

mTORC1 - Mechanistic Target of Rapamycin Complex 1

SPY complex - (contextual, not explicitly defined but related to mitochondrial proteases)

YME1L - an AAA protease in the IMM

WN - (contextual, refers to a motif in MIC13, not a standard abbreviation)

MIB - Mitochondrial Intermembrane space Bridge

3 Introduction

3.1. Mitochondria: A semi-autonomous organelle

Mitochondria are remarkable and essential organelles found within the cells of eukaryotic organisms. These double-membraned structures play a central role in energy conversion, metabolism, and a variety of other cellular processes. One of the intriguing aspects of mitochondria is their semi-autonomous nature, which is characterized by their unique evolutionary origin, distinct genetic material, and the ability to divide and replicate independently within the cell. The semi-autonomous nature of mitochondria is rooted in their unique evolutionary history. It is widely believed that mitochondria originated from a symbiotic relationship between an α -proteobacterium engulfed by ancestral cell, possibly resembling a modern-day species like *Rickettsia* (Anderson et al., 1981; Andersson et al., 1998). This ancient endosymbiotic event led to the establishment of a mutually beneficial partnership where the host cell provided protection and nutrients to the engulfed bacterium, and in return, the bacterium contributed its metabolic prowess (Lynn Margulis, 1970). Over time, this symbiotic relationship evolved, with the engulfed bacterium becoming more specialized to perform essential cellular functions such as adenosine triphosphate (ATP) production. Evidence for this endosymbiotic theory includes the presence of a double membrane surrounding mitochondria, like the structure of modern free-living bacteria, as well as the fact that mitochondria possess their own genetic material, known as mitochondrial DNA (mtDNA) (Sagan, 1967). Unlike the nuclear DNA found in the nucleus, mtDNA is a small, circular, and self-replicating molecule. It encodes a limited number of genes, typically involved in the OXPHOS pathway, which is crucial for ATP production (Anderson et al., 1981). The retention of mtDNA within mitochondria is a relic of their bacterial ancestry. This genetic autonomy allows mitochondria to produce some of the proteins necessary for their function independently, without relying solely on the nuclear DNA. It also enables mitochondria to respond quickly to changing cellular energy demands (Wallace, 2005). Another key aspect of semi-autonomous nature of mitochondria is their ability to replicate and divide independently within the cell. Mitochondria can increase in number to meet the cell's energy needs or adapt to environmental conditions. This process, known as mitochondrial fission, involves the division of an existing mitochondrion into two or more daughter mitochondria (Youle & van der Bliek, 2012). Mitochondrial fission is regulated by a variety of proteins, including Drp1 (Dynamin-related protein 1), Fis1 (Fission 1), and Mfn2 (Mitofusin 2), which help control the balance between mitochondrial fusion and fission. Mitochondrial fusion, on the other hand, involves the merging of two or more mitochondria to create a single, larger mitochondrion. This process is important for the exchange of genetic material and components between mitochondria (Chan, 2012).

3.2. Mitochondria: A functional perspective

One of the most well-known functions of mitochondria is the generation of ATP, the cell's primary energy currency. ATP is converted from ADP through a process called oxidative phosphorylation (OXPHOS), which takes place within the inner mitochondrial membrane (IMM). During this process, electrons are transported through a series of protein complexes, collectively known as the electron transport chain (ETC), embedded in the IMM. The flow of electrons creates a proton gradient across the membrane, and the enzyme F_1F_0 ATP synthase utilizes the energy of this gradient to synthesize ATP from adenosine diphosphate (ADP) and inorganic phosphate (Pi) (Neupane et al., 2019). This ATP generation is crucial for fueling various cellular processes, including muscle contraction, active transport, and biosynthesis. The number of mitochondria in a cell can vary depending on its energy requirements. Highly energy-demanding cells, such as muscle cells, contain numerous mitochondria to meet their needs. Mitochondria are at the crossroads of cellular metabolism, playing a pivotal role in the breakdown of carbohydrates, fats, and amino acids to generate energy and metabolic intermediates. This role is demonstrated by the citric acid cycle, also known as the Krebs cycle, which takes place in the mitochondrial matrix. During this cycle, acetyl-CoA derived from various fuel sources is oxidized to produce ATP and metabolic precursors, including NADH and FADH₂, which feed electrons into the ETC (Martínez-Reyes & Chandel, 2020). Mitochondria also participate in β -oxidation, the process by which fatty acids are broken down into acetyl-CoA. This allows cells to use stored fat as an energy source during times of increased energy demand or nutrient deprivation. Furthermore, amino acids can be metabolized in mitochondria through a series of reactions that lead to the production of ATP, intermediates for biosynthesis, and waste products like ammonia (Adeva-Andany et al., 2019). Mitochondria are a major source of reactive oxygen species (ROS), which are chemically reactive molecules containing oxygen. While ROS are typically produced as natural byproducts of mitochondrial respiration, they can be harmful when overproduced. Excessive ROS can cause oxidative stress, leading to damage to cellular components such as lipids, proteins, and DNA. This damage is associated with a wide range of diseases, including neurodegenerative disorders and cancer. Mitochondria have their own antioxidant defense systems to regulate ROS production and prevent oxidative damage. Enzymes like superoxide dismutase (SOD) and glutathione peroxidase help detoxify ROS. However, imbalances in ROS regulation can lead to pathological conditions (Murphy, 2009).

Mitochondria also play a crucial role in calcium ion (Ca^{2+}) homeostasis and signaling. They act as Ca^{2+} sinks, temporarily sequestering Ca^{2+} ions released from the endoplasmic reticulum (ER) or entering the cell through voltage-gated Ca^{2+} channels. This uptake of Ca^{2+} into the mitochondrial matrix can stimulate various metabolic pathways and influence cell fate. Mitochondrial Ca^{2+} signaling is involved in processes such as muscle contraction, cell

proliferation, and apoptosis. Dysregulation of mitochondrial Ca^{2+} handling can have profound effects on cell physiology and is implicated in diseases like neurodegenerative disorders and heart disease (Rizzuto et al., 2012). Mitochondria are intimately involved in programmed cell death, known as apoptosis. When triggered by various cellular signals, mitochondria release proteins such as Cytochrome *c* from the mitochondrial intermembrane space into the cytoplasm. Cytochrome *c*, along with other factors, activates a cascade of events that ultimately lead to cell dismantling and death. This mitochondrial pathway of apoptosis is tightly regulated and serves critical roles in normal development, tissue homeostasis, and defense against damaged or infected cells. Dysregulation of apoptosis can lead to cancer, autoimmune diseases, and neurodegenerative disorders (Green & Kroemer, 2004).

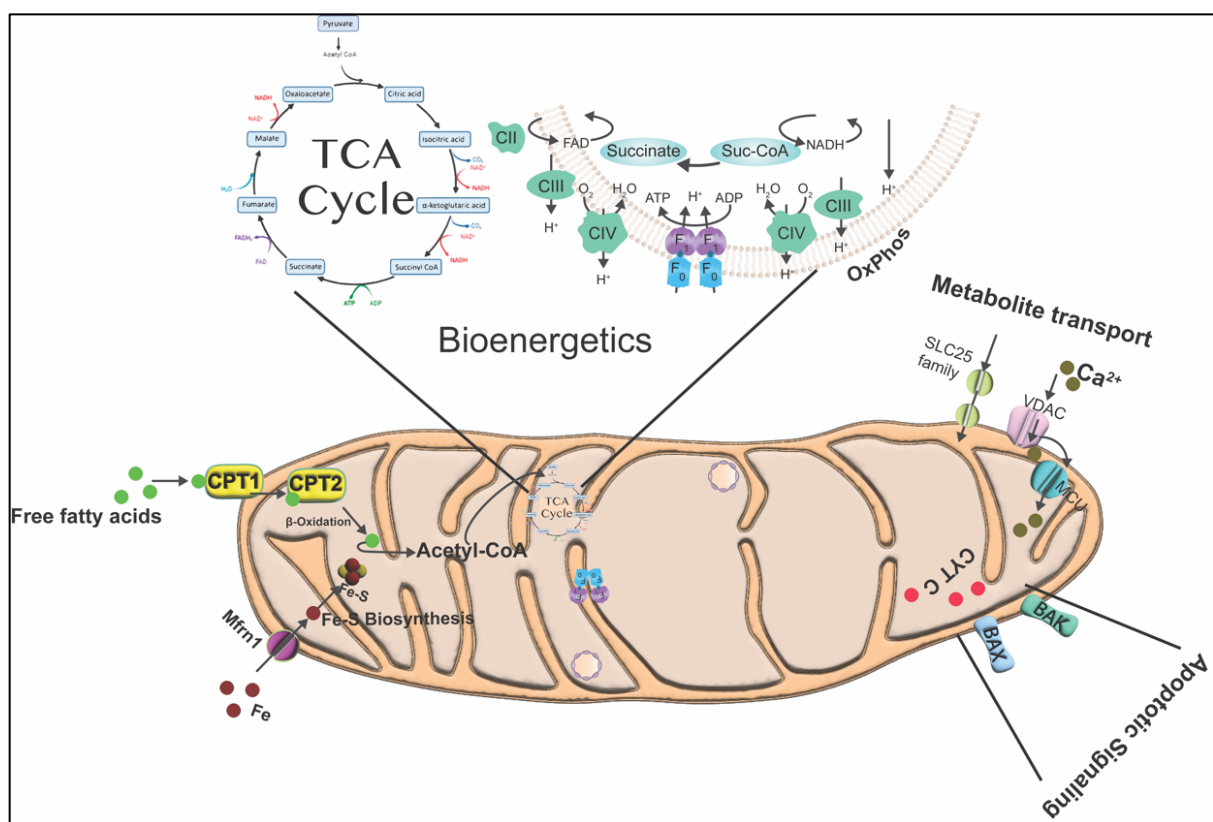


Figure 1: Overview of mitochondrial functions. This diagram highlights some of the key roles of mitochondria in cellular processes. It illustrates ATP production through oxidative phosphorylation and the TCA cycle, emphasizing its role in energy metabolism. Additionally, it displays mitochondria's involvement in Ca^{2+} buffering, iron-sulfur cluster biosynthesis, fatty acid beta-oxidation, and the apoptosis pathway, demonstrating its multifaceted contributions beyond energy production.

3.3. The dynamic nature of mitochondria

Mitochondrial morphology and distribution are regulated by a delicate balance between two opposing processes: mitochondrial fission and fusion. These processes play crucial roles in maintaining mitochondrial function, cellular homeostasis, and adapting to the ever-changing energy demands of the cell. Mitochondrial fission is the process by which a single

mitochondrion divides into two or more daughter mitochondria. This dynamic process is mediated by a family of proteins, with Drp1 (Dynamin-related protein 1) being a central player. Drp1 is recruited to the mitochondrial outer membrane (OM), where it assembles into a ring-like structure and constricts the membrane, leading to mitochondrial fragmentation (Youle & van der Bliek, 2012). A delicate balance between mitochondrial fusion and fission plays a critical role in removing damaged or dysfunctional mitochondria. When a mitochondrion is impaired, it undergoes fission, segregating the damaged portion from the healthy network. Fission facilitates the segregation of damaged mitochondria, enabling their removal via mitophagy. However, it's the impaired fusion, often due to altered OPA1 processing, that is critical for isolating damaged mitochondria from the network. Proper OPA1 processing is thus vital for the selective degradation of dysfunctional mitochondrial components. This enables the damaged mitochondrion to be targeted for degradation via mitophagy, a selective form of autophagy (Westermann, 2010). Fission is essential for distributing mitochondria evenly throughout the cell. This ensures that mitochondria are strategically positioned near areas of high energy demand, such as the cell periphery or along microtubules in neurons (Chan, 2012). Conversely, mitochondrial fusion is the process by which two or more mitochondria merge, forming a single, interconnected mitochondrion. Key fusion proteins include Mitofusin 1 (Mfn1), Mitofusin 2 (Mfn2), and Opa1 (Optic Atrophy 1) (Liesa & Shirihai, 2013). Fusion allows for the exchange of contents, including lipids, proteins, and DNA, between mitochondria. This intermixing can help rescue partially damaged mitochondria by providing essential components, enabling the recovery of function. Fusion can rescue mtDNA mutations by allowing mitochondria with different mtDNA variants to complement each other. This process, known as mtDNA complementation, can mitigate the effects of harmful mutations. Fusion maintains a functional mitochondrial network, preventing excessive fragmentation. This network facilitates efficient energy production and communication between mitochondria (Mishra & Chan, 2016). Mitochondrial fission and fusion are not isolated processes but are intricately linked and finely regulated. The balance between these processes is crucial for cellular health, and disruptions can have profound consequences. For example, an imbalance that favors excessive fission can lead to fragmented mitochondria, impairing their function and increasing susceptibility to mitophagy. On the other hand, an imbalance that promotes excessive fusion can result in elongated, interconnected mitochondria that may hinder efficient transport within cells (Chan, 2012). Mitochondrial fission and fusion are essential processes that play diverse and interconnected roles in cellular physiology. Fission serves as a part of the quality control mechanism and distribution function of mitochondria, while fusion enables repair, complementation, and network maintenance. Together, these processes ensure that mitochondria adapt to changing cellular demands, respond to damage, and maintain optimal function. Dysregulation of mitochondrial dynamics can contribute to various diseases, including

neurodegenerative disorders and metabolic syndromes, underscoring the importance of understanding these fundamental processes.

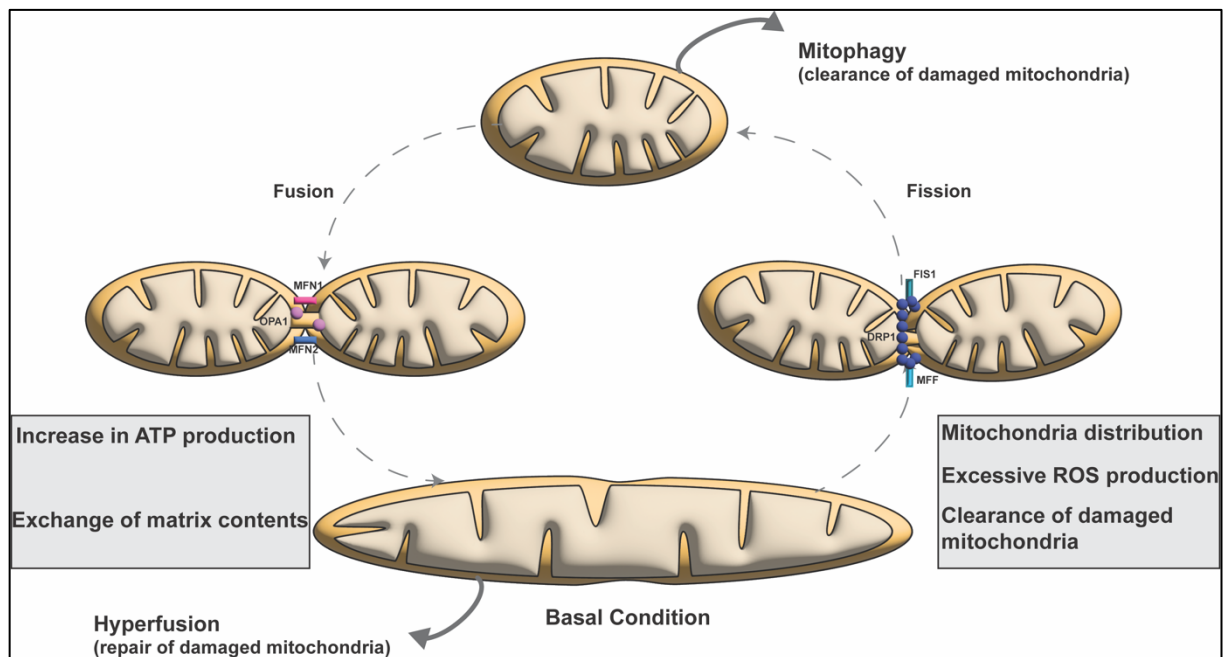


Figure 2: Mitochondrial fission and fusion Processes. This figure illustrates the dynamic processes of mitochondrial fission and fusion. Fission, the division of a single mitochondrion into two, is crucial for mitochondrial quality control and distribution in cells. Fusion, the merging of two mitochondria, promotes genetic and biochemical homogeneity and enhances mitochondrial function. These processes are fundamental for maintaining mitochondrial health and adapting to changing cellular energy demands.

3.4. Mitochondrial ultrastructure

Mitochondria orchestrate a multitude of vital processes, including ATP conversion and cellular homeostasis. Central to their multifaceted functionality is their organized structure, encompassing the outer membrane, inner membrane, cristae, CJs and matrix.

3.4.1. Mitochondrial outer membrane

The mitochondrial OM defines the mitochondrion from the cytoplasm while coordinating a wide array of vital cellular processes. Its unique structural and functional attributes make it a focal point of research, elucidating its roles in protein import, mitochondrial dynamics, and beyond. The OM is a phospholipid bilayer, fundamentally similar to the cell's plasma membrane, but distinct in several key features. A salient aspect is its permeability. Contrary to the selectively permeable inner membrane (IM), the OM freely permits the passage of small molecules, a feature attributed to voltage-dependent anion channels (VDACs) (Colombini, 1989). VDACs govern the flux of ions and metabolites, including ATP and ADP, bridging the energy demands of the cell with mitochondrial output (Rostovtseva & Bezrukov, 2008; Shoshan-Barmatz et al., 2010). Proteomic analyses of the OM paint an array of multifunctionality. Beyond VDACs, the OM embeds the translocase of the outer membrane (TOM) complex, a primary protein complex for mitochondrial protein import (Neupert & Herrmann, 2007). The majority of mitochondrial

proteins are cytosolically synthesized and the TOM complex recognizes the mitochondrial targeting sequences and translocate them inside the mitochondria (Chacinska et al., 2009). A seminal role of the OM is in apoptosis. Members of the Bcl-2 family, particularly Bax and Bak, orchestrate oligomerization on the OM. This triggers the release of cytochrome c and other pro-apoptotic factors into the cytosol, thereby initiating a cascade culminating in programmed cell death (Czabotar et al., 2014; Wei et al., 2001; Westphal et al., 2011). Beyond the confines of protein transport and apoptosis, the OM has been established as an important player in lipid trafficking (Flis & Daum, 2013; Leterme & Michaud, 2023). This nexus of lipid metabolism underscores the OM's significance in balancing the lipid equilibrium of mitochondrial membranes. Inter-organelle communication is yet another arena where the OM plays a vital role. At contact sites with the ER, the OM mediates lipid exchange, Ca^{2+} signaling, and influences mitochondrial dynamics (Friedman et al., 2011; Kornmann et al., 2009; Raturi & Simmen, 2013). These organelles are in close physical contact at regions termed mitochondria-associated ER membranes (MAMs). The MAMs serve as platforms for numerous physiological processes, encompassing lipid synthesis and transport, Ca^{2+} signaling, and the modulation of mitochondrial morphology (Rowland & Voeltz, 2012). Lipid transfer between the ER and mitochondria, specifically involving phospholipids such as phosphatidylserine and its derivative phosphatidylethanolamine, is indispensable for maintaining mitochondrial membrane integrity and functionality (Vance, 1991). The ER serves as the primary site for phospholipid synthesis, with lipids subsequently being transferred to mitochondria to support their biogenesis (Tatsuta et al., 2014). Another vital function of the MAMs is in Ca^{2+} signaling. Ca^{2+} ions are transferred from the ER to mitochondria, which is essential for various mitochondrial functions including ATP production. This transfer is crucial for the modulation of mitochondrial membrane potential and can even steer the cell towards apoptosis under certain conditions (Csordás et al., 2006). Moreover, the ER has a decisive role in mitochondrial dynamics, particularly in mitochondrial fission. ER tubules encircle and mark sites on mitochondria where division will later occur, thereby influencing mitochondrial distribution and morphology (Friedman et al., 2011).

In summary, the mitochondrial OM, far from being a mere boundary, emerges as an active site underpinning a plethora of cellular activities. The continuous discovery of novel functions of the OM centers its position in cellular physiology.

3.4.2. Mitochondrial inner membrane

The inner mitochondrial membrane (IM), being densely packed and complex in its morphology, encapsulates the mitochondrial matrix from the intermembrane space. The lipid composition of the IM is integral to its architecture and functions. Unlike other biological membranes, the IM is unique for its high content of cardiolipin (Paradies et al., 2014). Cardiolipin, a distinct dimeric phospholipid, is pivotal not just for the structural integrity of the IM but also for

facilitating the operation of numerous protein complexes embedded within it (Zhang et al., 2002). This phospholipid is essential for maintaining the curvature of the membrane and is crucial for the formation of the cristae (Daum & Vance, 1997). IM has low content of phosphatidylcholine (PC) and relatively high content of phosphatidylethanolamine (PE) (Horvath & Daum, 2013). PE has been proposed to play a role in maintaining the unique architecture of the IMM, maintains IM potential ($\Delta\psi$) and facilitates import of preproteins across IM (Birner & Daum, 2003; Böttinger et al., 2012). IM houses a cascade of large multimeric protein complex, vital to cellular functions. The translocase of the inner membrane (TIM) complex is a facilitator of protein import into the mitochondrial matrix (Chacinska et al., 2009). Both the TIM23 complex, responsible for the import of matrix-targeted proteins, and the TIM22 complex, essential for the insertion of multi-pass membrane proteins, are primarily found in the IM (Sim et al., 2023). IM, being a semi-permeable membrane, accommodates several transporter proteins necessary for cellular homeostasis. A prominent group of transporter proteins in the IM are the mitochondrial carriers. The ADP/ATP carrier (AAC), also known as the adenine nucleotide translocase (ANT), is one of the most abundant and well-studied in this category. It plays a pivotal role in shuttling ADP into the mitochondria and ATP out into the cytoplasm, supporting the cell's energetic demands (Klingenberg, 2008; Kunji et al., 2016). Another significant transporter is the phosphate carrier (PiC), responsible for importing inorganic phosphate into the matrix, a necessary substrate for ATP synthesis (Palmieri & Monné, 2016). Moreover, Ca^{2+} transport across the IM is vital for regulating mitochondrial metabolism and cell death. The mitochondrial Ca^{2+} uniporter (MCU) is central in this regard, allowing Ca^{2+} ions to enter the matrix and regulate metabolic pathways (Baughman et al., 2011). The mitochondrial pyruvate carrier (MPC), facilitating the entry of pyruvate into the matrix for oxidative decarboxylation, is another transporter with ramifications on cellular metabolism, the bridge between glycolysis and the citric acid cycle (Herzig et al., 2012). IMM's transporters play an indispensable role in various physiological processes, from energy production and metabolic regulation to ion homeostasis and signaling pathways. In addition to transporter proteins, IM houses several protein complexes that are indispensable for mitochondrial functions. Prohibitins (PHB1 and PHB2) are evolutionarily conserved proteins that form ring-like structures in the IM (Artal-Sanz & Tavernarakis, 2009). These proteins are essential for mitochondrial morphology and integrity. Additionally, prohibitins play roles in mitochondrial protein stability, and there is evidence that they may have a chaperone-like function, assisting in the folding and assembly of IM proteins (Osman et al., 2009). The OXA1L (Oxidase Assembly 1-like) protein is vital for the biogenesis of respiratory chain complexes. Positioned in the IMM, OXA1L is involved in the insertion and assembly of protein subunits, ensuring they're correctly integrated into the membrane (Hell et al., 2001). Its role is not limited to the respiratory chain; OXA1L also facilitates the integration of other IM proteins,

underscoring its importance in maintaining a functional mitochondrial membrane. IM accommodates a vast repertoire of transporters, the SLC25 family of proteins, each with specific substrates ranging from nucleotides to amino acids (Palmieri, 2013). Finally, IM contains infoldings termed as cristae, which increases the surface area of the IM to house large multimeric protein complexes, mainly the ETC complex.

3.4.3. Cristae: An architectural marvel of mitochondria

Cristae are the infoldings of the inner mitochondrial membrane (IM), protruding into the matrix. These structures significantly increase the surface area of the IM, offering more space for the protein complexes of the ETC and ATP synthase, thus enhancing ATP production capacity (Cogliati et al., 2016). The ETC complexes and ATP synthase predominantly localize in the cristae membranes. This arrangement enhances the efficiency of OXPHOS. By increasing the surface area of the IM, cristae provide more space for these complexes, thereby maximizing the potential for ATP generation (Mannella, 2006). Cristae are not isolated structures; they are connected to the IM via narrow openings called CJs. These junctions are more than mere architectural features; they serve as barriers, restricting the diffusion of lipids and proteins between the cristae and the rest of the IM (Frey & Mannella, 2000). The presence of these junctions indicates a high level of compartmentalization within the mitochondria, which may have profound functional implications, particularly in the regulation of apoptosis (Scorrano et al., 2002). CJs are the narrow openings, typically measuring 12-40 nm, that connect the cristae membrane to the main body of the IM (Mannella et al., 1994).

The biogenesis and dynamics of cristae and CJs are driven by a coordinated play of several protein complexes and individual proteins. One of the most vital proteins being OPA1, a dynamin-related GTPase. Positioned in the IM, OPA1 is involved in controlling the shape and size of cristae. It has been shown that OPA1 promotes the fusion of the IM and assisted by MFN1 triggers mitochondrial fusion (Cipolat et al., 2004). Additionally, OPA1 has a direct hand in maintaining the integrity of CJs. Under conditions of cellular stress, a loss of OPA1 function can lead to the widening of CJs and cristae remodeling, impacting mitochondrial function (Frezza et al., 2006). Together with OPA1, the 'Mitochondrial contact site and crista organizing system' (MICOS) plays a pivotal role as part of the essential protein complexes that ensure the stability and maintenance of CJs, thus preserving the structural integrity of cristae (Khosravi & Harner, 2020; Kondadi et al., 2020; Kozjak-Pavlovic, 2017; Mukherjee et al., 2021; Stephan et al., 2020). Beyond OPA1 and MICOS, several other proteins also contribute to the dynamic nature of cristae and their junctions. For instance, the ATP synthase, when oligomerized, induces a curvature in the IM that favors cristae formation (R. S. Strauss, 2000). The combination of lipid dynamics, notably the role of cardiolipin, and protein-induced membrane curvature drives the morphogenesis and maintenance of the distinctive cristae morphology (Eydt et al., 2017; Khosravi & Harner, 2020; Stephan et al., 2020).

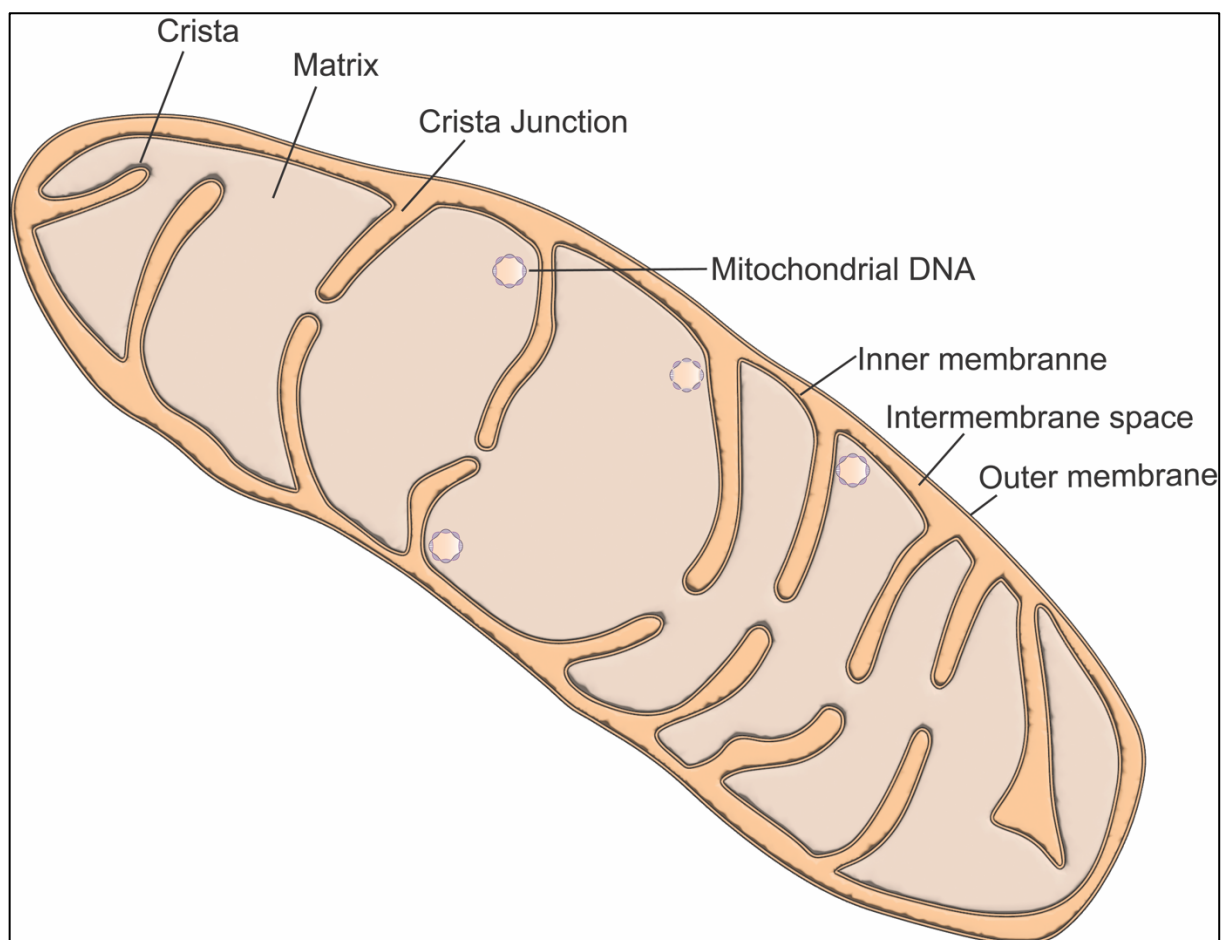


Figure 3: Illustration of mitochondrial ultrastructure depicting mitochondrial sub-compartments and mitochondrial DNA

3.5. Proteins shaping IM

The inner mitochondrial membrane (IMM) is a site of critical cellular processes, including ATP synthesis, regulation of metabolic pathways, and apoptosis. The IM is distinguished by its high protein-to-lipid ratio and unique cristae structures, which increase the surface area for metabolic processes. Proteins within the IM are involved in various functions, including OXPHOS, ion transport, and protein import.

3.5.1. MICOS complex: the sentinel of crista junctions

The MICOS complex in mammals are composed of seven core subunits: MIC10, MIC13, MIC19, MIC25, MIC26, MIC27, and MIC60, with their naming reflective of their molecular weight (Pfanner et al., 2014). These subunits function collaboratively, alongside other interacting proteins, to maintain and modulate the structure and dynamic nature of of cristae junction (Hu et al., 2020). Essential to IM structure, the MICOS complex, particularly through its critical subunits MIC60 and MIC10, is vital for cristae junction integrity, with their absence leading to loss of CJs (Alkhaja et al., 2012; John et al., 2005). The MIC10 subcomplex primarily includes MIC13, MIC26, and MIC27. MIC10 is an 8.8 kDa protein within the IM, featuring two

transmembrane α -helices. In yeast, the Glycine-rich motif within Mic10 aids in its oligomerization at CJs, albeit not essential for interaction with other MICOS proteins, thereby contributing to IM folding and cristae junction formation (Bohnert et al., 2015; Milenkovic & Larsson, 2015). Recent discoveries have shed light on MIC13's role as a crucial link in maintaining CJs by connecting MICOS subcomplexes (MIC60 and MIC10 subcomplex), where its depletion leads to the disappearance of CJs and induces atypical crista structures (Anand et al., 2016; Guarani et al., 2015). In *Drosophila*, MIC13 is further recognized for its extensive involvement in mitochondrial dynamics, such as fission/fusion equilibrium, mitophagy, and membrane potential regulation, underscoring its importance in mitochondrial structure and overall cellular balance (Wang et al., 2020).

The apolipoprotein MIC26 (APOO) was previously thought to be present in two forms: a 22 kDa non-glycosylated mitochondrial form, a 55 kDa glycosylated secretory form associated with the ER/Golgi network (Koob et al., 2015; Lamant et al., 2006). Recent study with extensive biochemical assays and mass-spectrometry confirmed MIC26 to exist as a bona fide subunit of MICOS complex existing only as one form which resides only in the mitochondria (Lubeck, Derkum, et al., 2023). Similarly, Mic27 (APOOL) is located in the IM and forms a subcomplex with Mic10, crucial for mitochondrial architecture (Weber et al., 2013). While Mic10 is capable of oligomerization independent of Mic27 in yeast, Mic27 is necessary for stabilizing these structures (Zerbes et al., 2016). Additionally, Mic27 has been implicated in the assembly of higher oligomers of the F_1F_0 ATP synthase complex in yeast, an interaction that awaits clarification in mammalian systems (Eydt et al., 2017). Both MIC26 and MIC27 are pivotal for the oligomeric state and assembly of MIC10's subcomplex (Rampelt et al., 2018). Double knockout cell studies indicate that MIC26 and MIC27 have redundant functions, and their expression is interdependently regulated, with both being crucial for maintaining respiratory chain complexes and CJs. Cardiolipins, dimeric anionic phospholipids in the IM, are essential for structural membrane integrity. Disruption of MIC26/27 levels affects cardiolipin content but can be remedied by overexpression of the Cardiolipin Synthase gene, implicating these apolipoproteins in cardiolipin biosynthesis (Anand et al., 2020).

The MIC60 subcomplex is constituted by proteins with two homologous coiled-coil helix-coiled domains, MIC19 (CHCHD3) and MIC25 (CHCHD6) with high sequence similarities but distinct functions (Tang et al., 2020). MIC60 is found abundantly in mitochondria and exists in 88 kDa and 90 kDa isoforms (Gieffers et al., 1997). MIC60 loss disrupts cristae junction formation, leading to concentric ring-like cristae (John et al., 2005), and impacts the stability of various mitochondrial proteins (Ding et al., 2015; Li et al., 2016; Ott et al., 2015). MIC19 is integral to cristae junction maintenance, connecting directly with MIC60 and other structural proteins such as OPA1 and SAM50, thus linking to the OM (Darshi et al., 2011). MIC19 is unique among MICOS proteins, existing in different redox states, which influences its regulatory role on the

complex's functionality, as evidenced in both yeast and mammalian systems (Sakowska et al., 2015). Mic25, akin to Mic19, is a core MICOS component, engaging with Mic60 and forming a subcomplex with Mic19. Though its depletion does not prevent crista formation, it results in a decreased number of CJs and elongated mitochondrial morphology (Ott et al., 2015).

Moreover, the MICOS complex subunits, MIC19 together with MIC60 is associated with the Sorting and Assembly Machinery 50 (SAM50) along with Metaxins (MTX1, MTX2, MTX3) complex that integrates β -barrel proteins into the OM and forms the mitochondrial intermembrane space bridge (MIB) complex. Disruption of the MIB complex affects the assembly of the OXPHOS system (Ott et al., 2012). The assembly of both MIB and MICOS complexes is coordinated during mitochondrial biogenesis, which means that defects in one complex can lead to secondary defects in the other, highlighting the importance of their interdependence (Zerbes et al., 2012).

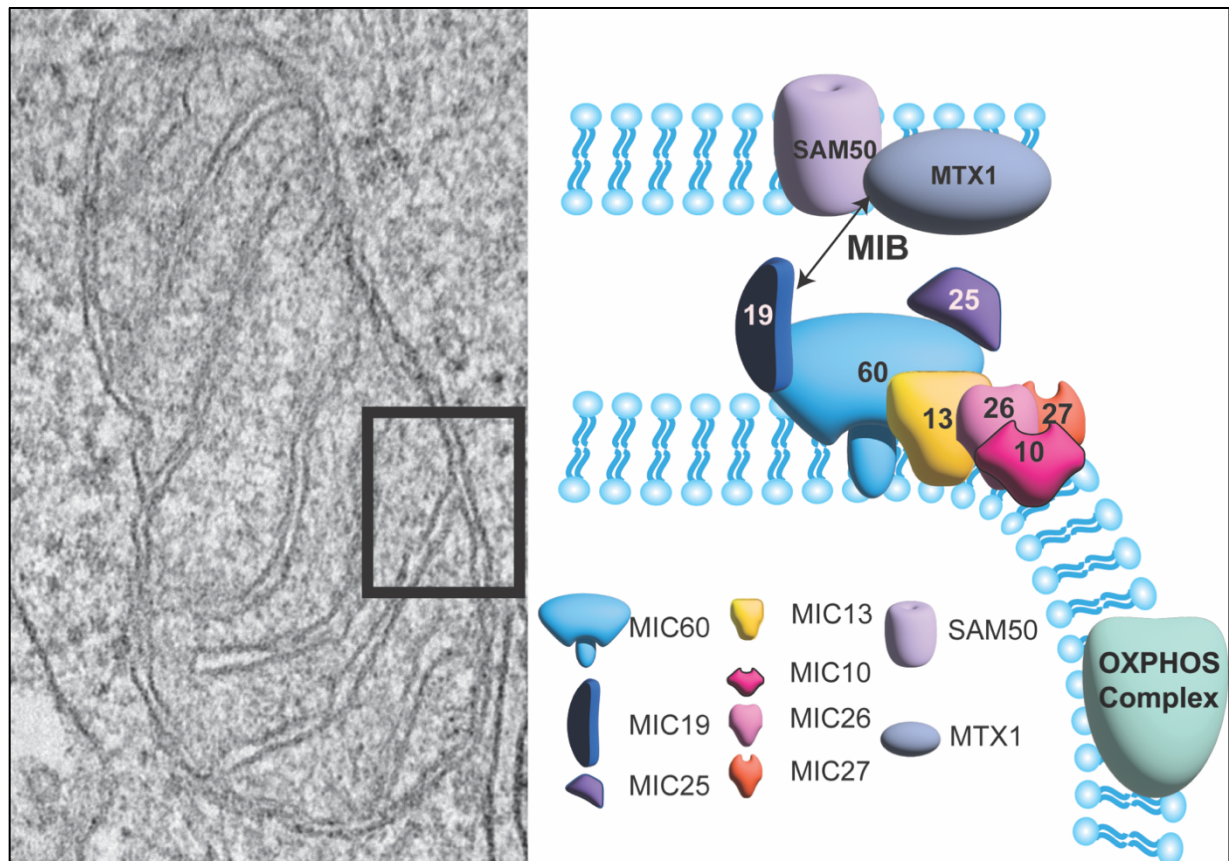


Figure 4: Classical model of MICOS assembly. MICOS, divided into MIC60 and MIC10 subcomplex, is the primary protein complex responsible for formation and maintenance of cristae and CJs. Together with SAM50, it forms the contact between IM and OM termed as the MIB complex

3.5.2. Regulation of IM by OPA1 and F_1F_0 ATP Synthase

The IM is a site of critical biochemical processes, including oxidative phosphorylation, and its intricate architecture, characterized by numerous invaginations called cristae, is essential for mitochondrial function. Two key proteins, OPA1 and ATP synthase dimers, play pivotal roles

in the formation and maintenance of these cristae structures, highlighting their significance in the overall mitochondrial architecture and function.

OPA1 is a pivotal GTPase protein that resides in the IM, playing a critical role in the regulation of mitochondrial dynamics, specifically in the maintenance of cristae structures and mitochondrial fusion. The intricate architecture of the IM, characterized by the presence of cristae, is essential for mitochondrial function, as it houses the ETC involved in oxidative phosphorylation. OPA1 is integral to maintaining this architecture, ensuring optimal mitochondrial efficiency and health. OPA1's involvement in cristae remodeling is crucial for maintaining the structural integrity of mitochondria. It orchestrates the shaping of cristae, which are vital for the proper organization and function of the ETC complexes. The regulation of cristae structure by OPA1 is essential for mitochondrial respiratory efficiency, as it influences the assembly of respiratory chain supercomplexes and the optimal functioning of ATP synthase (Cogliati et al., 2013; Frezza et al., 2006). Moreover, OPA1 mediates mitochondrial fusion, a process that is fundamental for mitochondrial quality control, enabling the mixing of mitochondrial contents and the dilution of damaged components. OPA1 also plays a significant role in regulating the release of cytochrome *c* from the intermembrane space into the cytosol, a critical step in the intrinsic apoptotic pathway. The tight control over cristae morphology by OPA1 ensures that cytochrome *c* release is precisely regulated, preventing unintended apoptosis under physiological conditions (Frezza et al., 2006; Olichon et al., 2003). This function highlights the importance of OPA1 not only in mitochondrial dynamics and bioenergetics but also in cell survival and death decisions. Dysfunction in OPA1 has been directly linked to a spectrum of mitochondrial disorders, most notably autosomal dominant optic atrophy, illustrating the critical role of OPA1 in neuronal health and mitochondrial integrity. The connection between OPA1 mutations and mitochondrial dysfunctions underscores the protein's importance in cellular energy metabolism and the potential for targeted therapeutic interventions (Alexander et al., 2000; Del Dotto et al., 2018).

ATP synthase is a fundamental enzyme complex in the IM that plays a crucial role in cellular energy production through the synthesis of ATP from ADP and inorganic phosphate. Beyond its bioenergetic function, ATP synthase has a structural role in shaping the mitochondrial cristae, where its organization into dimers and higher-order oligomers is essential for the maintenance of mitochondrial architecture and function. The dimerization of ATP synthase is key to the formation of the highly curved edges of cristae. This process is crucial for defining the characteristic invaginations of the inner mitochondrial membrane, which are vital for optimal mitochondrial function. The curvature induced by ATP synthase dimers facilitates the segregation of proteins involved in oxidative phosphorylation and optimizes the efficiency of ATP production. Studies have shown that the dimerization and subsequent oligomerization of ATP synthase are mediated by specific subunits within the complex, highlighting the intricate

regulation of its structural functions (Davies et al., 2011; M. Strauss et al., 2008). The organization of ATP synthase into dimers and oligomers on the cristae membranes is not just a structural feature; it also plays a pivotal role in enhancing the efficiency of mitochondrial respiration. By optimizing the arrangement of respiratory chain complexes and ATP synthase within the cristae, mitochondria can maximize ATP production in response to cellular energy demands. This efficient organization is crucial for the proper functioning of the electron transport chain and for minimizing reactive oxygen species (ROS) production, thereby protecting cells from oxidative stress (Cogliati et al., 2013; Frezza et al., 2006). Alterations in ATP synthase dimerization and oligomerization can lead to significant changes in cristae morphology, affecting mitochondrial respiration and energy production. Such dysregulation is implicated in a range of mitochondrial disorders and has been linked to neurodegenerative diseases, highlighting the importance of ATP synthase in mitochondrial health and disease (Cogliati et al., 2016; Davies et al., 2011).

3.6. SLP2: A Mitochondrial Scaffold

Mitochondrial scaffolding proteins are essential for maintaining the structure and function of mitochondria. They participate in organizing the mitochondrial IM, regulating mitochondrial dynamics, and influencing bioenergetics and signaling pathways. The SPFH superfamily, encompassing stomatin, prohibitin, flotillin, and HflC/K proteins, consists of scaffold proteins known for forming ring-like configurations. These structures play a crucial role in determining the specific composition of proteins and lipids in various cellular membranes. Stomatin-Like Protein 2 (SLP2) is a member of this family characterized by the presence of a stomatin domain. It is predominantly localized in the mitochondrial IM and plays a significant role in various mitochondrial functions. SLP2 lacks a transmembrane domain and resides in the IM through an unknown mechanism (Lapatsina et al., 2012). SLP2 is implicated in mitochondrial quality control by promoting stress induced mitochondrial hyperfusion (SIMH) via interaction with MFN1 and regulation of OMA1 mediated OPA1 processing (Tondera et al., 2009; Wai et al., 2016). SLP2 is involved in stabilizing specific mitochondrial proteins, particularly the subunits of complexes I and IV in the respiratory chain (Da Cruz et al., 2008). Its deficiency in T cells has been linked to increased uncoupled mitochondrial respiration, diminished formation of supercomplexes, reduced mitochondrial membrane potential, and a mild defect in mitochondrial translation (Mitsopoulos et al., 2017). Within the IM, SLP2 forms a large complex of approximately 2 megadaltons, known as the 'SPY complex', in conjunction with the i-AAA protease YME1L and the presenilin-associated rhomboid-like protease PARL. SLP2, as part of the SPY complex, has been shown to aid in the PARL-mediated cleavage of PTEN-induced putative kinase protein 1 (PINK1) and to play a role in inhibiting the processing of phosphoglycerate mutase family member 5 (PGAM5) by PARL under stress conditions (Wai et al., 2016). SLP2 is a multifaceted protein that plays a vital role in maintaining mitochondrial

integrity and function. Its interactions with various mitochondrial proteins and involvement in key mitochondrial processes like dynamics, bioenergetics, and apoptosis make it a significant factor in cellular health, although the specific role of SLP2 in shaping cristae architecture is yet to be elucidated.

3.7. Mitochondrial Proteases: Guardians of Quality Control in Association with SLP2

Mitochondrial proteases play vital roles in the maintenance of mitochondrial function and integrity. These specialized enzymes are involved in various aspects of mitochondrial homeostasis, including protein quality control, mitochondrial dynamics, and apoptosis. OMA1, a zinc metallopeptidase located in the inner mitochondrial membrane, is integral to mitochondrial homeostasis and dynamics through its role in processing OPA1. The activity of OMA1 is tightly regulated and particularly upregulated upon mitochondrial stress, leading to the cleavage of the GTPase, OPA1. The proteolytic processing of OPA1 by OMA1 serves as a critical regulatory switch in mitochondrial dynamics, particularly in response to changes in mitochondrial membrane potential and stress signals. When mitochondria are depolarized, OMA1 becomes activated and cleaves the long isoforms of OPA1, leading to a shift in the balance of OPA1 isoforms towards the shorter forms, which are associated with mitochondrial fission or impaired fusion and the release of cytochrome c, a pro-apoptotic factor (Duvezin-Caubet et al., 2006; Ehses et al., 2009; Head et al., 2009). This mechanism underscores the role of OPA1 and OMA1 in mitochondrial quality control, as it can trigger the removal of dysfunctional mitochondria through mitophagy, thereby preventing the accumulation of damaged components that could otherwise contribute to cellular aging and disease pathogenesis (Baker et al., 2014; Griparic et al., 2007). The precise regulation of OPA1 by OMA1 highlights the intricate control of mitochondrial architecture and its importance in cellular resilience and metabolic adaptation. Beyond its interaction with OPA1, OMA1 is functionally linked to the MICOS complex, contributing to the maintenance of connectivity between mitochondrial membranes. Utilizing a synthetic construct, comprising the N-terminal region of the IM protein SCO1 fused to the transmembrane domain of the OM protein TOMM20, a mitoT chimera was engineered to emulate MICOS-MIB function. Depletion of OMA1 disrupted the assembly of MIC60 and MIC19 within the MICOS complex, yet reintroduction of the mitoT chimera into OMA1-null cells reinstated normal MICOS protein levels and assembly. This suggests a proteolytic degradation of MICOS subunits in absence of OMA1, which can be rescued upon restoring the link between IM and OM with mitoT. This observation underscores the need for a comprehensive mechanistic exploration to delineate the exact role of OMA1 in facilitating the intermembrane linkage mediated by the MICOS complex (Viana et al., 2021). Central to the maintenance of mitochondrial dynamics is YME1L, a protease embedded in the IM and a member of the AAA (ATPases Associated with diverse cellular Activities) protease family. YME1L is involved in the regulation of mitochondrial dynamics, balancing the processes

of mitochondrial fusion and fission. It processes the dynamin-like GTPase OPA1, which exists in long and short forms. The long forms promote mitochondrial fusion, while the short forms are associated with mitochondrial fission. The proteolytic activity of YME1L on OPA1, therefore, has direct consequences on mitochondrial shape and function (Anand et al., 2014). Misfolded proteins within respiratory chain complexes can disrupt the ETC, leading to a decrease in energy production and an increase in the production of harmful reactive oxygen species. The absence of YME1L protease activity results in the buildup of unprocessed proteins in the mitochondrial respiratory chain, underlining the enzyme's critical function in maintaining mitochondrial protein homeostasis. Restoring active YME1L can reverse these effects, emphasizing its importance for cellular health and mitochondrial structure (Stiburek et al., 2012). YME1L is essential for the metabolic flexibility of mitochondria, a feature crucial for cell survival and adaptation under changing environmental conditions. Under hypoxic conditions, YME1L plays a critical role in adapting mitochondrial function to the altered metabolic demands. Its proteolytic activity increases, reshaping the mitochondrial proteome to support cell survival and proliferation. This increase in proteolysis is regulated by hypoxia-inducible factor 1 α (HIF1 α), which, although not directly altering YME1L transcription, influences its activity through the inhibition of the mTORC1 kinase complex. The inhibition of mTORC1 affects lipid signaling pathways within the mitochondria, particularly impacting phosphatidylethanolamine (PE) levels in the IM, which in turn modulates YME1L's proteolytic function. This regulation allows YME1L to adapt mitochondrial protein and lipid homeostasis in response to hypoxic stress, ensuring efficient mitochondrial and cellular function under low oxygen conditions (MacVicar et al., 2019). YME1L's proteolytic activity targets a wide array of proteins within the IM and intermembrane space. This includes over 40 different proteins, many of which are involved in vital mitochondrial functions. Key among these are lipid transfer proteins like STARD7, PRELID1, and PRELID3B, as well as components of the protein import machinery, such as subunits of the TIM23 and TIM22 complexes. By degrading these proteins, YME1L regulates crucial aspects of mitochondrial function, including phospholipid biogenesis and the import of newly synthesized mitochondrial proteins (Potting et al., 2013; Rainbolt et al., 2013; Richter et al., 2019; Saita et al., 2018). YME1L is part of the SPY complex, a proteolytic hub within the IM that includes PARL and SLP2 (Wai et al., 2016). Although the substrates specific to SLP2 mediated YME1L regulation are yet to be identified.

Another crucial component of SPY complex, PARL is involved exclusively in mitochondrial quality control. The primary substrate of PARL is PINK1 (PTEN-induced putative kinase 1), a sensor of mitochondrial health. PARL cleaves PINK1 in healthy mitochondria, and this process is vital for sensing mitochondrial integrity (Deas et al., 2011). In damaged mitochondria, PINK1 accumulation in OM triggers Parkin recruitment and subsequent mitophagy (Pickles et al., 2018). PGAM5 (Phosphoglycerate mutase family member 5), another substrate of PARL, is

implicated in apoptosis and necroptosis pathways, with PARL-mediated cleavage of PGAM5 triggers a pro-apoptotic signal (Lu et al., 2014; Siebert et al., 2022). SLP2, within the SPY complex, influences the activity of PARL, affecting its processing of substrates like PGAM5 and PINK1 differentially. Association of SLP2 with PARL promotes cleavage of PINK1 while the knockout of SLP2 leads to accelerated processing of PGAM5 by PARL, suggesting that SLP2 may modulate PARL-mediated proteolysis in a substrate-specific manner (Wai et al., 2016). The functions of mitochondrial proteases OMA1, YME1L, and PARL, especially within the context of the SPY complex, underscore their significance in mitochondrial quality control. Their interactions, particularly with SLP2, demonstrate a complex regulation essential for maintaining mitochondrial integrity and responding to environmental changes. These proteases, through their intricate roles and regulation within the SPY complex, are fundamental to cellular resilience, health, and longevity.

3.8. Mitochondrial ultrastructure: Decoding links to human diseases

Mitochondrial dysfunction is a hallmark of a group of conditions known as mitochondrial diseases, which arise from mutations either in mtDNA or nuclear genes that encode mitochondrial components (Schon & Przedborski, 2011). These mutations often lead to structural abnormalities in mitochondria, manifesting in diseases due to aberration in mitochondrial functions. Mitochondrial dysfunction has been well correlated with several metabolic, neurological, and inherited disorders, malignant transformations, and obstetric complications (Chakrabarty et al., 2018; Naha et al., 2020; Russell et al., 2020). Mitochondrial ultrastructural defects, characterized by alterations in cristae morphology and mitochondrial membrane integrity, are implicated in a wide range of diseases, from neurodegenerative disorders to metabolic and aging-related conditions. These defects often result from mutations or dysfunctions in critical mitochondrial proteins, leading to a cascade of cellular malfunctions. In the realm of neurodegenerative diseases, Parkinson's Disease (PD) serves as a prime example where mitochondrial dysfunction is central to its pathogenesis. The protein MIC60, integral to MICOS complex, is crucial in shaping cristae and maintaining mitochondrial integrity. In PD, mutations in MIC60, such as the c.G50T, disrupt its function, leading to a loss of CJs and the formation of onion-like cristae. This structural disarray in mitochondria contributes significantly to neuronal cell death and the overall progression of PD. Further complicating this scenario is the phosphorylation of MIC60 mediated by PINK1, which is essential for the assembly of the MICOS complex. Dysfunctions in this process, often arising from mutations in PINK1, culminate in impaired mitochondrial dynamics, a hallmark of PD. However, an overexpression of Mic60 had a protective effect on PD fly model with PINK1 knockout by improving crista architecture among other beneficial effect such as improving complex-I activity, behavioral defects and increasing ATP levels and, which are commonly compromised in PD (Tsai et al., 2018). Recent studies have linked mutations at positions

R145Q and Q126X in the CHCHD2 protein, which contains a coiled-coil helix domain, with PD. Advanced super-resolution microscopy (STED) revealed the presence of CHCHD2 in physical proximity with the MICOS complex. The proteins with these specific mutations exhibited diminished MICOS levels, leading to reduced crista formation and the development of hollow mitochondria. Moreover, the interaction between CHCHD2 and another protein with a similar structure, CHCHD10, was notably decreased at the CJs. This decrease contributed to an overall reduction in the interaction of both CHCHD proteins with the MICOS complex (Zhou et al., 2019). Optic Atrophy demonstrates the critical balance between mitochondrial dynamics and cellular health. Mutations in the OPA1 gene, responsible for inner mitochondrial membrane fusion and cristae remodeling, lead to dysregulated mitochondrial dynamics, contributing to neurodegenerative diseases (Kazamel et al., 2014; Votruba et al., 1998). Beyond optic atrophy, mutations in OPA1 are also associated with various neurological and neurodegenerative conditions, including spastic paraparesis, cerebellar ataxia, and Tourette syndrome, among others (Kazamel et al., 2014; Kitao et al., 2019; Nasca et al., 2017; Spiegel et al., 2016; van de Warrenburg et al., 2016; Willsey et al., 2017). Furthermore, the Solute Carrier Family 25 Member 46 (SLC25A46) protein, which interacts with MIC60, plays a vital role in maintaining the structural integrity of the IM (Janer et al., 2016). Mutations in SLC25A46 are linked to optic atrophy and related disorders, exhibiting symptoms like cerebellar atrophy and muscle wasting. Research on zebrafish mutants has shown that loss of function in SLC25A46 leads to increased mitochondrial connectivity and significant impacts on neuronal development and maintenance (Abrams et al., 2015). SLC25A46's engagement with mitochondrial dynamics is underscored by its proximity to pivotal fusion and fission proteins such as MFN1, MFN2, and OPA1, along with the MICOS complex member MIC19, emphasizing its crucial role in modulating mitochondrial morphology. Positioned at mitochondrial branch points, SLC25A46 is integral to the orchestration of mitochondrial architecture changes. Its impact on the oligomerization states of OPA1 and MFN2 further highlights its significant influence on the structural integrity of mitochondria (Schuettpeitz et al., 2023). Leigh syndrome (LS) is an early-onset neurodegenerative disorder characterized by lesions in the central nervous system. It's linked to mutations in SLC25A46, leading to reduced expression of Mic19 and Mic60 in fibroblasts, causing changes in mitochondrial crista morphology and function (Janer et al., 2016). Additionally, LS is associated with mutations in USMG5, affecting ATP synthase dimerization and resulting in cristae structure alterations, which can disrupt the MICOS complex and CJs, potentially leading to neurodegeneration (Rampelt & van der Laan, 2017; Siegmund et al., 2018).

Cardiolipins, located near the ETC, are prone to peroxidation, disrupting their function and leading to the accumulation of oxidized cardiolipins in the OM. This accumulation can trigger apoptotic pathways and release cytochrome c into the cytosol (Paradies et al., 2009; Schug &

Gottlieb, 2009). Oxidation and alteration of cardiolipins adversely affect mitochondrial functions, including OXPHOS and crista dynamics (Pfeiffer et al., 2003; Xu et al., 2005), with the binding of the pro-apoptotic protein Bid to cardiolipin inducing crista remodeling and mitochondrial dysfunction (Kim et al., 2004). Tafazzin (TAZ), a phospholipid–lysophospholipid transacylase, is crucial for cardiolipin remodeling. TAZ deficiency leads to altered cardiolipin content and species composition, impacting neuronal functions and brain mitochondrial respiration (Cole et al., 2018). Mutations in the TAZ gene, associated with cardiolipin alterations, are implicated in Barth Syndrome and affect the assembly of the MICOS complex and respiratory chain supercomplexes (Desmurs et al., 2015; Garlid et al., 2020; Van Strien et al., 2019). In a Parkinson's Disease (PD) mouse model, a reduction in cardiolipin levels was observed, suggesting a selective impairment in cardiolipin biosynthesis pathway (Ellis et al., 2005). The role of cardiolipins in maintaining crista dynamics and mitochondrial functions, therefore, is crucial in neuronal health, with alterations potentially leading to mitochondrial dysfunction and apoptosis. Further research is needed to understand the impact of cardiolipins on crista dynamics in neurodegenerative disorders.

MIC26, an apolipoprotein and part of the MICOS complex, plays a critical role in the formation and maintenance of CJs. Its mutation, specifically an X-linked recessive substitution from isoleucine to threonine at amino acid position 117, has been linked to mitochondrial myopathy, lactic acidosis, and cognitive impairments including autistic features. This mutation disrupts MIC26 function, impairing its integration into the IM and consequently altering MICOS complex assembly, leading to cristae junction disruption and the associated phenotype. Additionally, MIC26, along with MIC27, regulates the levels of cardiolipins, crucial for the integrity of respiratory chain supercomplexes. Depletion of MIC26 is associated with increased mitochondrial fragmentation, highlighting its role in mitochondrial structure and function maintenance (Anand et al., 2020; Benincá et al., 2020; Ott et al., 2015; Peifer-Weiß et al., 2023). Apart from MIC26, mutations in CHCHD10, specifically double substitutions at G58R and R15S, are implicated in mitochondrial myopathy and lead to mitochondrial fragmentation (Ajroud-Driss et al., 2015). Research using a double knockout mouse model reveals a close relationship between CHCHD2 and CHCHD10, with knockout leading to increased cleavage of L-OPA1, which disrupts crista structure (Liu et al., 2020). CHCHD10 mutations are also associated with defects in mtDNA repair after oxidative damage, potentially causing deleted mtDNA, loss of CJs, and nucleoid defects. These mutations contribute to the development of various neurological disorders, including Charcot–Marie–Tooth disease type 2 and frontotemporal dementia-amyotrophic lateral sclerosis (Bannwarth et al., 2014; Genin et al., 2016).

MIC13 being an integral component of MICOS complex plays pivotal role in maintaining cristae ultrastructure. Mic13 has been extensively implicated in facilitating interconnections between

two MICOS subcomplexes. Experimental evidence demonstrates that loss of Mic13 predominantly compromises the stability of the MIC10 subcomplex, while exerting a comparatively minimal effect on the MIC60 subcomplex (Anand et al., 2016; Guarani et al., 2015; Urbach et al., 2021). Pathogenic mutations in the Mic13 gene have been correlated with the onset of hepato-encephalopathy in clinical cases (Gödiker et al., 2018; Guarani et al., 2015; Zeharia et al., 2016). The phenotypic manifestations postnatally encompass a spectrum of metabolic and neurological disorders including hypoglycemia, lactic acidosis, hypothermia, and hepatic dysfunction. Progression of the pathology is marked by the emergence of microcephaly by four months of age, followed by a gradual neurological decline and mild hepatic anomalies, culminating in profound neurodegenerative outcomes and mortality prior to the age of three years (Guarani et al., 2015). Additional clinical observations in a patient with MIC13 mutations included intrauterine growth retardation, microcephaly manifesting at ten months, bilateral optic atrophy, and cerebellar and vermis hypoplasia, accompanied by compromised hepatic function (Zeharia et al., 2016). Molecular characterization of these mutations revealed substantial impairments in the assembly of the MICOS complex, characterized by a reduced expression of certain subunits such as Mic10 and associated depletion of mtDNA (Kishita et al., 2020). Functional assays conducted on Mic13 in *Drosophila* models have delineated its pivotal role in maintaining mitochondrial architecture and function. The absence of Mic13 in flies resulted in the loss of CJs, alterations in mitochondrial morphology, diminished mitochondrial membrane potential, an imbalance in mitochondrial dynamics, and an upregulation of mitophagy, ultimately leading to mitochondrial-dependent muscular dysfunction as evidenced by impaired climbing capabilities, indicative of mitochondrial myopathy (Wang et al., 2020). Loss of MIC13 exerts a detrimental effect because of substantial reduction in cristae and CJs, although the detailed mechanistic functions remain to be elucidated.

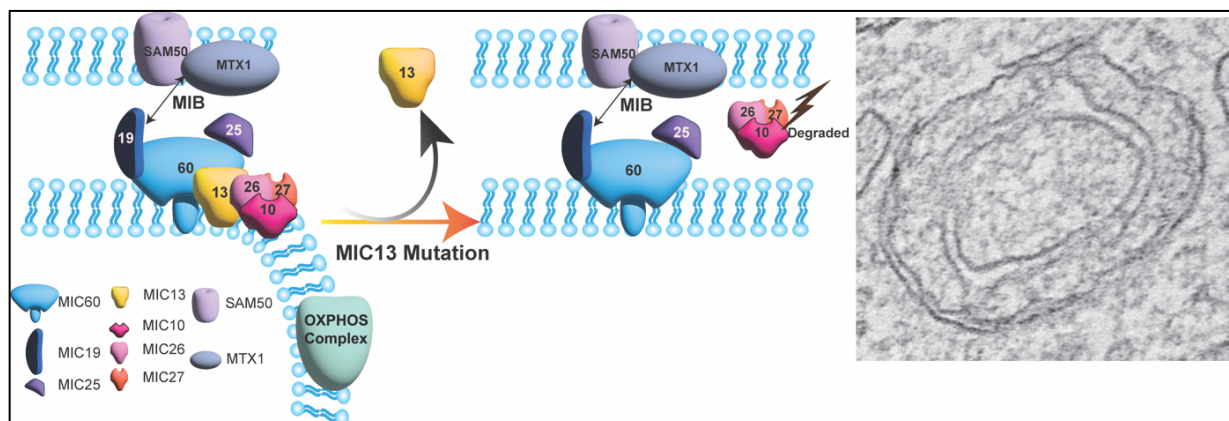


Figure 5: Mutations in *MIC13* results in reduction of MIC10 subcomplex with associated loss in CJs and substantial reduction in cristae number.

4 Aim of the project

MIC13, as a pivotal component of the MICOS complex, plays a central role in maintaining mitochondrial integrity and function. Mutations in MIC13 has been previously associated with severe metabolic disorders and neurodegeneration, mitochondrial hepato-encephalopathy.

By dissecting MIC13's interactions within the mitochondria and elucidating its role in maintaining mitochondrial integrity, this project aims to advance our understanding of fundamental cellular processes. The ultimate goal is to uncover primary molecular mechanism behind MIC13-dependent loss in CJs furthering our understanding towards MICOS assembly and extrapolate the mechanisms towards potential therapeutic targets and strategies for intervention of mitochondrial hepato-encephalopathy. Therefore, this study would address the key objectives towards deciphering the code to cristae morphogenesis:

1. **Characterize role of MIC13 in MICOS complex:** This aims to elucidate the functional significance of MIC13 within the MICOS complex. We hope to understand how MIC13 contributes to the stability and organization of key MICOS subunits and how its absence affects mitochondrial cristae morphology. We will explore how MIC13 may stabilize the MIC10 subcomplex, therefore addressing the primary function of MIC13.
2. **Explore the MIC13-SLP2 interaction:** Building on our preliminary MIC13 interactome analysis, which identified SLP2 as a top interactor, we aim to investigate the functional implications of the MIC13-SLP2 interaction. This study aims to determine how SLP2 influences CJs and whether it plays a role in modulating MIC13's functions within the MICOS complex.
3. **Define the impact on MICOS assembly and mitochondrial ultrastructure:** The project aims to investigate the consequences of MIC13 deficiency on mitochondrial ultrastructure, with a focus on cristae morphology. This includes assessing how the MIC13-SLP2 interaction influences the organization and stability of the MIC10 subcomplex and the MIC60 subcomplex.
4. **Develop a comprehensive model of MICOS assembly and cristae morphogenesis:** The final aim is to integrate the findings into a comprehensive model that explains the intricate interactions and functions of MIC13 and SLP2 within the MICOS complex. This model will provide insights into the regulatory mechanisms governing mitochondrial architecture and contribute to our understanding of mitochondrial diseases and potential therapeutic interventions.

5 Results

5.1. Conserved GxxxG and WN motifs of MIC13 are essential for bridging two MICOS subcomplexes



Contents lists available at ScienceDirect

BBA - Biomembranes

journal homepage: www.elsevier.com/locate/bbamem

Conserved GxxxG and WN motifs of MIC13 are essential for bridging two MICOS subcomplexes

Jennifer Urbach, Arun Kumar Kondadi, Céline David, Ritam Naha, Kim Deinert, Andreas S. Reichert^{*}, Ruchika Anand^{*}

Institute of Biochemistry and Molecular Biology I, Heinrich-Heine-University Düsseldorf, Medical Faculty and University Hospital Düsseldorf, Düsseldorf, Germany

ARTICLE INFO

Keywords:

Cristae
Crista junction
Mitochondrial disease
MICOS
Conserved motifs

ABSTRACT

Mitochondrial ultrastructure is highly adaptable and undergoes dynamic changes upon physiological and energetic cues. MICOS (mitochondrial contact site and cristae organizing system), a large oligomeric protein complex, maintains mitochondrial ultrastructure as it is required for formation of crista junctions (CJs) and contact sites. MIC13 acts as a critical bridge between two MICOS subcomplexes. Deletion of *MIC13* causes loss of CJs resulting in cristae accumulating as concentric rings and specific destabilization of the MIC10-subcomplex. Mutations in MIC13 are associated with infantile lethal mitochondrial hepato-encephalopathy, yet functional regions within MIC13 were not known. To identify and characterize such regions, we systemically generated 20 amino-acids deletion variants across the length of MIC13. While deletion of many of these regions of MIC13 is dispensable for its stability, the N-terminal region and a stretch between amino acid residues 84 and 103 are necessary for the stability and functionality of MIC13. We could further locate conserved motifs within these regions and found that a GxxxG motif in the N-terminal transmembrane segment and an internal WN motif are essential for stability of MIC13, formation of the MIC10-subcomplex, interaction with MIC10- and MIC60-subcomplexes and maintenance of cristae morphology. The GxxxG motif is required for membrane insertion of MIC13. Overall, we systematically found important conserved residues of MIC13 that are required to perform the bridging between the two MICOS subcomplexes. The study improves our understanding of the basic molecular function of MIC13 and has implications for its role in the pathogenesis of a severe mitochondrial disease.

1. Introduction

Mitochondria are key organelles that are required for many important cellular processes including energy conversion and various metabolic processes. The internal structure of the mitochondria is versatile and undergoes dynamic alterations upon changing cellular and energetic cues. The most important feature of this double membrane-enclosed organelle is the invaginations of the inner membrane (IM) termed cristae. The protein and lipid composition of the cristae membrane (CM) is different from the inner boundary membrane (IBM) that runs parallel to the outer membrane (OM) [1–3]. This could be mainly due to the presence of crista junctions (CJs) that are very small opening at the neck of the cristae and could act as a diffusion barrier for proteins or metabolites [4–6]. Recently it was shown that individual crista in a mitochondrion can maintain distinct levels of membrane potentials

probably due to the diffusion barrier created by CJs [7]. Moreover, a pro-apoptotic molecule cytochrome *c* that mostly resides within the cristae lumen can apparently only be released into cytosol during apoptotic signaling subsequent to opening of CJs [8]. In the recent years, the long-standing perception of cristae as largely static entities was changed with the advent of diffraction-unlimited super-resolution techniques, including STED (stimulated emission depletion) microscopy, where IM structures were imaged at unprecedented detail in living cells revealing the general dynamic nature of cristae membranes [9–13]. Using Live-STED super-resolution nanoscopy and other complementary approaches, we found that CJs and cristae continuously undergo dynamic remodeling, which comprise the reversible and balanced events of merging and splitting of CJs and of cristae at a timescale of seconds [11,13]. We devised cristae fusion assays supporting that cristae merging could lead to content mixing between

^{*} Corresponding authors at: Institute of Biochemistry and Molecular Biology I, Heinrich-Heine-University Düsseldorf, Medical Faculty and University Hospital Düsseldorf, Universitätsstr. 1, 40225 Düsseldorf, Germany.

E-mail addresses: Jennifer.Urbach@hhu.de (J. Urbach), Kondadi@hhu.de (A.K. Kondadi), Celine.David@hhu.de (C. David), ritam.naha@hhu.de (R. Naha), kim.deinert@hhu.de (K. Deinert), reichert@hhu.de (A.S. Reichert), anand@hhu.de (R. Anand).

<https://doi.org/10.1016/j.bbamem.2021.183683>

Received 16 March 2021; Received in revised form 11 June 2021; Accepted 15 June 2021

Available online 13 July 2021

0005-2736/© 2021 Elsevier B.V. This article is made available under the Elsevier license (<http://www.elsevier.com/open-access/userlicense/1.0/>).

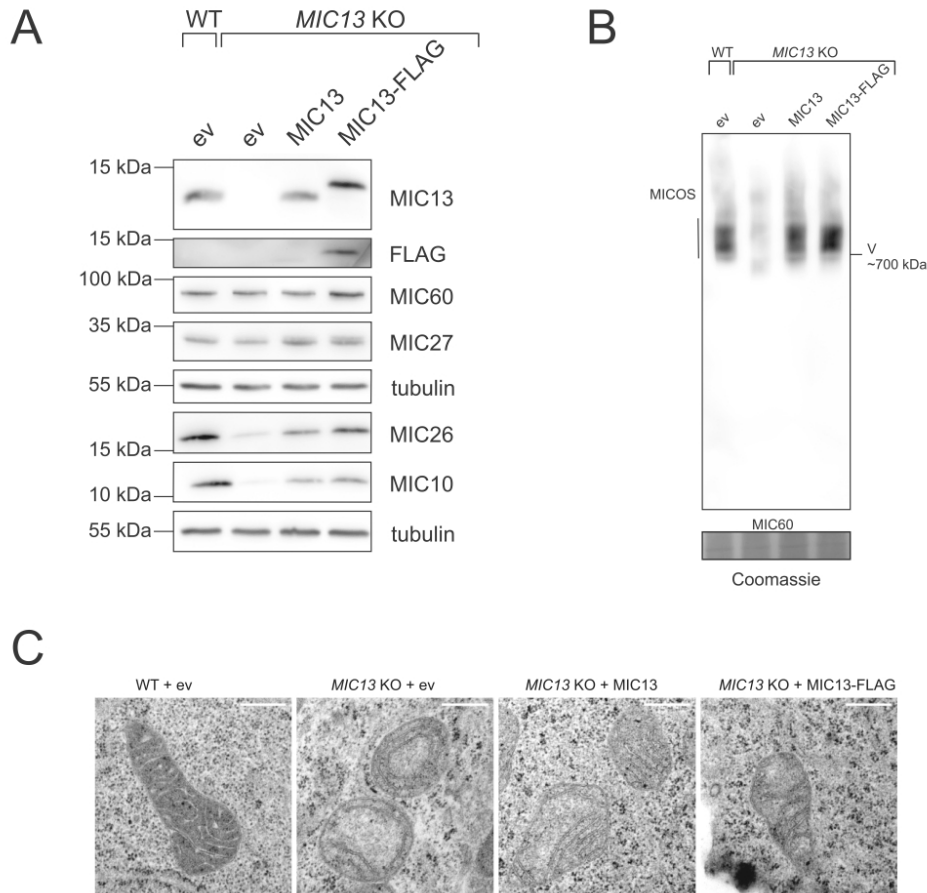


Fig. 1. Transient expression of MIC13 or MIC13-FLAG can restore the defects associated with *MIC13* KO. A) HEK-293T WT or *MIC13* KO cells were transfected with pMSCVpuro empty vector (ev), pMSCVpuro-MIC13, or pMSCVpuro-MIC13-FLAG and analysed for steady state levels of components of MIC10-subcomplex. The steady state levels of MIC10, MIC26 and MIC27 were restored upon overexpression of MIC13 or MIC13-FLAG in *MIC13* KO. B) BN-PAGE with isolated mitochondria show the restoration of MICOS complex after overexpressing MIC13 or MIC13-FLAG in *MIC13* KO. C) Representative EM pictures show that *MIC13* KO contain concentric ring-like cristae. These cristae structures were rescued and appeared normal after overexpression of MIC13 or MIC13-FLAG in *MIC13* KO. Scale bar 0.5 μ m.

cristae and therefore proposed the 'Cristae Fusion and Fission (CriFF) model'. Cristae (and CJs) remodeling depends on the presence of a fully assembled MICOS ('Mitochondrial Contact Site and Cristae Organizing System') complex [11]. MICOS is a conserved heterooligomeric complex that is enriched at the CJs and is required for the formation of CJs and contact sites between IM and OM [14–17]. Seven bonafide subunits of MICOS have been identified in mammalian system that are named as MIC 'X' (MIC10 to MIC60) according to a uniform nomenclature regime [18]. Apart from their role in CJs and contact site formation, various subunits of MICOS are required for cellular respiration, protein import, mtDNA organization, mitochondrial translation, apoptosis, autophagy, and phospholipid biogenesis [13,19,20]. Changes in steady state levels or protein modification of MICOS subunits are associated with several human diseases including diabetic cardiomyopathy, Down's syndrome, Parkinson's disease, diabetes and epilepsy [21–23]. Mutations in three subunits of MICOS namely *MIC60*, *MIC13* and *MIC26* are found in Parkinson's disease [24], infantile lethal mitochondrial hepato-

encephalopathy [25–29] and mitochondrial myopathy with lactic acidosis, cognitive impairment and autistic features [30] respectively.

At a molecular level, the MICOS complex is composed of two sub-complexes, a MIC60-containing complex (MIC60-MIC25-MIC19) for contact site formation between IM and OM and a MIC10-containing membrane sculpting subcomplex (MIC10-MIC13-MIC26-MIC27) [19,31]. The MIC60 subcomplex interacts with several OM proteins including SAM and TOM complexes to form a bigger complex termed MIB, mitochondrial intermembrane space bridging complex [3,15,19,32,33]. MIC60 and MIC10 are the key subunits of MICOS that also possess membrane-bending abilities [34–37]. MIC13 is proposed to act as a bridge between the two subcomplexes of MICOS. In mammalian cells, the deletion of *MIC13* leads to nearly complete loss of CJs with the concomitant accumulation of cristae that are arranged in concentric rings, the phenotype reminding of loss of MICOS subunits in mammalian cells [11,38,39] and bakers' yeast cells [14–17,40]. Additionally, MIC13 is required for the assembly of the MIC10-containing

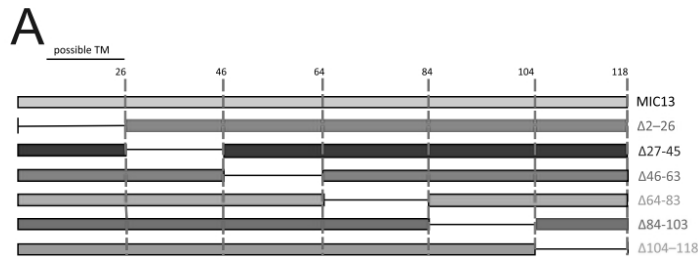
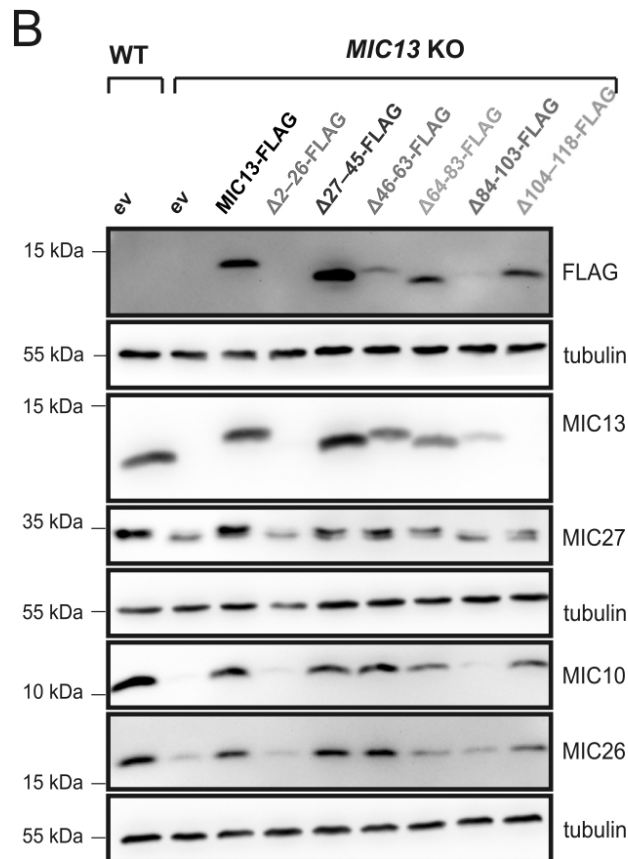


Fig. 2. Expression of the deletion variants of MIC13 in *MIC13* KO variably restores MIC10-subcomplex. (A) Schematic overview of the MIC13 deletion variants. All deletion variants were created with a FLAG tag. (B) HEK-293T WT or *MIC13* KO stable cell lines expressing pMSCVpuro empty vector (ev) or respective MIC13-FLAG variant were analysed for steady state levels of components of MIC10-subcomplex. Most of the deletion variants show good expression levels and could restore the expression of MIC10, MIC26 and MIC27 except the MIC13^{Δ2-26} and MIC13^{Δ84-103}.



subcomplex as loss of MIC13 causes destabilization of this complex with reduced steady state levels of its components namely MIC10, MIC26 and MIC27. The MIC60-subcomplex remains intact in *MIC13* KO cells albeit it has a reduced size compared to control cells. Likewise, MIC12, a MIC13 homolog of baker's yeast, was shown to participate in coupling between the MIC60- and MIC10-subcomplexes [41]. The importance of MIC13 for human health and survival is evident as mutations in *MIC13*/

Qil1 cause infantile lethal mitochondrial hepato-encephalopathy [25–29]. Patients die at an early age ranging from a few months old to 5 years. Pleiotropic symptoms include neurodegeneration with cerebellar and vermis atrophy, acquired microcephaly, and optic atrophy accompanied with liver disease that could lead to acute liver failure in several patients. Kidney stones and cardiac hypertrophy were also observed in some patients. Patients showed excessive secretion of 3-

Table 1
Overview of phenotypes observed in various deletion variants of MIC13.

Variant	Stability	Restore MIC10 levels	Restore MIC26 levels	Restore MIC27 levels	Incorporation in MIC10-subcomplex	Size restoration of MIC60-subcomplex	Nanosopic localization	Interaction MIC10-subcomplex	Interaction MIC60-subcomplex	Cristae morphology rescue
MIC13-FLAG	+++	+++	+++	+++	+++	+++	+++	+++	+++	+++
MIC13 ^{Δ2-20}	-	-	-	-	-	-	-	-	-	-
MIC13 ^{Δ27-45}	+++	+++	+++	++	+	+++	+++	+++	+++	++
MIC13 ^{Δ46-63}	+	+++	+++	++	+	+++	+++	+++	+++	+++
MIC13 ^{Δ64-83}	++	+++	+	++	+	+++	+++	+++	+++	++
MIC13 ^{Δ84-103}	-	-	-	+	-	+++	+++	-	-	-
MIC13 ^{Δ104-118}	+++	+++	+++	++	+	+++	+++	+++	+++	+++

methylglutaconic acids often indicating mitochondrial dysfunction. Moreover, increased plasma levels of lactic acid, methionine, tyrosine, and Krebs cycle intermediates were found. In all the reported cases, the MIC13 protein was completely lost and the patient tissues showed mitochondria with swollen cristae that were arranged in concentric rings similar to what has been observed in the *MIC13* KO cell lines indicating that altered cristae structure could be the main trigger that leads to mitochondrial defects and progression of pathological symptoms. Furthermore, a point mutation (glycine to serine) at the C-terminal region of *MIC13* in Rhodesian Ridgeback Dog was found to be associated with cardiac ventricular arrhythmias and sudden cardiac arrest [42].

MIC13 is a small protein with 118 aa, however no structural or functional homology has been associated with any other known proteins so far. Additionally, loss of MIC13 leads to degradation of MIC10-subcomplex accompanied by impaired assembly of MICOS complex that makes it tricky to determine the specific function of MIC13. Overexpression of MIC10 or MIC26 in the patient cell lines could only partially rescue the MIC13 defects [28]. To determine the exact molecular role of MIC13 and identify its functional regions, we took an unbiased systematic approach to generate deletion variants of MIC13 across its length. We found that large parts of the MIC13 sequence were dispensable for its functionality, except N-terminal region and a region between 84 and 103 aa were crucial for its stability and for stabilization of MIC10-subcomplex. Within these regions, we found that two conserved motifs, namely a GxxxG motif and a WN motif played an important role for assembly of the MICOS complex and interaction with other MICOS components therefore affecting mitochondrial ultrastructure.

2. Results

2.1. Generation and expression of *MIC13* deletion variants in *MIC13* KO

In order to identify the important functional regions of MIC13, we planned to systematically generate the deletion variants of MIC13 spanning the whole length. A MIC13-FLAG, where FLAG moiety was linked to the MIC13 at C-terminus, was generated and its functionality was verified by overexpressing MIC13-FLAG or MIC13 (untagged) in *MIC13* KO. Both the constructs were able to efficiently restore the loss of the subunits of MIC10-subcomplex in *MIC13* KO (Fig. 1A) and assembly of the MICOS complex (Fig. 1B). *MIC13* KO causes loss of CJs with cristae that are arranged as concentric rings. Overexpression of MIC13 or MIC13-FLAG in *MIC13* KO fully rescued the cristae morphology defects of the *MIC13* KO (Fig. 1C), indicating that the FLAG moiety does not interfere with the function of MIC13. MIC13-FLAG was then used to systematically generate approximately 20 aa deletions across the length of MIC13 using site-directed, ligase-independent mutagenesis (SLIM) [43,44] as depicted in Fig. 2A. Individual deletion variants or MIC13-FLAG or pMSCVpuro empty vector (ev) were stably expressed in *MIC13* KO using retroviral transduction methods and the expression levels of each of the deletion variants of MIC13 were analysed using western blotting. Despite the deletion of 20 amino acids, most of the

deletion variants of MIC13 showed significant levels of expression except for MIC13^{Δ2-26} and MIC13^{Δ84-103}. The expression of MIC13^{Δ46-63} in *MIC13* KO was also lower compared to MIC13-FLAG (Fig. 2B). The MIC13 antibody used in this study binds to the C-terminus of MIC13 and therefore could not recognize the C-terminal deletion variant MIC13^{Δ104-118} that was subsequently detected using FLAG antibody in the western blots (Fig. 2B). Next, we checked whether the expression of these deletion variants of MIC13 in *MIC13* KO could restore the steady state levels of the components of the MIC10-subcomplex. *MIC13* KO (+ev) showed reduced levels of MIC10, MIC26, and MIC27 accompanied by a slight shift in the molecular weight of MIC27 compared to WT (+ev), which was restored upon expression of MIC13-FLAG (Fig. 2B). Except for MIC13^{Δ2-26} or MIC13^{Δ84-103}, the stable expression of the other deletion variants (MIC13^{Δ27-45}, MIC13^{Δ46-63}, MIC13^{Δ64-83} or MIC13^{Δ104-118}) in *MIC13* KO were able to restore the levels of MIC10 comparable to MIC13-FLAG. The levels of MIC26 were restored by stable expression of MIC13^{Δ27-45}, MIC13^{Δ46-63} and MIC13^{Δ104-118}. Expression of MIC13^{Δ64-83} in *MIC13* KO that showed restoration of MIC10 levels could only partially restore the steady state levels of MIC26. MIC13^{Δ2-26} or MIC13^{Δ84-103} expressed in *MIC13* KO were unable to restore the steady state levels of MIC26 as well. It is noteworthy that MIC13^{Δ46-63} show restoration of MIC10 and MIC26 levels despite showing lower expression levels compared to MIC13-FLAG. With respect to MIC27 levels, while MIC13-FLAG was able to restore the steady state levels as well as the shift in molecular weight of MIC27 in *MIC13* KO, most of the other deletion variants (MIC13^{Δ27-45}, MIC13^{Δ46-63}, MIC13^{Δ64-83} and MIC13^{Δ104-118}) showed the presence of both the forms of MIC27. Stable cells expressing MIC13^{Δ2-26} or MIC13^{Δ84-103} in *MIC13* KO failed to restore the levels or the size shift of MIC27. Overall, we conclude that most of the deletion variants of MIC13 could restore the steady state levels of MIC10-subcomplexes except for two variants encompassing the N-terminal region and a region between amino acid residues 84 and 103 (Table 1). This observation is in line with the expression levels of these variants as they fail to express properly in the stable cell lines and are required for the stability of MIC13.

2.2. N-terminal (2–26aa) and middle region (84–103aa) of *MIC13* are required for its interaction with other MICOS subunits

To determine how the deletion variants of MIC13 affect the distribution of MIC13 within mitochondria and assembly of the MICOS complex, we analysed them using dual-colour super-resolution STED nanoscopy and native gel electrophoresis respectively. The stable cell lines expressing the individual deletion variants were stained using FLAG and MIC60 antibody and imaged using STED nanoscopy. *MIC13* KO showed typical rail-like distribution of MIC60 that is consistent with our earlier finding that MIC60 acts as a primer for CJ formation and could form discrete punctate even in absence of CJs [11]. FLAG antibody marking MIC13-FLAG showed characteristic punctate-like staining across the mitochondria that colocalized with MIC60-specific puncta (Fig. 3). The staining pattern in deletion variants MIC13^{Δ27-45}, MIC13^{Δ46-63} and MIC13^{Δ104-118} were similar to MIC13-FLAG suggesting

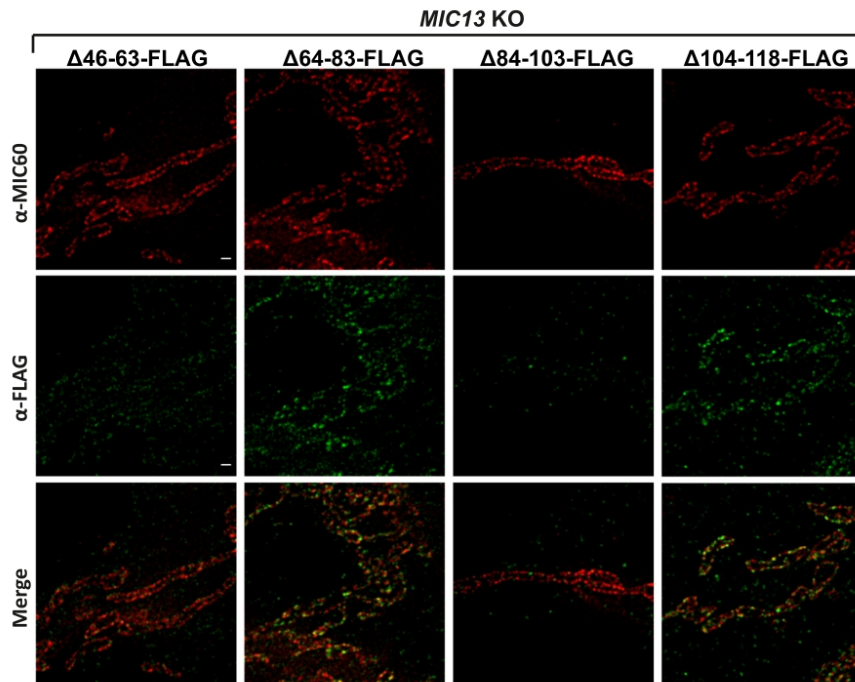
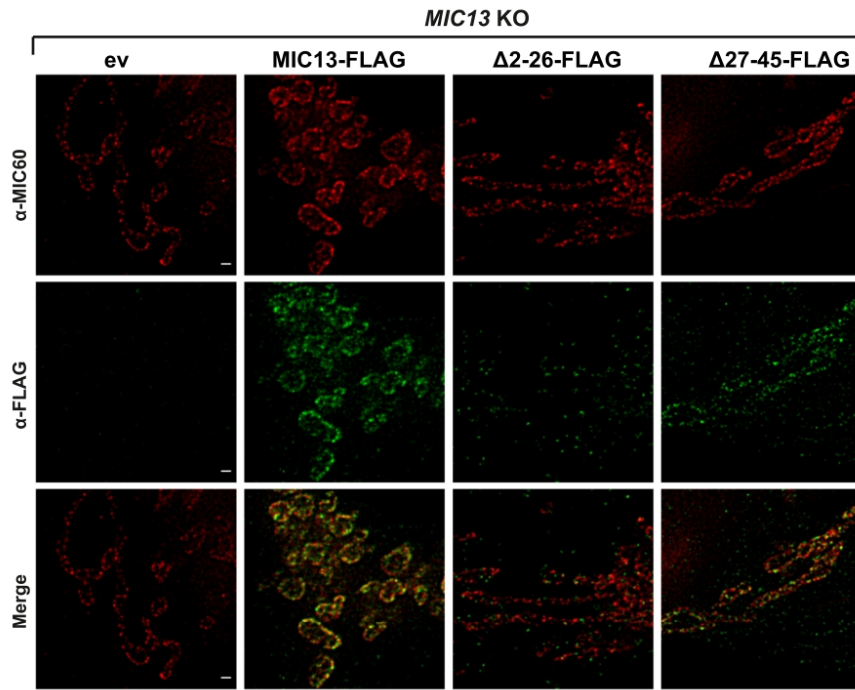


Fig. 3. Staining pattern of deletion variants of MIC13 using STED nanoscopy. Representative STED super-resolution images of HEK-293T *MIC13* KO stable cell lines expressing pMSCV/puro empty vector (ev) or respective MIC13-FLAG variant. Cells were immunostained with MIC60 (red) and FLAG (green) antibodies. Bottom image shows merged image, colocalization is seen in yellow. Scale bar 0.5 μm . (For interpretation of the references to colour in this figure legend, the reader is referred to the web version of this article.)

that these residues do not interfere in the formation of MIC13-specific puncta and their colocalization to MIC60 in mitochondria (Fig. 3). Although, MIC13^{Δ46-63} showed a weak signal of FLAG due to lower expression level, it still marked the MIC13-specific puncta that were arranged similar to MIC13-FLAG and showed colocalization to MIC60. For MIC13^{Δ2-26} and MIC13^{Δ84-103} a very sparsely localized, disturbed pattern of FLAG staining was observed with little or no colocalization with MIC60 (Fig. 3), which could be either due to their lower expression or lack of integration into MICOS. We further analysed whether the deletion variants of MIC13 can restore the stability and integrity of the MICOS complex in *MIC13* KO using blue-native gel electrophoresis (BN-PAGE). Loss of MIC13 leads to degradation of the MIC10-subcomplex (Fig. 4A) accounting for a shift in size of the remaining MICOS complex/MIC60-subcomplex to a lower molecular weight [38] (Fig. 4B). MIC13-FLAG rescued the assembly and stability of MICOS complex in *MIC13* KO as shown by incorporation of MIC10 and MIC27 into the complex (Fig. 4A) and the restoration of the molecular size of MICOS marked by MIC60 and MIC25 (Fig. 4B). *MIC13* KO expressing MIC13^{Δ2-26} failed to restore the assembly of the MICOS complex and incorporation of MIC10 and MIC27 in the MICOS complex (Fig. 4A, B) consistent with its reduced levels of expression (Fig. 2B). Expression of MIC13^{Δ27-45}, MIC13^{Δ46-63}, MIC13^{Δ64-83}, and MIC13^{Δ104-118} in *MIC13* KO showed the restoration in molecular size of MIC60-subcomplex (Fig. 4B) but only partial incorporation of MIC10 and MIC27 in the MICOS complex (Fig. 4A) suggesting that these residues may have additional roles in the assembly of MIC10 and MIC27 in the MICOS complex. Interestingly, these deletion variants were able to restore the steady state levels of MIC10 and partially the levels and shift of the MIC27 (Fig. 2B). Deletion variant MIC13^{Δ84-103} fail to restore the shift of the MIC60-subcomplex (Fig. 4B) as well as the incorporation of MIC10 in the MICOS complex (Fig. 4A), but could sparsely restore the MIC27 incorporation (Figs. 4A, 2B). Interestingly, in *MIC13* KO cells expressing MIC13^{Δ2-26}, MIC13^{Δ27-45} and MIC13^{Δ104-118}, an increase in a lower molecular weight complex marked by MIC27, which could be a MIC26-MIC27 complex was observed (Fig. 4A).

Next, we determined which residues of MIC13 are required for its interaction with other subunits of the MICOS complex using co-immunoprecipitation (co-IP) experiments with FLAG-antibody. Firstly, we compared the input and elution fractions of ev control and MIC13-FLAG for MICOS subunits and found that MIC13-FLAG specifically eluted all the MICOS subunits (Fig. 4C). Prohibitin was used as a negative control as it did not show any interaction with MIC13-FLAG. As MIC13^{Δ2-26} and MIC13^{Δ84-103} in *MIC13* KO had very low expression levels, we decided on purpose to select blots and suitable exposure times showing similar signal intensities in the input fractions for relative comparisons of co-IP efficiencies for different MIC13 variants. Both MIC13^{Δ2-26} and MIC13^{Δ84-103} show significant pull down with FLAG antibody that indicates the success of the co-IP in these very low expressing deletion variants (Fig. 4C). Interestingly, MIC13^{Δ2-26} and MIC13^{Δ84-103} showed no detectable interaction with MIC10, MIC26, MIC25, and MIC60 and considerably reduced interaction with MIC27 compared to MIC13-FLAG. The interaction of the deletion variants MIC13^{Δ27-45}, MIC13^{Δ46-63}, MIC13^{Δ64-83}, and MIC13^{Δ104-118} with subunits of MICOS were similar to MIC13-FLAG (Fig. 4C). Therefore, we concluded that the N-terminal region (2 to 26 aa) and a middle stretch (84 aa to 103 aa) of MIC13 are required for its interaction with other MICOS subunits and hence are crucial for the stability and assembly of the MICOS complex (Table 1). Concomitantly, we also analysed the interaction between MIC60 and other MICOS subunits in the cells expressing deletion variants using a MIC60-specific antibody (Fig. S1A).

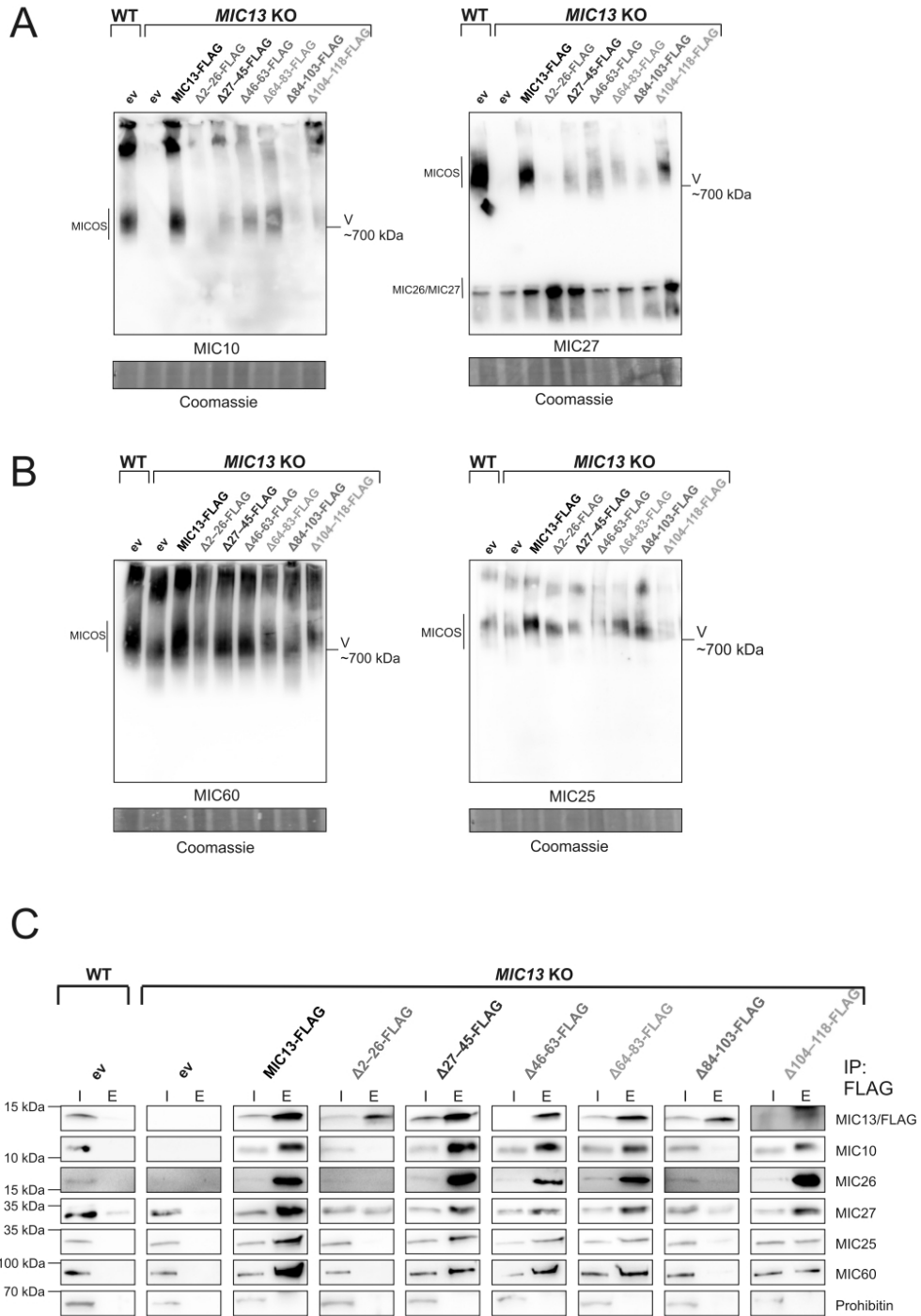
We found significant interaction between MIC60 and other MICOS subunits in the cell expressing MIC13-FLAG in *MIC13* KO. Most of the deletion variants showed similar pull-down efficiencies between MIC60 and MICOS subunits when compared to MIC13-FLAG. However, MIC13^{Δ2-26} and MIC13^{Δ84-103} showed a considerable decrease in the levels MIC10, MIC13 and MIC26 in the elution fraction compared to the MIC13-FLAG, confirming the importance of these residues for bridging the interaction between the MIC10- and MIC60- subcomplexes (Fig. S1A).

2.3. Effect of expression of deletion variants of MIC13 on cristae morphology in *MIC13* KO

To determine the role of various regions of MIC13 in maintaining normal cristae structure, we analysed the mitochondrial ultrastructure of stable cells expressing various deletion variants using electron microscopy (EM) analysis. Firstly, we confirmed that overexpression of MIC13-FLAG fully rescued the mitochondrial morphology as described earlier (Figs. 5A and 1C). At the first glance, we noticed that the deletion variants of MIC13 differ in their ability to rescue cristae structure (Fig. 5A) despite being able to restore the steady state levels of components of the MIC10-subcomplex (Fig. 2B). We performed a detailed quantification to find the extent of rescue among different deletion variants and determined the percentage of mitochondria that contained normal or abnormal cristae in each condition (Fig. 5B). We also determine the number of cristae and CJs per mitochondrial section in each cell line (Fig. 5C). While *MIC13* KO expressing MIC13^{Δ46-63} or MIC13^{Δ104-118} showed an overall normal cristae morphology that was comparable to MIC13-FLAG, MIC13^{Δ64-83} and MIC13^{Δ27-45} showed a partial rescue of the cristae morphology with prevalence of some abnormal cristae (Fig. 5A). Some instances of interconnected cristae were found in *MIC13* KO expressing MIC13^{Δ64-83}. Expression of MIC13^{Δ2-26} and MIC13^{Δ84-103} in *MIC13* KO showed the lowest extent of rescue among all the deletion variants, which was expected considering their lower expression levels and the observed loss of the MIC10-subcomplex.

2.4. Conserved GxxxG and WN motif of MIC13 are required for its bridging role in MICOS assembly

Our systematic analysis for identifying the functional regions in MIC13 showed that N-terminal region and a region between amino acids 84 and 103 are crucial for its stability, restoration of MIC10-subcomplex, interaction with MICOS subunits and cristae ultrastructure (summarized in Table 1). Therefore, we decided to focus within these regions to pinpoint any conserved smaller motifs that are important for MIC13 function. The N-terminal region has a putative transmembrane segment and sequence alignment of MIC13 from different species showed conserved ¹⁵GxxxG¹⁹ motifs in this region [38]. A frameshift mutation G15Efs*75 in the same motif of MIC13 was described in patient suffering with MIC13-mediated mitochondrial hepato-encephalopathy [27]. In addition, a highly conserved ⁸⁴WN⁸⁵ motif was also earlier shown by homology sequence alignment in MIC13 [3], which was often preceded by a positive (K/R) and/or a negatively charged (E/D) amino acid [3]. *Homo sapiens*' MIC13 consists of ⁸¹RDSWN⁸⁵ motif. Furthermore, we decided to analyse the point mutation of MIC13 at the residue 109 (glycine to serine) that was found to be associated with cardiac death in Rhodesian ridgeback dogs [41], to independently determine how this pathological mutation affects the stability or integrity of MICOS subunits in human cell lines (Fig. S2A). Point mutations or small deletions in



(caption on next page)

Fig. 4. MICOS assembly and interaction with other MICOS components in MIC13 deletion variants. (A) BN-PAGE with isolated mitochondria of HEK-293T WT or *MIC13* KO stable cell lines expressing pMSCVpuro empty vector (ev) or respective MIC13-FLAG variant. Coomassie image was used as loading control. Samples were stained with antibodies against MIC10 or MIC27 to visualize MIC10-subcomplex. (B) BN-PAGE with isolated mitochondria of HEK-293T WT or *MIC13* KO stable cell lines expressing pMSCVpuro empty vector (ev) or respective MIC13-FLAG variant. Coomassie image was used as loading control. Samples were stained with antibodies against MIC60 or MIC25 to visualize MIC60-subcomplex. (C) Co-immunoprecipitation with mitochondria isolated from HEK-293T WT or *MIC13* KO stable cell lines expressing pMSCVpuro empty vector (ev) or respective MIC13-FLAG variant. Pulldown was performed with FLAG antibody and probed with MIC13/FLAG, MIC10, MIC26, MIC27, MIC25, and MIC60. Prohibitin was used as a negative control. I: Input (5%); E: Elution (50%). MIC13^{Δ2-26} and MIC13^{Δ4-103} show reduced interaction with the other MICOS subunits.

these motifs were generated using mutagenesis methods that are depicted in a scheme in Fig. 6A. ¹⁵GxxxG¹⁹ region of MIC13 was mutated to either one (G15L or G19L) or two (G15L, G19L) amino acid substitutions of glycine to leucine. We also decided to generate MIC13-G15E6⁷⁵ to analyse the effect of pathological mutation at G15 position of ¹⁵GxxxG¹⁹ motif. Two sets of variants were generated for ⁸¹RDSWN⁸⁵ motif, either in whole ⁸¹RDSWN⁸⁵ motif or separately in RD or WN of this motif to determine if the different parts of the motif have any specific effects compared to the whole motif. We stably expressed all these MIC13 mutation variants in *MIC13* KO cells using retroviral transduction and analysed the steady state levels of all MICOS subunits (Figs. 6B, S3A). For the GxxxG substitutions, we found that while expression of the MIC13^{G15L} or MIC13^{G19L} in *MIC13* KO does not affect the steady state levels of MIC13 or other MICOS subunits, MIC13^{G15L}, MIC13^{G19L} caused destabilization of MIC13 and loss of the components of MIC10-subcomplex, underlining the importance of whole GxxxG motif for the stability and integrity of MIC13 and MIC10-subcomplex (Fig. S3A). Similar to MIC13^{G15L}, MIC13^{G15L} was able to rescue levels of MIC10, MIC26 and MIC27 (Fig. S3A) and therefore further experiments were performed only with MIC13^{G19L}. MIC13^{G15E6⁷⁵} generated the truncated version of MIC13 that was not detectable in the western blots and consequently could not restore the levels of MIC10, MIC26 or MIC27 in *MIC13* KO (Fig. S3A). Among cells expressing MIC13^{ΔRD} or MIC13^{ΔWN} in *MIC13* KO, MIC13^{ΔRD} showed no obvious change in steady state levels of MIC13 or other MICOS component but MIC13^{ΔWN} showed a reduced expression and loss of MIC10 and reduced levels of MIC26 compared to MIC13-FLAG. MIC13^{ΔRDSWN} showed a similar extent of decrease in levels of MIC13, MIC10, and MIC26 as found for MIC13^{ΔWN} indicating the significance of WN motif in the whole RDSWN motif. The substitution mutation MIC13^{W84A, W85A} showed slightly lower defects compared to the deletion variant MIC13^{ΔWN}. The substitution mutation MIC13^{R81A, D82A} showed no change in levels of MIC13 or other components of MIC10-subcomplex. MIC13^{G1099} did not show any change in the levels of MIC13 or other MICOS subunits and therefore was not studied in detail (Fig. S2B).

We further analysed the ability of these mutant variants to interact with other MICOS subunits using co-IP (Fig. 6C). While the expression of the single substitution mutation MIC13^{G19L} in *MIC13* KO showed interaction with MICOS subunits that was comparable to MIC13-FLAG, the double substitution MIC13^{G15L, G19L} showed a drastic decrease in its ability to interact with MICOS subunits (Fig. 6C), indicating a central role of GxxxG motif of MIC13 in interaction with other MICOS components. Both MIC13^{ΔWN} and MIC13^{ΔRDSWN} also showed reduced ability to interact with other MICOS subunits, while MIC13^{ΔRD} showed no defect in the efficiency of interaction compared to MIC13-FLAG (Fig. 6C), implying a necessary role of the WN motif in regulating the stability and the interaction of MIC13 with MICOS subunits. MIC13^{W84A, W85A} showed a more efficient pulldown of MIC60, than MIC10, suggesting, that this mutation disrupts only the interaction with MIC10 and not with MIC60 (Fig. 6C). Additionally, effects of the MIC13 variants on assembly of MICOS subunit MIC10 were analysed using BN-PAGE, where the variants MIC13^{G15L, G19L}, MIC13^{ΔWN} and MIC13^{ΔRDSWN} were not able to rescue assembly of MIC10 into MICOS complex (Fig. S3B). We performed cross-linking with DSG to identify the specific bands that represent cross-link between MIC13 and other MICOS subunits (Fig. 6D). The crosslink experiments revealed dimers of both MIC10 and MIC13, as well as a MIC10-MIC13 band in the control (MIC13-FLAG).

This MIC10-MIC13 dimer was missing in both MIC13^{G15L, G19L} and MIC13^{ΔWN}, suggesting a loss of the MIC10-MIC13 interaction in these two variants (Fig. 6D) that reinforce that GxxxG and WN motif are required for direct interaction between MIC13 and MIC10. In summary, we find that two conserved motifs, GxxxG and WN, of MIC13 are required for the interaction of MIC13 with other MICOS components and maintaining the stability of the MIC10-subcomplex (summarized in Table 2).

GxxxG is a known dimerization motif of transmembrane segments [45] and therefore we wanted to check whether this variant affects MIC13 association with or integration into the mitochondrial membrane using the standard alkaline extraction assay (Fig. 6E). Western blot analysis revealed two forms for MIC13^{G15L, G19L}, one similar to the size of MIC13-FLAG and another at a slightly higher molecular weight. The lower form was more soluble compared to MIC13-FLAG but the higher form was more resistant to alkaline extraction and showed more stringent association with membrane almost similar to the integral membrane protein TOM20 (Fig. 6E). The identity of the higher running band is not known, yet could represent e.g. a precursor, an import intermediate, a post-translationally modified or cofactor-/lipid-bound variant, or an alternative conformation of the variant protein.

2.5. Conserved GxxxG and WN of MIC13 are necessary for the formation of crista junctions

We further analysed how does the expression of mutated versions of GxxxG and WN motif in *MIC13* KO affect the cristae morphology using EM. We found that although expression of MIC13^{G19L} in *MIC13* KO was able to completely rescue defects in cristae morphology in *MIC13* KO, the expression of MIC13^{G15L, G19L} showed more drastic defects with complete loss of CJs, widening of cristae and accumulation of interconnected cristae, emphasizing on a very crucial and necessary role of GxxxG motif for the formation of CJs and maintenance of proper cristae morphology (Fig. 7A, B, C). Expression of MIC13^{ΔWN} or MIC13^{ΔRDSWN} in *MIC13* KO could not rescue cristae morphology, but expression of MIC13^{ΔRD} showed normal cristae structure again highlighting the vital role of WN motif in regulating the formation of CJs (Fig. 7A, B, C). Expression of MIC13^{W84A, W85A} showed only partial rescue which is consistent with the previous observation that this could partially recover the MIC10-subcomplex (Fig. 6A). The loss of CJs was observed upon deletion of *MIC13* and could also be observed in cells expressing the mutated proteins MIC13^{G15L, G19L}, MIC13^{ΔWN}, MIC13^{W84A, W85A}, and MIC13^{ΔRDSWN} (Fig. 7C). Overall, we found that GxxxG and WN motifs of MIC13 are essential for maintaining the stability of MIC10-subcomplex, interaction with MICOS subunits, and maintenance of cristae morphology (Table 2). These conserved regions seem to be important for the stability and insertion of MIC13 into the membrane, as well as for the interaction with both of the MICOS subcomplexes, underlining the function of MIC13 as a bridge between the two MICOS subcomplexes.

3. Discussion

MIC13 is very important subunit of MICOS complex and its mutations are associated with infantile lethal mitochondrial hepatocerebralopathy [25–29]. It was apparently difficult to identify its homologous proteins because there was very little sequence conservation [3]. No structural or functional regions of MIC13 have been found yet.

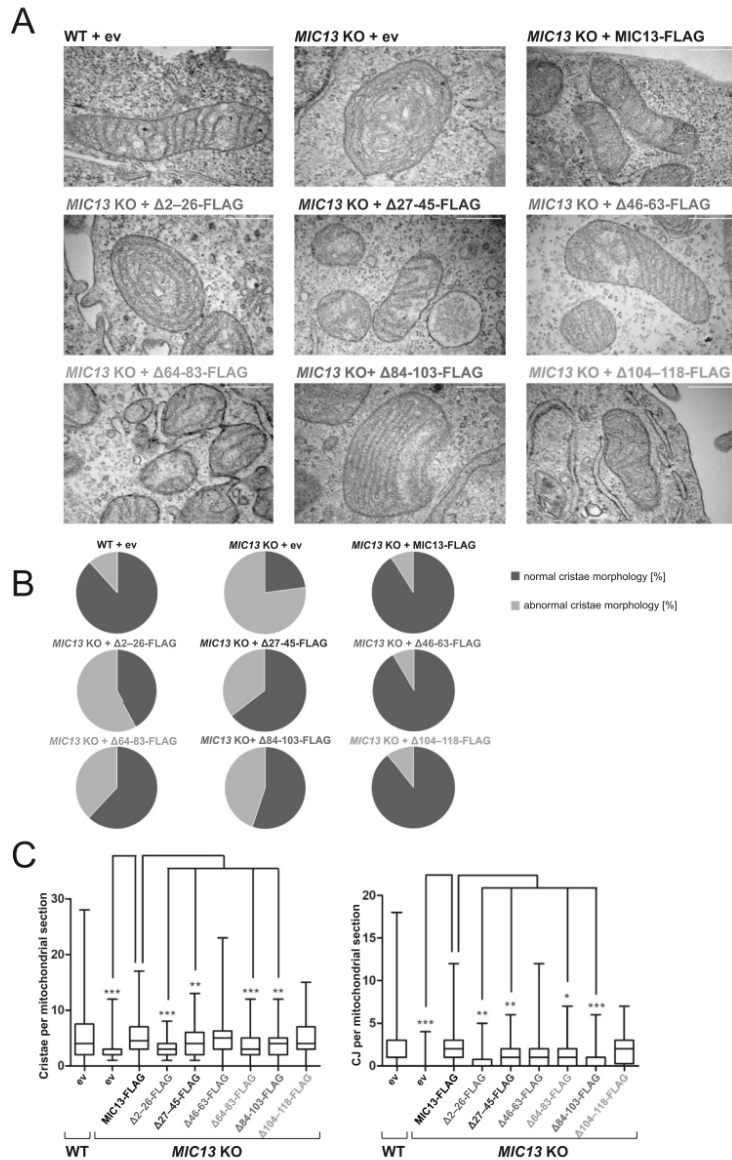


Fig. 5. Expression of deletion variants of MIC13 in MIC13 KO variably affects cristae morphology. (A) Representative EM pictures of HEK-293T WT or MIC13 KO stable cell lines expressing pMSCVpuro empty vector (ev) or respective MIC13-FLAG variant. Scale bar 0.5 μm. (B) Quantification of normal versus abnormal cristae morphology in percentage from all imaged mitochondria in HEK-293T stable cell lines expressing pMSCVpuro empty vector (ev) or respective MIC13-FLAG variant using EM represented as pie chart. (C) Quantification of cristae and CJs per mitochondrial section from different mitochondria in HEK-293T stable cell lines expressing pMSCVpuro empty vector (ev) or respective MIC13-FLAG variant using EM represented as boxplots. Boxplots show median and interquartile range from 25 to 75 percentile, and whiskers represent minimum and maximum value. Data from n = 69 to 121 mitochondria from two biological replicates. Student's t-test was used for statistical analysis.

Therefore, in this study we took an unbiased and systematic approach to identify the functional regions of MIC13 by generating the deletion variants of 20 amino acids across the length of MIC13. We have methodically analysed these deletion variants for various parameters pertaining to function of MIC13 (summarized in Table 1). Most of the 20 aa deletion variants were stably expressed and could restore the levels of MIC10-subcomplex in *MIC13* KO except the deletion of the N-terminal region and a region between 84 and 103 aa. These regions were specifically required for the interaction of MIC13 with the other MICOS subunits and maintaining normal cristae structure. MIC13^{Δ27-45} and MIC13^{Δ64-83} that could restore the levels of MIC10 and MIC27 and interaction with MICOS subunits, still contained partially perturbed cristae when expressed in *MIC13* KO. The partial defect in incorporation of MIC10 and MIC27 into MICOS complex was observed for MIC13^{Δ27-45} and MIC13^{Δ64-83} as well as MIC13^{Δ46-63} and MIC13^{Δ104-118}, but the latter could rescue the cristae structure, which suggest that this is not the reason for partial cristae defects found in MIC13^{Δ27-45} and MIC13^{Δ64-83}. We speculate that MIC13^{Δ27-45} and MIC13^{Δ64-83} could partially maintain the cristae structure independent of the MIC10-subcomplex and MICOS assembly. These regions might be important for interactions with other interactors of MIC13. The interaction of MIC13 with outer membrane proteins like SAMM50, MTX1, and MTX2, and matrix proteins GK, DNAJC1, and TMEM11 was shown before [39]. One of the limitations of this study could be the lower expression levels and possible variability of expression within the transduced cells, despite that our experimental results provides clear evidence about the residues that are required for the stability and functionality of MIC13.

Using mutational analysis (summarized in Table 2), we identified that GxxxG motif in the N-terminus and a WN motif in the middle region are essential for stability of MIC13 and MIC10-subcomplex, interaction with other MICOS subunits and cristae morphology. Using homology sequence alignment, WN was indicated as the most conserved motif in MIC13 across all the species analysed [3]. It was found to be preceded by charged amino acids [3], which are R and D in case of humans. The W of the WN was suggested to be the associated with a pattern of conserved hydrophobic residues at the distances of 3/4 amino acids which indicate appearance of an amphipathic helix [3]. On the other hand, the GxxxG motif in the transmembrane region of MIC13 is a well-known dimerization motif, with ~12% of transmembrane helices presenting this motif [46,47]. Here, we found that GxxxG motif is important for the stability of MIC13 as well as for the interaction with other MICOS components. This glycine-rich motif is known to promote protein-protein interaction between helical transmembrane structures [45,48]. Furthermore, mutations of the conserved glycine to leucine in this motif in subunit e of the yeast F₁F₀-ATP synthase leads to a defect in oligomerization [49]. Another MICOS component MIC10 is also known to harbour a conserved glycine rich sequence (GxGxGxG) in the transmembrane region that plays a crucial role for MIC10 oligomerization, which contributes to its membrane shaping ability and ultimately to proper mitochondrial ultrastructure [36]. In many cases, the presence of GxxxG motifs hints at dimerization of the protein due to the interaction of two transmembrane domains and this has been shown for more than 20 different proteins [50]. The formation and stabilization of homodimeric helices containing such a motif could be favoured by steric reasons or alternatively by the existence of a weak hydrogen bond formation via Cα-H...O=C located in a single region and the GxxxG dimer have a right-handed parallel conformation, packed as a compact helix-helix structure [51]. Using infrared spectroscopy, the stretching mode of CD2 of Cα-H donor in the Glycophorin A transmembrane domain was estimated to be about -0.88 kcal/mol contributed by such a weak hydrogen bond [52]. Contrary to the previous observation, the mutation of a Cα-H...O side chain hydroxyl acceptor (Thr-24) in the multispanned transmembrane protein, bacteriorhodopsin, revealed that this hydrogen bond was not stabilizing [53]. The precise function of hydrogen bonding in transmembrane protein folding and homodimerization is still not well established, regardless of whether the donor is a Cα-H or a more

"canonical" N-H or O-H group [54]. The GxxxG motif can also be important for interactions between transmembrane domains of different proteins, even if this motif is only present in one of the two interacting helices [55]. In certain instances, GxxxG motif can play regulatory role as it has also been linked to aggregation of β amyloid and induction of neurotoxicity in Alzheimer's disease [56]. Mutation in either one of the residues i.e. MIC13^{G15L} or MIC13^{G19L} do not substantially alter the function, but MIC13^{G15L,G19L} completely disrupts the function of MIC13, suggesting both substitutions are required to impart the functional consequence of GxxxG mutation in MIC13. We showed using alkaline extraction methods that MIC13^{G15L,G19L} is less associated to the membrane than MIC13-FLAG, indicating the importance of the GxxxG motif for the insertion of MIC13 into the membrane. This is in line with the literature that also postulates other roles of the GxxxG motif, for example in protein interaction, lipid interactions, correct orientation of the soluble domain, and also cell localization [57-59]. Interestingly MIC13^{G15L,G19L} showed a second band in western blot analysis, which had a stronger association to the membrane and migrated at a higher molecular weight than MIC13. We speculate that the mutation in the GxxxG motif could prevent cleavage of the precursor sequence or efficient import of the protein and this second band could therefore be a precursor or an import intermediate. Another possibility would be that it represents a posttranslational modification of the protein or alternative folding of the mutated MIC13 that renders it insoluble to alkaline extraction and alters its running behaviour in the SDS-PAGE.

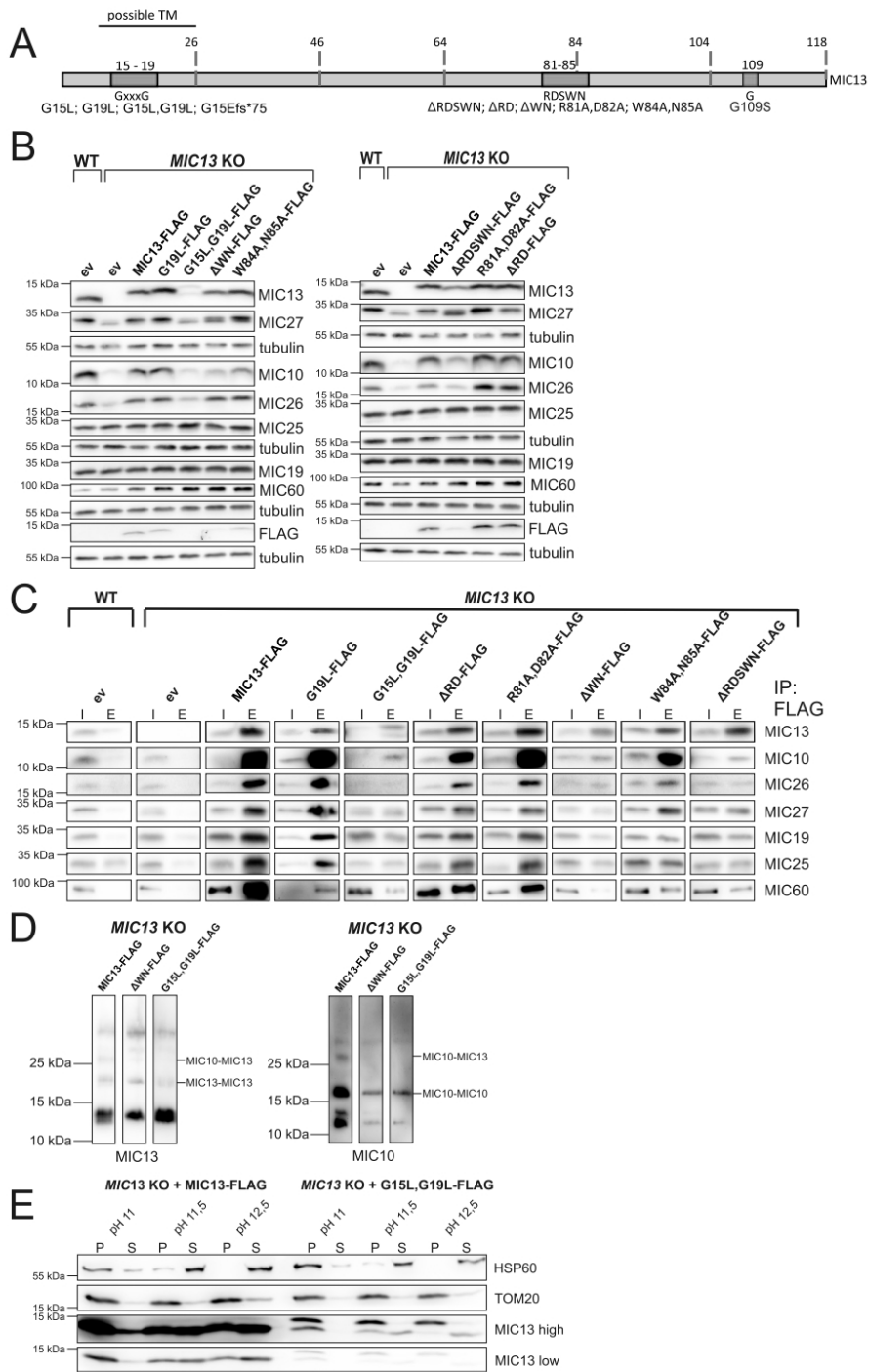
A conserved glycine in the MIC13 sequence was found to be mutated in Rhodesian ridgeback dogs diagnosed with cardiac arrhythmia [42]. Overexpression of the similar mutations MIC13^{G199S} in *MIC13* KO cell lines didn't show any defect in stability of MICOS subunits or cristae morphology, indicating that this mutation doesn't affect the stability of MIC13 or other MICOS components (Fig. S2). Though further experiments will be required to understand how this mutation causes the severe cardiac arrhythmia in dogs, the following can explain why we didn't observe any defects in MIC13^{G199S}. A) This specific mutation could have an organism-specific (only dogs) or tissue-specific role, for example, cardiac cells with more energy demands are more prone to mitochondrial defects. B) Mutation affects unidentified function of MIC13 that could be independent to its role in cristae and MICOS biogenesis and could be mediated by yet unidentified interactors of MIC13.

Overall, we found that distinct conserved residues, GxxxG and WN in MIC13 play an important role in the assembly of the MICOS. These results lead to the postulation of a model with MIC13 as a bridge between the MIC60-subcomplex and MIC10-subcomplex and the conserved GxxxG and WN motif as interaction sites to these subcomplexes. With the introduction of mutated versions into a *MIC13* KO cell line we found a powerful tool to identify and study the functional motifs in MIC13. This study helps to extend our understanding on the role and the molecular function of MIC13 which is important to determine due to the increasing numbers of patients associated with MIC13 deficiency [25-29].

4. Materials and methods

4.1. Cell lines, cell culture, and transfection

All the cells were cultured using Dulbecco's Modified Eagle's Medium (DMEM, D5546, Sigma) with 1 g/L of glucose supplemented with 10% fetal bovine serum (PAN biotech), 2 mM glutamax (Gibco), 1 mM sodium pyruvate (Gibco) and 1% penicillin and streptomycin (Gibco), incubated at 37 °C at 5% CO₂. *MIC13* KO HEK-293T and *MIC13* KO HeLa cells were described before [11,38]. Cells were transfected with 1 μg of corresponding plasmid using GeneJuice (Novagen) according to the manufacturer's instruction.



(caption on next page)

Fig. 6. MIC13 have conserved regions that affects MICOS levels and interactions. (A) Schematic overview highlighting the conserved motifs in MIC13 and their respective mutations that were generated. All variants were created with a FLAG tag. (B) RIPA lysates of HEK-293T WT or *MIC13* KO stable cell lines expressing pMSCVpuro empty vector (ev) or respective MIC13-FLAG mutant variant. Western blot was decorated with antibodies against MIC13, MIC27, tubulin, MIC10, MIC26, MIC25, MIC19, MIC60, and FLAG. (C) Co-immunoprecipitation with mitochondria isolated from HEK-293T WT or *MIC13* KO stable cell lines expressing pMSCVpuro empty vector (ev) or respective MIC13-FLAG variants. Pull-down was performed with FLAG antibody and decorated with MIC13/FLAG, MIC10, MIC26, MIC27, MIC19, MIC25, and MIC60. (D) Crosslinking of isolated mitochondria from HEK-293T *MIC13* KO stable cell lines expressing pMSCVpuro empty vector (ev) or respective MIC13-FLAG variant by treatment with 1 mM DSG for 1 h. Western blots are stained with antibodies against MIC10 and MIC13. A common band marked by MIC10 and MIC13 was identified as a crosslink between MIC10 and MIC13. This crosslink between MIC13 and MIC10 was not present in MIC13^{G15L,G19L} and MIC13^{ΔWN} variant of MIC13. (E) Alkaline extraction of freshly isolated mitochondria from HEK-293T *MIC13* KO stable cell lines expressing MIC13-FLAG and MIC13^{G15L,G19L}. Alkaline extraction was performed at pH 11, pH 11.5, and pH 12 and after centrifugation supernatant (S) and pellet fraction (P) were subjected to western blot. Proteins were visualized with antibodies against HSP60, TOM20, and MIC13 (two different exposures are shown here).

4.2. Molecular cloning

Human *MIC13-FLAG* was cloned into pMSCVpuro vector [20] using Gibson Assembly Cloning Kit (NEB). Deletions across the whole sequence of *MIC13-FLAG* were obtained with Site-directed, Ligase-Independent Mutagenesis (SLIM) [44]. Point mutations and other deletions were obtained with the Q5 mutagenesis kit (NEB) using manufacturer's protocols.

4.3. Generating stable cells with viral transduction

For viral transduction, Plat-E cells were transfected with 1.9 µg of the respective pMSCVpuro-based plasmid and 1 µg pVSV-G as described earlier [20] using FuGENE6 transfection reagent (Promega) according to the manufacturer's instruction. After 48 h the supernatant of these cells was added to HEK-293T WT and *MIC13* KO cells and incubated for at least 24 h before addition of selection medium with 1 µg/mL puromycin.

4.4. SDS electrophoresis and western blotting

Cells were scraped in PBS and proteins were extracted with RIPA lysis buffer. Protein concentration was determined by Lowry method (Bio-Rad) and samples were prepared with Laemmli loading buffer. For protein separation, 10% SDS-PAGE, 15% SDS-PAGE or 4%–20% gradient SDS-PAGE (BioRad) were used. The proteins were subsequently transferred on a nitrocellulose membrane and probed with following antibodies: MIC10 (Abcam, 84969), MIC13 (custom made by Pineda (Berlin) against human MIC13 peptide CKAREYSKEGWYVKARTK), MIC19 (Proteintech, 25625-1-AP), MIC25 (Proteintech, 20639-1-AP), MIC26 (ThermoFisher Scientific, MA5-15493 or custom made by Pineda (Berlin) against human MIC26 peptide CQETYSQTKPKMQ), MIC27 (Atlas Antibodies, HPA000612), MIC60 (custom made by Pineda (Berlin) against human MIC60 peptide CTDHPEIGEGKPTALSEEAS), FLAG (Sigma, F3165), TOM20 (Santa Cruz Biotechnology, sc-114115), beta-tubulin (Cell Signalling Technology, 2128S), HSP60 (sigma,

SAB4501464), Prohibitin (LSBio, LS-B2316-50). Chemiluminescent signal was recorded with VILBER LOURMAT Fusion SL (Peqlab) and quantification was performed with Image Studio Lite Ver 5.2.

4.5. Mitochondrial isolation and carbonate extraction

Cells were cultured in petri dishes, scraped with a cell scraper in PBS (Sigma), and pelleted at 500 g for 5 min. The pellet was resuspended in an isotonic buffer (220 mM mannitol, 70 mM sucrose, 1 mM EDTA, 20 mM HEPES (pH 7.5) and 1 × protease inhibitor cocktail (Roche)) with 0.1% BSA (Roth) and incubated on ice for 10 min. Cells were homogenized by mechanical rupture using a syringe with a 21 G cannula and repeatedly soaking the suspension in and releasing it in a stroke for 20 times. Lysed cells were centrifuged at 1000g and 4 °C for 10 min. The supernatant was then centrifuged at 10,000g and 4 °C for 15 min and the pellet was resuspended in the isotonic buffer to obtain crude mitochondria. Mitochondria were divided into aliquots and frozen using freezing buffer (300 M trehalose, 10 mM KCl, 1 mM EDTA, 10 mM HEPES and 0.1% BSA). For carbonate extraction 50 µg mitochondria were used directly after isolation and centrifuged at 10,000g and 4 °C for 10 min. The pellet was resuspended in 100 mM freshly prepared sodium carbonate at different pH and incubated on ice for 30 min. After centrifugation at 21,000g and 4 °C for 20 min, supernatant and pellet were collected and subjected to SDS electrophoresis.

4.6. Isolation of macromolecular complexes by blue native gels

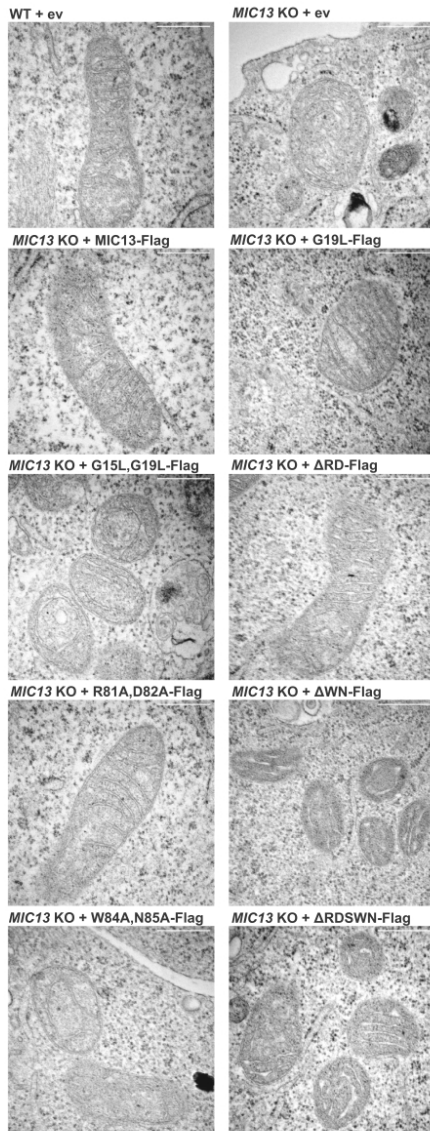
Mitochondrial aliquots of 150 µg were pelleted and resuspended in 15 µL isotonic buffer (50 mM NaCl, 2 mM aminohexanoic acid, 50 mM imidazole/HCl pH 7, 1 mM EDTA, protease inhibitor cocktail). 3 µL 10% Digitonin (Serva) was added to reach a detergent to protein ratio of 2 g/g and incubated on ice for 10 min. After centrifugation at 21,000g and 4 °C for 20 min, 4 µL of 50% glycerol and 1.5 µL of 1% Coomassie brilliant blue G-250 with 10% glycerol was added and samples were loaded on a 3%–18% gradient gel. Protein complexes were transferred to a PVDF

Table 2
Overview of phenotypes observed in various mutation variants of MIC13.

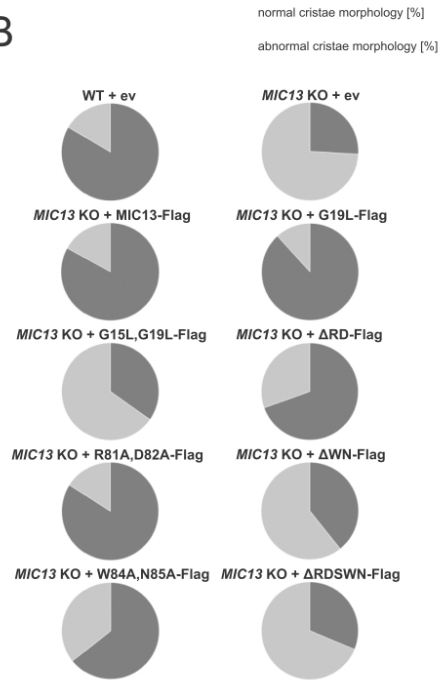
Variant	Stability	Restore MIC10 levels	Restore MIC26 levels	Restore MIC27 levels	Incorporation in MIC10-subcomplex	Size restoration of MIC60-subcomplex	Interaction MIC10-subcomplex	Interaction MIC60-subcomplex	Cristae morphology rescue
MIC13-FLAG	+++	+++	+++	+++	+++	+++	+++	+++	+++
MIC13 ^{G15L}	+++	+++	+++	+++	+++	+++	+++	+++	+++
MIC13 ^{G15L}	+++	+++	+++	+++	nd	nd	nd	nd	nd
MIC13 ^{G15L,G19L}	+	–	–	+	–	–	–	–	–
MIC13 ^{G15E6+75}	–	–	–	–	nd	nd	nd	nd	nd
MIC13 ^{ΔRDSWN}	++	–	+	++	–	+	–	–	–
MIC13 ^{ΔRD}	+++	+++	+	++	+++	++	+++	+++	++
MIC13 ^{ΔWN}	++	–	++	++	–	–	–	–	–
MIC13 ^{W54A, N58A}	+++	+	+++	++	++	++	+++	+	++
MIC13 ^{R81A, D62A}	+++	+++	+++	+++	+++	+++	+++	+++	+++
MIC13 ^{G109S}	+++	+++	+++	+++	nd	nd	nd	nd	+++

nd = not determined.

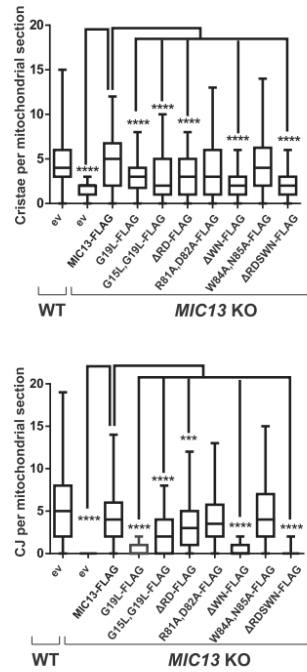
A



B



C



(caption on next page)

Fig. 7. Conserved regions of MIC13 are important for mitochondrial ultrastructure. (A) Representative EM pictures of HEK-293T WT or MIC13 KO stable cell lines expressing pMSCVpuro empty vector (ev) or respective MIC13-FLAG mutant variant. Scale bar 0.5 μm . (B) Quantification of normal versus abnormal cristae morphology in percentage represented as a pie chart from all imaged mitochondria in HEK-293T stable cell lines expressing pMSCVpuro empty vector (ev) or respective MIC13-FLAG mutant variant using EM. (C) Quantification of cristae and CJs per mitochondrial section from different mitochondria in HEK-293T WT or MIC13 KO stable cell lines expressing pMSCVpuro empty vector (ev) or respective MIC13-FLAG mutant variant using EM represented as boxplots. Boxplots show median and interquartile range from 25 to 75 percentile, and whiskers represent minimum and maximum value. Data from $n = 87$ to 150 mitochondria from two biological replicates. Student's *t*-test was used for statistical analysis.

membrane and probed with following antibodies: MIC10 (Abcam, 84969), MIC25 (Proteintech, 20639-1-AP), MIC27 (Atlas Antibodies, HPA000612), MIC60 (custom made by Pineda (Berlin) against human MIC60 peptide CTDHPEIGEGKTPALSEEAS). Chemiluminescent signal was recorded with VILBER LOURMAT Fusion SL (Peqlab).

4.7. Co-immunoprecipitation and crosslinking experiment

For co-immunoprecipitation mitochondrial aliquots of 250 μg were pelleted and resuspended in an isotonic buffer (150 mM NaCl, 10 mM Tris/HCl (pH 7.5), 5 mM EDTA, protease inhibitor cocktail). 5 μL 10% Digitonin (Serva) was added to reach a detergent to protein ratio of 2 g/g and incubated on ice for 10 min. After centrifugation at 21,000g and 4 °C for 20 min, the input was subjected to the respective beads. For co-IP with Flag anti-Flag M2 affinity beads (Sigma) were used, for Co-IP with MIC60, protein A sepharose beads (ThermoFisher Scientific, 101041) were incubated over night with MIC60 (custom made by Pineda (Berlin) against human MIC60 peptide CTDHPEIGEGKTPALSEEAS). Before addition of the input on the beads, the beads were washed with PBS and with the isotonic buffer with the same concentration of digitonin. Beads were incubated with the sample for at least 4 h at 4 °C and washed with the isotonic buffer with 0.01% digitonin. Proteins were eluted with Laemmli buffer without beta-mercaptoethanol at 65 °C for 10 min. After separating the elution from the beads 1 μL beta-mercaptoethanol was added to the elution and samples were subjected to SDS electrophoresis and western blotting.

For crosslinking experiments, isolated mitochondria were resuspended in 2 mM DSG (ThermoFisher Scientific) in PBS and were incubated for 1 h at room temperature. Crosslink was stopped with the addition of TRIS (pH 7.5) to a total concentration of 50 mM and 15 min of incubation. Samples were centrifuged for 10 min at 4 °C and 10,000 g and the pellet was dissolved in Laemmli buffer and subjected to SDS PAGE and western blot analysis.

4.8. Electron microscopy

Cells were grown on petri dishes until they reached 80% confluency. Chemical fixation using 3% glutaraldehyde buffered with 0.1 M sodium cacodylate buffer, pH 7.2 was performed on the petri dish, followed by scraping the cells using a cell scraper and collecting them as a pellet. The pellet was washed with 0.1 M sodium cacodylate, pH 7.2, and subsequently embedded in 2% agarose. The cells were stained with 1% osmium tetroxide for 50 min followed by 1% uranyl acetate/1% phosphotungstic acid for 1 h. For dehydration graded acetone series was used and the samples were embedded in spur epoxy resin for polymerization at 65 °C for 24 h. The ultrathin sections were prepared using microtome and images were acquired using transmission electron microscope (Hitachi, H600) at 75 V equipped with Bioscan model 792 camera (Gatan) and analysed with ImageJ software. The data was analysed by Graph Pad Prism 7 and outliers were removed.

4.9. Dual-colour STED nanoscopy

For imaging with stimulated emission depletion super resolution nanoscopy stable transfected HEK-293T cells were fixed in 4% paraformaldehyde, permeabilized with 0.15% Triton-X100 and blocked using 10% goat serum, followed by incubation with antibodies against MIC60 (custom made by Pineda (Berlin) against human MIC60 peptide

CTDHPEIGEGKTPALSEEAS) and FLAG (Sigma, F3165) over night at 4 °C. Cells were washed three times with PBS and incubated with secondary antibody goat anti-rabbit Abberior STAR 635P (Abberior, ST635P-1001) and goat anti-mouse Abberior STAR 580 (Abberior, ST580-1001) for 1 h at room temperature. Cells were imaged as described before [11].

Author contributions

J Urbach: investigation, methodology, data curation, formal analysis, visualization, writing- original draft.

AK Kondadi: data curation, formal analysis, supervision, validation, investigation, visualization, methodology.

C David: investigation, methodology, formal analysis.

R Naha: investigation, methodology, formal analysis, writing- review and editing.

K Deinert: investigation, methodology.

AS Reichert: conceptualization, data curation, supervision, funding acquisition, investigation, project administration, writing - review and editing.

R Anand: conceptualization, data curation, formal analysis, supervision, investigation, visualization, methodology, funding acquisition, project administration, writing - original draft, writing - review and editing.

Declaration of competing interest

The authors declare that they have no known competing financial interests or personal relationships that could have appeared to influence the work reported in this paper.

Acknowledgements

We thank Andrea Borchardt for her excellent technical assistance in electron microscopy experiments and in cell culture. STED nanoscopy experiments were performed at Centre for Advanced Imaging (CAI) facility, Düsseldorf. The research was supported by funding from Medical faculty of Heinrich Heine University Düsseldorf, Foko-02/2015 (RA & ASR) and FoKo-37/2015 (AKK), and Deutsche Forschungsgemeinschaft (DFG) grant, AN 1440/3-1 (RA) and RE 1575/2-1 (ASR). Data were partly collected within the Collaborative Research Center 1208: Identity and dynamics of membrane systems – from molecules to cellular functions funded by the Deutsche Forschungsgemeinschaft (DFG, German Research Foundation) – Project-ID 267205415 – SFB 1208 - project B12 (ASR).

Appendix A. Supplementary data

Supplementary data to this article can be found online at <https://doi.org/10.1016/j.bbmem.2021.183683>.

References

- [1] F. Vogel, C. Børnhovd, W. Neupert, A.S. Reichert, Dynamic subcompartmentalization of the mitochondrial inner membrane, *J. Cell Biol.* 175 (2006) 237–247.
- [2] C.A. Wurm, S. Jakobs, Differential protein distributions define two sub-compartments of the mitochondrial inner membrane in yeast, *FEBS Lett.* 580 (2006) 5628–5634.

- [3] M.A. Huynen, M. Muhlmeister, K. Gotthardt, S. Guerrero-Castillo, U. Brandt, Evolution and structural organization of the mitochondrial contact site (MICOS) complex and the mitochondrial intermembrane space bridging (MIB) complex, *Biochim. Biophys. Acta* 1863 (2016) 91–101.
- [4] C.A. Mannella, W.J. Lederer, M.S. Jafri, The connection between inner membrane topology and mitochondrial function, *J. Mol. Cell. Cardiol.* 62 (2013) 51–57.
- [5] C.A. Mannella, D.R. Pfeiffer, P.C. Bradshaw, I.I. Moraru, B. Slepchenko, L.M. Loew, et al., Topology of the mitochondrial inner membrane: dynamics and bioenergetic implications, *IUBMB Life* 52 (2001) 93–100.
- [6] C.A. Mannella, The relevance of mitochondrial membrane topology to mitochondrial function, *Biochim. Biophys. Acta* 1762 (2006) 140–147.
- [7] D.M. Wolf, M. Segawa, A.K. Kondadi, R. Anand, S.T. Bailey, A.S. Reichert, et al., Individual cristae within the same mitochondrion display different membrane potentials and are functionally independent, *EMBO J.* 38 (2019), e101056.
- [8] L. Scorrano, M. Ashiya, K. Buttler, S. Weiler, S.A. Oakes, C.A. Mannella, et al., A distinct pathway remodels mitochondrial cristae and mobilizes cytochrome c during apoptosis, *Dev. Cell* 2 (2002) 55–67.
- [9] C. Wang, M. Taki, Y. Sato, Y. Tamura, H. Yaginuma, Y. Okada, et al., A photostable fluorescent marker for the superresolution live imaging of the dynamic structure of the mitochondrial cristae, *Proc. Natl. Acad. Sci. U. S. A.* 116 (2019) 15817–15822.
- [10] T. Stephan, A. Roesch, D. Riedel, S. Jakobs, in: *Live-cell STED Microscopy of Mitochondrial Cristae*, 2019, p. 640920, bioRxiv.
- [11] A.K. Kondadi, R. Anand, S. Hansch, J. Urbach, T. Zobel, D.M. Wolf, et al., Cristae undergo continuous cycles of membrane remodeling in a MICOS-dependent manner, *EMBO Rep.* 21 (2020), e49776.
- [12] X. Huang, J. Fan, L. Li, H. Liu, R. Wu, Y. Wu, et al., Fast, long-term, super-resolution imaging with hessian structured illumination microscopy, *Nat. Biotechnol.* 36 (2018) 451–459.
- [13] A.K. Kondadi, R. Anand, A.S. Reichert, Cristae membrane dynamics - a paradigm change, *Trends Cell Biol.* 30 (2020) 923–936.
- [14] R. Rabl, V. Soubannier, R. Scholz, F. Vogel, N. Mendi, A. Vasiljev-Neumeyer, et al., Formation of cristae and crista junctions in mitochondria depends on antagonism between Fcjl1 and su e/g, *J. Cell Biol.* 185 (2009) 1047–1063.
- [15] K. von der Malsburg, J.M. Muller, M. Bohnert, S. Oeljeklaus, P. Kwiatkowska, T. Becker, et al., Dual role of mitofilin in mitochondrial membrane organization and protein biogenesis, *Dev. Cell* 21 (2011) 694–707.
- [16] M. Harner, C. Korner, D. Walther, D. Mokranjac, J. Kaesmacher, U. Welsch, et al., The mitochondrial contact site complex, a determinant of mitochondrial architecture, *EMBO J.* 30 (2011) 4356–4370.
- [17] S. Hoppins, S.R. Collins, A. Cassidy-Stone, E. Hummel, R.M. Devay, L.L. Lackner, A mitochondrial-focused genetic interaction map reveals a scaffold-like complex required for inner membrane organization in mitochondria, *J. Cell Biol.* 195 (2011) 323–340.
- [18] N. Pfanner, M. van der Laan, P. Amati, R.A. Capaldi, A.A. Caudy, A. Chacinska, et al., Uniform nomenclature for the mitochondrial contact site and cristae organizing system, *J. Cell Biol.* 204 (2014) 1083–1086.
- [19] S. Khosravi, M.E. Harner, The MICOS complex, a structural element of mitochondria with versatile functions, *Biol. Chem.* 401 (2020) 765–778.
- [20] R. Anand, A.K. Kondadi, J. Meisterknecht, M. Golombek, O. Nortmann, J. Riedel, et al., MIC26 and MIC27 cooperate to regulate cardiolipin levels and the landscape of OXPHOS complexes, *Life Sci. Alliance*. 3 (2020).
- [21] R.M. Zerbes, I.J. van der Klei, M. Veenhuis, N. Pfanner, M. van der Laan, M. Bohnert, Mitofilin complexes: conserved organizers of mitochondrial membrane architecture, *Biol. Chem.* 393 (2012) 1247–1261.
- [22] L. Colina-Tenorio, P. Horten, N. Pfanner, H. Rampelt, Shaping the mitochondrial inner membrane in health and disease, *J. Intern. Med.* 287 (2020) 645–664.
- [23] M.J. Eramo, V. Lisnyak, L.E. Formosa, M.T. Ryan, The ≈mitochondrial contact site and cristae organising system≈ (MICOS) in health and human disease, *J. Biochem.* 167 (2020) 243–255.
- [24] P.I. Tsai, C.H. Lin, C.H. Hsieh, A.M. Papakyriakos, M.J. Kim, V. Napolioni, et al., PINK1 phosphorylates MIC60/Mitofilin to control structural plasticity of mitochondrial crista junctions, *Mol. Cell* 69 (744–56) (2018), e6.
- [25] J. Godlker, M. Gruneberg, I. DuChesne, J. Reunert, S. Rust, C. Westermann, et al., QIL1-dependent assembly of MICOS complex-lethal mutation in C19ORF70 resulting in liver disease and severe neurological retardation, *J. Hum. Genet.* 63 (2018) 707–716.
- [26] B.E. Russell, K.G. Whaley, K.E. Bove, A. Labilloy, R.C. Lombardo, R.J. Hopkin, et al., Expanding and underscoring the hepato-encephalopathic phenotype of QIL1/MIC13, *Hepatology* 70 (2019) 1066–1070.
- [27] A. Zeharia, J.R. Friedman, A. Tobar, A. Saada, O. Konen, Y. Fellig, et al., Mitochondrial hepato-encephalopathy due to deficiency of QIL1/MIC13 (C19orf70), a MICOS complex subunit, *Eur. J. Hum. Genet.* 24 (2016) 1778–1782.
- [28] V. Guarani, C. Jardel, D. Chretien, A. Lombes, P. Benit, C. Labasse, et al., QIL1 mutation causes MICOS disassembly and early onset fatal mitochondrial encephalopathy with liver disease, *elife* 5 (2016).
- [29] Y. Kishita, M. Shimura, M. Kohda, M. Akita, A. Imai-Okazaki, Y. Yatsuka, et al., A novel homozygous variant in MICOS13/QIL1 causes hepato-encephalopathy with mitochondrial DNA depletion syndrome, *Mol. Genet. Genomic Med.* 8 (2020), e1427.
- [30] C. Beninca, V. Zanette, M. Brischigliaro, M. Johnson, A. Reyes, D.A.D. Valle, et al., Mutation in the MICOS subunit gene APOO (MIC26) associated with an X-linked recessive mitochondrial myopathy, lactic acidosis, cognitive impairment and autistic features, *J. Med. Genet.* 58 (2021) 155–167.
- [31] H. Rampelt, R.M. Zerbes, M. van der Laan, N. Pfanner, Role of the mitochondrial contact site and cristae organizing system in membrane architecture and dynamics, *Biochim. Biophys. Acta Mol. Cell Res.* 1864 (2017) 737–746.
- [32] C. Ott, K. Ross, S. Straub, B. Thiede, M. Gotz, C. Goomann, et al., Sam50 functions in mitochondrial intermembrane space bridging and biogenesis of respiratory complexes, *Mol. Cell Biol.* 32 (2012) 1173–1188.
- [33] J. Xie, M.F. Marusch, P. Souda, J. Whitelegge, R.A. Capaldi, The mitochondrial inner membrane protein mitofilin exists as a complex with SAM50, metaxins 1 and 2, coiled-coil-helix coiled-coil-helix domain-containing protein 3 and 6 and DnaJC11, *FEBS Lett.* 581 (2007) 3545–3549.
- [34] M. Hessenberger, R.M. Zerbes, H. Rampelt, S. Kunz, A.H. Xavier, B. Purfurst, et al., Regulated membrane remodeling by Mic60 controls formation of mitochondrial crista junctions, *Nat. Commun.* 8 (2017) 15258.
- [35] D. Tarasenko, M. Barbot, D.C. Jans, B. Kroppen, B. Sadowski, G. Heim, et al., The MICOS component Mic60 displays a conserved membrane-bending activity that is necessary for normal cristae morphology, *J. Cell Biol.* 216 (2017) 889–899.
- [36] M. Bohnert, R.M. Zerbes, K.M. Davies, A.W. Muhleip, H. Rampelt, S.E. Horvath, et al., Central role of Mic10 in the mitochondrial contact site and cristae organizing system, *Cell Metab.* 21 (2015) 747–755.
- [37] M. Barbot, D.C. Jans, C. Schulz, N. Denkert, B. Kroppen, M. Hoppert, et al., Mic10 oligomerizes to bend mitochondrial inner membranes at crista junctions, *Cell Metab.* 21 (2015) 756–763.
- [38] R. Anand, V. Strecker, J. Urbach, I. Wittig, A.S. Reichert, Mic13 is essential for formation of crista junctions in mammalian cells, *PLoS One.* 11 (2016), e0160258.
- [39] V. Guarani, McNeill EM, J.A. Paulo, E.L. Huttlin, F. Frohlich, S.P. Gygi, QIL1 is a novel mitochondrial protein required for MICOS complex stability and cristae morphology, *elife* (2015) 4.
- [40] K. Eyd, K.M. Davies, C. Behrendt, I. Wittig, A.S. Reichert, Cristae architecture is determined by an interplay of the MICOS complex and the F1FO ATP synthase via Mic27 and Mic10, *Microb. Cell* 4 (2017) 259–272.
- [41] R.M. Zerbes, P. Hoss, N. Pfanner, M. van der Laan, M. Bohnert, Distinct roles of Mic12 and Mic27 in the mitochondrial contact site and cristae organizing system, *J. Mol. Biol.* 428 (2016) 1485–1492.
- [42] K.M. Meurs, S.G. Friedenberg, N.J. Olby, J. Condit, J. Weidman, S. Rosenthal, et al., A QIL1 variant associated with ventricular arrhythmias and sudden cardiac death in the juvenile rhodesian ridgeback dog, *Genes (Base)* 10 (2019).
- [43] J. Chiu, P.E. March, R. Lee, D. Tillett, Site-directed, ligase-independent mutagenesis (SLIM): a single-tube methodology approaching 100% efficiency in 4 h, *Nucleic Acids Res.* 32 (2004), e174.
- [44] J. Chiu, D. Tillett, I.W. Davies, P.E. March, Site-directed, ligase-independent mutagenesis (SLIM) for highly efficient mutagenesis of plasmids greater than 8kb, *J. Microbiol. Methods* 73 (2008) 195–198.
- [45] W.P. Russ, D.M. Engelman, The GxxxG motif: a framework for transmembrane helix-helix association, *J. Mol. Biol.* 296 (2000) 911–919.
- [46] A. Senes, M. Gerstein, D.M. Engelman, Statistical analysis of amino acid patterns in transmembrane helices: the GxxxG motif occurs frequently and in association with beta-branched residues at neighboring positions, *J. Mol. Biol.* 296 (2000) 921–936.
- [47] S. Unterreitmeier, A. Fuchs, T. Schaffner, R.G. Heym, D. Frisman, D. Langosch, Phenylalanine promotes interaction of transmembrane domains via GxxxG motifs, *J. Mol. Biol.* 374 (2007) 705–718.
- [48] A. Senes, D.E. Engel, W.F. DeGrado, Folding of helical membrane proteins: the role of polar, GxxxG-like and proline motifs, *Curr. Opin. Struct. Biol.* 14 (2004) 465–479.
- [49] G. Arselin, M.F. Giraud, A. Dautant, J. Vaillier, D. Brethes, B. Coulyar-Salin, et al., The GxxxG motif of the transmembrane domain of subunit e is involved in the dimerization/oligomerization of the yeast ATP synthase complex in the mitochondrial membrane, *Eur. J. Biochem.* 270 (2003) 1875–1884.
- [50] M.G. Teese, D. Langosch, Role of GxxxG motifs in transmembrane domain interactions, *Biochemistry* 54 (2015) 5125–5135.
- [51] B.K. Mueller, S. Subramaniam, A. Senes, A frequent, GxxxG-mediated, transmembrane association motif is optimized for the formation of interhelical Ca-H hydrogen bonds, *Proc. Natl. Acad. Sci. U. S. A.* 111 (2014) E888–E895.
- [52] E. Arbely, I.T. Arkin, Experimental measurement of the strength of a C alpha-H...O bond in a lipid bilayer, *J. Am. Chem. Soc.* 126 (2004) 5362–5363.
- [53] S. Yohannan, S. Faham, D. Yang, D. Grosfeld, A.K. Chamberlain, J.U. Bowie, A C alpha-H...O hydrogen bond in a membrane protein is not stabilizing, *J. Am. Chem. Soc.* 126 (2004) 2284–2285.
- [54] J.U. Bowie, Membrane protein folding: how important are hydrogen bonds? *Curr. Opin. Struct. Biol.* 21 (2011) 42–49.
- [55] T.L. Lau, C. Kim, M.H. Ginsberg, T.S. Ulmer, The structure of the integrin alphaIIb beta3 transmembrane complex explains integrin transmembrane signalling, *EMBO J.* 28 (2009) 1351–1361.
- [56] D. Sarkar, I. Chakraborty, M. Condorelli, B. Ghosh, T. Mass, M. Weingarh, et al., Self-assembly and neurotoxicity of beta-amyloid (21–40) peptide fragment: the regulatory role of GxxxG motifs, *ChemMedChem* 15 (2020) 293–301.
- [57] M. Stangl, D. Schneider, Functional competition within a membrane: lipid recognition vs. transmembrane helix oligomerization, *Biochim. Biophys. Acta* 1848 (2015) 1886–1896.
- [58] B.C. Monk, T.M. Tomasiak, M.V. Keniya, F.U. Huschmann, J.D. Tyndall, J. D. O'Connell 3rd, et al., Architecture of a single membrane spanning cytochrome P450 suggests constraints that orient the catalytic domain relative to a bilayer, *Proc. Natl. Acad. Sci. U. S. A.* 111 (2014) 3865–3870.
- [59] P. Cosson, J. Perrin, J.S. Bonifacino, Anchors aweigh: protein localization and transport mediated by transmembrane domains, *Trends Cell Biol.* 23 (2013) 511–517.

5.2. Mitochondrial Apolipoprotein MIC26 is a metabolic rheostat regulating central cellular fuel pathways

1 **Mitochondrial Apolipoprotein MIC26 is a metabolic rheostat**
2 **regulating central cellular fuel pathways**

3 Melissa Lubeck¹, Ritam Naha¹, Yulia Schaumkessel¹, Philipp Westhoff^{2,3}, Anja Stefanski⁴,
4 Patrick Petzsch⁵, Kai Stühler^{4,6}, Karl Köhrer⁵, Andreas P. M. Weber^{2,3}, Ruchika Anand¹,
5 Andreas S. Reichert¹, Arun Kumar Kondadi^{1*}

6 ¹Institute of Biochemistry and Molecular Biology I, Medical Faculty and University Hospital
7 Düsseldorf, Heinrich Heine University Düsseldorf, Düsseldorf, Germany

8 ²Institute of Plant Biochemistry, Cluster of Excellence on Plant Sciences (CEPLAS), Heinrich
9 Heine University Düsseldorf, Düsseldorf, Germany

10 ³Plant Metabolism and Metabolomics Laboratory, Cluster of Excellence on Plant Sciences
11 (CEPLAS), Heinrich Heine University, D-40225 Düsseldorf, Germany

12 ⁴Molecular Proteomics Laboratory, Medical Faculty and University Hospital, Heinrich Heine
13 University Düsseldorf, Düsseldorf, Germany

14 ⁵Genomics & Transcriptomics Laboratory, BMFZ, Heinrich Heine University Düsseldorf,
15 Düsseldorf, Germany

16 ⁶Institute of Molecular Medicine, Protein Research, Medical Faculty and University Hospital,
17 Heinrich Heine University Düsseldorf, Düsseldorf, Germany

18 Correspondence: kondadi@hhu.de

19 **Summary**

20 Mitochondria play central roles in metabolism and metabolic disorders such as type 2 diabetes.
21 MIC26, a MICOS complex subunit, was linked to diabetes and modulation of lipid metabolism.
22 Yet, the functional role of MIC26 in regulating metabolism under hyperglycemia is not
23 understood. We employed a multi-omics approach combined with functional assays using WT
24 and *MIC26* KO cells cultured in normoglycemia or hyperglycemia, mimicking altered nutrient
25 availability. We show that MIC26 has an inhibitory role in glycolysis and cholesterol/lipid
26 metabolism under normoglycemic conditions. Under hyperglycemia, this inhibitory role is
27 reversed demonstrating that MIC26 is critical for metabolic adaptations. This is partially
28 mediated by alterations of mitochondrial metabolite transporters. Furthermore, *MIC26* deletion
29 led to a major metabolic rewiring of glutamine utilization as well as oxidative phosphorylation.
30 We propose that MIC26 acts as a metabolic 'rheostat', that modulates mitochondrial metabolite
31 exchange via regulating mitochondrial cristae, allowing cells to cope with nutrient overload.

32 **Key words**

33 Mitochondria, Apolipoproteins, MIC26, MICOS complex and Fatty acid metabolism

34 Introduction

35 The increasing prevalence of global obesity is a huge biological risk factor for development of
36 a range of chronic diseases including cardiovascular diseases, musculoskeletal and metabolic
37 disorders (Collaborators *et al*, 2017). At the cellular level, obesity is associated with DNA
38 damage, inflammation, oxidative stress, lipid accumulation and mitochondrial dysfunction
39 (Włodarczyk & Nowicka, 2019). Mitochondria play central roles in anabolic and catabolic
40 pathways (Spinelli & Haigis, 2018) and as a consequence mitochondrial dysfunction is
41 associated with a variety of metabolic diseases such as type 2 diabetes mellitus (T2DM)
42 (Szendroedi *et al*, 2011). Mitochondrial dysfunction is often linked to abnormal mitochondrial
43 ultrastructure (Eramo *et al*, 2020; Kondadi *et al*, 2020b; Zick *et al*, 2009) and abnormal
44 mitochondrial ultrastructure was also associated with diabetes (Bugger *et al*, 2008; Xiang *et al*,
45 2020). Mitochondria harbour two membranes, the mitochondrial outer membrane (OM) and
46 the inner membrane (IM). The part of the IM closely apposed to the OM is termed the inner
47 boundary membrane (IBM) whereas the IM which invaginates towards the mitochondrial matrix
48 is termed the cristae membrane (CM). Crista junctions (CJs) are pore-like structures around
49 12 to 25 nm in diameter, separating the IBM and CM, and are proposed to act as diffusion
50 barriers for proteins and metabolites (Frey & Mannella, 2000; Mannella *et al*, 2013). Formation
51 of CJs depends on Mic60 (Fcj1, Mitofilin, IMMT) which was shown to be located at CJs
52 regulating cristae formation in concert with the F₁F₀ ATP synthase (Rabl *et al*, 2009). Mic60 is
53 a subunit of the 'mitochondrial contact site and cristae organising system' (MICOS) complex
54 (Harner *et al*, 2011; Hoppins *et al*, 2011; von der Malsburg *et al*, 2011) which consists of seven
55 proteins organised into two subcomplexes: MIC60/MIC19/MIC25 and MIC10/MIC26/MIC27
56 with MIC13 stabilizing the MIC10 subcomplex in mammals (Anand *et al*, 2016; Guarani *et al*,
57 2015; Urbach *et al*, 2021). MIC26/APOO harbours an apolipoprotein A1/A4/E family domain
58 and therefore was classified as an apolipoprotein (Koob *et al*, 2015; Lamant *et al*, 2006).
59 Traditionally, apolipoproteins mediate lipid and cholesterol metabolism by facilitating the
60 formation of lipoproteins and regulating their distribution to different tissues via the blood
61 stream (Mehta & Shapiro, 2022). Initially, MIC26 was identified as a protein of unknown
62 function in cardiac transcriptome of dogs fed with high-fat diet (HFD) (Philip-Couderc *et al*,
63 2003) and was incorrectly assumed to exist as a 55 kDa O-linked glycosylated protein as it
64 was immunopositive to a custom-generated MIC26 antibody in samples of human serum, heart
65 tissue and HepG2 cell line (Lamant *et al*, 2006). However, the recombinant protein was only
66 observed at the expected size of 22 kDa (Lamant *et al*, 2006) and it was later shown that this
67 22 kDa form is located to mitochondria (Koob *et al*, 2015; Ott *et al*, 2015). Moreover, using
68 several cellular MIC26 deletion models and different antibodies, we showed recently that
69 MIC26 is exclusively present as a 22 kDa mitochondrial protein and not as a 55 kDa protein
70 (Lubeck *et al*, 2023). In light of these findings, the primary physiological function of MIC26 in

71 diabetes is linked to its role in the mitochondrial IM and not to an earlier proposed secreted
72 form of MIC26.

73 Mutations in *MIC26* were reported to result in mitochondrial myopathy, lactic acidosis and
74 cognition defects (Beninca *et al*, 2021) as well as a lethal progeria-like phenotype (Peifer-Weiß
75 *et al*, 2023). Interestingly, there is an intricate connection between MIC26 and metabolic
76 disorders. Patients with diabetes (Lamant *et al.*, 2006) and dogs fed with a HFD for 9 weeks
77 (Philip-Couderc *et al.*, 2003) showed increased *Mic26* transcripts in the heart. Accordingly,
78 adenovirus-mediated human *MIC26* overexpression in mice, administered through the tail
79 vein, led to increased levels of triacylglycerides (TAG) in murine plasma, when fed with HFD,
80 and TAG accumulation in the murine liver (Tian *et al*, 2017). In another study, MIC26
81 transgenic mice hearts displayed an increase of diacylglycerides (DAG) but not TAG (Turkieh
82 *et al*, 2014) as in the previous described study (Tian *et al.*, 2017) suggesting modulatory roles
83 of MIC26 in lipid metabolism. Recently, in mitochondria-rich brown adipose tissue (BAT),
84 downregulation of *Mic26* mRNA and protein levels were reported in diet-induced or leptin-
85 deficient obese (*ob/ob*) murine models compared to the respective controls. Mice with an
86 adipose tissue specific deletion of *Mic26* which were fed with a HFD gained more total body
87 weight and adipose tissue fat mass than control mice (Guo *et al*, 2023). Hence, we hypothesize
88 that MIC26 has an unidentified regulatory role under nutrient-enriched conditions. Therefore,
89 in order to understand the function of MIC26, we used WT and *MIC26* KO cells as a model
90 system under standard glucose culture conditions as well as excessive glucose culture
91 conditions termed normoglycemia and hyperglycemia, respectively. We employed a multi-
92 omics approach encompassing transcriptomics, proteomics and targeted metabolomics to
93 investigate the pathways regulated by MIC26. We found that the function of MIC26 is critical
94 in various pathways regulating fatty acid synthesis, oxidation, cholesterol metabolism and
95 glycolysis. Interestingly, we observed an entirely antagonistic effect of cellular *de novo*
96 lipogenesis in *MIC26* KO cells compared to WT cells depending on the applied nutrient
97 conditions. This showed that the response to high glucose conditions is strongly dependent on
98 the presence of MIC26. In addition, we found that cells deleted for *MIC26* displayed alterations
99 of mitochondrial glutamine usage and oxidative phosphorylation. Overall, we propose that
100 MIC26 is a unique mitochondrial apolipoprotein functioning as a mitochondrial fuel sensor that
101 regulates central metabolic pathways to meet mitochondrial and thus cellular energy demands.

102 Results

103 Mitochondrial apolipoprotein MIC26 is selectively increased in cells exposed to 104 hyperglycemia

105 There is a strong link between metabolic abnormalities and pattern of *MIC26* expression.
106 Increased levels of *MIC26* transcripts were observed in diabetic patients (Lamant *et al.*, 2006)
107 and increased accumulation of lipids were found upon *Mic26* overexpression in the mouse
108 (Tian *et al.*, 2017; Turkieh *et al.*, 2014). In order to understand the role of MIC26 in cellular
109 metabolism, we used hepatocyte-derived HepG2 cells as the cellular model and generated
110 *MIC26* KO cells using the CRISPR-Cas9 system. WT and *MIC26* KO cells were grown in
111 standard (5.5 mM) and excessive concentrations of glucose (25 mM), defined as
112 normoglycemic and hyperglycemic conditions respectively throughout the manuscript, for a
113 prolonged period of three weeks to investigate long term effects of nutritional overload. Initially,
114 we checked whether there is a difference in the amounts of various MICOS proteins in WT
115 HepG2 cells grown in normoglycemia and hyperglycemia. Western blot (WB) analysis showed
116 a significant increase of MIC26 and MIC27 along with MIC25 in cells grown in hyperglycemia
117 compared to normoglycemia (**Fig 1A & B**). We did not observe any significant changes in the
118 amounts of MIC19, MIC60, MIC10 and MIC13 in WT-Hyperglycemia (WT-H) compared to WT-
119 Normoglycemia (WT-N) condition. This pointed to a specific role of the MICOS subunits,
120 MIC26, MIC27 and MIC25 when cultured in hyperglycemia compared to normoglycemia. The
121 significant increase of MIC27 and MIC25 observed in WT-H when compared to WT-N was
122 abolished in *MIC26* KOs indicating a requirement of MIC26 in this response under nutrient-
123 enriched conditions (**Fig 1A & B**).

124 The MICOS proteins regulate the IM remodelling by working in unison to maintain CJs and
125 contact sites between IM and OM (Anand *et al.*, 2021). Still, deficiency of different MICOS
126 proteins shows variable effects on the extent of CJs loss and cristae ultrastructure (Anand *et al.*
127 *et al.*, 2020; Kondadi *et al.*, 2020a; Stephan *et al.*, 2020; Weber *et al.*, 2013). MIC10 and MIC60
128 have been considered as core regulators of IM remodelling displaying severe loss of CJs
129 (Kondadi *et al.*, 2020a; Stephan *et al.*, 2020). The extent of mitochondrial ultrastructural
130 abnormalities upon *MIC26* deletion varies among different cell lines tested (Anand *et al.*, 2020;
131 Koob *et al.*, 2015; Stephan *et al.*, 2020). Therefore, we performed transmission electron
132 microscopy (TEM) in WT and *MIC26* KO HepG2 cells which revealed a reduction of cristae
133 content (cristae number per unit mitochondrial length per mitochondria) in *MIC26* KOs
134 compared to WT cells in both nutrient conditions (**Fig 1C & E**). Thus, the loss of cristae was
135 dependent on MIC26 and independent of the glucose concentration used in cell culture. In
136 addition, there was a decrease in cristae number in WT cells grown in hyperglycemia
137 compared to normoglycemia showing that higher glucose levels lead to decreased cristae

138 density, which is a common phenotype in diabetic mice models (Bugger *et al.*, 2008; Xiang *et*
139 *al.*, 2020). As the number of cristae were already decreased in certain conditions, we analysed
140 the number of CJs normalised to cristae number and found that a significant decrease of CJs
141 was observed in *MIC26* KOs independent of the nutrient conditions (**Fig 1D & E**). Overall, the
142 loss of *MIC26* leads to mitochondrial ultrastructural abnormalities accompanied by reduced
143 number of cristae as well as CJs compared to WT cells (**Fig 1C-E**).

144

145 **Hyperglycemia confers antagonistic regulation of lipid and cholesterol pathways, in** 146 ***MIC26* KO vs WT cells, compared to normoglycemia**

147 In order to understand the role of *MIC26* in an unbiased manner, we compared WT and
148 *MIC26* KO cells cultured under respective nutrient conditions by employing quantitative
149 transcriptomics and proteomics analyses. A total of 21,490 genes were obtained after the initial
150 mapping of the RNA-Seq data, of which 2,933 were significantly altered in normoglycemic
151 *MIC26* KO compared to WT cells (fold change of ± 1.5 and Bonferroni correction $P \leq 0.05$),
152 while in hyperglycemia, *MIC26* KO had 3,089 significantly differentially expressed genes
153 (DEGs) as compared to WT-N cells. A clustering analysis of identified transcripts involving all
154 four conditions along with respective replicates is depicted (**Fig S1A**). A Treemap
155 representation shows comparison of significantly upregulated clustered pathways in
156 *MIC26* KOs cultured in normoglycemia compared to WT (**Fig 2A**). Interestingly, the pathways
157 relating to sterol, cholesterol biosynthetic processes and regulation of lipid metabolic
158 processes were significantly upregulated in *MIC26* KO-N compared to WT-N. On the contrary,
159 in *MIC26* KO-H compared to WT-H, pathways involved in sterol, secondary alcohol
160 biosynthetic processes along with cholesterol biosynthesis and cellular amino acid catabolic
161 processes including fatty acid oxidation (FAO) were mainly downregulated (**Fig 2B**). Thus, an
162 antagonistic regulation is observed upon *MIC26* deletion when normoglycemia and
163 hyperglycemia are compared. A detailed pathway enrichment analysis for significantly
164 upregulated genes in *MIC26* KO vs WT cells grown in normoglycemia also revealed genes
165 involved in cholesterol, steroid biosynthetic pathways, fatty acid synthesis and oxidation as
166 well as glycolysis and gluconeogenesis (**Fig 2C**). The genes involved in cholesterol
167 biosynthetic pathways, glycolysis and gluconeogenesis, FAO and fatty acid synthesis were
168 significantly downregulated in *MIC26* KOs grown in hyperglycemia compared to WT cells (**Fig**
169 **2D**). The antagonistic behaviour of cholesterol metabolism observed using transcriptomics
170 data (**Fig 2**) was also confirmed in the pathway enrichment analysis for proteomics (**Fig S1B**
171 **& C**). Detailed analysis of the transcriptomics data in *MIC26* KO-N compared to WT-N showed
172 that $\approx 80\%$ of the genes regulating cholesterol biosynthesis were significantly upregulated upon
173 normoglycemia (**Fig S2A**) while the opposite was true for hyperglycemia (**Fig S2B**). At the

6

174 proteome level, the effect of *MIC26* deletion was mainly observed in normoglycemic conditions
175 where 8 out of 12 detected proteins involved in cholesterol biosynthesis showed a significant
176 increase in peptide abundances, while this increase was diminished in *MIC26* KO-H compared
177 to WT-H cells (**Fig S2C-N**). Thus, the loss of *MIC26* strongly impacts cholesterol biosynthesis
178 in a nutrient-dependent manner. In conclusion, under normoglycemic conditions, *MIC26* acts
179 as a repressor of cholesterol biosynthesis whereas under hyperglycemic conditions *MIC26*
180 rather drives this pathway. We further employed targeted metabolomics to decipher any
181 altered cholesterol biosynthesis by quantifying the cholesterol amounts at steady state. In
182 accordance with cholesterol synthesis promoting role of *MIC26* in hyperglycemia, cholesterol
183 levels were strongly reduced in *MIC26* KO-H compared to WT-H cells. Moreover, cholesterol
184 levels were significantly increased in WT-H cells compared to WT-N which was not the case
185 and even reversed in *MIC26* KO cells (**Fig S2O**). Thus, *MIC26* is required to maintain
186 cholesterol homeostasis and cellular cholesterol demand in a nutrient dependent manner and
187 is of particular importance under hyperglycemia.

188

189 ***MIC26* maintains the glycolytic function**

190 Besides an antagonistic regulation of the cholesterol biosynthetic pathway, we also observed
191 an opposing trend of genes involved in lipid metabolism as well as glycolysis (**Fig 2C & D**). In
192 order to gain further insights about the role of *MIC26* regarding the differential regulation of
193 glycolytic pathways in normoglycemia and hyperglycemia, we re-visited our transcriptomics
194 (**Fig S3**) and proteomics (**Fig 3A-C and H-J**) datasets and investigated the genes regulating
195 glycolysis upon *MIC26* deletion. On the one hand, in *MIC26* KO-N compared to WT-N, we
196 found that the transcripts encoding hexokinase (*HK*) 1, phosphofruktokinase 1 (*PFK1*) (**Fig**
197 **S3A**) and aldolase (*ALDOC*) protein levels were significantly upregulated (**Fig 3A**), while
198 glyceraldehyde-3-phosphate dehydrogenase (*GAPDH*) (**Fig 3B**) and enolase (*ENO*) were
199 downregulated (**Fig S3A**). On the other hand, in *MIC26* KO-H compared to WT-H, we observed
200 decreased *GAPDH* and glucose-6-phosphate isomerase (*GPI*) proteins and transcripts (**Fig**
201 **3B & C, Fig S3B**). This could indicate that in hyperglycemia, deletion of *MIC26* leads to
202 deregulation of the glycolysis pathway resulting in increased accumulation of glucose (**Fig 3D**)
203 and decreased glycolysis end products. Therefore, to evaluate the metabolic effect of
204 differentially expressed genes (**Fig S3A & B**) and proteins involved in glucose uptake (**Fig 3**
205 **H-J**) and glycolysis (**Fig 3A-C**), we checked whether the glycolytic function is altered in *MIC26*
206 KOs using a Seahorse Flux Analyzer with the glycolysis stress test (**Fig 3E & F**). Based on the
207 extracellular acidification rate (ECAR), the 'glycolytic reserve' is an index of the ability to
208 undergo a metabolic switch to glycolysis achieved by the cells upon inhibition of mitochondrial
209 ATP generation whereas the 'glycolytic capacity' measures the maximum rates of glycolysis

7

210 which the cell is capable to undergo. Overall 'glycolytic function' is measured after cellular
211 glucose deprivation for 1 h and subsequently by quantifying the ECAR primarily arising from
212 cellular lactate formation after providing the cell with saturating glucose amounts. We observed
213 that the glycolytic reserve was significantly increased only in cells cultured in normoglycemia
214 and not in hyperglycemia upon deletion of *MIC26* (**Fig 3F**), while the glycolysis function as well
215 as glycolytic capacity were not significantly increased in *MIC26* KO under both nutrient
216 conditions (**Fig S3C & D**). Therefore, the ability of *MIC26* KO cells (compared to WT) to
217 respond to energetic demand by boosting glycolysis is increased under normoglycemia, while
218 *MIC26* KO cells primed to hyperglycemia were not able to increase glycolytic reserve indicating
219 a clearly different regulation of glycolysis under normoglycemia versus hyperglycemia. In order
220 to understand this better, we quantified the intracellular glucose levels, at steady state in WT
221 and *MIC26* KO, which were significantly increased upon *MIC26* deletion only in hyperglycemia
222 but not normoglycemia compared to the respective WT cells (**Fig 3D**). We further checked
223 whether the increased glucose levels in cells cultured in hyperglycemia is due to increased
224 glucose uptake. In normoglycemia, a glucose uptake assay showed a modest but significant
225 increase of glucose uptake in *MIC26* KOs compared to WT cells (**Fig 3G**) which is consistent
226 with a strong increase in GLUT3 amounts (**Fig 3H**) albeit accompanied by a downregulation
227 of GLUT1 upon *MIC26* depletion (**Fig 3I**). GLUT2 levels remained unchanged in all conditions
228 (**Fig 3J**). However, the observed increased glucose uptake in *MIC26* KO-N (compared to WT-
229 N) was abolished in *MIC26* KO-H (compared to WT-H) and accordingly accompanied by no
230 increase in GLUT3 levels showing that the high amounts of glucose in *MIC26* KO cells grown
231 in hyperglycemia cannot be explained by an increased glucose uptake under these conditions
232 (**Fig 3G**). In *MIC26* KO-N compared to WT-N, even though we observed an increase of glucose
233 uptake, the amount of glycolysis end products, namely pyruvate (**Fig 3K**) and lactate (**Fig 3L**)
234 were unchanged. In hyperglycemia, a significant reduction of pyruvate (**Fig 3K**) and lactate
235 (**Fig 3L**) amounts were observed at steady-state despite increased glucose levels upon *MIC26*
236 deletion. Overall, upon *MIC26* deletion pyruvate and lactate levels were decreased in
237 hyperglycemia while no change was observed in normoglycemia. These results combined with
238 the already discussed differentially regulated transcripts and proteins involved in glycolysis
239 prompted us to check whether there is a difference of shuttling metabolic intermediates from
240 glycolysis towards lipid anabolism. Glycerol-3-phosphate (G3P) is a precursor for lipid
241 biosynthesis synthesized from dihydroxyacetone phosphate which is derived from glycolysis.
242 We observed an increase in G3P levels upon *MIC26* deletion in normoglycemic conditions,
243 while G3P levels were significantly reduced in *MIC26* KO-H cells, compared to the respective
244 WT cells (**Fig 3M**). This opposing trend, together with the previously described antagonistic
245 enrichment in fatty acid biosynthesis (**Fig 2C & D**), indicates that *MIC26* deletion rewires
246 glycolytic function to drive lipogenesis in normoglycemia with an antagonistic effect in

247 hyperglycemia. Further, we checked the cellular effect of *MIC26* loss on lipid anabolism in
248 normo- as well as hyperglycemia.

249

250 **The loss of *MIC26* leads to metabolic rewiring of cellular lipid metabolism via CPT1 and**
251 **dysregulation of fatty acid synthesis**

252 The respective increase and decrease of G3P (**Fig 3M**) in normoglycemia and hyperglycemia
253 upon *MIC26* deletion when compared to WT as well as an opposing trend in fatty acid
254 biosynthesis reflected in our transcriptomics data (**Fig 2C & D**) prompted us to explore the
255 regulation of cellular lipid metabolism. Lipid droplets (LDs) play a key role in energy metabolism
256 and membrane biology by acting as reservoirs to store TAG and sterol esters which are
257 released to the relevant pathways according to cellular demand (Thiam *et al*, 2013). Using
258 BODIPY staining, we checked the cellular LD content in unstimulated and palmitate-stimulated
259 WT and *MIC26* KO cells grown in normoglycemia and hyperglycemia, respectively. The
260 number of LDs and the respective fluorescence intensity of BODIPY are indicative of cellular
261 lipid content (Chen *et al*, 2022). We observed a general increase of LD number in *MIC26* KOs
262 irrespective of treatment conditions (**Fig 4A & B**). However, the increased intensity of BODIPY
263 staining observed in normoglycemia was not evident in *MIC26* KO-H compared to respective
264 WT cells (**Fig 4C & D**). Further, when we fed free fatty acids (FFAs) in the form of palmitate,
265 there was again increased BODIPY intensity in *MIC26* KOs in normoglycemia even at a higher
266 level. In contrast, under hyperglycemia *MIC26* KO cells showed lower LD intensity when
267 compared to WT cells again demonstrating an antagonistic role of *MIC26* when normoglycemia
268 was compared to hyperglycemia (**Fig 4C & D**). These experiments allow us to conclude that
269 the effect of *MIC26* deletion on LD accumulation depends on the nutrient condition which is
270 enhanced under nutrient-rich (high-glucose/high-fat-like) conditions. Overall, *MIC26* is
271 essential to regulate the amount of cellular LD content in a nutrient-dependent manner (**Fig**
272 **4D**).

273 LD biogenesis is closely linked to increased cellular FFA levels (Zadoorian *et al*, 2023). Using
274 targeted metabolomics, we investigated the steady state levels of long chain FFAs in WT and
275 *MIC26* KO cell lines cultured in normoglycemia and hyperglycemia (**Fig 4E**). We identified that
276 there was either no change or an increase of saturated FFAs including lauric (12:0), myristic
277 (14:0), palmitic (16:0), stearic (18:0), arachidic (20:0) as well as behenic (22:0) acid in
278 normoglycemia in *MIC26* KOs compared to WT cells (**Fig 4E, Fig S4**). In contrast, we
279 consistently found a decrease in most of the above-mentioned saturated FFAs in *MIC26* KO-
280 H compared to WT-H. This trend was also observed in unsaturated FFAs like oleic acid (18:1).
281 Overall, we conclude that there is a consistent decrease of saturated FFAs in *MIC26* KO-H as
282 opposed to *MIC26* KOs grown in normoglycemic conditions consistent to the observed trend

9

283 in LD formation. Increased level of FFAs and LDs can arise from increased FFAs biosynthesis
284 as well as reduced FFA catabolism via mitochondrial β -oxidation (Afshinnia *et al*, 2018).
285 Mitochondrial β -oxidation requires import of long chain FFAs using the carnitine shuttle
286 comprised of carnitine palmitoyl transferase 1 (CPT1) and 2 (CPT2) and carnitine-acylcarnitine
287 translocase (CACT), into the mitochondrial matrix. Depletion of CPT1A, which is the rate
288 limiting step of FAO, coincides with lipid accumulation in the liver (Sun *et al*, 2021). Therefore,
289 we determined the CPT1A amounts using WB analysis (**Fig 4F & G**) which were in line with
290 transcriptomics and quantitative PCR data (**Fig S5A & B**). *MIC26* deletion revealed a reduction
291 of CPT1A in normoglycemia compared to WT cells. In WT cells, hyperglycemia already
292 triggered a reduction in CPT1A level and there was no further decrease of CPT1A in
293 *MIC26* KO cells grown in hyperglycemia (**Fig 4F & G**). In order to understand the functional
294 significance of CPT1A reduction on mitochondrial function, we checked the FAO capacity of
295 respective cell lines by feeding them with palmitate and analysing the induced basal respiration
296 and spare respiratory capacity (SRC) of mitochondria compared to BSA control group (**Fig 4H**
297 **and I, Fig S5C & D**). SRC is the difference between FCCP stimulated maximal respiration and
298 basal oxygen consumption and therefore is the ability of the cell to respond to an increase in
299 energy demand. We observed a significant reduction in palmitate-induced basal respiration as
300 well as SRC in *MIC26* KO-N compared to WT-N determining decreased mitochondrial long
301 chain fatty acid β -oxidation. It is important to note that we already observed a significant
302 decrease in mitochondrial β -oxidation in WT-H condition which was not further affected in
303 *MIC26* KO-H in agreement with the reduced CPT1A levels (**Fig 4F & G**). We further analysed
304 the reduction of oxygen consumption rate (OCR) induced by etomoxir inhibition of CPT1A (**Fig**
305 **4J**). In *MIC26* KO-N compared to WT-N, palmitate-induced OCR was reduced moderately, yet
306 this was not significant. For the respective hyperglycemic conditions, we did not observe a
307 change which was again in line with the observed CPT1A levels. Thus, reduced β -oxidation in
308 *MIC26* KO-N compared to WT-N is apparently contributing to increased FFA levels and LD
309 content and could be mediated, at least in part, via the reduced levels of CPT1A resulting in
310 reduced transport of FFAs into mitochondria.

311 We further checked whether FFA biosynthesis plays a role in the nutrition-dependent
312 antagonistic regulation of lipid anabolism in *MIC26* KO cell line. FFA biosynthesis is initiated
313 with the export of citrate generated in TCA cycle from mitochondria to the cytosol. The export
314 is mediated by the citrate/malate exchanger SLC25A1 which is present in the mitochondrial
315 IM. Proteomics and transcriptomics data showed that SLC25A1 was increased in
316 normoglycemia in *MIC26*-KOs (compared to respective WT), but not in hyperglycemia (**Fig**
317 **S5E & F**). We then checked for further changes in the transcriptome and proteome levels of
318 key enzymes playing a role in FFA synthesis. We found that ATP citrate lyase (ACLY, **Fig**

319 **S5G**), acetyl-Co-A carboxylase (ACACA, **Fig S5H & I**) which converts acetyl-CoA into malonyl-
320 CoA, fatty acid synthase (FASN, **Fig S5J & K**) and acetyl-CoA desaturase (SCD, **Fig S5L &**
321 **M**) were increased in normoglycemia in *MIC26* KO cells but mostly unchanged in hyperglycemia.
322 In addition, hyperglycemia resulted in an increase of glycerol kinase (GK) in WT cells which
323 was absent in *MIC26* KO cells (**Fig S5N**). Therefore, our data indicate that the FFA
324 biosynthesis pathway is upregulated upon loss of *MIC26* KO in normoglycemia but not in
325 hyperglycemia compared to respective WT conditions. An upregulation of FFA biosynthesis
326 along with reduced mitochondrial β -oxidation partially mediated by reduced CPT1A amount in
327 *MIC26* KO-N and a shift of glycolytic intermediates resulting in G3P accumulation show that
328 loss of *MIC26* leads to a cumulative metabolic rewiring towards increased cellular lipogenesis.

329

330 ***MIC26* deletion leads to hyperglycemia-induced decrease in TCA cycle intermediates**

331 To synthesize FFA, citrate first needs to be generated by the TCA cycle in the mitochondrial
332 matrix before it is exported to the cytosol. Using targeted metabolomics, we checked whether
333 the TCA cycle metabolism is altered upon *MIC26* deletion at steady state in both nutrient
334 conditions (**Fig 5A**). As previously described, glycolysis resulted in decreased pyruvate levels
335 upon *MIC26* deletion in hyperglycemia, while no change was observed in normoglycemia (**Fig**
336 **3N**). Furthermore, most of the downstream metabolites including (iso-)citrate, succinate,
337 fumarate and malate consistently showed a significant decrease in *MIC26* KO cells cultured in
338 hyperglycemia, compared to WT condition, but not in normoglycemia following the previously
339 observed trend in pyruvate levels. To elucidate a possible defect of mitochondrial pyruvate
340 import, we checked mitochondrial pyruvate carrier 1 (MPC1) and MPC2 abundances (**Fig 5B**
341 **& C**) as well as mitochondrial respiration after blocking mitochondrial pyruvate carrier (glucose
342 / pyruvate dependency) using UK5099 inhibitor (**Fig 5D**). While we observed a downregulation
343 of MPC1 in *MIC26* KO-N compared to WT-N, MPC1 abundances in *MIC26* KO-H compared
344 to WT-H remained unchanged. Further we did not observe any changes in MPC2 level. Also,
345 mitochondrial glucose/pyruvate dependency remained unchanged in the respective
346 hyperglycemia combination while we observed a minor but significant decrease in *MIC26* KO-
347 N compared to WT-N. In addition, elucidation of abundances of mitochondrial enzymes
348 catalyzing TCA cycle metabolites (**Fig S6A-K**) as well as the respective cytosolic enzymes
349 (**Fig S6L-N**) interestingly revealed an upregulation of citrate synthase (**Fig S6A**) and
350 mitochondrial aconitase 2 (**Fig S6B**) in *MIC26* KO cells independent of nutrient conditions.
351 Furthermore, the immediate downstream enzyme isocitrate dehydrogenase 2 which generates
352 α -ketoglutarate (α -KG) was upregulated in *MIC26* KO condition (**Fig S6C**). In contrast to all
353 previously described metabolites, the α -KG levels were increased in hyperglycemia in
354 *MIC26* KO compared to WT. The accumulation of α -KG possibly arises from a significant

11

355 downregulation of α -KG dehydrogenase in *MIC26* KO independent of the nutrient condition
356 (**Fig S6E**). Following, an accumulation of α -KG by downregulation of α -KG dehydrogenase
357 would further explain the decreased formation of succinate in *MIC26* KO-H compared to WT-H.
358 Succinate dehydrogenases (**Fig S6G & H**) as well as fumarase (**Fig S6I**) did not show any
359 changes in abundances upon the respective *MIC26* KO to WT comparison reflecting the
360 uniform metabolite trend in succinate, fumarate and malate. Overall, we observed a general
361 decrease in several TCA cycle metabolites in *MIC26* KO-H compared to WT-H. Therefore, we
362 propose that a downregulation of FFA biosynthesis in *MIC26* KO-H compared to WT-H results
363 from a limited formation of citrate via the mitochondrial TCA cycle presumably arising from
364 reduced utilization of glucose.

365

366 **Aberrant glutamine metabolism is observed in *MIC26* KOs independent of nutritional** 367 **status**

368 Glutaminolysis feeds α -KG in the TCA cycle. To check whether the increase in α -KG could be
369 (apart from downregulation of α -KG dehydrogenase amounts) derived from glutaminolysis, we
370 also checked glutamine (**Fig 6A**) and glutamate levels (**Fig 5A**). The amounts of glutamine at
371 steady-state were uniformly increased in *MIC26* KOs irrespective of nutrient conditions (**Fig**
372 **6A**). Glutamate was decreased in *MIC26* KO-N compared to WT-N (**Fig 5A**). Mitochondria
373 mainly oxidise three types of cellular fuels namely pyruvate (from glycolysis), glutamate (from
374 glutaminolysis) and FFAs. We used a 'mito-fuel-flex-test' for determining the contribution of
375 glutamine as a cellular fuel. The contribution of glutamine as cellular fuel could be determined
376 using BPTES, an allosteric inhibitor of glutaminase (GLS1), which converts glutamine to
377 glutamate. The extent of reduction of mitochondrial oxygen consumption upon BPTES
378 inhibition is used as a measure for determining the glutamine dependency while the capacity
379 is the ability of mitochondria to oxidise glutamine when glycolysis and FFA oxidation are
380 inhibited. Intriguingly, we observed that the *MIC26* KOs do not depend on glutamine as a fuel
381 (**Fig 6B**, left histogram). However, they still can use glutamine when the other two pathways
382 were inhibited (**Fig 6B**, right histogram). The glutamine oxidation capacity of *MIC26* KO cells
383 cultured in normoglycemia as well as hyperglycemia appears slightly decreased compared to
384 WT but this decrease is not statistically significant. Overall, we observe a remarkable metabolic
385 rewiring of *MIC26* KOs to bypass glutaminolysis. In order to understand whether the
386 independency on glutamine as fuel arises due to the possibility of aberrant transport of
387 glutamine into the mitochondria, we analysed transcripts and proteins that were not only
388 significantly downregulated but also present in the mitochondria IM and interacted with *MIC26*.
389 For this, we investigated putative *MIC26* interactors by compiling a list using BioGRID,
390 NeXtProt and IntAct databases. SLC25A12, an antiporter of cytoplasmic glutamate and

12

391 mitochondrial aspartate, was significantly downregulated (**Fig S7A**) while showing up in the
392 interactome of MIC26 (**Fig S7E**). Accordingly, WB analysis reveal a reduction of SLC25A12 in
393 MIC26 KOs compared to WT HepG2 cells in both normoglycemia and hyperglycemia (**Fig 6C**
394 **& D**). Further, it is known that a variant of SLC1A5 transcribed from an alternative transcription
395 start site and present in the mitochondrial IM is responsible for transporting glutamine into
396 mitochondria (Yoo *et al*, 2020a). Transcriptomics data revealed a reduction of SLC1A5 in
397 MIC26 KOs while proteomics revealed a significant reduction in normoglycemia and non-
398 significant reduction in hyperglycemia in MIC26 KOs compared to WT (**Fig S7B & C**). An
399 increase of cellular glutamine levels in MIC26 KOs (**Fig 6A**) along with reduced levels of
400 SLC1A5 and reduced mitochondrial glutamine dependency (**Fig 6B**) indicate a reduced
401 transport of glutamine destined for glutaminolysis into mitochondria.

402 In order to delineate whether the increased glutamine levels at steady-state are due to
403 decreased glutamine utilisation or increased flux, we performed a metabolic tracing experiment
404 where WT and MIC26 KO cells, cultured in normoglycemia and hyperglycemia, were fed with
405 labelled glutamine [$U\text{-}^{13}\text{C}_5$, $^{15}\text{N}_2$] for 0.5 h and 6 h (**Fig 6E-O**). Glutamine is converted to
406 glutamate by glutaminase (GLS) in the mitochondria. The GLS amounts were not altered in
407 MIC26 KO cells when compared to respective WT cells grown in normoglycemia and
408 hyperglycemia (**Fig S7D**). In line, label enriched glutamate species (m+1 - m+4) did not show
409 major differences in all four conditions at both timepoints (**Fig 6E**). Following this, we
410 hypothesize that accumulation of glutamine in MIC26 KO cells arises from other cellular
411 pathways utilising glutamine being impaired, for example synthesis of purine, pyrimidine or
412 amino acids. However, labelled α -KG (m+1 - m+5) was increased upon MIC26 deletion with a
413 pronounced effect in cells cultured in hyperglycemia similar to the detected steady-state
414 amounts of α -KG (**Fig 6F**). To check the conversion rates of different metabolite reactions, we
415 determined the enzyme conversion rates by calculating the ratio of the highest labelled species
416 from the end-metabolite compared to the starting-metabolite. In accordance to the observed
417 level of α -KG, the conversion ratio from glutamate to α -KG was significantly increased in
418 MIC26 KO cells (**Fig 6K**). We further checked the flux of TCA metabolites downstream to α -
419 KG namely succinate, fumarate and malate. Despite the increased α -KG levels, the labelled
420 succinate species (m+1 - m+4) was decreased in MIC26 KO cells (**Fig 6H**). In line, the
421 conversion rate from α -KG to succinate was significantly downregulated in MIC26 KO cells
422 independent of glucose concentrations and timepoints (**Fig 6M**). However, the conversion ratio
423 from succinate to fumarate catalysed by mitochondrial complex II subunits, succinate
424 dehydrogenases A-D, was increased in MIC26 KO cell lines at the 6 h timepoint compared to
425 WT in both normoglycemia and hyperglycemia (**Fig 6N**). Despite the increase in fumarate
426 conversion, the labelled fumarate and malate were decreased in MIC26 KO compared to WT
427 in normoglycemia but not in hyperglycemia (**Fig 6I & J**) while there were minor differences at

428 0.5 h. The conversion ratio from α -KG to malate was decreased upon *MIC26* deletion in both
429 nutrient conditions at 0.5 h and 6 h of glutamine labelling. Thus, despite increased conversion
430 of succinate to fumarate as well as increased flux from glutamate to α -KG (in hyperglycemia)
431 upon loss of *MIC26*, cellular glutaminolysis does not function optimally. We also checked the
432 labelled citrate levels which showed minor changes after 0.5 h treatment but a major change
433 in all labelled species (m+1 - m+5) after 6 h (**Fig 6G**). Correspondingly, the levels of citrate in
434 WT-N cells were highly increased compared to all three other conditions. Conversion rates
435 from α -KG (m+5) to citrate (m+5) were significantly reduced in *MIC26* KO cell lines compared
436 to the respective WT cells (**Fig 6L**). Overall, the flux of glutamine through the TCA cycle is
437 accompanied by decreased conversion of TCA cycle intermediates. Therefore, we conclude
438 that aberrant glutaminolysis is observed upon loss of *MIC26*.

439

440 ***MIC26* regulates mitochondrial bioenergetics by restricting the ETC activity and** 441 **OXPHOS (super-)complex formation**

442 We have shown that the loss of *MIC26* leads to dysregulation of various central fuel pathways.
443 In order to understand the effect of *MIC26* deletion on cellular bioenergetics, we checked the
444 mitochondrial membrane potential ($\Delta\Psi_m$) of WT and *MIC26* KO cells in both nutrient conditions
445 by employing TMRM dye (**Fig 7A & B**). Loss of *MIC26* leads to decreased $\Delta\Psi_m$ compared to
446 control cells in both normoglycemia and hyperglycemia. It is well known that mitochondrial loss
447 of membrane potential is connected to mitochondrial dynamics (Giacomello *et al*, 2020). Thus,
448 we checked the mitochondrial morphology and observed that loss of *MIC26* consistently leads
449 to a significant increase of mitochondrial fragmentation compared to WT-N (**Fig 7C & D**). In
450 addition, WT cells grown in hyperglycemia despite maintaining the $\Delta\Psi_m$ exhibited fragmented
451 mitochondria. We also checked the levels of major mitochondrial dynamic regulators: MFN1,
452 MFN2, DRP1 as well as OPA1 processing into short forms. WB analysis showed that MFN1
453 levels were significantly decreased upon *MIC26* deletion in both normoglycemia and
454 hyperglycemia compared to respective WT cells (**Fig S8A & B**) which could account for
455 increased fragmentation. There was no major effect on the amounts of other factors which
456 could account for mitochondrial fragmentation. Thus, *MIC26* deletion is characterized by
457 reduced $\Delta\Psi_m$ and fragmentation of mitochondria which indicate altered mitochondrial
458 bioenergetics. To determine this, we checked the mitochondrial function in WT and *MIC26* KO
459 cells by using a mitochondrial oxygen consumption assay (**Fig 7E**). We observed an increased
460 basal respiration in *MIC26* KOs in both normoglycemia and hyperglycemia compared to the
461 respective WT (**Fig 7F**). The ATP production was increased in *MIC26* KO cells in
462 hyperglycemia compared to WT-H (**Fig S8C**). In addition, decreased SRC was observed in
463 *MIC26* KO-N when compared to WT-N condition (**Fig S8D**). Overall, *MIC26* KOs demonstrate

14

464 higher basal respiration in both nutrient conditions. In order to elucidate the increased basal
465 respiration, we performed blue native PAGE to understand the assembly of OXPHOS
466 complexes along with in-gel activity assays (**Fig 7G**). *MIC26* deletion consistently led to an
467 increase in the levels of OXPHOS complexes I, III, IV and dimeric and oligomeric complex V
468 (shown in green arrows) (**Fig 7G**, left blots respectively for each complex). The increased
469 assembly of OXPHOS complexes was also accompanied by respective increase of in-gel
470 activity (shown in blue arrows) (**Fig 7G**, right blots respectively for each complex). This is
471 consistent with the previously observed increased basal respiration (**Fig 7F**) and the succinate
472 to fumarate conversion representing an increased complex II activity (**Fig 6N**). Altogether, we
473 conclude that formation and stability of OXPHOS (super-) complexes as well as their activity
474 is dependent on *MIC26*.

475

476 Discussion

477 Our study identifies *MIC26* as a critical regulator at the crossroads of several major metabolic
478 pathways. Based on detailed multi-omics analyses, we deciphered an intricate interplay
479 between *MIC26*, a mitochondrial IM protein, and global cellular metabolic adaptations. To
480 understand these metabolic changes and their dependency on mitochondrial ultrastructure and
481 function is of high medical relevance as nutrient-overload is known to cause obesity and T2DM
482 in humans. In fact, *MIC26* mutations are also associated with mitochondrial myopathy, lactic
483 acidosis (Beninca *et al.*, 2021) as well as lethality and progeria-like phenotypes (Peifer-Weiß
484 *et al.*, 2023). We showed that cellular fatty acid synthesis, cholesterol biosynthesis and LD
485 formation is promoted by *MIC26* under high glucose conditions but that these pathways are
486 conversely inhibited by *MIC26* under normal glucose concentrations (**Fig 7H**). The important
487 role of *MIC26* in channelling nutrient excess from glucose into lipids underscores its reported
488 links to obesity (Tian *et al.*, 2017) and diabetes (Lamant *et al.*, 2006) as it known that ectopic
489 lipid accumulation is a common feature of the development of metabolic diseases including
490 NAFLD and insulin resistance. Moreover, metabolism of glutamine via glutaminolysis is
491 strongly impaired in the absence of *MIC26*. First, we discuss, how and why *MIC26* promotes
492 lipid anabolism in hyperglycemia and what is known from earlier studies in this context.
493 Previously in mammalian cells, we characterised the role of *MIC26*, which contained a
494 conserved apolipoprotein A1/A4/E family domain, in regulating mitochondrial ultrastructure and
495 function (Koob *et al.*, 2015). We showed that both an increase and decrease of *MIC26* was
496 detrimental to mitochondrial function indicating that optimal *MIC26* amounts are essential for
497 cellular homeostasis. Despite the demonstration of an increase of mitochondrial structural
498 proteins, like *MIC60*, *SAMM50* and *MIC19*, connected with upregulation of key metabolic
499 pathways in mice fed with HFD compared to normal diet (Guo *et al.*, 2013), the interplay of

15

500 MICOS proteins, including MIC26, and metabolism is not clear. Since, classically
501 apolipoproteins bind to lipids and mediate their transport in the bloodstream (Mehta & Shapiro,
502 2022), the presence of MIC26 in a non-classical environment like the IM raises various
503 questions about its function. Interestingly, a previous report revealed a connection between
504 increased levels of *MIC26* transcripts and nutrient conditions mimicked by oleic acid treatment
505 (Wu *et al.*, 2013). How does the loss of MIC26 alter central metabolic pathways including lipid
506 metabolism in hyperglycemia? In this study, we found an increase of MIC26 in WT cells
507 cultured in hyperglycemia. Concomitant to MIC26 increase, we found that MIC26 stimulates
508 the formation of LDs when glucose is in excess. We demonstrate that MIC26 is essential for
509 glucose utilisation and channelling glycolytic intermediates towards lipid anabolism regulating
510 the accumulation of the LD content. This is supported by several findings including the
511 determined levels of pyruvate and TCA cycle intermediates indicating that by boosting
512 pyruvate levels, MIC26 further increases the amounts of the TCA cycle metabolites including
513 citrate levels which serve as a precursor for cholesterol as well as FFA synthesis. This
514 connection between lipid synthesis and MIC26 is further strengthened by earlier reports in the
515 context of diabetes or obese models. Dogs fed with a HFD for 9 weeks (Philip-Couderc *et al.*,
516 2003) and diabetic patients (Lamant *et al.*, 2006) showed increased *Mic26* transcripts in the
517 heart. Increased TAG and DAG were found upon *MIC26* overexpression in murine liver (Tian
518 *et al.*, 2017) and hearts (Turkieh *et al.*, 2014) respectively showing modulatory roles of MIC26
519 in lipid metabolism. Our data reveals a major MIC26-dependent alteration of metabolite
520 transporters of the mitochondrial IM and also metabolite levels. Thus, loss of MIC26 either
521 alters the level, the activity, or the submitochondrial distribution of various metabolite
522 transporters. In line with our data, the export of citrate from the mitochondrial matrix to the
523 cytosol is presumably of particular importance. MIC26 could regulate metabolite exchange
524 mechanistically either via protein-protein interactions of MIC26 to distinct metabolite
525 transporters such as SLC25A12, by altering the accessibility of metabolites to various
526 transporters due to altered cristae morphology. Overall, we propose that MIC26 regulates
527 metabolite exchange between the cytosol and mitochondria and vice versa in a nutrient-
528 dependent manner which is critical for adaptations to excess of glucose.

529 Under balanced nutrient conditions, MIC26 plays a different role compared to nutrient excess
530 conditions. MIC26 decreases the key enzymes regulating the upper half of glycolytic pathway
531 involved in ATP consumption phase. MIC26 prevents an increase of FFAs and G3P
532 culminating in uncontrolled accumulation of LD content. In line with this, it was recently shown
533 that the loss of MIC26 in BAT led to upregulation of glycolysis and fatty acid synthesis
534 pathways (Guo *et al.*, 2023). This was accompanied by impaired thermogenic activity of BAT,
535 mitochondrial ultrastructure and function which reiterates the role of MIC26 in metabolic
536 reprogramming. In normoglycemia, we found that the presence of MIC26 leads to a decrease

537 of majority of the transcripts enzymes participating in cholesterol biosynthesis, including the
538 sterol regulatory element binding transcription factor 2 (SREBP2) (**Fig S9C**) which is a master
539 regulator of genes involved in sterol and fatty acid synthesis (Madison, 2016). However, we
540 observed equal amounts of cholesterol in *MIC26* KO and WT cells under normoglycemia.
541 Thus, *MIC26* in normoglycemia facilitates equal metabolite distribution to either cholesterol
542 biosynthesis or lipogenesis. This *MIC26*-mediated metabolic switch based on the amount/type
543 of cellular fuel is essential for maintaining key metabolic pathways. A balanced amount of
544 *MIC26* is essential for how much glucose is channelled into lipid synthesis. In congruence with
545 our observations, key lipid metabolism genes were altered upon *Mic26* overexpression with an
546 interesting antagonistic regulation of *de novo* lipid synthesis genes depending on nutritional
547 conditions (Tian *et al.*, 2017). This study demonstrated an increase of important transcripts
548 regulating lipid synthesis like *ACACA*, *FASN* and *SCD* in mice, overexpressing *Mic26*, fed with
549 normal diet and a decrease when fed with HFD, compared to respective control mice. We
550 further observed a decrease in *CPT1A* level and activity in *MIC26* KO cell lines as well as WT-
551 H. *CPT1A* activity is known to be regulated either on a transcriptional level via peroxisome
552 proliferator activated receptor α (*PPAR α*) and peroxisome proliferator-activated receptor
553 gamma coactivator 1 alpha (*PGC-1 α*) or by allosteric inhibition through malonyl-CoA (López-
554 Viñas *et al.*, 2007; Song *et al.*, 2010). A recent study demonstrated the downregulation of
555 *PPAR α* protein level in BAT in adipose tissue-specific *MIC26* KO mice (Guo *et al.*, 2023).
556 Further, we observed a high upregulation of *ACACA* enzyme, which converts acetyl-CoA to
557 malonyl-CoA during *de novo* lipogenesis. Accordingly, it is possible that *MIC26* deletion in
558 normoglycemia could on one hand reduce the expression of *PPAR α* leading to decreased
559 *CPT1A* expression and on the other hand increase malonyl-CoA formation leading to
560 decreased *CPT1A* activity. Taken together, we used a multi-omics approach as well as a
561 variety of functional assays to decipher that loss of *MIC26* leads to an antagonistic regulation
562 of glycolysis, lipid as well as cholesterol synthesis dependent on cellular nutritional stimulation.

563 Besides the antagonistic regulation mediated by *MIC26* in different nutrient conditions, there
564 are general roles of *MIC26* in metabolic pathways which are independent of nutrient conditions.
565 Among the *MICOS* proteins, proteins like *MIC60* are considered as core components as *MIC60*
566 deletion leads to a consistent loss of CJs (Kondadi *et al.*, 2020a; Stephan *et al.*, 2020) while
567 the effect of *MIC26* deletion on loss of CJs varies with the cell line. Loss of CJs was observed
568 in 143B (Koob *et al.*, 2015) and HAP1 cells (Anand *et al.*, 2020) in contrast to HeLa cells
569 (Stephan *et al.*, 2020). *MIC26* deletion in HepG2 cells in this study revealed a significant
570 reduction of CJs when normalised to the cristae number, highlighting a possible major role of
571 *MIC26* in liver-derived cell lines. Concomitant to the reduction of CJs, we also observed
572 alterations of vital transporters in the mitochondrial IM and OM. It was recently described that
573 deletion of stomatin-like protein 2 (*SLP2*) leads to a drastic *MIC26* degradation mediated by

574 the YME1L protease (Naha *et al*, 2023). SLP2 was proposed as a membrane scaffold for PARL
575 and YME1L named as the SPY complex (Wai *et al*, 2016). It is therefore conceivable that
576 MIC26 could be concentrated in lipid-enriched nanodomains of the IM justifying its
577 apolipoprotein nomenclature. When we checked the mitochondrial function upon *MIC26*
578 deletion in HepG2 cells, we found that RCCs have enhanced respiratory capacity which was
579 due to: a) increase in the levels of native RCCs as well as supercomplexes and b) increase in
580 the activity of RCCs corresponding to increased RCC amounts. Thus, MIC26 could perform
581 structural as well as functional roles which may or may not be mutually exclusive to the MICOS
582 complex. A reduction of SLC25A12, an antiporter of cytoplasmic glutamate and mitochondrial
583 aspartate, which is present in the IM was observed upon *MIC26* deletion independent of the
584 nutritional status. We also found that SLC25A12 could be an interactor of MIC26 upon using
585 standard interaction databases available online. Presumably, the interaction of SLC25A12 with
586 MIC26 is important for the stability of the former. Such an intricate relationship between MIC26
587 and metabolite transporters in the IM makes it tempting to speculate that mitochondrial
588 membrane remodelling is linked to its metabolic function. In fact, a closer look at the
589 mitochondrial carrier family (SLC25) transcriptomics and proteomics data sets revealed that a
590 majority of the SLC25 transporters were differentially regulated upon *MIC26* deletion in
591 normoglycemia as well as hyperglycemia (**Fig S9A & B**). A prominent example is the reduction
592 of SLC1A5 in *MIC26* KO when compared to WT in hyperglycemia as well as normoglycemia.
593 A recent study showed that a variant of SLC1A5 present in the mitochondrial IM is responsible
594 for transporting glutamine into the mitochondria (Yoo *et al.*, 2020a). *MIC26* deletion leading to
595 reduced total amounts of SLC1A5 also indicates reduced transport of glutamine into
596 mitochondria. This was in line with an accumulation of glutamine upon loss of MIC26 at steady
597 state. However, using glutamine tracing experiments we did not observe a decrease in labelled
598 glutamate species but we observed an accumulation of α -KG. This could be due to the
599 observed decrease in α -KG dehydrogenase resulting in reduced conversion of α -KG to other
600 metabolites of the TCA cycle in particular under high glucose conditions. On the other hand,
601 besides mitochondrial glutamine usage to fuel the TCA cycle, glutamine is known to be an
602 essential source for nucleotide biosynthesis (Yoo *et al*, 2020b). *MIC26* KO cells showed a
603 decreased growth rate (**Fig S9D-F**). Hence, glutamine accumulation and with that reduced
604 conversion to nucleotides is a possible mechanism leading to growth deficiencies of *MIC26* KO
605 cells. We found that the transcripts as well as protein levels of NUBPL were prominently
606 downregulated upon *MIC26* deletion independent of the glucose concentrations of the cell
607 culture media (**Fig S9G & H**). NUBPL was demonstrated to function as an assembly factor for
608 complex I (Sheftel *et al*, 2009). Despite the prominent reduction of NUBPL, we did not find any
609 discrepancy in complex I assembly or its activity most likely due to increased RCC amounts.
610 We also found that the transcripts and protein levels of DHRS2 were significantly reduced in

611 **MIC26 KO (Fig S9I & J).** DHRS2 is implicated in reprogramming of lipid metabolism (Li *et al*,
612 2021) and was found to be downregulated in T2DM (De Silva K 2022).

613 We further found that hyperglycemia as well as *MIC26* deletion resulted in a fragmented
614 mitochondrial morphology compared to WT-N. Mitochondrial dynamics and cellular
615 metabolism including nutritional demands are closely interlinked (Mishra & Chan, 2016).
616 Nutritional overload was associated with increased mitochondrial fragmentation (Yu *et al*,
617 2006) while starvation led to formation of a tubular mitochondrial network (Gomes *et al*, 2011).
618 Further, mice lacking the ability to undergo mitochondrial fission by liver specific deletion of
619 *Drp1* were protected from lipid accumulation in the liver as well as insulin resistance upon HFD
620 feeding (Wang *et al*, 2015). Obesity is associated with increased mitochondrial fragmentation
621 in multiple studies. A recent study showed that mitochondrial fragmentation is positively
622 correlated to mitochondrial long chain FFA oxidation capacity via an increased activity of
623 CPT1A (Ngo *et al*, 2023). A stronger membrane curvature resulting from mitochondrial
624 fragmentation induces a conformational change leading to a decreased inhibitory binding
625 ability of malonyl-CoA on CPT1 activity. Even though we observed mitochondrial fragmentation
626 upon *MIC26* deletion, we did not observe increased FAO. This discrepancy could be explained
627 by a reduction of CPT1A amount on one hand and likely increased production of malonyl-CoA
628 on the other hand due to increased amounts of SLC25A1 and ACACA participating in fatty acid
629 synthesis. Hence, deletion of *MIC26*, leading to mitochondrial fragmentation, contributes to
630 ectopic cellular lipid accumulation but not FAO.

631 In sum, under balanced nutrient availability, we provide evidence that *MIC26* is important to
632 allow efficient metabolite channelling, mainly via glycolysis, thereby preventing unwanted
633 channelling into lipogenesis. In addition, *MIC26* is important to promote exactly the latter when
634 glucose is in excess. This is important for cells to adapt to nutrient overload and explains earlier
635 reports linking *MIC26* to diabetes. We propose that *MIC26* acts as a sensor and valve that
636 opens towards lipid synthesis only when glucose is in excess. Future studies will have to
637 decipher how changes in IM structure directly affect metabolite exchange and how this is
638 regulated dynamically.

639

640 **Acknowledgments**

641 A.K.K received Deutsche Forschungsgemeinschaft (DFG, German Research Foundation)
642 Grant KO 6519/1-1. A.S.R received grants from DFG Graduiertenkolleg VIVID RTG 2576 and
643 DFG SFB 1208, project B12 (ID 267205415). R.A received DFG Grant AN 1440/3-1. We thank
644 Gisela Pansegrau and Andrea Borchardt for technical assistance in western blot and electron
645 microscopy experiments, respectively. We are thankful for excellent technical support by Maria

19

646 Graf, Elisabeth Klemp, and Katrin Weber (CMML). RNA-sequencing was performed at the
647 Genomics & Transcriptomics facility, Biological and Medical Research Center (BMFZ), Medical
648 Faculty, Heinrich-Heine-University Düsseldorf. Computational infrastructure and support were
649 provided by the Centre for Information and Media Technology at Heinrich Heine University
650 Düsseldorf. Proteome experiments were performed at the proteomics facility, BMFZ, HHU,
651 Düsseldorf. Metabolite analyses were supported by the CEPLAS Plant Metabolism and
652 Metabolomics Laboratory, which is funded by the DFG under Germany's Excellence Strategy
653 – EXC-2048/1 – project ID 390686111.

654

655 **Author Contributions**

656 A.K.K. and A.S.R. conceptualized the research goals and the experiments of the study. M.L.
657 planned, performed and analysed the results from majority of the experiments. R.N analysed
658 and visualized proteomics and transcriptomics data. Y.S. planned, performed and analysed
659 BN-PAGE and CN-PAGE. P.W. and A.P.M.W. performed and analysed metabolomics data.
660 A.S. and K.S. performed and analysed proteomics data. P.P. and K.K. performed and analysed
661 transcriptomics data. R.A. contributed with scientific and critical inputs to the study. A.K.K. and
662 M.L. wrote the manuscript with input from all authors. A.K.K. supervised the study.

663

664 **Declaration of interests**

665 The authors declare no competing interests

666 **Figure legends**

667 **Figure 1. Mitochondrial apolipoprotein MIC26 is selectively increased in cells exposed**
668 **to hyperglycemia**

669 (A and B) Western blot analysis of all MICOS subunits from HepG2 WT and *MIC26* KO cells
670 cultured in normo- and hyperglycemia (N = 3-5). Chronic hyperglycemia treatment leads to
671 increased levels of MIC27, MIC26 and MIC25 in WT cells. Loss of MIC26 is accompanied by
672 decreased MIC10 in normoglycemia.

673 (C, D and E) Electron microscopy data including quantification of cristae number per unit length
674 (μm) per mitochondrial section (C) as well as crista junctions per cristae per mitochondrial
675 section (D), along with representative images (E) from HepG2 WT and *MIC26* KO cells cultured
676 in normo- and hyperglycemia (N = 2). Loss of MIC26 led to decreased cristae number and
677 crista junctions independent of normo- and hyperglycemia. Red arrows in lower row indicate
678 outer membrane (OM) or cristae. Scale bar represents 500 nm.

679 Data are represented as mean \pm SEM (B, C and D). Statistical analysis was performed using
680 one-way ANOVA with $*P < 0.05$, $**P < 0.01$, $***P < 0.001$, $****P < 0.0001$. N represents the
681 number of biological replicates.

682 **Figure 2. Hyperglycemia confers antagonistic regulation of lipid and cholesterol**
683 **pathways, in *MIC26* KO vs WT cells, compared to normoglycemia**

684 (A and B) Hierarchical Treemap clustering of significant gene ontology (GO) enriched terms of
685 biological processes upregulated in normoglycemic *MIC26* KO (A) and downregulated in
686 hyperglycemic *MIC26* KO (B) compared to respective WT. Each rectangle represents one
687 BioProcess pathway. Every colour represents clustering of different sub-pathways to pathway
688 families. The rectangle sizes indicate the *P*-value of the respective GO term.

689 (C and D) WikiPathway enrichment using EnrichR analysis of differentially expressed genes
690 (C) upregulated in normoglycemic *MIC26* KO and (D) downregulated in hyperglycemic
691 *MIC26* KO cells compared to respective WT. Arrows indicate antagonistically regulated
692 metabolic pathways including glycolysis, cholesterol biosynthesis, fatty acid synthesis and
693 oxidation.

694 Differentially expressed genes were considered statistically significant with a cut-off fold
695 change of ± 1.5 and Bonferroni correction $P \leq 0.05$. Treemap representation of GO enrichment
696 was plotted with statistically significant pathways with cut-off $P \leq 0.05$.

697 **Figure 3. MIC26 maintains the glycolytic function**

698 (A – C) Peptide abundances of enzymes involved in glycolysis pathway curated from
699 proteomics data (N = 5).

700 (D) Steady state metabolomics (GC-MS) data reveals increased cellular glucose accumulation
701 upon *MIC26* deletion in hyperglycemia (N = 3-4).

702 (E and F) Representative glycolysis stress test seahorse assay analysis, with sequential
703 injection of glucose, oligomycin and 2-deoxyglucose, reveals a tendency towards increased
704 glycolysis upon *MIC26* deletion (E) (n = 23). Quantification from various biological replicates
705 shows a significant increase of cellular glycolytic reserve in normoglycemic, but not in
706 hyperglycemic conditions (F) (N = 3).

707 (G) Cellular glucose uptake was measured using Glucose uptake Glo assay normalized to WT-
708 N. *MIC26* deletion leads to an increased glucose uptake upon normoglycemia (N = 3).

709 (H – J) Peptide abundances of transporters involved in glucose uptake namely GLUT3 (H),
710 GLUT1 (I) and GLUT2 (J) curated from proteomics data (N = 5).

711 (K and L) Steady state metabolomics (GC-MS) shows unaltered cellular pyruvate (K) and
712 lactate (L) levels in *MIC26* KO cell lines in normoglycemia but decreased levels upon *MIC26*
713 deletion in hyperglycemia (N = 3-4).

714 (M) *MIC26* deletion increases glycerol-3-phosphate amount in normoglycemia with an
715 antagonistic effect in hyperglycemia compared to the respective WT (N = 3-4).

716 Data are represented as mean \pm SEM (A-M). Statistical analysis was performed using one-
717 way ANOVA with * $P < 0.05$, ** $P < 0.01$, *** $P < 0.001$, **** $P < 0.0001$. N represents the number
718 of biological replicates and n the number of technical replicates.

719 **Figure 4. The loss of MIC26 leads to metabolic rewiring of cellular lipid metabolism via**
720 **CPT1A and dysregulation of fatty acid synthesis**

721 (A – D) Analysis of lipid droplet formation in WT and *MIC26* KO cells cultured in normo- and
722 hyperglycemia either in standard growth condition (CTRL) or upon palmitate stimulation
723 (100 μ M, 24 h). Representative confocal images of lipid droplets stained using BODIPY
724 493/503 are shown (A). Quantification shows number of lipid droplets normalized to the total
725 cell area [μ m²] (B) and mean fluorescence intensity per cell normalized to mean intensity of
726 WT-N in all biological replicates (C). *MIC26* deletion leads to a nutritional-independent
727 increase in lipid droplet number. However, an opposing effect, leading to increase or decrease
728 of mean fluorescence intensity of lipid droplets, upon comparison of *MIC26* KO to WT was

729 observed in normo- and hyperglycemia respectively, with a pronounced effect upon feeding
730 palmitate (N = 3). Scale bar represents 5 μ m.

731 (E) Heat map representing the abundance of steady state FFA species in WT and *MIC26* KO
732 cells cultured in normo- and hyperglycemia. 11 out of 19 of the FFA species represent an
733 antagonistic behavior upon comparing *MIC26* KO to WT in normo- (increase) and
734 hyperglycemia (decrease) (N = 3-4).

735 (F and G) Western blot analysis (F), along with respective quantification (G) of WT and
736 *MIC26* KO cells cultured in normo- and hyperglycemia, show a reduction of CPT1A in WT-H,
737 *MIC26* KO-N and *MIC26* KO-H compared to WT-N (N = 3).

738 (H – J) Mitochondrial fatty acid oxidation analyzed using Seahorse XF analyzer shows a
739 decreased palmitate-induced basal respiration (H) and spare respiratory capacity (I) and a
740 nonsignificant reduction of etomoxir-sensitive OCR decrease upon comparing *MIC26* KO to
741 WT in normoglycemia (N = 3).

742 Data are represented as mean \pm SEM (B-C and G-J). Statistical analysis was performed using
743 one-way ANOVA with **P* < 0.05, ***P* < 0.01, ****P* < 0.001, *****P* < 0.0001. N represents the
744 number of biological replicates.

745 **Figure 5. *MIC26* deletion leads to hyperglycemia-induced decrease in TCA cycle**
746 **intermediates**

747 (A) Representation of the relative amounts (GC-MS) of TCA cycle metabolites and associated
748 precursors at steady state in WT and *MIC26* KO cells cultured in normo- and hyperglycemia.
749 All the TCA cycle metabolites with the exception of α -ketoglutarate showed a decreasing trend
750 upon *MIC26* KO when compared to WT in hyperglycemia (N = 3-4).

751 (B and C) Mitochondrial pyruvate carrier 1 (MPC1) (B), but not MPC2 (C), is significantly
752 decreased in *MIC26* KO-N compared to WT-N, as revealed by peptide abundances from
753 proteomics data (N = 5).

754 (D) Mitochondrial glucose / pyruvate dependency analysis, using Seahorse XF analyzer mito
755 fuel flex test assay, reveals a decreased mitochondrial respiratory dependency of *MIC26* KO
756 on glucose / pyruvate in normoglycemia (N = 3).

757 Data are represented as mean \pm SEM (A-C). Statistical analysis was performed using one-
758 way ANOVA with **P* < 0.05, ***P* < 0.01, ****P* < 0.001, *****P* < 0.0001. N represents the number
759 of biological replicates.

760 **Figure 6. Aberrant glutamine metabolism is observed in *MIC26* KOs independent of**
761 **nutritional status**

762 (A) Metabolomics analysis (GC-MS) shows that glutamine levels were strongly increased in
763 *MIC26* KO cells cultured in both normo- and hyperglycemia at steady state compared to
764 respective WT (N = 3-4).

765 (B) Quantification of mitochondrial glutamine dependency and capacity analysis, using
766 Seahorse XF analyzer mito fuel flex test assay, shows a diminished mitochondrial respiratory
767 dependency on glutamine. A nonsignificant mitochondrial respiratory decreased capacity of
768 *MIC26* KO cells was observed compared to respective WT conditions (N = 3).

769 (C and D) Western Blot analysis (C) along with respective quantification (D) show reduced
770 amounts of the glutamate aspartate antiporter SLC25A12 (ARALAR / AGC1), present in
771 mitochondria, in *MIC26* KO cell lines compared to respective WT cells (N = 3).

772 (E – J) Representation of labeled (m+1 - m+6) and unlabeled (m+0) species of glutamate (GC-
773 MS) (E), and TCA cycle metabolites (AEC-MS) α -KG (F), citrate (G), succinate (H), fumarate
774 (I) and malate (J), from glutamine tracing experiments after labelling for 0.5 h and 6 h (N = 4).

775 (K – O) Conversion rates from different TCA cycle reactions calculated using the ratio of
776 highest labeled species abundances for the conversions of glutamate to α -KG (K), α -KG to
777 citrate (L), α -KG to succinate (M), succinate to fumarate (N) and α -KG to malate (N = 4).

778 Data are represented as mean \pm SEM (A-B and D-O). Statistical analysis was performed using
779 one-way ANOVA with * P < 0.05, ** P < 0.01, *** P < 0.001, **** P < 0.0001. N represents the
780 number of biological replicates.

781 **Figure 7. *MIC26* regulates mitochondrial bioenergetics by restricting the ETC activity**
782 **and OXPHOS (super-)complex formation**

783 (A and B) Representative pseudocolour rainbow LUT intensities from confocal images of WT
784 and *MIC26* KO HepG2 cells stained with TMRM show a reduction in $\Delta\Psi_m$ upon *MIC26* deletion
785 in both normoglycemia and hyperglycemia when compared to respective WT cells (A).
786 Quantification represents mean TMRM fluorescence intensity per cell normalized to mean
787 intensity of WT-N in all biological replicates (B) (N = 3). Scale bar represents 5 μ m.

788 (C and D) Representative confocal images of mitochondrial morphology, visualized by
789 MitoTracker green staining (C), show that loss of *MIC26* shifts mitochondrial morphology from
790 tubular mitochondrial network in WT normoglycemic conditions to fragmented phenotype
791 irrespective of supplemented glucose amount (D) (N = 3). Scale bar represents 5 μ m.

792 (E and F) Representative mitochondrial stress test with Seahorse XF analyzer, with sequential
793 injection of oligomycin, FCCP and rotenone/antimycin (E) (n = 19-23). Quantification from
794 various biological replicates shows a significant increase of basal respiration in *MIC26* KOs
795 cultured in both normo- and hyperglycemia (F) (N = 3).

796 (G) Blue native (respective left panel) and clear native (respective right panel) PAGE analysis
797 reveals an overall increase of OXPHOS complex formation (for CI, CIII, CIV and CV, green
798 arrows) as well as corresponding increased in-gel activity of supercomplexes, and complex
799 III₂IV (blue arrows) upon *MIC26* deletion. CV shows no in-gel activity alterations while a
800 decreased in-gel activity of F₁ occurs upon loss of *MIC26*. Native PAGEs were performed in
801 three biological replicates and representative gels are shown.

802 (H) Model representing the antagonistic regulation of metabolic pathways encompassing
803 glucose usage, lipid droplet formation, cholesterol synthesis, as well as decrease in TCA cycle
804 metabolites in *MIC26* deficient HepG2 cells dependent on nutritional conditions compared to
805 respective WT cells. An increase of glutamine levels as well as assembly of various OXPHOS
806 complexes is observed in *MIC26* KOs independent of the nutritional status. Arrows indicate
807 respective up (red) or downregulated (blue) protein/metabolite or activity levels, respectively.
808 In the model, left panel indicates normoglycemic while the right panel represents the
809 hyperglycemic conditions.

810 Data are represented as mean ± SEM (B and D-F). Statistical analysis was performed using
811 one-way ANOVA with **P* < 0.05, ***P* < 0.01, ****P* < 0.001, *****P* < 0.0001. N represents the
812 number of biological replicates and n the number of technical replicates.

813 **Supplementary Information**

814 **S1 Figure. MIC26 loss leads to an opposing regulation of cholesterol biosynthesis**
815 **pathway upon nutritional stimulation**

816 (A) Overview of transcriptomics clustering analysis showing upregulated (red) and
817 downregulated (blue) transcripts (without fold change or significance cut-offs). All sample
818 replicates are represented (N = 4).

819 (B and C) Proteomics data represented by WikPathway enrichment using EnrichR analysis
820 comparing pathways upregulated in normoglycemia (B) and downregulated in hyperglycemia
821 (C) upon *MIC26* deletion compared to respective WT (N = 5). Arrows indicate increased levels
822 of proteins participating in cholesterol synthesis and glycolysis pathways similar to those
823 observed with transcriptomics data (Fig 2C and D). Differentially expressed proteins were
824 considered statistically significant with a cut-off value of fold change of ± 1.5 and Bonferroni
825 correction $P \leq 0.05$.

826 **S2 Figure. Loss of MIC26 leads to an opposing regulation of cholesterol biosynthesis**
827 **pathway in normoglycemia and hyperglycemia**

828 (A and B) The transcripts of various enzymes regulating cholesterol synthesis are represented
829 using Cytoscape software comparing log₂FC data of *MIC26* KO and WT cell lines in normo-
830 (A) and hyperglycemia (B) (N = 4). In *MIC26* KO cell lines, normoglycemia strongly increases
831 transcripts of enzymes participating in cholesterol biosynthesis while an opposing effect is
832 observed in hyperglycemia.

833 (C – N) Peptide abundances of various enzymes participating in cholesterol biosynthesis
834 curated from proteomics data (N = 5).

835 (O) Metabolomics data reveals that cholesterol levels are exclusively decreased in *MIC26* KO
836 at steady state in hyperglycemia compared to WT but not in normoglycemia (N = 3-4).

837 Data are represented as mean \pm SEM (C-O). Statistical analysis was performed using one-
838 way ANOVA with * $P < 0.05$, ** $P < 0.01$, *** $P < 0.001$, **** $P < 0.0001$. N represents the number
839 of biological replicates.

840 **S3 Figure. MIC26 deletion causes opposing transcriptional regulation of genes involved**
841 **in glycolysis**

842 (A and B) The transcripts of various enzymes participating in glycolysis are represented using
843 Cytoscape software comparing log₂FC data of *MIC26* KO and WT cell lines in normo- (A) and
844 hyperglycemia (B) (N = 4).

845 (C and D) Glycolysis stress test Seahorse assay reveals a nonsignificant tendency towards
846 increased glycolysis and glycolytic capacity upon *MIC26* KO in normoglycemic, but not in
847 hyperglycemic conditions (N = 3).

848 Data are represented as mean \pm SEM (C and D). Statistical analysis was performed using one-
849 way ANOVA with * $P < 0.05$, ** $P < 0.01$, *** $P < 0.001$, **** $P < 0.0001$. N represents the number
850 of biological replicates.

851 **S4 Figure. Majority of free fatty acid species are antagonistically regulated upon *MIC26***
852 **deletion in normoglycemia and hyperglycemia when compared to respective to WT cells**

853 Detailed representation of abundances of various free fatty acid species in WT and *MIC26* KO
854 cell lines cultured in normo- and hyperglycemia (N = 3-4).

855 Data are represented as mean \pm SEM. Statistical analysis was performed using one-way
856 ANOVA with * $P < 0.05$, ** $P < 0.01$, *** $P < 0.001$, **** $P < 0.0001$. N represents the number of
857 biological replicates.

858 **S5 Figure. *MIC26* deletion leads to alteration of key enzymes regulating lipid metabolism**

859 (A and B) The transcripts of mitochondrial long-chain fatty acid importer CPT1A are strongly
860 decreased in WT-H and *MIC26* KO conditions, compared to WT-N, as shown from
861 transcriptomics data (A) (N = 4) and quantitative PCR (B) (N = 3) analysis.

862 (C and D) Representative fatty acid oxidation assay analyzed using oxygen consumption rates
863 of WT and *MIC26* KO HepG2 cells cultured in normoglycemia (C) and hyperglycemia (D) upon
864 feeding either with BSA or palmitate (n = 8-12).

865 (E and F) Mitochondrial citrate malate exchanger (SLC25A1) is significantly increased upon
866 *MIC26* deletion in normoglycemia compared to WT as detected using proteomics (E) (N = 5)
867 and transcriptomics (F) (N = 4) data.

868 (G – M) Transcripts and available peptide abundances of key genes involved in lipid
869 metabolism curated from transcriptomics (N = 4) and proteomics data (N = 5). Under
870 normoglycemic conditions, loss of *MIC26* increases the expression of ATP citrate lyase (G),
871 acetyl-CoA carboxylase 1 (H and I), fatty acid synthase (J and K) and acetyl-CoA desaturase
872 (L and M).

873 (N) Peptide abundances of glycerol kinase is increased in WT-H compared to WT-N but similar
874 in *MIC26* KO-N and *MIC26* KO-H (N = 5).

875 Data are represented as mean \pm SEM (A-N). Statistical analysis was performed using one-
876 way ANOVA with * $P < 0.05$, ** $P < 0.01$, *** $P < 0.001$, **** $P < 0.0001$. N represents the number
877 of biological replicates and n the number of technical replicates.

27

878 **S6 Figure. TCA cycle enzymes are altered upon *MIC26* knockout**

879 (A – K) Representation of peptide abundances of various mitochondrial TCA cycle enzymes
880 curated from proteomics data (N = 5).

881 (L – N) Peptide abundances of cytosolic enzymes involved in metabolite conversion (N = 5).

882 Data are represented as mean \pm SEM (A-N). Statistical analysis was performed using one-
883 way ANOVA with * $P < 0.05$, ** $P < 0.01$, *** $P < 0.001$, **** $P < 0.0001$. N represents the number
884 of biological replicates.

885 **S7 Figure. Mitochondrial glutamine and glutamate carriers are downregulated upon loss
886 of *MIC26***

887 (A) Transcripts of mitochondrial glutamate aspartate antiporter *SLC25A12* (A) are decreased
888 upon *MIC26* deletion in normo- and hyperglycemia (N = 4).

889 (B and C) Transcripts (B) (N = 4) and peptide abundances (C) (N = 5) of cellular and
890 mitochondrial glutamine importer *SLC1A5* are significantly decreased upon *MIC26* deletion in
891 both normo- and hyperglycemia in relation to respective WT cells.

892 (D) Peptide abundances of glutaminase (GLS) are unaltered upon loss of *MIC26* compared to
893 respective WT conditions.

894 (E) *MIC26* interactome, based cumulatively on BioGRID, NeXtProt and IntAct databases,
895 generated with Cytoscape software. From this study, downregulated transcripts comparing
896 *MIC26* KO and WT in normoglycemic condition are highlighted in blue while upregulated
897 transcripts are highlighted in red.

898 Data are represented as mean \pm SEM (A-D). Statistical analysis was performed using one-
899 way ANOVA with * $P < 0.05$, ** $P < 0.01$, *** $P < 0.001$, **** $P < 0.0001$. N represents the number
900 of biological replicates.

901 **S8 Figure. *MIC26* maintains mitochondrial morphology and bioenergetics**

902 (A and B) Western Blots (A) and quantification (B) show a decrease of key mitochondrial fusion
903 mediator MFN1 in *MIC26* KO cells while MFN2 was unchanged. Mitochondrial fission mediator
904 DRP1 is decreased in *MIC26* KO-H compared to WT-H. OPA1 processing shows no significant
905 changes upon *MIC26* deletion and nutritional status (N = 3-4).

906 (C and D) ATP production (C) and spare respiratory capacity (D) determined by mito stress
907 test using Seahorse XF analyzer. Deletion of *MIC26* caused increased ATP production and
908 decreased metabolic flexibility (indicated by SRC) in normoglycemia (N = 3).

909 Data are represented as mean \pm SEM (B-D). Statistical analysis was performed using one-
910 way ANOVA with $*P < 0.05$, $**P < 0.01$, $***P < 0.001$, $****P < 0.0001$. N represents the number
911 of biological replicates.

912 **S9 Figure. *MIC26* deletion induces alterations of SLC25 mitochondrial carrier protein**
913 **family expression and induces growth defects**

914 (A and B) Heat map overview from mean z-score of transcripts (A) (N = 4) and peptide
915 abundances (B) (N = 5) of mitochondrial transporters belonging to SLC25 family.

916 (C) Transcript abundances of *SREBP2* (C) of WT and *MIC26* KO cells grown in normo- and
917 hyperglycemia (N = 4).

918 (D – F) Proliferation of respective cell lines after 24 h (C), 48 h (D) and 72 h (E) determined
919 using SRB assay normalized to WT-N (N = 4).

920 (G – J) Transcripts (N = 4) and peptide abundances (N = 5) of NUBPL (G and H) and DHRS2
921 (I and J) are respectively shown.

922 Data are represented as mean \pm SEM (C-J). Statistical analysis was performed using one-way
923 ANOVA with $*P < 0.05$, $**P < 0.01$, $***P < 0.001$, $****P < 0.0001$. N represents the number of
924 biological replicates.

925 **Supplementary Tables**

926 **Supplementary Table S1**

927 Raw data of targeted metabolomics at steady state including polar metabolites (sheet 1) and
928 free fatty acids (FFAs) (sheet 2) indicating corresponding cell line, group, replicate, cell
929 number, multiplication factor, measured compound name, internal standard (ISTD) name,
930 measured total compound response, ISTD response, ratio of total compound response to ISTD
931 response, relative response and technical procedure data. Relative response is calculated
932 from compound response normalized to ISTD response and cell number multiplied by
933 multiplication factor and used for data representation.

934 **Supplementary Table S2**

935 Raw data of targeted metabolomics from tracing experiments including AEC-MS (sheet 1) and
936 GC-MS (sheet 2) data including cell line group analysed, compound isotopologue species,
937 corrected ratio to naturally occurring isotopologues timepoint and technical information.

938 **Supplementary Table S3**

939 Proteomics raw data analysis including gene description, mean abundance ratio, adjusted *P*-
940 value, mean abundances per group, total measured abundances of all replicate samples and
941 technical data are represented in sheet 1. Filtered significantly (adj. *P*-value ≤ 0.05) altered
942 peptide abundances with $\log_2FC > \pm 1.5$ for *MIC26* KO-N vs WT-N or *MIC26* KO-H and WT-H
943 are represented in sheet 2 and 3 respectively. Detected peptides with less than three out of
944 five hits in both of the compared groups were not considered.

945 **Supplementary Table S4**

946 Transcriptomics raw data analysis with sheet 1 representing raw data for all sample replicates,
947 including gene description. Calculated \log_2FC , FC, *P*-Value, FDR adjusted *P*-Value and
948 Bonferroni correction, as well as raw data from total reads, RPKM, TPM and CPM. DEGs
949 filtered by Bonferroni correction ≤ 0.05 and $\log_2FC > \pm 1.5$ for *MIC26* KO-N vs WT-N and
950 *MIC26* KO-H vs WT-H are represented in sheet 2 and 3 respectively. Sheet 4 is showing an
951 overview of number of differentially expressed genes including respective cut-offs.

952 **Materials and Methods**

953 **Key resources table**

954

REAGENT or RESOURCE	SOURCE	IDENTIFIER
Antibodies		
MIC26	Invitrogen	Cat# PA5-116197 RRID: AB_2900831
MIC27	Sigma-Aldrich	Cat# HPA000612 RRID: AB_1078594
MIC10	Abcam	Cat# ab84969 RRID: AB_1924831
MIC13	Pineda	custom made
MIC25	Protein tech	Cat# 20639-1-AP RRID: AB_1069767
MIC60	Abcam	Cat# ab110329 RRID: AB_10859613
MIC19	Protein tech	Cat# 25625-1-AP RRID: AB_2687533
MFN1	Santa Cruz Biotechnologies	Cat# sc-50330 RRID: AB_2250540
MFN2	Abcam	Cat# ab50838 RRID: AB_881507
OPA1	Pineda	custom made
DRP1	Cell Signaling Technologies	Cat# 5391 RRID: AB_11178938
β -Actin	Invitrogen	Cat# MA1-744 RRID: AB_2223496
HSP60	Sigma Aldrich	Cat# SAB4501464 RRID: AB_10746162
CPT1A	Proteintech	Cat# 15184-1-AP RRID: AB_2084676
Goat IgG anti-Mouse IgG	Abcam	Cat# ab97023 RRID: AB_10679675
Goat IgG anti-Rabbit IgG	Dianova	Cat# SBA-4050-05 RRID: AB_2795955
NDUFB4	Abcam	Cat# ab110243 RRID: AB_10890994
UQCRC2	Abcam	Cat# ab14745 RRID: AB_2213640
COXIV	Abcam	Cat# ab16056 RRID: AB_443304
ATP5A	Abcam	Cat# ab14748 RRID: AB_301447
SLC25A12	Santa Cruz Biotechnologies	Cat# sc-271056 RRID: AB10608837
Bacterial and virus strains		
N/A		
Biological samples		
N/A		
Chemicals, peptides, and recombinant proteins		
Etomoxir	Sigma Aldrich	Cat# E1905; CAS: 828934-41-4
3,3'-diaminobenzidine tetrahydrochloride	Sigma Aldrich	Cat# 32750; CAS: 868272-85-9

31

horse heart cytochrome c	Thermo Scientific	Cat# 147530010; CAS: 9007-43-6
NADH	Biomol	Cat# 16132.1 CAS: 606-68-8
Nitroblue tetrazolium chloride	Biomol	Cat# 06428.1 CAS: 298-83-9
Adenosine 5' triphosphate (ATP)	Sigma Aldrich	Cat# A7699 CAS: 34369-07-8
Lead (II) nitrate / Pb(NO ₃) ₂	Sigma Aldrich	Cat# 1073980100 CAS: 10099-74-8
MitoTracker Green	Invitrogen	Cat# M7514 CAS: 201860-17-5
TMRM	Invitrogen	Cat# T668
BODIPY 493/503	Cayman Chemicals	Cat# Cay25892-5 CAS: 121207-31-6
Poly-D-lysine	Sigma Aldrich	Cat# P7886 CAS: 2796-99-4
Stable Glutamine	PAN-Biotech	Cat# P04-82100
PenStrep	PAN-Biotech	Cat# P06-07100
BSA	Biomol	Cat#Cay29556
Palmitate-BSA	Biomol	Cat#Cay29558
L-Carnitine	Sigma Aldrich	Cat#C0283 CAS: 645-46-1
Ribitol	Sigma Aldrich	Cat# A5502
L-Glutamine-13C5-15N2	Sigma Aldrich	Cat# 607983 CAS: 607983
Critical commercial assays		
Glycolysis Stress Test	Agilent Technologies	Cat# 103020-100
Mito Stress Test	Agilent Technologies	Cat# 103015-100
Mito Fuel Flex Test	Agilent Technologies	Cat# 103260-100
Glucose Uptake Glo	Promega	Cat# J1241
GoScript Reverse Transcription Mix, Oligo(dT)	Promega	Cat# A2791
GoTaq qPCR Master Mix	Promega	Cat# A6002
RNeasy Mini Kit	Qiagen	Cat# 74106
Deposited data		
MIC26 interactome	N/A	Nextprot, Intact BioGrid
Experimental models: Cell lines		
HepG2	Sigma Aldrich	Cat# 85011430 RRID: CVCL_0027
Experimental models: Organisms/strains		
N/A		
Oligonucleotides		
Primer CPT1A Forward GATCCTGGACAATACCTCGGAG	This paper	N/A
Primer CPT1A Reverse CTCCACAGCATCAAGAGACTGC	This paper	N/A
Primer HPRT1 Forward 5'- CATTATGCTGAGGATTTGGAAAGG- 3'	This paper	N/A
Primer HPRT1 Reverse 5'- CTTGAGCACACAGAGGGCTACA-3'	This paper	N/A
Recombinant DNA		
Double Nickase Plasmid MIC26 KO	Santa Cruz Biotechnology	Cat# sc-413137-NIC
Software and algorithms		

Prism	GraphPad	RRID: SCR_002798
Seahorse Wave	Agilent Technologies	RRID: SCR_014526
R Studio	Posit PBC	RRID: SCR_000432
Cytoscape	Cytoscape Consortium	RRID: SCR_003032
Volocity 3D Image Analysis Software	Perkin Elmer	RRID: SCR_002668
MassHunter Qualitative	Agilent Technologies	RRID: SCR_015040
BCL Convert Tool	Illumina	N/A
CLC Genomics Workbench	Qiagen	RRID: SCR_017396
CLC Gene Set Enrichment Test	Qiagen	RRID: SCR_003199
Proteome Discoverer	Thermo Fischer Scientific	RRID: SCR_014477
Other		
DMEM 1 g/L glucose	PAN-Biotech	Cat# P04-01500
DMEM 4.5 g/L glucose	PAN-Biotech	Cat# P04-82100
FBS	Capricorn Scientific	Cat# FBS-11A

955 **Cell culture and treatment conditions**

956 HepG2 cells were cultured in 1 g/L glucose DMEM (PAN-Biotech) supplemented with 10%
 957 FBS (Capricorn Scientific), 2 mM stable glutamine (PAN-Biotech) and penstrep (PAN-Biotech,
 958 penicillin 100 U/mL and 100 µg/mL streptomycin). Cells were grown at 37°C supplied with 5%
 959 CO₂. *MIC26* HepG2 KO cells were generated using the double nickase method as described
 960 before (Lubeck *et al.*, 2023). Cells cultured in standard growth media were divided equally into
 961 two cell culture flasks and grown in either 1 g/L glucose DMEM (normoglycemia) or 4.5 g/L
 962 glucose DMEM (hyperglycemia) (PAN-Biotech) supplemented with above-mentioned
 963 reagents. Cells were cultured in normoglycemia and hyperglycemia for a prolonged duration
 964 of three weeks. During the three weeks, cell splitting was carried out twice a week with the
 965 corresponding media.

966 **SDS gel electrophoresis and Western Blotting**

967 After three washes with 2 mL DPBS (PAN-Biotech), the cells were harvested by scraping and
 968 resuspending in an appropriate volume of RIPA buffer (150 mM NaCl, 0.1 % SDS, 0.05 %
 969 Sodium deoxycholate, 1 % Triton-X-100, 1 mM EDTA, 1mM Tris, pH 7.4, 1x protease inhibitor
 970 (Sigma-Aldrich), PhosSTOP (Roche). Protein concentration was determined using DCTM
 971 protein assay Kit (BIO-RAD, 5000116). SDS samples were prepared with Laemmli buffer and
 972 heated for 5 min at 95°C. Depending on the proteins investigated, a variety of SDS
 973 electrophoresis gels (8%, 10%, 12% or 15%) were used for running and separating protein
 974 samples. Subsequently, proteins were transferred onto nitrocellulose membranes and stained
 975 using Ponceau S (Sigma Aldrich). After destaining, nitrocellulose membranes were blocked
 976 with 5 % milk in 1x TBS-T for 1 h, washed three times with TBS-T and probed at 4°C overnight
 977 with the following primary antibodies: *MIC26* (Invitrogen, 1:1000), *MIC27* (Sigma-Aldrich,
 978 1:2000), *MIC10* (Abcam, 1:1000), *MIC13* (Pineda custom-made, 1:1000), *MIC25* (Proteintech,
 979 1:1000), *MIC60* (Abcam, 1:1000), *MIC19* (Proteintech, 1:1000), *MFN1* (Santa Cruz

980 Biotechnologies, 1:1000), MFN2 (Abcam, 1:1000), OPA1 (Pineda custom-made, 1:1000),
981 DRP1 (Cell Signaling Technology, 1:1000), β -Actin (Invitrogen, 1:2000), HSP60 (Sigma-
982 Aldrich, 1:2000) and CPT1A (Proteintech, 1:1000). Goat IgG anti-Mouse IgG (Abcam,
983 1:10000) and Goat IgG anti-Rabbit IgG (Dianova, 1:10000) conjugated to HRP were used as
984 secondary antibodies. The chemiluminescent signals were obtained using Signal Fire ECL
985 reagent (Cell Signaling Technology) and VILBER LOURMAT Fusion SL equipment (Peqlab).

986 **Blue Native and Clear Native PAGE**

987 5×10^6 HepG2 cells were seeded onto 15 cm dishes and cell culture medium was replaced
988 every two days until 80 % confluency was reached. Cells were washed three times with cold
989 PBS, scraped and pelleted at 900 g, 4°C for 5 min. Cell pellets were resuspended in 1 mL lysis
990 buffer (210 mM mannitol, 70 mM sucrose, 1 mM EDTA, 20 mM HEPES, 0,1 % BSA, 1x
991 protease inhibitor) and incubated on ice for 10 min. Mitochondria were isolated by repetitive
992 strokes of mechanical disruption using a 20G canula and sequential centrifugation steps at
993 1000 x g, 4°C for 10 min to remove cell debris and 10,000 x g, 4°C for 15 min to pellet
994 mitochondria. Mitochondrial pellet was resuspended in BSA-free lysis buffer and protein
995 concentration was determined using DC Protein Assay Kit.

996 For blue native page, 100 μ g of mitochondria was solubilized for 1 h on ice using 2.5 g/g of
997 digitonin to protein ratio. The samples were centrifuged for 20 min at 20,000 x g and 4°C to
998 pellet insolubilized material. The supernatants were supplemented with loading buffer (50%
999 glycerol, 8 g/g Coomassie to detergent ratio) and immediately loaded onto 3-13% gradient gel.
1000 Complexes were separated at 150 V, 15 mA for 16 h. Thereafter, protein complexes were
1001 transferred onto PVDF membrane and blocked overnight with 5 % milk in TBS-T at 4°C. For
1002 identification of relevant protein complexes, the membranes were decorated with the following
1003 antibodies: NDUFB4 (Abcam, 1:1000), UQCRC2 (Abcam, 1:1000), COXIV (Abcam, 1:1000)
1004 ATP5A (Abcam, 1:1000) Goat IgG anti-Mouse IgG (Abcam, 1:10000) and Goat IgG anti-Rabbit
1005 IgG (Dianova, 1:10000) conjugated to HRP. The chemiluminescent signals were obtained
1006 using Pierce™ SuperSignal™ West Pico PLUS chemiluminescent substrate reagent (Thermo
1007 Scientific) and VILBER LOURMAT Fusion SL equipment (Peqlab).

1008 For clear native gels, 300 μ g mitochondria was solubilized on ice for 1 h with 2.5 g/g digitonin
1009 to protein ratio. The samples were centrifuged for 20 min at 20,000 x g and 4°C to pellet
1010 insolubilized material. The supernatants were supplemented with loading buffer (50% glycerol,
1011 0.01 % Ponceau S) and immediately loaded onto 3-13% gradient gels. Complexes were
1012 separated at 150 V, 15 mA for 16 h. To assess complex in-gel activity, the gel slices were
1013 incubated in respective buffer solutions for several hours at room temperature. For complex I
1014 activity, the gel was incubated in 5 mM Tris-HCl (pH 7.4), 0.1 mg/mL NADH and 2.5 mg/mL
1015 nitro blue tetrazolium chloride (NBT). For complex III, the gel was incubated in 50 mM sodium

1016 phosphate buffer (pH 7.2), 0.1 % 3,3'-diaminobenzidine tetrahydrochloride (DAB). To assess
1017 complex IV activity, the gel was incubated in 50 mM sodium phosphate buffer (pH 7.2), 0.05
1018 % DAB and 50 μ M horse heart cytochrome c and for complex V, the gel was incubated in 35
1019 mM Tris-base, 270 mM glycine, 14 mM MgSO₄, 0.2 % (w/v) Pb(NO₃)₂ and 8 mM ATP.

1020 **RNA isolation and quantification**

1021 Total RNA was extracted from cell pellets using RNeasy Mini Kit (Qiagen) according to the
1022 manufacturer's protocol. RNA quality and quantity were assessed using BioSpectrometer
1023 (Eppendorf). cDNA synthesis from 5 μ g RNA was performed using the GoScript™ Reverse
1024 Transcriptase Kit (Promega). Next, quantitative real-time PCR was performed in Rotor Gene
1025 6000 (Corbett Research) using GoTagR qPCR Master Mix (Promega) according to
1026 manufacturer's instructions with the following primers:

- 1027 1. *CPT1A*:
1028 Forward: 5'- GATCCTGGACAATACCTCGGAGC-3'
1029 Reverse: 5'- CTCCACAGCATCAAGAGACTGC-3'
- 1030 2. *HPRT1* (Housekeeping gene):
1031 Forward: 5'-CATTATGCTGAGGATTTGGAAAGG-3'
1032 Reverse: 5'-CTTGAGCACACAGAGGGCTACA-3'

1033

1034 C_t values were normalized to housekeeping gene *HPRT1* followed by normalization of Δ C_t
1035 values to average Δ C_t of WT-N control group.

1036 **Transcriptomics**

1037 Cells were seeded in quadruplicates onto 10 cm dishes in corresponding cell culture media
1038 and medium was replaced every two days until 80 % cell confluency was obtained. For
1039 preparation of RNA, cells were washed three times with cold PBS and subsequently scraped
1040 and pelleted. RNA isolation from cell pellets was performed using RNeasy Mini Kit (Qiagen)
1041 including DNase digestion according to the manufacturer's protocol. Sample concentration
1042 was determined and 1 μ g RNA was aliquoted for transcriptomics analysis. Total RNA samples
1043 were quantified (Qubit RNA HS Assay, Thermo Fisher Scientific, MA, USA) and quality
1044 measured by capillary electrophoresis using the Fragment Analyzer and the 'Total RNA
1045 Standard Sensitivity Assay' (Agilent Technologies, Inc. Santa Clara, CA, USA). All samples in
1046 this study showed RNA Quality Numbers (RQN) with a mean of 10.0. The library preparation
1047 was performed according to the manufacturer's protocol using the 'VAHTS™ Stranded mRNA-
1048 Seq Library Prep Kit' for Illumina®. Briefly, 700 ng total RNA were used as input for mRNA
1049 capturing, fragmentation, the synthesis of cDNA, adapter ligation and library amplification.
1050 Bead purified libraries were normalized and finally sequenced on the NextSeq2000 system
1051 (Illumina Inc. San Diego, CA, USA) with a read setup of 1x100 bp. The BCL Convert Tool

35

1052 (version 3.8.4) was used to convert the bcl files to fastq files as well for adapter trimming and
1053 demultiplexing.

1054 Data analyses on fastq files were conducted with CLC Genomics Workbench (version 22.0.2,
1055 Qiagen, Venlo, Netherlands). The reads of all probes were adapter trimmed (Illumina TruSeq)
1056 and quality trimmed (using the default parameters: bases below Q13 were trimmed from the
1057 end of the reads, ambiguous nucleotides maximal 2). Mapping was done against the *Homo*
1058 *sapiens* (hg38; GRCh38.107) (July 20, 2022) genome sequence. After grouping of samples
1059 (four biological replicates) according to their respective experimental conditions, the statistical
1060 differential expression was determined using the CLC differential expression for RNA-Seq tool
1061 (version 2.6, Qiagen, Venlo, Netherlands). The resulting *P* values were corrected for multiple
1062 testing by FDR and Bonferroni-correction. A *P* value of ≤ 0.05 was considered significant. The
1063 CLC gene set enrichment test (version 1.2, Qiagen, Venlo, Netherlands) was done with default
1064 parameters and based on the GO term 'biological process' (*H. sapiens*; May 01, 2021).

1065 The data discussed in this publication have been deposited in NCBI's Gene Expression
1066 Omnibus (Edgar *et al*, 2002) and are accessible through GEO Series accession number
1067 GSE248848.

1068 **Proteomics**

1069 Cells were seeded in quintuplicates onto 10 cm dishes in corresponding cell culture media and
1070 medium was replaced every two days until 80 % cell confluency was obtained. Cells were
1071 washed four times with PBS, scraped and pelleted in a pre-weighed Eppendorf tube. After
1072 complete removal of PBS, cells were immediately frozen in liquid nitrogen and sample weight
1073 was determined for normalization. Proteins were extracted from frozen cell pellets as described
1074 elsewhere (Poschmann *et al*, 2014). Briefly, cells were lysed and homogenized in urea buffer
1075 with a TissueLyser (Qiagen) and supernatants were collected after centrifugation for 15 min at
1076 14,000 x g and 4°C. Protein concentration was determined by means of Pierce 660 nm protein
1077 assay (Thermo Fischer Scientific). For LC-MS analysis, a modified magnetic bead-based
1078 sample preparation protocol according to Hughes and colleagues was applied (Hughes *et al*,
1079 2019). Briefly, 20 µg total protein per sample was reduced by adding 10 µL 100 mM DTT
1080 (dithiothreitol) and shaking for 20 min at 56°C and 1000 rpm, followed by alkylation with the
1081 addition of 13 µL 300 mM IAA and incubation for 15 min in the dark. A 20 µg/µL bead stock of
1082 1:1 Sera-Mag SpeedBeads was freshly prepared and 10 µL was added to each sample.
1083 Afterwards, 84 µL ethanol was added and incubated for 15 min at 24°C. After three rinsing
1084 steps with 80% EtOH and one rinsing step with 100% ACN, beads were resuspended in 50 mM
1085 TEAB buffer and digested with final 1:50 trypsin at 37°C and 1,000 rpm overnight. Extra-
1086 digestion was carried out by adding trypsin (final 1:50) and shaking at 37°C and 1000 rpm for

1087 4 h. The supernatants were collected and 500 ng of each sample digest was subjected to LC-
1088 MS.

1089 For the LC-MS acquisition, an Orbitrap Fusion Lumos Tribrid Mass Spectrometer (Thermo
1090 Fisher Scientific) coupled to an Ultimate 3000 Rapid Separation liquid chromatography system
1091 (Thermo Fisher Scientific) equipped with an Acclaim PepMap 100 C18 column (75 μ m inner
1092 diameter, 25 cm length, 2 μ m particle size from Thermo Fisher Scientific) as separation column
1093 and an Acclaim PepMap 100 C18 column (75 μ m inner diameter, 2 cm length, 3 μ m particle
1094 size from Thermo Fisher Scientific) as trap column was used. A LC-gradient of 180 min was
1095 applied. Survey scans were carried out over a mass range from 200-2,000 m/z at a resolution
1096 of 120,000. The target value for the automatic gain control was 250,000 and the maximum fill
1097 time 60 ms. Within a cycle time of 2 s, the most intense peptide ions (excluding singly charged
1098 ions) were selected for fragmentation. Peptide fragments were analysed in the ion trap using
1099 a maximal fill time of 50 ms and automatic gain control target value of 10,000 operating in rapid
1100 mode. Already fragmented ions were excluded for fragmentation for 60 seconds.

1101 Data analysis was performed with Proteome Discoverer (version 2.4.1.15, Thermo Fisher
1102 Scientific). All RAW files were searched against the human Swissprot database (Download:
1103 23.01.2020) and the Maxquant Contaminant database (Download: 20.02.2021), applying a
1104 precursor mass tolerance of 10 ppm and a mass tolerance of 0.6 Da for fragment spectra.
1105 Methionine oxidation, N-terminal acetylation, N-terminal methionine loss and N-terminal
1106 methionine loss combined with acetylation were considered as variable modifications,
1107 carbamidomethylation as static modification as well as tryptic cleavage specificity with a
1108 maximum of two missed cleavage sites. Label-free quantification was performed using
1109 standard parameters within the predefined workflow. Post processing, proteins were filtered to
1110 1% FDR and a minimum of 2 identified peptides per protein. The mass spectrometry
1111 proteomics data have been deposited to the ProteomeXchange Consortium via the PRIDE
1112 (Perez-Riverol *et al*, 2022) partner repository with the dataset identifier PXD047246.

1113 **Metabolomics**

1114 Metabolites were analyzed by gas chromatography (GC) and anion exchange chromatography
1115 (AEC) coupled to mass spectrometry (MS). 1.5×10^6 cells were seeded in quadruplicates onto
1116 6 cm dishes and cultured in the corresponding media overnight. For glutamine tracing
1117 experiments, medium was replaced with corresponding growth media containing 2 mM labeled
1118 glutamine [$U\text{-}^{13}\text{C}_5$, $^{15}\text{N}_2$] (Sigma-Aldrich) either for 30 min or 6 h prior to cell harvesting. For
1119 metabolite extraction, cells were washed five times with ice-cold isotonic NaCl solution (0.9 %),
1120 followed by scraping of cells in 1 mL ice-cold MeOH. Cells were transferred to a 15 mL tube
1121 and diluted with 1 mL MilliQ water. Cell suspension was immediately frozen in liquid nitrogen.

1122 After thawing on ice, 0.5 mL MilliQ water was added supplemented with 10 μ M internal
1123 standard ribitol (Sigma Aldrich) for polar metabolite analysis. After that 1.5 mL MTBE was
1124 added containing 5.4 μ L heptadecanoic acid (1mg/ml) as internal standard for free fatty acid
1125 analysis. After repetitive mixing, samples were incubated on ice for 10 min. Subsequently,
1126 polar and nonpolar phases were separated by centrifugation at 4000 x g for 10 min at 4°C. The
1127 apolar phase was collected, frozen at -80°C and used for free fatty acid analysis. The aqueous
1128 phase was diluted with MilliQ water to decrease the organic proportion below 15 %. The
1129 sample was then frozen at -80°C, dried by lyophilization reconstituted in 500 μ L MilliQ water
1130 and filtered prior to analysis.

1131 For GC-MS, 100 μ L was dried by vacuum filtration. Metabolite analysis was conducted using
1132 a 7890B gas chromatography system connected to a 7200 QTOF mass spectrometer (Agilent
1133 Technologies) as described previously (Shim *et al*, 2019). In brief, methoxyamine
1134 hydrochloride and N-methyl-N-(trimethylsilyl)trifluoroacetamide were subsequently added to
1135 the dried sample to derivatize functional groups of polar compounds. With an injection volume
1136 of 1 μ L, samples were introduced into the GC-MS system and compounds were separated on
1137 a HP-5MS column (30m length, 0.25mm internal diameter and 0.25 μ m film thickness). The
1138 software MassHunter Qualitative (v b08, Agilent Technologies) was used for compound
1139 identification by comparing mass spectra to an in-house library of authentic standards and to
1140 the NIST14 Mass Spectral Library (<https://www.nist.gov/srd/nist-standard-reference-database-1a-v14>). Peak areas were integrated using MassHunter Quantitative (v b08, Agilent
1142 Technologies) and normalized to the internal standard ribitol and cell number. To determine
1143 the ¹³C and ¹⁵N incorporation, isotopologues for individual fragments were analyzed according
1144 to the number of possible incorporation sites. The normalized peak areas were corrected for
1145 the natural abundance using the R package IsoCorrector (Heinrich *et al*, 2018).

1146 For the analysis of anionic compounds by AEC-MS, samples were diluted with MilliQ water
1147 (1:2 v/v). Measurements were performed using combination of a Dionex ICS-6000 HPIC and
1148 a high field Thermo Scientific Q Exactive Plus quadrupole-Orbitrap mass spectrometer (both
1149 Thermo Fisher Scientific) as described earlier with minor modifications (Curien *et al*, 2021). 10
1150 μ L of sample was injected via a Dionex AS-AP autosampler in push partial mode. Anion
1151 exchange chromatography was conducted on a Dionex IonPac AS11-HC column (2 mm X 250
1152 mm, 4 μ m particle size, Thermo Scientific) equipped with a Dionex IonPac AG11-HC guard
1153 column (2 mm X 50 mm, 4 μ m, Thermo Scientific) at 30°C. The mobile phase was established
1154 using an eluent generator with a potassium hydroxide cartridge to produce a potassium
1155 hydroxide gradient. The column flow rate was set to 380 μ L min⁻¹ with a starting KOH
1156 concentration of 5 mM for one minute. The concentration was increased to 85 mM within 35
1157 min and held for 5 min. The concentration was immediately reduced to 5 mM and the system

38

1158 equilibrated for 10 min. Spray stability was achieved with a makeup consisting of methanol
1159 with 10 mM acetic acid delivered with 150 $\mu\text{L min}^{-1}$ by an AXP Pump. The electro spray was
1160 achieved in the ESI source using the following parameters: sheath gas 30, auxiliary gas 15,
1161 sweep gas 0, spray voltage - 2.8 kV, capillary temperature 300°C, S-Lens RF level 45, and
1162 auxiliary gas heater 380°C. For the untargeted approach, the mass spectrometer operated in
1163 a combination of full mass scan and a data-dependent Top5 MS2 (ddMS2) experiment. The
1164 full scan (60-800 m/z) was conducted with a resolution of 140,000 and an automatic gain
1165 control (AGC) target of 10^6 ions with a maximum injection time of 500 ms. The Top5 ddMS2
1166 experiment was carried out with a resolution of 17,500 and an AGC target of 10^5 and a
1167 maximum IT of 50 ms. The stepped collision energy was used with the steps (15, 25, 35) to
1168 create an average of NCE 25. Data analysis was conducted using Compound Discoverer
1169 (version 3.1, Thermo Scientific) using the “untargeted Metabolomics workflow” for steady state
1170 analysis. Compound identification was achieved on the level of mass accuracy (MS1 level),
1171 fragment mass spectra matching (MS2 level) and retention time comparison with authentic
1172 standards. For the enrichment analysis with stable heavy isotopes, the standard workflow for
1173 “stable isotope labelling” was chosen with the default settings 5 ppm mass tolerance, 30 %
1174 intensity tolerance and 0.1 % intensity threshold for isotope pattern matching and a maximum
1175 exchange rate was of 95%.

1176 For free fatty acid analysis via GC-MS, lipids were hydrolysed and free fatty acids were
1177 methylated to fatty acid methyl esters (FAMES). To do so, the organic phase was transferred
1178 into a glass vial and dried under a stream of nitrogen gas. The dried sample was resuspended
1179 in 1 mL of methanolic hydrochloride (MeOH/3 N HCl) and incubated at 90°C for 1 h. One mL
1180 of hexane and 1 mL of NaCl solution (1%) were added before centrifugation at 2000 g for 5 min.
1181 The FAME-containing organic phase (top layer) was collected in a clean glass vial and stored
1182 at -20°C until measurement as described recently (Vasilopoulos *et al*, 2023).

1183 **Quantification of mitochondrial morphology, membrane potential ($\Delta\Psi_m$) and cellular** 1184 **lipid droplets**

1185 HepG2 cells (0.25×10^6 cells) were seeded onto 35 mm Poly-D-Lysine-coated (50 $\mu\text{g/ml}$) live-
1186 imaging dishes (MATTEK P35G-1.5-14-C) and incubated for 24 h at 37°C, 5 % CO_2 in the
1187 corresponding normoglycemic or hyperglycemic media. The assessment of mitochondrial
1188 morphology, $\Delta\Psi_m$ and cellular lipid droplets was performed by addition of MitoTracker Green
1189 (Invitrogen, 200 nM), TMRM (Invitrogen, 50 nM), BODIPY 493/503 (Cayman Chemicals,
1190 10 μM) respectively for 30 min at 37°C, followed by washing thrice. Live-cell microscopy was
1191 performed using a spinning disc confocal microscope (PerkinElmer) equipped with a 60x oil-
1192 immersion objective (N.A = 1.49) and a Hamamatsu C9100 camera (1000 X 1000 pixel). The

1193 cells were maintained at 37°C in DMEM supplemented with 10 mM HEPES for the imaging
1194 duration. MitoTracker Green and BODIPY 493/503 were excited with a 488 nm laser while
1195 TMRM was excited with a 561 nm laser. The images were obtained at emission wavelength of
1196 527 nm (W55) and 615 nm (W70) for 488 nm and 561 nm excitation respectively. The cell
1197 population was classified into tubular, intermediate and fragmented mitochondrial morphology
1198 based on the majority of mitochondria belonging to the respective class. Cells classified as
1199 tubular and fragmented contained mostly long tubular and short fragments respectively
1200 whereas cells classified as intermediate had a mixture of mostly short pieces, few long tubes
1201 as well as fragmented mitochondria. Volocity image analysis software was used for the
1202 quantification regarding $\Delta\Psi_m$ and lipid droplets. The total fluorescence intensities of TMRM
1203 and BODIPY were obtained per cell after respective background subtraction. Each cell was
1204 manually demarcated by drawing a ROI. Lipid droplet number within a ROI was obtained
1205 automatically using find spots by setting threshold of brightest spot within a radius of 0.5 μm
1206 and compartmentalization to ROI.

1207 **Glucose Uptake Assay**

1208 3×10^4 HepG2 cells were seeded in triplicates onto a dark 96-well plate overnight and in parallel
1209 onto a clear-96 well plate for cell normalization. Cellular glucose uptake was measured using
1210 Glucose Uptake-Glo™ Assay kit (Promega), according to the manufacturer's protocol.
1211 Luminescence was measured by microplate reader (CLARIOstar Plus, BMG LABTECH) with
1212 1 s integration after 1 h of incubation. Normalization was performed using Hoechst staining
1213 and mean of signal intensity was used for normalizing luminescence intensities. Luciferase
1214 signals were normalized to WT-N measurement.

1215 **Mitochondrial respirometry**

1216 A variety of respirometry experiments were performed using Seahorse XFe96 Analyzer
1217 (Agilent). HepG2 cells were seeded onto Poly-D-Lysine-coated (50 $\mu\text{g}/\text{ml}$) Seahorse XF96 cell
1218 culture plate (Agilent) at a density of 3.0×10^4 cells per well. For mitochondrial stress test,
1219 mitochondrial fuel flexibility test and glycolysis stress test, cells were incubated overnight in
1220 standard growth media. For fatty acid oxidation (FAO) test, standard growth medium was
1221 replaced by serum-deprived growth medium (DMEM without glucose, pyruvate and glutamine),
1222 containing 1 % FBS, 0.5 mM glucose, 0.5 mM L-Carnitine (Sigma Aldrich) and 1.0 mM
1223 glutamine 10 h after cell seeding and incubated overnight.

1224 Prior to performing the assay, old medium was removed and cells were washed twice after
1225 which cells were supplemented with the corresponding assay media followed by 45 min CO_2 -
1226 free incubation. Mitochondrial stress test was performed using Seahorse assay media (Agilent)
1227 supplemented with 10 mM glucose, 2 mM stable glutamine and 1 mM sodium pyruvate.

1228 Mitochondrial oxygen consumption was measured after sequential addition of oligomycin
1229 (1 μ M), FCCP (0.25 μ M) and rotenone/antimycin (0.5 μ M) according to the manufacturer's
1230 protocol. Mitochondrial fuel flexibility test was performed using Seahorse assay media
1231 containing 10 mM glucose, 2 mM stable glutamine and 1 mM sodium pyruvate. After initial
1232 acquisition of basal respiration, glucose, glutamine and FAO dependency and capacity was
1233 assessed according to manufacturer's protocol by sequential incubation with UK5099 (2 μ M)
1234 and Etomoxir (4 μ M) / BPTES (3 μ M), BPTES (3 μ M) and Etomoxir (4 μ M) / UK5099 (2 μ M) or
1235 Etomoxir (4 μ M) and UK5099 (2 μ M) / BPTES (3 μ M) respectively. Glycolysis stress test was
1236 performed in Seahorse assay media supplemented with 2 mM glutamine. After 15 min of basal
1237 ECAR determination, glycolysis was induced by addition of glucose (10 mM), followed by
1238 oligomycin (1 μ M) and lastly 2-DG (50 mM). For assessment of FAO, cells were pretreated
1239 with Seahorse assay media containing BSA (Biomol, 200 μ M) or Palmitate (Biomol, 200 μ M).
1240 FAO was measured by sequential addition of etomoxir (Sigma Aldrich, 4 μ M) or media and
1241 mitochondrial stress test kit chemicals oligomycin (1.5 μ M), FCCP (1 μ M), rotenone/antimycin
1242 A (0.5 μ M). Cell numbers were normalized using Hoechst (10 μ g/mL) staining intensity
1243 assessed by microplate reader (Tecan M200 pro). Data were analyzed using wave software
1244 (Agilent) and Microsoft Excel.

1245 **Electron Microscopy**

1246 4×10^6 HepG2 cells were grown overnight in 10 cm petri dishes at 37°C with 5% CO₂ in the
1247 corresponding treatment media. Cells were fixed using 3 % glutaraldehyde, 0.1 M sodium
1248 cacodylate buffer at pH 7.2 and subsequently pelleted. Cell pellets were washed in fresh 0.1
1249 M sodium cacodylate buffer at pH 7.2 and embedded in 3 % low melting agarose. Cells were
1250 stained using 1% osmium tetroxide for 50 min, washed twice with 0.1 M sodium cacodylate
1251 buffer and once using 70% ethanol for 10 min each. Thereafter, cells were stained using 1%
1252 uranyl acetate/1% phosphotungstic acid in 70% ethanol for 1 h. Stained samples were
1253 embedded in spur epoxy resin for polymerization at 70°C for 24 hours. Ultrathin sections were
1254 prepared using a microtome and imaged on a transmission electron microscope (Hitachi,
1255 H600) at 75 V equipped with Bioscan 792 camera (Gatan). Image analysis was performed
1256 using ImageJ software.

1257 **Sulforhodamine B (SRB) assay**

1258 Cell viability was assessed by SRB colorimetry assay. 2.5×10^4 HepG2 cells were seeded in
1259 24 well plates and incubated for 24 h, 48 h or 72 h. Subsequently, cells were washed with PBS
1260 and fixed with 10% (w/v) cold trichloroacetic acid solution (500 μ L/well) for 1 h at 4°C. After
1261 washing five times with MilliQ water, cells were dried at RT overnight. Fixed cells were stained
1262 with SRB solution (0.4% (w/v) in 1% acetic acid, 300 μ L/well) for 15 min at RT, washed five
1263 times with 1% acetic acid and dried at RT for 1 h. SRB extraction was performed by addition

41

1264 of 400 μ L TRIS-Base (10 mmol/l) per well. The absorbance was measured, after 5 min of
1265 shaking, at 492 nm and 620 nm using a microplate reader (Tecan M200 pro). Total intensity
1266 was calculated from signal intensity at 492 nm after background subtraction of 620 nm
1267 intensity. Proliferation was normalized to WT-N.

1268 **Statistics and data representation**

1269 Data are represented as mean \pm standard error mean (SEM). Statistical significance was
1270 determined by one-way ANOVA followed by Šídák's test for multiple comparisons of selected
1271 pairs with **P*-value \leq 0.05, ***P*-value \leq 0.01, ****P*-value \leq 0.001, *****P*-value \leq 0.0001. Data
1272 analysis was performed using Microsoft Excel. Data representation and statistical analysis was
1273 performed using GraphPad Prism.

1274 **References**

- 1275 Afshinnia F, Rajendiran TM, Soni T, Byun J, Wernisch S, Sas KM, Hawkins J, Bellovich K,
1276 Gipson D, Michailidis G *et al* (2018) Impaired β -Oxidation and Altered Complex Lipid Fatty
1277 Acid Partitioning with Advancing CKD. *J Am Soc Nephrol* 29: 295-306
- 1278 Anand R, Kondadi AK, Meisterknecht J, Golombek M, Nortmann O, Riedel J, Peifer-Weiss L,
1279 Brocke-Ahmadinejad N, Schlutermann D, Stork B *et al* (2020) MIC26 and MIC27 cooperate to
1280 regulate cardiolipin levels and the landscape of OXPHOS complexes. *Life Sci Alliance* 3:
1281 e202000711
- 1282 Anand R, Reichert AS, Kondadi AK (2021) Emerging Roles of the MICOS Complex in Cristae
1283 Dynamics and Biogenesis. *Biology (Basel)* 10
- 1284 Anand R, Strecker V, Urbach J, Wittig I, Reichert AS (2016) Mic13 Is Essential for Formation
1285 of Crista Junctions in Mammalian Cells. *PLoS one* 11: e0160258
- 1286 Beninca C, Zanette V, Brischigliaro M, Johnson M, Reyes A, Valle DAD, A JR, Degiorgi A,
1287 Yeates A, Telles BA *et al* (2021) Mutation in the MICOS subunit gene APOO (MIC26)
1288 associated with an X-linked recessive mitochondrial myopathy, lactic acidosis, cognitive
1289 impairment and autistic features. *J Med Genet* 58: 155-167
- 1290 Bugger H, Boudina S, Hu XX, Tuinei J, Zaha VG, Theobald HA, Yun UJ, McQueen AP,
1291 Wayment B, Litwin SE *et al* (2008) Type 1 diabetic akita mouse hearts are insulin sensitive but
1292 manifest structurally abnormal mitochondria that remain coupled despite increased uncoupling
1293 protein 3. *Diabetes* 57: 2924-2932
- 1294 Chen J, Yue F, Kuang S (2022) Labeling and analyzing lipid droplets in mouse muscle stem
1295 cells. *STAR Protoc* 3: 101849
- 1296 Collaborators GBDO, Afshin A, Forouzanfar MH, Reitsma MB, Sur P, Estep K, Lee A, Marczak
1297 L, Mokdad AH, Moradi-Lakeh M *et al* (2017) Health Effects of Overweight and Obesity in 195
1298 Countries over 25 Years. *N Engl J Med* 377: 13-27
- 1299 Curien G, Lyska D, Guglielmino E, Westhoff P, Janetzko J, Tardif M, Hallopeau C, Brugière S,
1300 Dal Bo D, Decelle J *et al* (2021) Mixotrophic growth of the extremophile *Galdieria sulphuraria*
1301 reveals the flexibility of its carbon assimilation metabolism. *New Phytol* 231: 326-338
- 1302 Edgar R, Domrachev M, Lash AE (2002) Gene Expression Omnibus: NCBI gene expression
1303 and hybridization array data repository. *Nucleic Acids Res* 30: 207-210
- 1304 Eramo MJ, Lisnyak V, Formosa LE, Ryan MT (2020) The 'mitochondrial contact site and cristae
1305 organising system' (MICOS) in health and human disease. *J Biochem* 167: 243-255
- 1306 Frey TG, Mannella CA (2000) The internal structure of mitochondria. *Trends in biochemical
1307 sciences* 25: 319-324
- 1308 Giacomello M, Pyakurel A, Glytsou C, Scorrano L (2020) The cell biology of mitochondrial
1309 membrane dynamics. *Nat Rev Mol Cell Biol*
- 1310 Gomes LC, Di Benedetto G, Scorrano L (2011) During autophagy mitochondria elongate, are
1311 spared from degradation and sustain cell viability. *Nat Cell Biol* 13: 589-598
- 1312 Guarani V, McNeill EM, Paulo JA, Huttlin EL, Frohlich F, Gygi SP, Van Vactor D, Harper JW
1313 (2015) QIL1 is a novel mitochondrial protein required for MICOS complex stability and cristae
1314 morphology. *eLife* 4

- 1315 Guo X, Hu J, He G, Chen J, Yang Y, Qin D, Li C, Huang Z, Hu D, Wei C *et al* (2023) Loss of
1316 APOO (MIC26) aggravates obesity-related whitening of brown adipose tissue via PPAR α -
1317 mediated functional interplay between mitochondria and peroxisomes. *Metabolism* 144:
1318 155564
- 1319 Guo Y, Darshi M, Ma Y, Perkins GA, Shen Z, Haushalter KJ, Saito R, Chen A, Lee YS, Patel
1320 HH *et al* (2013) Quantitative proteomic and functional analysis of liver mitochondria from high
1321 fat diet (HFD) diabetic mice. *Molecular & cellular proteomics : MCP* 12: 3744-3758
- 1322 Harner M, Korner C, Walther D, Mokranjac D, Kaesmacher J, Welsch U, Griffith J, Mann M,
1323 Reggiori F, Neupert W (2011) The mitochondrial contact site complex, a determinant of
1324 mitochondrial architecture. *The EMBO journal* 30: 4356-4370
- 1325 Heinrich P, Kohler C, Ellmann L, Kuerner P, Spang R, Oefner PJ, Dettmer K (2018) Correcting
1326 for natural isotope abundance and tracer impurity in MS-, MS/MS- and high-resolution-
1327 multiple-tracer-data from stable isotope labeling experiments with IsoCorrectoR. *Sci Rep* 8:
1328 17910
- 1329 Hoppins S, Collins SR, Cassidy-Stone A, Hummel E, Devay RM, Lackner LL, Westermann B,
1330 Schuldiner M, Weissman JS, Nunnari J (2011) A mitochondrial-focused genetic interaction
1331 map reveals a scaffold-like complex required for inner membrane organization in mitochondria.
1332 *The Journal of cell biology* 195: 323-340
- 1333 Hughes CS, Moggridge S, Müller T, Sorensen PH, Morin GB, Krijgsveld J (2019) Single-pot,
1334 solid-phase-enhanced sample preparation for proteomics experiments. *Nat Protoc* 14: 68-85
- 1335 Kondadi AK, Anand R, Hansch S, Urbach J, Zobel T, Wolf DM, Segawa M, Liesa M, Shirihai
1336 OS, Weidtkamp-Peters S *et al* (2020a) Cristae undergo continuous cycles of membrane
1337 remodelling in a MICOS-dependent manner. *EMBO Rep* 21: e49776
- 1338 Kondadi AK, Anand R, Reichert AS (2020b) Cristae Membrane Dynamics - A Paradigm
1339 Change. *Trends Cell Biol* 30: 923-936
- 1340 Koob S, Barrera M, Anand R, Reichert AS (2015) The non-glycosylated isoform of MIC26 is a
1341 constituent of the mammalian MICOS complex and promotes formation of crista junctions.
1342 *Biochimica et biophysica acta* 1853: 1551-1563
- 1343 Lamant M, Smih F, Harmancey R, Philip-Couderc P, Pathak A, Roncalli J, Galinier M, Collet
1344 X, Massabuau P, Senard JM *et al* (2006) ApoO, a novel apolipoprotein, is an original
1345 glycoprotein up-regulated by diabetes in human heart. *J Biol Chem* 281: 36289-36302
- 1346 Li Z, Liu H, Bode A, Luo X (2021) Emerging roles of dehydrogenase/reductase member 2
1347 (DHRS2) in the pathology of disease. *Eur J Pharmacol* 898: 173972
- 1348 López-Viñas E, Bentebibel A, Gurunathan C, Morillas M, de Arriaga D, Serra D, Asins G,
1349 Hegardt FG, Gómez-Puertas P (2007) Definition by functional and structural analysis of two
1350 malonyl-CoA sites in carnitine palmitoyltransferase 1A. *J Biol Chem* 282: 18212-18224
- 1351 Lubeck M, Derkum NH, Naha R, Strohm R, Driessen MD, Belgardt BF, Roden M, Stühler K,
1352 Anand R, Reichert AS *et al* (2023) MIC26 and MIC27 are bona fide subunits of the MICOS
1353 complex in mitochondria and do not exist as glycosylated apolipoproteins. *PLoS one* 18:
1354 e0286756
- 1355 Madison BB (2016) Srebp2: A master regulator of sterol and fatty acid synthesis. *J Lipid Res*
1356 57: 333-335

- 1357 Mannella CA, Lederer WJ, Jafri MS (2013) The connection between inner membrane topology
1358 and mitochondrial function. *Journal of molecular and cellular cardiology* 62: 51-57
- 1359 Mehta A, Shapiro MD (2022) Apolipoproteins in vascular biology and atherosclerotic disease.
1360 *Nat Rev Cardiol* 19: 168-179
- 1361 Mishra P, Chan DC (2016) Metabolic regulation of mitochondrial dynamics. *The Journal of cell*
1362 *biology*
- 1363 Naha R, Strohm R, Urbach J, Wittig I, Reichert AS, Kondadi AK, Anand R (2023) MIC13 and
1364 SLP2 seed the assembly of MIC60-subcomplex to facilitate crista junction formation. *bioRxiv*:
1365 2023.2009.2004.556207
- 1366 Ngo J, Choi DW, Stanley IA, Stiles L, Molina AJA, Chen PH, Lako A, Sung ICH, Goswami R,
1367 Kim MY *et al* (2023) Mitochondrial morphology controls fatty acid utilization by changing CPT1
1368 sensitivity to malonyl-CoA. *The EMBO journal*: e111901
- 1369 Ott C, Dorsch E, Fraunholz M, Straub S, Kozjak-Pavlovic V (2015) Detailed analysis of the
1370 human mitochondrial contact site complex indicate a hierarchy of subunits. *PLoS one* 10:
1371 e0120213
- 1372 Peifer-Weiß L, Kurban M, David C, Lubeck M, Kondadi AK, Nemer G, Reichert AS, Anand R
1373 (2023) A X-linked nonsense APOO/MIC26 variant causes a lethal mitochondrial disease with
1374 progeria-like phenotypes. *Clin Genet*
- 1375 Perez-Riverol Y, Bai J, Bandla C, García-Seisdedos D, Hewapathirana S, Kamatchinathan S,
1376 Kundu DJ, Prakash A, Frericks-Zipper A, Eisenacher M *et al* (2022) The PRIDE database
1377 resources in 2022: a hub for mass spectrometry-based proteomics evidences. *Nucleic Acids*
1378 *Res* 50: D543-d552
- 1379 Philip-Couderc P, Smih F, Pelat M, Vidal C, Verwaerde P, Pathak A, Buys S, Galinier M,
1380 Senard JM, Rouet P (2003) Cardiac transcriptome analysis in obesity-related hypertension.
1381 *Hypertension* 41: 414-421
- 1382 Poschmann G, Seyfarth K, Besong Agbo D, Klafki HW, Rozman J, Wurst W, Wiltfang J, Meyer
1383 HE, Klingenspor M, Stuhler K (2014) High-fat diet induced isoform changes of the Parkinson's
1384 disease protein DJ-1. *J Proteome Res* 13: 2339-2351
- 1385 Sheftel AD, Stehling O, Pierik AJ, Netz DJ, Kerscher S, Elsässer HP, Wittig I, Balk J, Brandt
1386 U, Lill R (2009) Human ind1, an iron-sulfur cluster assembly factor for respiratory complex I.
1387 *Mol Cell Biol* 29: 6059-6073
- 1388 Shim SH, Lee SK, Lee DW, Brillhaus D, Wu G, Ko S, Lee CH, Weber APM, Jeon JS (2019)
1389 Loss of Function of Rice Plastidic Glycolate/Glycerate Translocator 1 Impairs Photorespiration
1390 and Plant Growth. *Front Plant Sci* 10: 1726
- 1391 Song S, Attia RR, Connaughton S, Niesen MI, Ness GC, Elam MB, Hori RT, Cook GA, Park
1392 EA (2010) Peroxisome proliferator activated receptor alpha (PPARalpha) and PPAR gamma
1393 coactivator (PGC-1alpha) induce carnitine palmitoyltransferase IA (CPT-1A) via independent
1394 gene elements. *Mol Cell Endocrinol* 325: 54-63
- 1395 Spinelli JB, Haigis MC (2018) The multifaceted contributions of mitochondria to cellular
1396 metabolism. *Nat Cell Biol* 20: 745-754

- 1397 Stephan T, Bruser C, Deckers M, Steyer AM, Balzarotti F, Barbot M, Behr TS, Heim G, Hubner
1398 W, Ilgen P *et al* (2020) MICOS assembly controls mitochondrial inner membrane remodeling
1399 and crista junction redistribution to mediate cristae formation. *The EMBO journal* 39: e104105
- 1400 Sun W, Nie T, Li K, Wu W, Long Q, Feng T, Mao L, Gao Y, Liu Q, Gao X *et al* (2021) Hepatic
1401 CPT1A Facilitates Liver-Adipose Cross-Talk via Induction of FGF21 in Mice. *Diabetes*
- 1402 Szendroedi J, Phielix E, Roden M (2011) The role of mitochondria in insulin resistance and
1403 type 2 diabetes mellitus. *Nat Rev Endocrinol* 8: 92-103
- 1404 Thiam AR, Farese RV, Jr., Walther TC (2013) The biophysics and cell biology of lipid droplets.
1405 *Nat Rev Mol Cell Biol* 14: 775-786
- 1406 Tian F, Wu CL, Yu BL, Liu L, Hu JR (2017) Apolipoprotein O expression in mouse liver
1407 enhances hepatic lipid accumulation by impairing mitochondrial function. *Biochem Biophys*
1408 *Res Commun* 491: 8-14
- 1409 Turkieh A, Caubere C, Barutaut M, Desmoulin F, Harmancey R, Galinier M, Berry M, Dambrin
1410 C, Polidori C, Casteilla L *et al* (2014) Apolipoprotein O is mitochondrial and promotes
1411 lipotoxicity in heart. *J Clin Invest* 124: 2277-2286
- 1412 Urbach J, Kondadi AK, David C, Naha R, Deinert K, Reichert AS, Anand R (2021) Conserved
1413 GxxxG and WN motifs of MIC13 are essential for bridging two MICOS subcomplexes. *Biochim*
1414 *Biophys Acta Biomembr* 1863: 183683
- 1415 Vasilopoulos G, Heflik L, Czolkoss S, Heinrichs F, Kleetz J, Yesilyurt C, Tischler D, Westhoff
1416 P, Exterkate M, Aktas M *et al* (2023) Characterization of multiple lysophosphatidic acid
1417 acyltransferases in the plant pathogen *Xanthomonas campestris*. *Febs j*
- 1418 von der Malsburg K, Muller JM, Bohnert M, Oeljeklaus S, Kwiatkowska P, Becker T,
1419 Loniewska-Lwowska A, Wiese S, Rao S, Milenkovic D *et al* (2011) Dual role of mitofilin in
1420 mitochondrial membrane organization and protein biogenesis. *Developmental cell* 21: 694-707
- 1421 Wai T, Saita S, Nolte H, Müller S, König T, Richter-Dennerlein R, Sprenger HG, Madrenas J,
1422 Mühlmeister M, Brandt U *et al* (2016) The membrane scaffold SLP2 anchors a proteolytic hub
1423 in mitochondria containing PARL and the i-AAA protease YME1L. *EMBO Rep* 17: 1844-1856
- 1424 Wang L, Ishihara T, Ibayashi Y, Tatsushima K, Setoyama D, Hanada Y, Takeichi Y, Sakamoto
1425 S, Yokota S, Mihara K *et al* (2015) Disruption of mitochondrial fission in the liver protects mice
1426 from diet-induced obesity and metabolic deterioration. *Diabetologia* 58: 2371-2380
- 1427 Weber TA, Koob S, Heide H, Wittig I, Head B, van der Blik A, Brandt U, Mittelbronn M,
1428 Reichert AS (2013) APOOL is a cardiolipin-binding constituent of the Mitofilin/MINOS protein
1429 complex determining cristae morphology in mammalian mitochondria. *PLoS one* 8: e63683
- 1430 Włodarczyk M, Nowicka G (2019) Obesity, DNA Damage, and Development of Obesity-
1431 Related Diseases. *Int J Mol Sci* 20
- 1432 Wu CL, Zhao SP, Yu BL (2013) Microarray analysis provides new insights into the function of
1433 apolipoprotein O in HepG2 cell line. *Lipids Health Dis* 12: 186
- 1434 Xiang RL, Huang Y, Zhang Y, Cong X, Zhang ZJ, Wu LL, Yu GY (2020) Type 2 diabetes-
1435 induced hyposalivation of the submandibular gland through PINK1/Parkin-mediated
1436 mitophagy. *J Cell Physiol* 235: 232-244

- 1437 Yoo HC, Park SJ, Nam M, Kang J, Kim K, Yeo JH, Kim JK, Heo Y, Lee HS, Lee MY *et al*
1438 (2020a) A Variant of SLC1A5 Is a Mitochondrial Glutamine Transporter for Metabolic
1439 Reprogramming in Cancer Cells. *Cell Metab* 31: 267-283.e212
- 1440 Yoo HC, Yu YC, Sung Y, Han JM (2020b) Glutamine reliance in cell metabolism. *Exp Mol Med*
1441 52: 1496-1516
- 1442 Yu T, Robotham JL, Yoon Y (2006) Increased production of reactive oxygen species in
1443 hyperglycemic conditions requires dynamic change of mitochondrial morphology. *Proc Natl*
1444 *Acad Sci U S A* 103: 2653-2658
- 1445 Zadoorian A, Du X, Yang H (2023) Lipid droplet biogenesis and functions in health and
1446 disease. *Nat Rev Endocrinol* 19: 443-459
- 1447 Zick M, Rabl R, Reichert AS (2009) Cristae formation-linking ultrastructure and function of
1448 mitochondria. *Biochimica et biophysica acta* 1793: 5-19

Figure 1

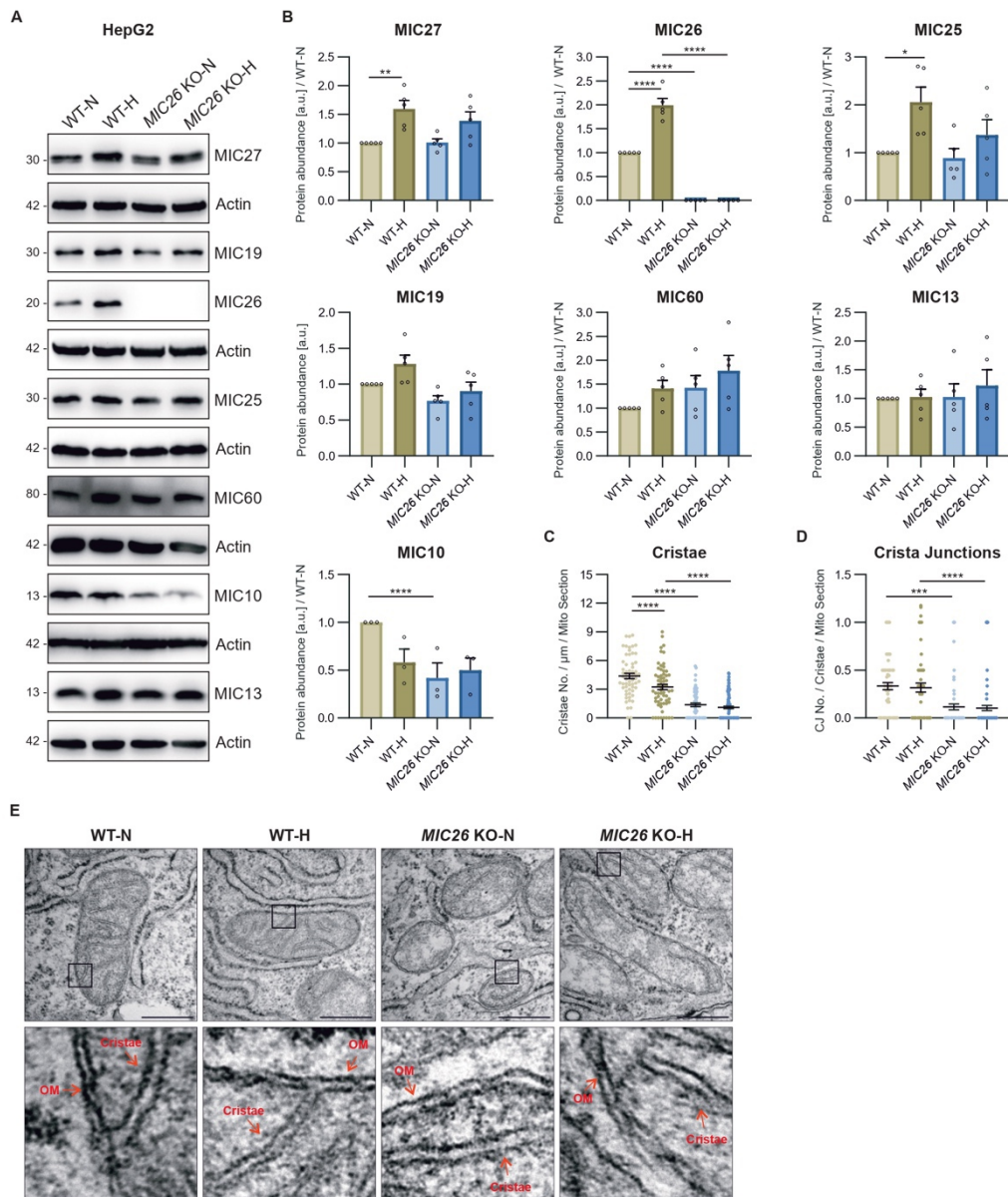


Figure 1. Mitochondrial apolipoprotein MIC26 is selectively increased in cells exposed to hyperglycemia

(A and B) Western blot analysis of all MICOS subunits from HepG2 WT and *MIC26* KO cells cultured in normo- and hyperglycemia (N = 3-5). Chronic hyperglycemia treatment leads to increased levels of MIC27, MIC26 and MIC25 in WT cells. Loss of MIC26 is accompanied by decreased MIC10 in normoglycemia.

(C, D and E) Electron microscopy data including quantification of cristae number per unit length (μm) per mitochondrial section (C) as well as crista junctions per cristae per mitochondrial section (D), along with representative images (E) from HepG2 WT and *MIC26* KO cells cultured in normo- and hyperglycemia (N = 2). Loss of MIC26 led to decreased cristae number and crista junctions independent of normo- and hyperglycemia. Red arrows in lower row indicate outer membrane (OM) or cristae. Scale bar represents 500 nm.

Data are represented as mean \pm SEM (B, C and D). Statistical analysis was performed using one-way ANOVA with * $P < 0.05$, ** $P < 0.01$, *** $P < 0.001$, **** $P < 0.0001$. N represents the number of biological replicates.

Figure 2



Figure 2. Hyperglycemia confers antagonistic regulation of lipid and cholesterol pathways, in *MIC26* KO vs WT cells, compared to normoglycemia

(A and B) Hierarchical Treemap clustering of significant gene ontology (GO) enriched terms of biological processes upregulated in normoglycemic *MIC26* KO (A) and downregulated in hyperglycemic *MIC26* KO (B) compared to respective WT. Each rectangle represents one BioProcess pathway. Every colour represents clustering of different sub-pathways to pathway families. The rectangle sizes indicate the *P*-value of the respective GO term.

(C and D) WikiPathway enrichment using EnrichR analysis of differentially expressed genes (C) upregulated in normoglycemic *MIC26* KO and (D) downregulated in hyperglycemic *MIC26* KO cells compared to respective WT. Arrows indicate antagonistically regulated metabolic pathways including glycolysis, cholesterol biosynthesis, fatty acid synthesis and oxidation.

Differentially expressed genes were considered statistically significant with a cut-off fold change of ± 1.5 and Bonferroni correction $P \leq 0.05$. Treemap representation of GO enrichment was plotted with statistically significant pathways with cut-off $P \leq 0.05$.

Figure 3

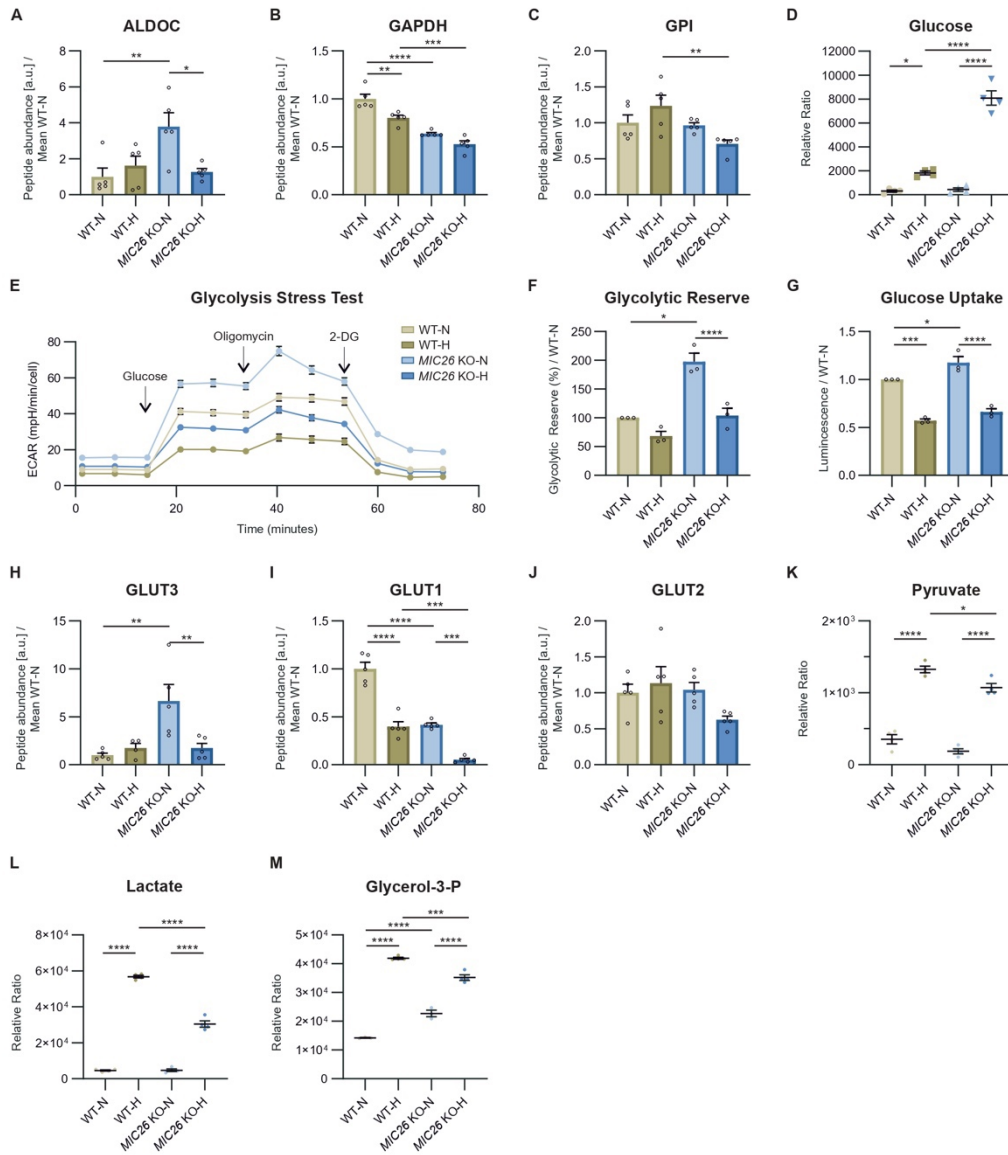


Figure 3. MIC26 maintains the glycolytic function

(A – C) Peptide abundances of enzymes involved in glycolysis pathway curated from proteomics data (N = 5).

(D) Steady state metabolomics (GC-MS) data reveals increased cellular glucose accumulation upon *MIC26* deletion in hyperglycemia (N = 3-4).

(E and F) Representative glycolysis stress test seahorse assay analysis, with sequential injection of glucose, oligomycin and 2-deoxyglucose, reveals a tendency towards increased glycolysis upon *MIC26* deletion (E) (n = 23). Quantification from various biological replicates shows a significant increase of cellular glycolytic reserve in normoglycemic, but not in hyperglycemic conditions (F) (N = 3).

(G) Cellular glucose uptake was measured using Glucose uptake Glo assay normalized to WT-N. *MIC26* deletion leads to an increased glucose uptake upon normoglycemia (N = 3).

(H – J) Peptide abundances of transporters involved in glucose uptake namely GLUT3 (H), GLUT1 (I) and GLUT2 (J) curated from proteomics data (N = 5).

(K and L) Steady state metabolomics (GC-MS) shows unaltered cellular pyruvate (K) and lactate (L) levels in *MIC26* KO cell lines in normoglycemia but decreased levels upon *MIC26* deletion in hyperglycemia (N = 3-4).

(M) *MIC26* deletion increases glycerol-3-phosphate amount in normoglycemia with an antagonistic effect in hyperglycemia compared to the respective WT (N = 3-4).

Data are represented as mean \pm SEM (A-M). Statistical analysis was performed using one-way ANOVA with * $P < 0.05$, ** $P < 0.01$, *** $P < 0.001$, **** $P < 0.0001$. N represents the number of biological replicates and n the number of technical replicates.

Figure 4

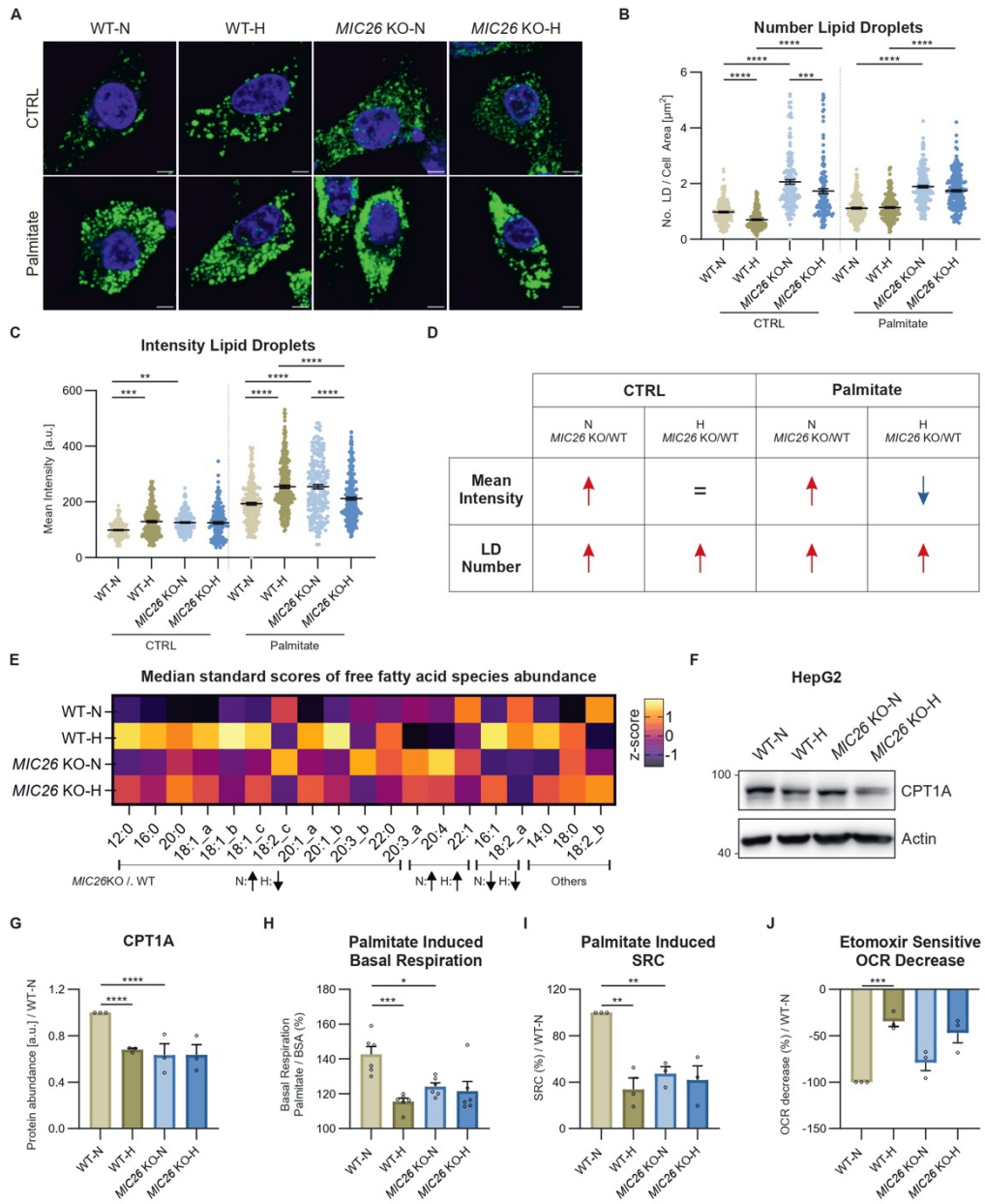


Figure 4. The loss of MIC26 leads to metabolic rewiring of cellular lipid metabolism via CPT1A and dysregulation of fatty acid synthesis

(A – D) Analysis of lipid droplet formation in WT and *MIC26* KO cells cultured in normo- and hyperglycemia either in standard growth condition (CTRL) or upon palmitate stimulation (100 μ M, 24 h). Representative confocal images of lipid droplets stained using BODIPY 493/503 are shown (A). Quantification shows number of lipid droplets normalized to the total cell area [μ m²] (B) and mean fluorescence intensity per cell normalized to mean intensity of WT-N in all biological replicates (C). *MIC26* deletion leads to a nutritional-independent increase in lipid droplet number. However, an opposing effect, leading to increase or decrease of mean fluorescence intensity of lipid droplets, upon comparison of *MIC26* KO to WT was observed in normo- and hyperglycemia respectively, with a pronounced effect upon feeding palmitate (N = 3). Scale bar represents 5 μ m.

(E) Heat map representing the abundance of steady state FFA species in WT and *MIC26* KO cells cultured in normo- and hyperglycemia. 11 out of 19 of the FFA species represent an antagonistic behavior upon comparing *MIC26* KO to WT in normo- (increase) and hyperglycemia (decrease) (N = 3-4).

(F and G) Western blot analysis (F), along with respective quantification (G) of WT and *MIC26* KO cells cultured in normo- and hyperglycemia, show a reduction of CPT1A in WT-H, *MIC26* KO-N and *MIC26* KO-H compared to WT-N (N = 3).

(H – J) Mitochondrial fatty acid oxidation analyzed using Seahorse XF analyzer shows a decreased palmitate-induced basal respiration (H) and spare respiratory capacity (I) and a nonsignificant reduction of etomoxir-sensitive OCR decrease upon comparing *MIC26* KO to WT in normoglycemia (N = 3).

Data are represented as mean \pm SEM (B-C and G-J). Statistical analysis was performed using one-way ANOVA with **P* < 0.05, ***P* < 0.01, ****P* < 0.001, *****P* < 0.0001. N represents the number of biological replicates.

Figure 5

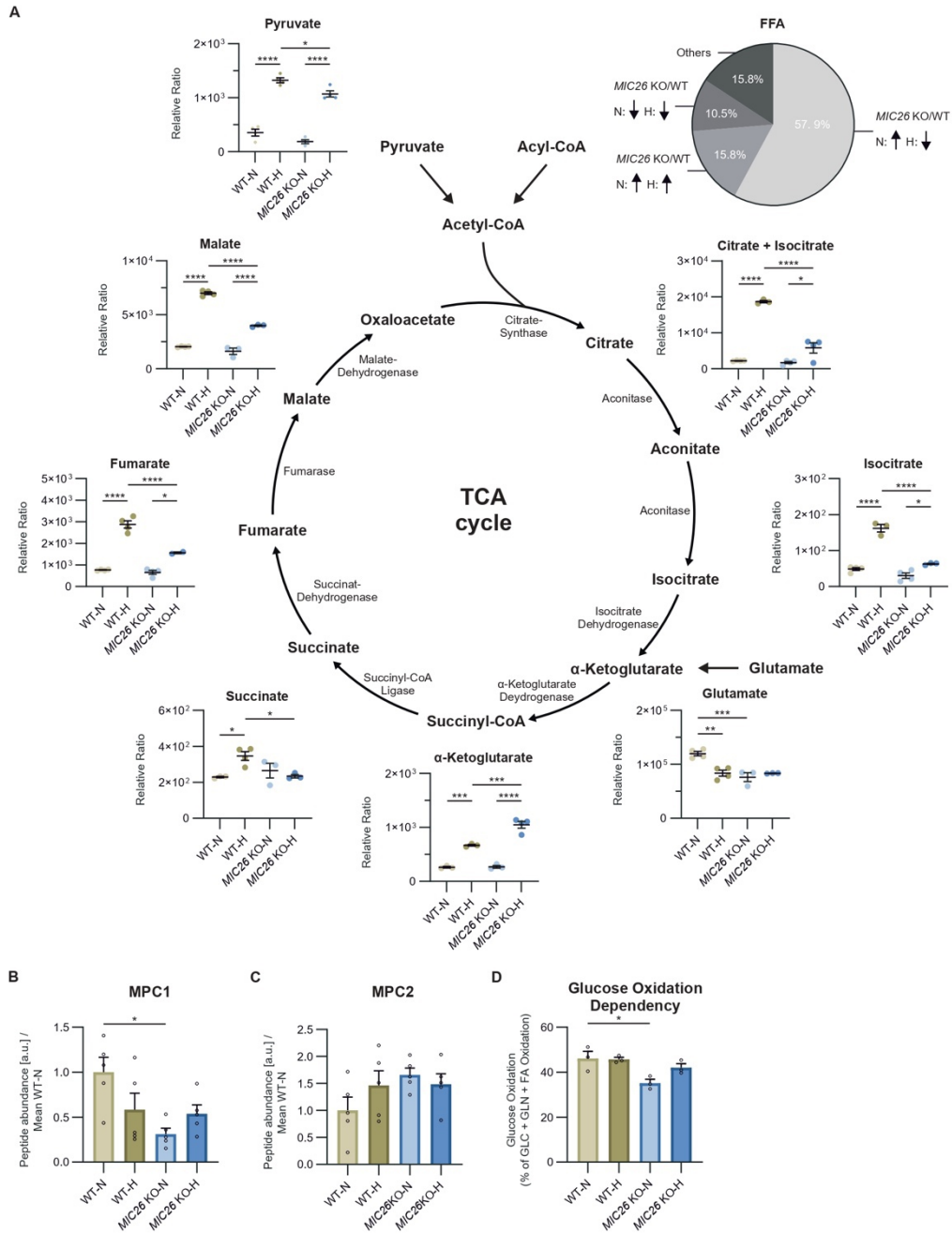


Figure 5. *MIC26* deletion leads to hyperglycemia-induced decrease in TCA cycle intermediates

(A) Representation of the relative amounts (GC-MS) of TCA cycle metabolites and associated precursors at steady state in WT and *MIC26* KO cells cultured in normo- and hyperglycemia. All the TCA cycle metabolites with the exception of α -ketoglutarate showed a decreasing trend upon *MIC26* KO when compared to WT in hyperglycemia (N = 3-4).

(B and C) Mitochondrial pyruvate carrier 1 (MPC1) (B), but not MPC2 (C), is significantly decreased in *MIC26* KO-N compared to WT-N, as revealed by peptide abundances from proteomics data (N = 5).

(D) Mitochondrial glucose / pyruvate dependency analysis, using Seahorse XF analyzer mito fuel flex test assay, reveals a decreased mitochondrial respiratory dependency of *MIC26* KO on glucose / pyruvate in normoglycemia (N = 3).

Data are represented as mean \pm SEM (A-C). Statistical analysis was performed using one-way ANOVA with * $P < 0.05$, ** $P < 0.01$, *** $P < 0.001$, **** $P < 0.0001$. N represents the number of biological replicates.

Figure 6

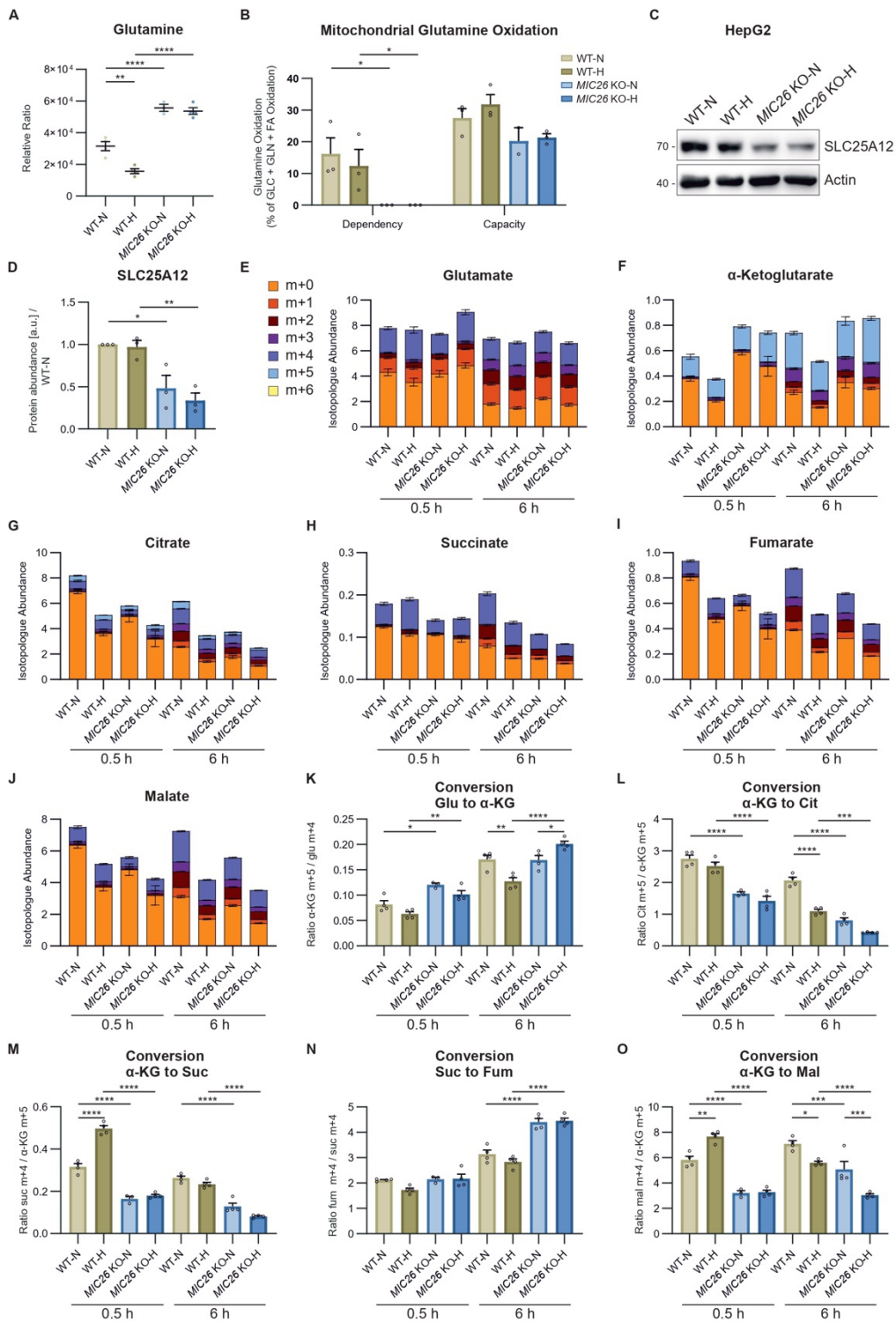


Figure 6. Aberrant glutamine metabolism is observed in *MIC26* KOs independent of nutritional status

(A) Metabolomics analysis (GC-MS) shows that glutamine levels were strongly increased in *MIC26* KO cells cultured in both normo- and hyperglycemia at steady state compared to respective WT (N = 3-4).

(B) Quantification of mitochondrial glutamine dependency and capacity analysis, using Seahorse XF analyzer mito fuel flex test assay, shows a diminished mitochondrial respiratory dependency on glutamine. A nonsignificant mitochondrial respiratory decreased capacity of *MIC26* KO cells was observed compared to respective WT conditions (N = 3).

(C and D) Western Blot analysis (C) along with respective quantification (D) show reduced amounts of the glutamate aspartate antiporter SLC25A12 (ARALAR / AGC1), present in mitochondria, in *MIC26* KO cell lines compared to respective WT cells (N = 3).

(E – J) Representation of labeled (m+1 - m+6) and unlabeled (m+0) species of glutamate (GC-MS) (E), and TCA cycle metabolites (AEC-MS) α -KG (F), citrate (G), succinate (H), fumarate (I) and malate (J), from glutamine tracing experiments after labelling for 0.5 h and 6 h (N = 4).

(K – O) Conversion rates from different TCA cycle reactions calculated using the ratio of highest labeled species abundances for the conversions of glutamate to α -KG (K), α -KG to citrate (L), α -KG to succinate (M), succinate to fumarate (N) and α -KG to malate (N = 4).

Data are represented as mean \pm SEM (A-B and D-O). Statistical analysis was performed using one-way ANOVA with * P < 0.05, ** P < 0.01, *** P < 0.001, **** P < 0.0001. N represents the number of biological replicates.

Figure 7

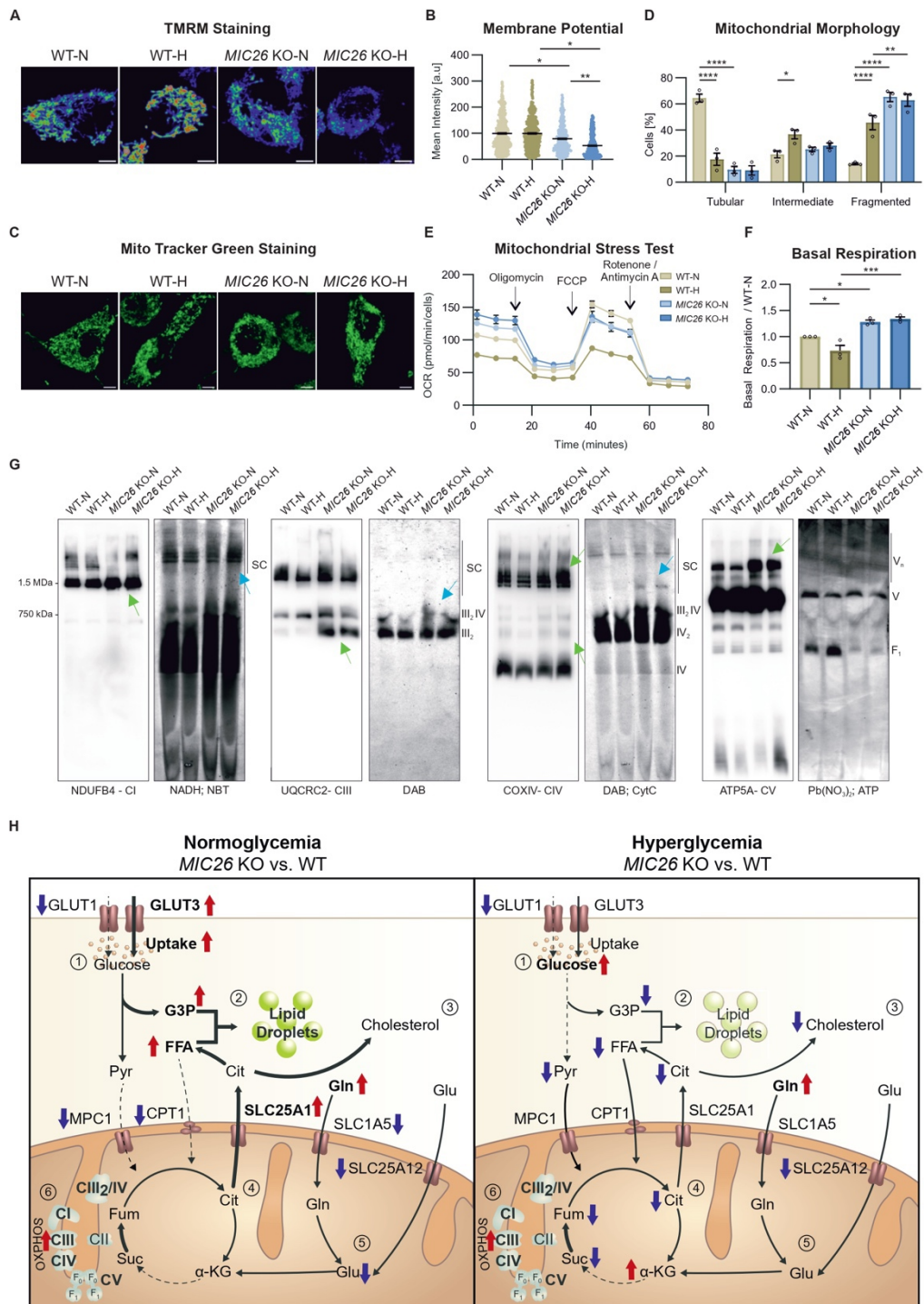


Figure 7. MIC26 regulates mitochondrial bioenergetics by restricting the ETC activity and OXPHOS (super-)complex formation

(A and B) Representative pseudocolour rainbow LUT intensities from confocal images of WT and *MIC26* KO HepG2 cells stained with TMRM show a reduction in $\Delta\Psi_m$ upon *MIC26* deletion in both normoglycemia and hyperglycemia when compared to respective WT cells (A). Quantification represents mean TMRM fluorescence intensity per cell normalized to mean intensity of WT-N in all biological replicates (B) (N = 3). Scale bar represents 5 μm .

(C and D) Representative confocal images of mitochondrial morphology, visualized by MitoTracker green staining (C), show that loss of *MIC26* shifts mitochondrial morphology from tubular mitochondrial network in WT normoglycemic conditions to fragmented phenotype irrespective of supplemented glucose amount (D) (N = 3). Scale bar represents 5 μm .

(E and F) Representative mitochondrial stress test with Seahorse XF analyzer, with sequential injection of oligomycin, FCCP and rotenone/antimycin (E) (n = 19-23). Quantification from various biological replicates shows a significant increase of basal respiration in *MIC26* KOs cultured in both normo- and hyperglycemia (F) (N = 3).

(G) Blue native (respective left panel) and clear native (respective right panel) PAGE analysis reveals an overall increase of OXPHOS complex formation (for CI, CIII, CIV and CV, green arrows) as well as corresponding increased in-gel activity of supercomplexes, and complex III₂IV (blue arrows) upon *MIC26* deletion. CV shows no in-gel activity alterations while a decreased in-gel activity of F₁ occurs upon loss of *MIC26*. Native PAGEs were performed in three biological replicates and representative gels are shown.

(H) Model representing the antagonistic regulation of metabolic pathways encompassing glucose usage, lipid droplet formation, cholesterol synthesis, as well as decrease in TCA cycle metabolites in *MIC26* deficient HepG2 cells dependent on nutritional conditions compared to respective WT cells. An increase of glutamine levels as well as assembly of various OXPHOS complexes is observed in *MIC26* KOs independent of the nutritional status. Arrows indicate respective up (red) or downregulated (blue) protein/metabolite or activity levels, respectively. In the model, left panel indicates normoglycemic while the right panel represents the hyperglycemic conditions.

Data are represented as mean \pm SEM (B and D-F). Statistical analysis was performed using one-way ANOVA with **P* < 0.05, ***P* < 0.01, ****P* < 0.001, *****P* < 0.0001. N represents the number of biological replicates and n the number of technical replicates.

5.3. MIC13 and SLP2 seed the assembly of MIC60-subcomplex to facilitate crista junction formation

MIC13 and SLP2 seed the assembly of MIC60-subcomplex to facilitate crista junction formation

Ritam Naha¹, Rebecca Strohm¹, Jennifer Urbach¹, Ilka Wittig^{2, 3}, Andreas S. Reichert¹, Arun Kumar Kondadi¹, Ruchika Anand^{1*}

¹Institute of Biochemistry and Molecular Biology I, Medical Faculty and University Hospital Duesseldorf, Heinrich Heine University Duesseldorf, Duesseldorf, Germany

²Functional Proteomics, Institute for Cardiovascular Physiology, Faculty of Medicine, Goethe-University, Frankfurt am Main, Germany.

³German Center of Cardiovascular Research (DZHK), Partner Site RheinMain, Frankfurt, Germany.

*Corresponding author: anand@hhu.de

Abstract

The MICOS complex, comprising two subcomplexes, is essential for mitochondrial cristae organization, with MIC13 as a crucial subunit. *MIC13* mutations cause severe mitochondrial hepato-encephalopathy with cristae defects and MIC10-subcomplex loss. Our study identifies stomatin-like protein 2 (SLP2) as a MIC13 interaction partner, crucial for modulating MICOS assembly and cristae morphology. SLP2 provides a large interaction hub for MICOS subunits, and its loss significantly alters cristae morphology. Deleting both *SLP2* and *MIC13* reduces MIC60 assembly, a core subunit, disrupting MIC60-specific punctae pattern and highlighting the importance of SLP2-MIC13 interplay in MICOS assembly and cristae formation. Importantly, we elucidated the specific role of MIC13 in stabilizing the MIC10-subcomplex. Additionally, mitochondrial *i*-AAA protease YME1L in coordination either with MIC13 or SLP2 differentially regulates MICOS assembly pathways thereby interlinking MIC13-specific or scaffolding-specific role of SLP2 with quality control and MICOS complex assembly. Taken together, we propose a “seeder” model for MICOS assembly, where SLP2-MIC10-subcomplex the assembly of MIC60 into MICOS complex and promote the formation of CJs by regulating the quality and stability of MIC10-subcomplex.

Introduction

Mitochondria, known for their multifaceted roles beyond energy conversion, perform vital functions such as calcium signaling, lipid metabolism, ROS production, amino acid metabolism, iron-sulfur cluster synthesis, and apoptosis regulation (Monzel et al., 2023). The inner membrane (IM) of mitochondria is highly adaptable, shaping itself according to the bioenergetic demands of the cell. Cristae are infoldings of the IM that provide the characteristic wrinkled shape of IM and offer large surface area for housing electron transport chain (ETC) complexes. In the 1990s, electron tomography techniques illustrated the intricate three-dimensional (3D) arrangement of the IM and proposed the crista junction model (Perkins et al., 1997), designating crista junctions (CJs) as small, highly curved openings at the neck of individual cristae with a high inward-directed curvature. Due to their minute diameter, CJs were proposed to function as diffusion barriers (Mannella et al., 2013; Perkins et al., 1997), subdividing mitochondria into distinct subcompartments and thus modulating several mitochondrial functions, including lipid transfer and metabolite exchange. Markedly, during apoptosis, CJs remodelling facilitates cytochrome c release, initiating the apoptotic cascade (Scorrano et al., 2002). Yet, how these intricate structures of cristae and CJs with steep membrane curvatures are formed and remodelled remained elusive for decades. Several recent findings shed light on this significant yet technically challenging question. The 'mitochondrial contact site and cristae organising system' (MICOS) complex has emerged as a crucial orchestrator in cristae and CJs formation (Anand et al., 2021; Kondadi & Reichert, 2024; Mukherjee et al., 2021; Stephan et al., 2020). Live-cell super-resolution (SR) nanoscopy showed that cristae and CJs are highly dynamic and undergo cycles of fusion and fission at a timescale of seconds in a MICOS-dependent manner (Kondadi, Anand, et al., 2020).

The mammalian MICOS complex comprises seven subunits namely MIC10, MIC13, MIC19, MIC25, MIC26, MIC27 and MIC60, that form two distinct subcomplexes, each contributing uniquely to mitochondrial integrity. The MICOS proteins are distributed into two subcomplexes, MIC60-subcomplex (MIC60-MIC19-MIC25) and MIC10-subcomplex (MIC10-MIC13-MIC26-MIC27). Deletion of individual MICOS subunits results in varying degrees of aberrant cristae morphology, often leading to the accumulation of cristae stacks or concentric rings (Kondadi, Anand, et al., 2020; Stephan et al., 2020). While MIC60 and MIC10 are core subunits harbouring membrane remodelling abilities (Barbot et al., 2015; Bock-Bierbaum et al., 2022; Bohnert et al., 2015; Hessenberger et al., 2017; Tarasenko et al., 2017), MIC13 acts as a critical bridge, modulating interactions within the complex and impacting cristae morphology (Anand et al., 2016; Guarani et al., 2015; Urbach et al., 2021; Zerbes et al., 2012). MIC19 and MIC25, belonging to coiled-coil helix coiled-coil helix (CHCH) family proteins, assist MIC60 in CJs and contact site formation (An et al., 2012; Sakowska et al., 2015), whereas MIC26 and MIC27, belonging to the apolipoprotein family, are essential for maintaining cristae

structure and integrity of ETC complexes (Anand et al., 2020). The interaction of the MICOS subunits with the outer membrane (OM) localized proteins SAMM50, metaxin1 (MTX1), metaxin2 (MTX2) and DNAJC11 leads to formation of the 'mitochondrial intermembrane space bridging' (MIB) complex (Huynen et al., 2016; Tang et al., 2020; Xie et al., 2007). MIB facilitates the contacts between IM and OM, essential for overall mitochondrial function and structural integrity.

MIC13, a key subunit of the MICOS complex, lacks comprehensive characterization and shows no resemblance to other protein families or domains (Urbach et al., 2021). Depletion of MIC13 affects cristae morphology and causes concomitant total loss of MIC10, MIC26 and partial loss of MIC27, making it difficult to delineate the specific roles of these proteins (Anand et al., 2016; Guarani et al., 2015). Previously, we have identified two critical motifs within the MIC13, namely the 'GxxxG' and the 'WN' motif, essential for its stability and functionality (Urbach et al., 2021). Nevertheless, it is an important component of the MICOS complex and mutations in *MIC13* are associated with a severe form of mitochondrial hepato-encephalopathy in paediatric patients, leading to the untimely demise, often within few months to five years (Guarani et al., 2016; Russell et al., 2019; Zeharia et al., 2016). The patients show a multi-system failure affecting the brain, liver, kidney and heart (Godiker et al., 2018; Guarani et al., 2016; Russell et al., 2019; Zeharia et al., 2016). Neurological defects include cerebellar and optic atrophy, acquired microcephaly and hypotonia, while liver complication frequently leads to acute liver failure. Increased plasma levels of lactic acid, methionine, tyrosine and Krebs cycle intermediates as well as increased excretion of 3-methylglutaconic acid were reported. In all the documented cases, MIC13 levels were not detectable, indicating the complete loss of MIC13 in these pathologies.

While mutations in MICOS subunits, including MIC60, MIC26, and notably MIC13, have been associated with severe mitochondrial diseases (Beninca et al., 2021; Guarani et al., 2016; Marco-Hernández et al., 2021; Peifer-Weiß et al., 2023; Russell et al., 2019; Tsai et al., 2018; Zeharia et al., 2016), a comprehensive understanding of the underlying pathobiology, particularly for non-ETC genes, remains limited. These mitochondrial diseases, a subset of rare metabolic errors affecting 1.6 in 5000 individuals, lack effective treatments (Stenton & Prokisch, 2020). In this study, we aim to unravel the molecular role of MIC13 in cristae and CJs formation within the MICOS complex, which offer fresh insights into severe mitochondrial disorders for potential therapeutic methods.

We aimed to decipher the role of MIC13 by mapping its interactome. Employing mass-spectrometry (MS) coupled with co-immunoprecipitation (co-ip) of MIC13, we identified Stomatin-like protein 2 (SLP2) as a highly enriched protein within the MIC13 interactome. Particularly, no prior studies had linked SLP2 to MICOS regulation or cristae morphogenesis. Our findings firmly establish SLP2 as a novel cristae modulator, revealing its multifaceted

involvement in governing MICOS assembly and cristae formation. SLP2 acts as a scaffold, forming a large interaction hub encompassing all known MICOS subunits. Depletion of SLP2 severely influences the cristae morphology. SLP2 was crucial for preserving the stability of MIC26 by regulating YME1L-mediated MIC26 proteolysis. Additionally, SLP2 plays a distinct and essential role in modulating the assembly kinetics of MIC60 upon re-introduction of MIC13, a core MICOS subunit, independent to its regulatory role in MIC26 via the SLP2-YME1L complex. The simultaneous depletion of MIC13 and SLP2 accentuates deficiencies in MIC60 assembly, emphasizing their collaborative roles in controlling assembly kinetics and formation of MIC60 punctae. Next to novel roles of SLP2, our study elucidates MIC13-specific contributions to MICOS assembly and cristae morphogenesis, pivotal for understanding the MIC13-associated pathophysiology. We propose a "seeder" model of MICOS assembly, where SLP2, along with assembled MIC10-subcomplex ("seeder" complex), facilitates the efficient incorporation or 'seeding' of MIC60 into the MICOS-MIB complex, highlighting the interdependence between two MICOS subcomplexes during MICOS assembly. This process ensures mitochondrial integrity and the establishment of CJs and contacts between IM and OM.

Results

Determining the MIC13 interactome

To unravel the elusive role of MIC13, particularly its influence on MICOS and/or processes independent of MICOS, we set out to determine the MIC13 interactome. Our methodology involved isolating mitochondria from HEK293 cells, followed by Co-IP using agarose beads conjugated with MIC13 antibody. We then analysed the eluate fraction via mass spectrometry (MS) to identify the proteins specifically and significantly enriched in WT cells compared to *MIC13* knockout (KO) cells. The analysis revealed numerous proteins constituting the interactome of MIC13 in mammalian cells (Fig 1A, supplementary Table 1). Among these proteins were members of MICOS and MIB complex or their known interactors, emphasizing the specificity of the experiment and highlighting the central role of MIC13 in MICOS-MIB regulation. Especially, our results also revealed SLP2 as a novel interaction partner, showing the highest fold enrichment in significance upon statistical analysis (Fig 1A). SLP2 belongs to the SPFH (stomatin, prohibitin, flotillin, HflC/K) superfamily of scaffolding proteins that can form microdomains in the membrane by local lipid-protein interactions. It can bind cardiolipin as well (Christie et al., 2011) and has been implicated in various mitochondrial functions including biogenesis, proteolysis and stress-induced mitochondrial hyperfusion (SIMH) regulation (Tondera et al., 2009). SLP2 interacts with mitochondrial proteases like PARL and YME1L, forming a large hub of proteases within the IM known as the SPY complex (Wai et al., 2016). A direct contribution of SLP2 to MICOS regulation and cristae morphology remains unexplored, prompting our focused investigation into this intriguing possibility.

SLP2 forms a stable interaction hub with all MICOS subunits

In order to confirm the direct interaction between MIC13 and SLP2 demonstrated by Co-IP experiment (Fig 1A), we performed Western blot (WB) analysis utilising the elution fraction obtained from MIC13-FLAG co-ip. Upon probing with an SLP2 antibody, we observed considerable increase in the intensity of the SLP2 band in *MIC13* KO cells expressing MIC13-FLAG compared to *MIC13* KO expressing an empty vector (EV), confirming the interaction of MIC13 and SLP2 (Fig 1B). The specificity of this Co-IP was validated by the absence of matrix protein HSP60 and ETC IV protein Mt-CO2 in the elution fraction (Fig 1B). We further substantiated the MIC13-SLP2 interaction by using SLP2 as bait in a Co-IP experiment. For this, we generated *SLP2* KO cells using CRISPR-Cas9 system and stably expressed SLP2 with a MYC tag at its C-terminus. Co-IP was performed using MYC-trap agarose and the elution fraction was probed for antibodies against SLP2, YME1L (known SLP2 interactor), and all MICOS subunits, along with HSP60 and Mt-CO2 serving as negative controls. The presence of SLP2 and YME1L and the absence of HSP60 and Mt-CO2 in the elution fraction showed the specificity of the Co-IP experiment (Fig 1C). All MICOS subunits, and not only MIC13, were present in the elution fraction, showing that SLP2 potentially interacts directly or indirectly with all the MICOS subunits (Fig 1C). To visually and definitively evaluate the proximity (interaction) between SLP2 and individual MICOS subunits, we employed the proximity ligation assay (PLA). Using antibodies specific to SLP2 and individual MICOS subunits, we observed numerous punctae in each cell, indicating interaction between SLP2 and individual MICOS subunits, unlike in the negative controls of Mt-CO2 & SLP2 or only SLP2 antibody (Fig 1D). Overall, several lines of evidence firmly establish the specific and reciprocal interaction of SLP2 with the MICOS complex.

Considering the inherent limitations of Co-IP experiments, we cannot specify whether SLP2 interacts individually with each MICOS subunit or whether there is a hierarchy in the interaction of MICOS subunits with SLP2. To determine whether the interaction between SLP2 and MICOS subunits relies on any particular MICOS subunit, we conducted Co-IP experiments in cells deleted for individual MICOS subunits (supplementary Fig 1). We generated KO cells lacking individual MICOS subunits (*MIC10*, *MIC26*, *MIC27*, *MIC19*, *MIC25* and *MIC60*) in HEK293 cell lines and stably expressed SLP2-Myc in these cell lines. As expected, the *MIC10* KO and *MIC13* KO cells showed loss (or decrease) of all subunits of the MIC10-subcomplex (*MIC10/13/26/27*) while KO of either *MIC26* or *MIC27* showed no pronounced alterations in other MICOS subunits (supplementary Fig 1A). Concerning the MIC60-subcomplex, *MIC60* KO cells demonstrated a drastic decrease in steady state levels of all other MICOS subunits, whereas *MIC19* KO cells showed a complete loss of *MIC10* and reduced *MIC60* and *MIC13* levels (supplementary Fig 1B). *MIC25* KO cells showed minimal effect on the levels of other MICOS subunits (supplementary Fig 1B). Despite the loss of MIC10-subcomplex in *MIC10* KO

and *MIC13* KO cells, SLP2 sustained interactions with YME1L, *MIC19*, *MIC25* and *MIC60* (supplementary Fig 1A). Similarly, despite individual deletions of *MIC26*, *MIC27* and *MIC25*, SLP2 maintained its interaction with the remaining MICOS subunits (supplementary Fig 1A, 1B). Particularly striking was the observation in *MIC60* KO cells with substantially reduced levels of all MICOS subunits in the input fraction, SLP2 showed interactions with residual *MIC13*, *MIC26*, *MIC27*, and *MIC19* (supplementary Fig 1B). These findings collectively suggest that SLP2 retains stable interaction with any remaining MICOS subunits despite the absence of specific individual subunits. These observations highlight the role of SLP2 as a scaffold, facilitating the formation of an interaction hub with all MICOS subunits in the IM.

Our data pointed to the formation of a large SLP2-MICOS interaction hub and therefore we employed blue-native gel electrophoresis (BN-PAGE) to analyse the high-molecular weight native complexes of both SLP2 and MICOS. MICOS subunits are typically organized into two distinct complexes: a large MICOS complex (~ 2000 kDa) known to include MIB subunits and a lower molecular weight MICOS complex (~700 kDa)(Anand et al., 2016). Our analysis revealed that SLP2 forms a high molecular weight complex running alongside the larger MICOS complex at approximately 2000 kDa (Fig 1E). This finding aligns with the complexome profiling data derived from HEK293 cells(Anand et al., 2016), which demonstrate the co-clustering of SLP2 and MICOS subunits within the 2000 kDa range (Fig 1F). Overall, these diverse lines of experimentation collectively support and firmly establish the interaction between SLP2 and MICOS, elucidating their functional interplay within mitochondrial architecture (Fig 1G).

SLP2 depletion impairs cristae and crista junction formation

Subsequently, we sought to determine the significance of the SLP2-MICOS interaction by investigating whether loss of SLP2 affects the stability of MICOS subunits and the MICOS complex as a whole or cristae structure. Through WB analysis, we evaluated the levels of MICOS subunits in *SLP2* KO cells and observed a substantial reduction specifically in the steady state levels of *MIC26*, while other MICOS subunits were largely unaltered, consistently supported by the quantitative analysis the western blot (Fig 2A, 2B). The MICOS assembly using a BN-PAGE showed that *MIC26* was sparsely present in the MICOS complex as expected from the steady state levels, however the incorporation of most other MICOS subunits into the MICOS complex appeared comparable to WT (supplementary Fig 2). We analysed whether the loss of *MIC26* in *SLP2* KO cells results from proteolysis via YME1L. To test this, we employed short hairpin RNA (shRNA) to deplete YME1L in *SLP2* KO cells and indeed observed a significant rescue of the levels of *MIC26* in *SLP2* KO cells (Fig 2C), indicating a specific role of SLP2 in safeguarding *MIC26* from YME1L-mediated degradation. Next, we conducted transmission electron microscopy (TEM) imaging on *SLP2* KO cells. Remarkably, the *SLP2* KO cells showed swollen cristae and a substantial reduction in the

number of cristae and CJs compared to WT cells (Fig 2D, 2E). Number of cristae and CJs were quantified in a double-blind fashion to eliminate any potential biases in the data (Fig 2E). Cristae appeared as isolated stacks within the mitochondria, devoid of CJs. To the best of our knowledge, this is the first study to establish SLP2 as a modulator of cristae structure. The observed decrease in CJ numbers and the accumulation of cristae stacks in *SLP2* KO resembles the defects found in MICOS KO models. This reinforces the importance of the interaction between SLP2 and MICOS in the cristae defects observed in *SLP2* KO cells. In an attempt to elucidate whether the observed cristae defects in *SLP2* KO cells were primarily due to the decreased levels of MIC26, we tried to restore MIC26 expression in *SLP2* KO cells. Despite multiple trials, we were unable to generate *SLP2* KO with stable MIC26 overexpression. Consequently, to assess the similarity in cristae morphology defects, we compared *SLP2* KO cells with *MIC26* KO cells. While *MIC26* KO cells displayed cristae branching and a slight reduction in the number of cristae compared to WT, they maintained a similar number of CJs (Fig 2E). The severity of cristae defects and the reduction in cristae and CJ numbers in *SLP2* KO cells exceeded those observed in *MIC26* KO cells. This indicates that the cristae defects in *SLP2* KO do not solely arise from the loss of MIC26. Instead, it implies an additional role of SLP2 in MICOS assembly and cristae morphology, distinct from its function in preserving MIC26 stability via YME1L regulation.

To further delineate the roles of SLP2 within MICOS assembly, we investigated whether SLP2 is necessary to facilitate the interaction between MIC13 and other MICOS components. We generated a double knockout model lacking both SLP2 and MIC13 (*MIC13-SLP2* DKO) and overexpressed MIC13-FLAG to examine how MIC13-FLAG interacts with MICOS subunits in the presence or absence of SLP2 (supplementary Fig 3). MIC13 was able to interact with all MICOS subunits even upon loss of SLP2, although the interaction with MIC26 was reduced due to MIC26 degradation in *SLP2* KO. This suggests that the interactions between MIC13 and MICOS subunits are independent of SLP2. Unexpectedly, while YME1L was initially employed as a control in our experiment, our findings revealed a specific interaction between YME1L and MIC13 that occurred independent of SLP2. This interaction had not been previously documented, adding a new dimension to our understanding of MIC13 function (supplementary Fig 3).

Given that SLP2 is involved in stress-induced mitochondrial hyperfusion (SIMH), we investigated whether the interaction between SLP2 and MICOS affects SIMH. We assessed mitochondrial morphology in single knockout (KO) cell lines as well as in cells lacking both MIC13 and SLP2 (*MIC13-SLP2* DKO). To induce SIMH, we inhibited protein synthesis with cycloheximide and monitored mitochondrial morphology over time. We observed the accumulation of hypertubular mitochondria in WT cells within 2 hours of treatment (Fig 2F, 2G). As expected, *SLP2* KO cells showed no response to SIMH induction as evidenced by

quantification of mitochondrial morphology (Fig 2H). Interestingly, *MIC13* KO cells displayed hyperfusion similar to WT cells, while *MIC13-SLP2* DKO cells mirrored the response seen in the single *SLP2* KO (Fig 2F, 2G). This suggests that *MIC13* is not implicated in the *SLP2*-mediated SIMH.

SLP2 and MIC13 synergistically contribute to the assembly and organization of the MIC60-subcomplex

During the evaluation of mitochondrial morphology in SIMH experiments, one of the interesting observations was that *MIC13-SLP2* DKO displayed a remarkably higher mitochondrial fragmentation compared to either of the single KOs (Fig 2G, 2H), underscoring the heightened impact of DKO of *SLP2* and *MIC13*. While mitochondrial morphology serves as a broad indicator of cellular fitness and stress, there could also be potential association between mitochondrial morphology and MICOS defects, for example deficiencies of *MIC19* and *MIC60* have been linked to altered mitochondrial morphology (Li et al., 2016; Tang et al., 2020). This promoted us to investigate any synergistic roles of *MIC13* and *SLP2* in MICOS assembly and cristae formation. To address this, we analysed the steady state levels and complexes of MICOS in *MIC13-SLP2* DKO cells. While the steady state levels of MICOS subunits remained comparable between single *MIC13* KO and *MIC13-SLP2* DKO, the *MIC26* levels appeared even more reduced in *MIC13-SLP2* DKO as compared to either single KO cells (Fig 3A). Strikingly, the assembly of *MIC60* into the MICOS complex was significantly reduced in *MIC13-SLP2* DKO cells compared to *MIC13* KO (Fig 3B, 3C). Notably, MICOS complex in a native gel set-up runs as a smear with high intensity bands at two distinct sizes. In *MIC13* KO, the MICOS complex showed incomplete assembly, running at a reduced size due to loss of the *MIC10*-subcomplex as evidenced by BN-PAGE probed with *MIC60* antibody (Fig 3B). We consistently found that the overall intensity of *MIC60* in these MICOS complexes was considerably reduced, while the intensity of the OXPHOS complexes appeared intact in *MIC13-SLP2* DKO. This is quantitatively validated using densitometry analysis (Fig 3C), confirming that the *MIC60* incorporation in the MICOS complex is reduced upon the simultaneous loss of *SLP2* and *MIC13*.

Our findings revealed a reduction in incorporation of *MIC60* into the MICOS complex in *MIC13-SLP2* DKO cells, despite the steady state levels of *MIC60* being comparable to controls (Fig 3A), suggesting that there might be a pool of floating *MIC60* in the IM that is not the part of the MICOS complex. This promoted us to investigate the nanoscale distribution of *MIC60* in the IM, using stimulated emission depletion (STED) SR nanoscopy, with *MIC60* antibody. Previous studies have shown that *MIC60* forms distinct punctate structures in IM, characterized by a coordinated distribution pattern and rail-like arrangement along opposing sides of mitochondria (Jans et al., 2013; Kondadi, Anand, et al., 2020; Stoldt et al., 2019). In accordance with these studies, *MIC60* displayed a punctate pattern with the rail-like arrangement in control

cells (Fig 3D). This pattern of MIC60 staining resembles the arrangement of CJs in the mitochondria. However, MIC60 staining in the *MIC13-SLP2* DKO was remarkably different and disturbed compared to the WT cells and single KOs, with fewer punctate structures and patches where the staining was more evenly spread along the IBM (Fig 3D). The staining of MIC60 in single *MIC13* KO and *SLP2* KO cells was also perturbed with the rail-like pattern being less prominent as some MIC60 spots were also seen inside the mitochondria and not only on the edges (Fig 3D). It is plausible that MIC60 is present on the inner cristae stacks that are accumulated in *MIC13* KO and *SLP2* KO. Overall, we show that the combined loss of *SLP2* and *MIC13* was detrimental to MIC60 puncta organization, demonstrating the critical roles of *SLP2* and *MIC13* in orchestrating MIC60 arrangement and assembly.

Given the crucial role of MIC60 as an anchor in formation of both MIC60-subcomplex and MIB complex, we analysed MIC19, another component of MIC60-subcomplex, along with MIB components, SAMM50 and MTX1 using BN-PAGE. All these components exhibited reduced assembly in *MIC13-SLP2* DKO compared to either single KOs (supplementary Fig 4). This shows that the loss of MIC60 assembly or arrangement further impairs the assembly of the MIC60-subcomplex as well as the MIB complex, impacting MICOS-MIB assembly and emphasizing the synergistic role of *SLP2* and *MIC13* in mediating the assembly of the MICOS-MIB complex.

To discern whether the loss of MIC60 assembly in *MIC13-SLP2* DKO arises from the absence of MICOS subunits or if it is a specific function of *SLP2* and *MIC13*, we employed *MIC10* KO as a comparative element. *MIC10* KO cells exhibit a similar loss of MICOS subunits as seen in *MIC13-SLP2* DKO cells. Interestingly, despite the comparable loss of MICOS subunits, *MIC10* KO did not impact MIC60 assembly (supplementary Fig 5). This observation suggests that the deficiency in MIC60 assembly observed in *MIC13-SLP2* DKO cells is not solely attributed to the loss of MICOS subunits alone. Instead, it highlights the unique collaborative function of *SLP2* and *MIC13* in regulating MIC60-subcomplex and MIB assembly.

Based on our finding, we propose that *SLP2-MIC13* functions as a “seeder” for the formation of MIC60 punctae in IM, thereby promoting the formation of CJs (Fig 3E). Stomatins are recognised as scaffolding proteins that create the microdomains within the lipid-bilayer to form large protein assemblies. Consequently, we speculate that *SLP2* and MIC10-subcomplex create a conducive lipid microenvironment, essential for ‘seeding’ the proper organization and formation of MIC60 punctae.

SLP2 selectively regulates the assembly kinetics of MIC60-subcomplex

One of the questions that intrigued us was the role of *SLP2* itself in the MICOS assembly, particularly as we were unable to earlier detect any apparent change in MIC60 assembly in the single *SLP2* KO. This lack of observable changes in *SLP2* KO may be attributed to compensatory effects that mask the underlying impact due to long-term depletion of a protein.

Therefore, to meticulously dissect the mechanistic role of SLP2 in MIC60 assembly, we decided to analyse the kinetics of MICOS assembly in a time-dependent manner and employed the Tet-On system that allow inducible and controlled gene expression over short timescales. We reintroduced MIC13 in *MIC13* KO (serving as control) and *MIC13-SLP2* DKO in a time-dependent manner and analysed the re-assembly dynamics of the subunits of the MICOS complexes. For this, we generated pLIX403-MIC13-FLAG and stably expressed it in the *MIC13* KO and *MIC13-SLP2* DKO using the lentiviral transduction method. The addition of doxycycline initiates the expression of MIC13-FLAG in a time-dependent manner. After eight hours of doxycycline induction, MIC13-FLAG started to express in both *MIC13* KO and *MIC13-SLP2* DKO (Fig 4A). MIC13-FLAG was gradually expressed and incorporated into the MICOS complex of both *MIC13* KO and *MIC13-SLP2* DKO cells as seen by BN-PAGE at different time points after induction of protein expression (Fig 4B). Both MIC10 and MIC27 also progressively assembled in the MICOS complex over time (Fig 4C). The emergence of the MIC10-subcomplex, as indicated by MIC10 or MIC27, exhibited a more rapid and efficient kinetics in *MIC13-SLP2* DKO cells compared to the *MIC13* KO cells. This could be attributed to a slightly higher expression of MIC13-FLAG in *MIC13-SLP2* DKO compared to the *MIC13* KO. On the contrary, the incorporation of MIC60 into the MICOS complex was slower in *MIC13-SLP2* DKO cells compared to the *MIC13* KO after expression of MIC13-FLAG (Fig 4C). This observation was corroborated quantitatively through densitometry analysis of MIC60 at the 8-hours' time point in different cell lines (Fig 4D). The arrows in the Fig 4C indicate the incorporation of MIC60 into MICOS complex required more time to recover (16 hours) in *MIC13-SLP2* DKO. This delay in MIC60 assembly was further confirmed through extended time points (up to 48 hours) (Supplementary Fig 6A, B), consistently showing that absence of SLP2 hampers the assembly of MIC60. Despite the presence of the already assembled MIC10-subcomplex, the assembly of MIC60 into the MICOS complex was notably delayed in the absence of SLP2. Thus, it is evident that the assembly kinetics of the MIC60-subcomplex, rather than the MIC10-subcomplex, is dependent on SLP2 (Fig 4D), highlighting the specific regulatory role of SLP2 in facilitating the incorporation of MIC60 into the MICOS complex upon gradual restoration of MIC13.

MIC13 mainly stabilizes MIC10-subcomplex to promote crista junction formation

MIC13 has been suggested as a bridge connecting the MIC60-subcomplex and MIC10-subcomplex (Guarani et al., 2015). However, it has been difficult to identify the precise molecular role of MIC13 because *MIC13* KO was always associated with loss of the MIC10-subcomplex making it hard to differentiate whether the effects were arising due to MIC10 or MIC13 loss. In order to clarify the specific role of MIC13 in MIC13-SLP2 alliance for assembly of MIC60-subcomplex, we aimed to distinguish the function of MIC13 from MIC10. Efforts to generate stable cell line expressing MIC10 in the absence of MIC13 proved challenging,

perhaps because of the tendency of overexpressed MIC10 to undergo rapid degradation in the absence of MIC13. To counter this, we aimed to restore MIC10 levels by preventing its degradation in *MIC13* KO. We took leads from two observations from our study: the identification of a novel interaction between YME1L and MIC13 which is independent of SLP2 (supplementary Fig 3) and an observed increase in MIC10 levels upon the YME1L downregulation in all the cell lines (Fig 2E). We hypothesized that YME1L-mediated degradation might be responsible for MIC10 degradation in *MIC13* KO. To solve this, we generated stable cell lines expressing YME1L-targeted shRNA in WT, *SLP2* KO, *MIC13* KO and *MIC13-SLP2* DKO cell lines. YME1L knockdown resulted in elevated levels of MIC10 (along with MIC26 and MIC27) not only in *MIC13* KO but also in *SLP2* KO and *MIC13-SLP2* DKO cells showing that MIC10 (along with MIC26 and MIC27) are novel YME1L substrates independently regulated of SLP2 (Fig 5A). Moreover, the restoration of MIC10 levels through YME1L downregulation in *MIC13* KO cells provided us an exclusive scenario to determine the specific roles of MIC13 that are independent to MIC10. Employing these tools, we checked whether the restored MIC10 could interact with MIC60, in line with the proposed role of MIC13 as a bridge of MICOS complex. Conducting Co-IP using MIC60 antibody, we analysed the interaction of MIC60 with the replenished MIC10 in *MIC13* KO. Surprisingly, despite the absence of MIC13, when YME1L-mediated MIC10 degradation was prevented, MIC60 exhibited interactions with MIC10, MIC26 and MIC27 (Fig 5B). This finding challenges our previous understanding of MICOS assembly, suggesting that MIC13 might not be essential to bridge the two subcomplexes for MICOS assembly. Instead, it appears to play a crucial role in stabilizing the MIC10-subcomplex and regulating its quality through YME1L-dependent proteolysis (Fig 5B). The re-established interaction of MIC60 and replenished MIC10 in the absence of MIC13 provides further support to our novel findings regarding the specific roles of MIC13 in MICOS assembly.

While MIC10 levels were restored upon depletion of YME1L, a noteworthy observation emerged regarding the MIC27 band pattern specific to *MIC13* KO (Fig 5A). MIC27 band exhibited a slightly lower molecular weight in *MIC13* KO. The identity of this MIC27 variant is yet unknown but notably the conversion of MIC27 to this lower size was MIC13-dependent, as it remained unaffected upon MIC10 replenishment. Even when the steady-state levels of MIC27 were successfully restored upon downregulation of YME1L in *MIC13* KO, the status of the MIC27 band size did not revert to its original form. This observation highlights that MIC13 appears to play a unique role in managing the structural status of MIC27 independent of its influence on MIC10 levels. Overall, our findings allow us to delineate the function of MIC13 from MIC10, disproving the previous notion of MIC13 solely acting as a bridge. Instead, we reveal that MIC13 is crucial for providing stability to the entire MIC10-subcomplex by safeguarding it from the proteolytic activity of YME1L. Furthermore, our study sheds light on

additional functions of MIC13, such as its role in regulating MIC27. The new insights in MIC13 roles, whether dependent or independent of MIC10, holds significant potential for advancing our understanding of the pathobiology underlying mitochondrial hepato-encephalopathy associated with *MIC13* mutations.

Stabilized MIC10 facilitates seeding of MIC60 and crista junction formation

Understanding the specific role of MIC13 in stabilizing MIC10, we wanted to use this knowledge to validate our “seeder” model for MICOS assembly and ask how stabilizing the MIC10-subcomplex might impact the formation of the MIC60-subcomplex in *MIC13-SLP2* DKO cells. To achieve this, we depleted YME1L in *MIC13-SLP2* DKO cells, thereby stabilizing the MIC10-subcomplex. Surprisingly, we observed a partial restoration in the assembly of MIC60 when MIC10 was stabilized through YME1L depletion in *MIC13-SLP2* DKO cells (Fig 5C), despite similar steady-state levels of MIC60 (Fig 5A). This observation is crucial as it suggests that MIC10, even in the absence of SLP2 or MIC13, can serve as a ‘docking platform’ facilitating the integration of MIC60 into the MICOS complex. MICOS assembly has been assumed to follow a hierarchical step with MIC60 being the first component. However, these findings challenge this notion and demonstrate an interdependence between the assembly of MIC60 and MIC10-subcomplex. Especially, this highlights that the role of MIC13 in the *MIC13-SLP2* interplay is to ensure the stability and assembly of MIC10-subcomplex. This assembled MIC10-subcomplex, along with SLP2, is crucial in seeding the assembly of MIC60 by providing an assembly platform. The partial restoration of MIC60 assembly also influences the assembly of MIC19 (supplementary Fig 7) and MIB complex protein MTX1 (Fig 5C) in *MIC13-SLP2* DKO cells depleted for YME1L. In summary, this data highlights the substantial role of the SLP2-MIC13 cooperation in efficient assembly of the MICOS-MIB complex, particularly in association with MIC60.

We delved into the next significant question regarding the impact of ‘seeder’ complex formation and MIC60 assembly on cristae morphology. To address this, we analysed the mitochondrial ultrastructure in the single and DKO cell lines of *SLP2* and *MIC13* with and without the depletion of YME1L. *MIC13* KO displayed onion-like cristae, while *SLP2* KO displayed a stack like cristae albeit with more swollen cristae (Fig 2C, 5D, 5E). Extensive quantification of EM images corroborated these findings, showing significant reduction in the number of cristae and CJs in both single KOs (Fig 5D, E), reminiscent of defects typically associated with MICOS KO. *MIC13-SLP2* DKO cells exhibited severe phenotype similar to *MIC13* KO cells, with a substantial decrease in the numbers of cristae and CJs. Remarkably, partial stabilization of MIC10-subcomplex in *MIC13* KO and *MIC13-SLP2* DKO cell lines through YME1L depletion had a moderate beneficial effect on mitochondrial ultrastructure, significantly restoring CJs (Fig 5D, 5E), which is consistent with partial restoration of MICOS assembly. The cristae in this scenario appeared to unfurl from the onion-like structures typical of *MIC13* KO and re-attach

to IM to form nascent CJs, providing a potential model for CJs formation. This phenomenon indicates that stabilized MIC10 has the potential to promote the formation of nascent CJs in *MIC13* KO or *MIC13-SLP2* DKO (Fig 5D, E). This finding has many fold implications. Firstly, regarding the specific role of MIC13 in cristae formation, our results indicate that the presence of a stabilized MIC10-subcomplex, even in the absence of MIC13, partially restores CJs formation, highlighting the significant contribution of MIC10 in the cristae phenotype observed in *MIC13* KO. This clarifies the specific role of MIC13, showing that the primary cristae defects observed in *MIC13* KO arise from the loss of MIC10 rather than MIC13 itself. This is particularly relevant to MIC13-associated mitochondrial hepato-encephalopathy, as patient cells also exhibit onion-like cristae structure. Secondly, depletion of YME1L in *SLP2* KO not only restored the loss of CJs but also visibly reduced cristae swelling. While swelling of cristae is not typically observed in MICOS KOs, it is likely that the swelling in *SLP2* KO arises from another unknown substrate regulated by SLP2-YME1L. However, based on our data, we firmly establish that SLP2 plays a vital role in MIC60 assembly kinetics in presence of MIC10-subcomplex, solidifying its functional relevance in facilitating cristae and CJ formation, further evident from the TEM images displaying a significant reduction in CJ and additional cristae swelling. Thirdly, the observed rescue in MIC60-subcomplex assembly and cristae phenotype upon stabilizing MIC10-subcomplex in *MIC13-SLP2* DKO cells further validates the 'seeder' model, adding a new layer towards understanding MICOS assembly, and its direct involvement in cristae and CJs formation.

We have consolidated our findings to present an updated a multi-step model for MICOS assembly, revealing novel insights and marking a significant shift in our understanding of MICOS assembly and cristae formation. We introduced SLP2 as a crucial regulator of cristae morphology, playing multifaceted roles in MICOS assembly and cristae formation. While SLP2 shields MIC26 from YME1L-mediated proteolysis, its function exceeds MIC26 stabilization, as it collaborates with MIC13 to regulate the kinetic assembly of MIC60 into the MICOS-MIB complex. In addition to the SLP2-YME1L, we have identified a novel interplay between MIC13 and YME1L, crucial for maintaining the integrity of the entire MIC10-subcomplex. This finding highlights the special role of MIC13 in stabilizing MIC10-subcomplex rather than acting as a bridge. Interestingly, the MIC13-YME1L interaction can occur independently of SLP2, revealing the intricate regulation of MICOS stabilization by different pathways, partially dependent of SLP2. Once stabilized, MIC10-subcomplex along with SLP2 forms what we term as the 'seeder' complex, facilitating the assembly of MIC60-subcomplex and MIB within the MICOS-MIB complex. Combined depletion of MIC13 and SLP2 disrupts MIC60's nanoscale distribution and its incorporation into MICOS complex. We propose that the 'seeder' complex promotes the nanoscale punctate distribution of MIC60 and assembly of MIC60, culminating in the formation of MICOS-MIB complex. Subsequently, the 'seeder' complex, thereby

facilitating MIC60-subcomplex assembly, contributes to the formation of nascent CJs (Fig 6). In addition to identifying SLP2 as a novel regulator of cristae morphology, our model highlights several key insights. These include the identification of intricate and partially overlapping quality control pathways in MICOS regulation, the elucidation of specific functions of MIC13, and the recognition of the interdependence between the MIC10- and MIC60-subcomplexes in the assembly of the MICOS-MIB complex. The proposed model represents a significant shift in our understanding of MICOS assembly and quality control mechanisms controlling the intricate process of CJs formation.

Discussion

MIC13 is a poorly characterized subunit of MICOS, representing a small protein with no known resemblance with any other identified protein so far. In order to elucidate the novel functions of MIC13, we set out to map its interactome. Employing a Co-IP coupled MS approach, we discovered SLP2 as an interactor of MIC13, revealing a previously unknown multi-layered role of SLP2 in maintaining MICOS assembly and cristae formation. To the best of our knowledge, no prior studies have identified SLP2 as a cristae modulator or explored the mechanism through which SLP2 regulates cristae formation. Our study comprehensively illustrates the role of SLP2 in MICOS assembly and cristae formation, substantiated by the following results: 1) Using KO models of individual MICOS subunits and stable overexpression cell lines, we determined that SLP2 not only interacts with MIC13 but also with each MICOS subunit, forming a large interaction hub of SLP2-MICOS in the mitochondrial IM. 2) Depletion of SLP2 resulted in pronounced cristae defects, including swollen cristae and reduced number of cristae and CJs, resembling the defects observed in MICOS KO model. 3) SLP2 was essential for preserving the stability of MIC26 by regulating YME1L-mediated proteolysis. However, the cristae defects in *SLP2* KO were substantially more severe compared to *MIC26* KO pointing towards the broader role of SLP2 in MICOS assembly and cristae formation. 4) The DKO of *MIC13* and *SLP2* exhibited additive defects, particularly in MIC60-subcomplex and MIB assembly into the MICOS complex, leading to perturbed nanoscale arrangement of MIC60 punctae in the inner membrane. This suggests a synergistic role of SLP2 and MIC13 in seeding the formation of MIC60 puncta and its incorporation into the MICOS complex. 5) The time-dependent restoration of MIC13 in *MIC13-SLP2* DKO cells showed a considerably slower kinetics of the assembly of MIC60 into MICOS complex compared to *MIC13* KO, demonstrating a critical role of SLP2 in specifically regulating MIC60 seeding into MICOS complex. 6) Interestingly, the restoration of MIC10-subcomplex in simultaneous depletion of *SLP2* and *MIC13* could restore MIC60 assembly and lead to formation of nascent CJs. By combining these findings, we introduce SLP2 as a novel cristae modulator, specifically contributing to MIC60-subcomplex and MIB assembly and facilitating cristae organization.

We further clarified the specific roles of MIC13 and found that, fundamentally, MIC13 is not essential for bridging MIC10- and MIC60-subcomplexes, instead its crucial function lies in shielding the MIC10-subcomplex by protecting it from YME1L-mediated proteolysis. Instead of relying on an overexpression strategy, we employed a unique approach of stabilizing MIC10-subcomplex with YME1L depletion in *MIC13* KO as a means to support and validate our model (Figure 5). This approach not only serves as a tool for validation but also offers additional insights into the pathological mechanisms underlying MIC13-mediated pathology. We observed that the restoration of MIC10 not only partially recovered the MIC60 assembly in the *MIC13-SLP2* DKO, but also prompted the re-formation of nascent CJs. This emphasizes the mutual interdependence of SLP2 and MIC13, particularly in stabilizing MIC10-subcomplex, for the MICOS assembly and the formation of cristae and CJs. Combining our data, which shows the absence of SLP2 delays the assembly of MIC60 and alterations of MIC60 foci formation in *MIC13-SLP2* DKO, we introduced the 'seeder' model for the assembly of the MICOS complex (Fig 6). Here, the combined actions of SLP2 and MIC10-subcomplex act as a seeding mechanism for the incorporation of MIC60-subcomplex into the MICOS complex, thereby, leading to formation MICOS-MIB complex further promoting cristae and CJs morphogenesis. The MIC10-subcomplex serves as a docking platform for further assembly of MIC60-subcomplex into the MICOS complex, illustrating an interdependence between MIC60- and MIC10-subcomplex during the formation of the MICOS complex. The concomitant reappearance of CJs upon stabilization of MIC10-subcomplex provides mechanistic insights for formation of nascent CJs. In summary, our study not only refines the model for MICOS assembly but also offers valuable insights into the intricate processes underlying the formation of cristae and CJs.

SLP2, a member of the SPFH superfamily, performs diverse roles in mitochondrial functions, involving mitochondrial dynamics during stress, quality control and cell survival (Tondera et al., 2009; Wai et al., 2016). It binds to cardiolipin to regulate mitochondrial biogenesis (Christie et al., 2011). Moreover, it serves as an anchor for a proteolytic hub in mitochondria called SPY complex regulating proteases such as YME1L and PARL (Wai et al., 2016). In our study, we show using several lines of evidences that SLP2 act as a scaffold, forming a large interaction hub within the IM with all the subunits of MICOS complex. This direct regulation of MICOS assembly and cristae formation prompts the question how SLP2 performs these tasks in the mitochondria, specifically in the context of cristae formation. While the regulation of MIC26 by SLP2 can be explained by the SLP2-YME1L interaction, introducing MIC26 as a novel player that is influenced by the SPY complex, understanding how SLP2 influences the seeding of MIC60-subcomplex assembly and its docking with MIC10-subcomplex remains a challenge. We speculate that SLP2 may generate a specialized lipid environment facilitating MIC60 punctae formation, possibly through direct interaction or cardiolipin recruitment. Moreover,

SLP2-delineated lipid domains, enriched in cardiolipin, could directly or indirectly impact cristae formation and MIC60 assembly. Furthermore, we speculate the presence of an unknown substrate of YME1L under regulation of SLP2, whose absence contributes towards cristae swelling and identification of this protein could broaden our understanding of its role in cristae morphogenesis. Addressing these complexities requires challenging experiments aimed at elucidating the lipid microenvironment of SLP2, providing crucial insights into how SLP2 contributes to the MICOS assembly and cristae formation.

MIC13, an integral component of the mitochondrial IM, plays a vital role in cristae morphogenesis and loss of MIC13 results in severe mitochondrial hepato-encephalopathy. Although previous research has extensively detailed the consequences of MIC13 depletion, the underlying molecular mechanisms leading to the phenotypes are largely unknown. The challenge arises in distinguishing the specific function of MIC13 from other MIC10-subcomplex proteins due to the concurrent loss of the MIC10-subcomplex in *MIC13* KO. Interestingly, upon depleting YME1L in *MIC13* KO, the MIC10-subcomplex could be restored, providing a unique scenario to study the specific role of MIC13. To our surprise, the restored MIC10-subcomplex exhibited the ability to interact with the MIC60-subcomplex even in the absence of MIC13. This finding shows that MIC13 is primarily required for MIC10 stability rather than serving as a bridging component. The presence of nascent CJs upon restoration of MIC10 in *MIC13* KO showed that the assembled MIC10-subcomplex could form CJs even in the absence of MIC13. MIC10 is known to oligomerize in a wedge-like shape that causes membrane bending and CJs formation (Barbot et al., 2015; Bohnert et al., 2015). However, it remains to be answered whether this CJs restoration is sufficient to address MIC13-specific mitochondrial defects or the associated pathology. In addition to maintaining MIC10 stability, we observed that MIC13 exclusively influences the status of MIC27, resulting in a lower molecular weight variant. Although the identity of this MIC27 variant remains unknown, its specificity to MIC13 suggests that MIC13 may have additional specialized roles critical for its function and associated pathology. In conclusion, we remain optimistic that future studies will further elucidate whether restoration of MIC10 serves as a novel tool to determine the mechanisms underlying MIC13-associated diseases and holds promise for the development of future therapeutics.

MICOS contains several subunits, each contributing uniquely in maintaining mitochondrial structural integrity, subdivided into two subcomplexes, MIC60-subcomplex and MIC10-subcomplex. Several previous studies have elucidated distinct function of each subcomplex, collectively contributing to overall functionality of MICOS. While the MIC60-subcomplex is responsible to connect IM and OM and shape CJs, MIC10-subcomplex controls lamellar cristae biogenesis and promotes CJs formation(Bohnert et al., 2015; Stephan et al., 2020; van der Laan et al., 2016). It was believed that MICOS assembly followed a hierarchical order, with the assembly of the MIC60-subcomplex preceding that of the MIC10-subcomplex. MIC60

was considered a master regulator in this assembly process(Ott et al., 2015; Zerbes et al., 2016). However, our results reveal an intricate interdependence between these two subcomplexes, wherein the kinetics of MICOS subcomplexes assembly progress in a mutually interdependent manner. This interdependence between the two MICOS subcomplexes ensures the quality of MICOS assembly, preventing the formation of futile subcomplexes unless the assembly can be completed. Our findings highlight a more integrated and coordinated assembly process in which SLP2 emerges as a key player in facilitating this process.

Our data also highlights the delicate balance between the regulation of mitochondrial proteases, specifically YME1L, and the integrity of MICOS assembly and mitochondrial cristae. While SLP2 protects MIC26 from YME1L-mediated proteolysis, we made a novel observation of MIC13 interacting YME1L independently of SLP2. The functional significance of this MIC13-YME1L interaction remains elusive, prompting future investigations to elucidate whether MIC13 directly influences YME1L activity or whether YME1L plays an indirect role during stress conditions induced by the deletion of MICOS subunits. Previous studies have implicated mitochondrial proteases in the control of cristae morphology, highlighting the broader impact of quality control pathways on the safety and integrity of mitochondrial membrane structures. MIC60 and SAMM50 were also shown to be proteolytic substrates of YME1L during *MIC19* downregulation (Li et al., 2016; Tang et al., 2020) showing the complexity of regulation of MICOS assembly. Additionally, OMA1, another IM protease also associated with the MICOS complex (Viana et al., 2021) and proteolytically regulated MIC19 assembly in the MIB complex(Tang et al., 2020). Overall, our study deciphers a novel quality control mechanism governing MICOS and MIB assembly, advancing our understanding of the factors orchestrating cristae morphogenesis.

The precise mechanisms underlying the function of CJs and contact sites remain incompletely understood. The MICOS subunits have been implicated in several important cellular functions including the import of mitochondrial proteins, biogenesis and transfer of phospholipids, mtDNA organization, apoptosis, mitophagy, mitochondrial transport, mitochondrial translation, mitochondrial morphology and inflammation(Anand et al., 2021; Kondadi, Anand, & Reichert, 2020). Exploring the role of SLP2 holds promise for providing new insights into many of these cellular processes. Future studies investigating these components and their interactions may reveal novel mechanisms into the intricate regulation of mitochondrial ultrastructure and its impact on broader cellular pathways.

Materials and methods

Cell culture

Flp-In T-REx HEK293 and HeLa cells were cultured in Dulbecco's modified Eagle medium (DMEM) with 1g/L glucose and sodium pyruvate (PAN-Biotech, P04-01500) supplemented

with 1% stable glutamine (P04-82100), 1% penicillin-streptomycin (Sigma-Aldrich, P4333-100ml), 10% fetal bovine serum (FBS) (Capricorn Scientific, FBS-11A). Plat-E and HEK293FT cells were cultured in DMEM high glucose medium (PAN-Biotech, P04-03500) supplemented with 10%FBS, 1% stable glutamine, 1% sodium pyruvate (Gibco, 11360070). GIPZ-Control-Flp-In T-REx HEK293 and GIPZ-YME1LshRNA- Flp-In T-REx HEK293 cells were cultured in DMEM 1g/L glucose medium containing sodium pyruvate supplemented with 1% stable glutamine, 10% FBS, 1% penicillin-streptomycin and 1% Non-Essential Amino Acids Solution (NEAA) (PAN-Biotech, P08-32100). All cells were cultured in at 37°C with 5% CO₂. All cell line generated are listed in Supplementary Table 2.

Co-immunoprecipitation coupled mass spectrometry

Co-IP was performed with Protein A Sepharose CL-4B beads (Invitrogen, 101041) and affinity purified MIC13 antibody was linked to the beads. Isolated mitochondria from Flp-In T-REx HEK293 WT or *MIC13* KO were solubilized with isotonic buffer (150 mM NaCl, 10 mM Tris/HCl (pH 7.5), 5 mM EDTA, 1x protease inhibitor cocktail) supplemented with 5 µl of 10% Digitonin (2g/g of protein) and added to the beads with subsequent incubation in 4°C under rotation conditions. Beads were washed several times, transferred into a new tube in 10mM Tris, pH 7.4. Beads were resuspended in 50 µl 6M GdmCl, 50 mM Tris/HCl, pH 8.5 and incubated at 95°C for 5 min. Sample were diluted with 25 mM Tris/HCl, pH 8.5, 10% acetonitrile to obtain a final GdmCl concentration of 0.6 M. Proteins were digested with 1 µg Trypsin (sequencing grade, Promega) overnight at 37°C under gentle agitation. Digestion was stopped by adding trifluoroacetic acid to a final concentration of 0.5%. Peptides were loaded on multi-stop-and-go tip (StageTip) containing six C18 discs. Purification and elution of peptides was performed as described in Kulak, *et al*(Kulak *et al.*, 2014). Peptides were eluted in wells of microtiter plates and peptides were dried and resolved in 1% acetonitrile, 0.1 % formic acid. Liquid chromatography/ mass spectrometry (LC/MS) was performed on Thermo Scientific™ Q Exactive Plus equipped with an ultra-high performance liquid chromatography unit (Thermo Scientific Dionex Ultimate 3000) and a Nanospray Flex Ion-Source (Thermo Scientific). Peptides were loaded on a C18 reversed-phase precolumn (Thermo Scientific) followed by separation on a with 2.4 µm Reprosil C18 resin (Dr. Maisch GmbH) in-house packed picotip emitter tip (diameter 100 µm, 30 cm long from New Objectives) using an gradient from mobile phase A (4% acetonitrile, 0.1% formic acid) to 60 % mobile phase B (99% acetonitrile, 0.1% formic acid) for 90 min with a flow rate 350 nl/min. MS data were recorded by data dependent acquisition Top10 method selecting the most abundant precursor ions in positive mode for HCD fragmentation. Lock mass option (Olsen *et al.*, 2005) was enabled to ensure high mass accuracy between multiple runs. The Full MS scan range was 300 to 2000 m/z with resolution of 70000, and an automatic gain control (AGC) value of 3*10⁶ total ion counts with a maximum ion injection time of 160 ms. Only higher charged ions (2+) were selected for MS/MS scans

with a resolution of 17500, an isolation window of 2 m/z and an automatic gain control value set to 105 ions with a maximal ion injection time of 150 ms. Selected ions were excluded in a time frame of 30s following fragmentation event. Fullscan data were acquired in profile and fragments in centroid mode by Xcalibur software. For data analysis MaxQuant 1.6.1.0 (Cox and Mann, 2008, Nat. Biotechnology), Perseus 1.5.6.0 (Tyranova et al 2016) and Excel (Microsoft Office 2013) were used. N-terminal acetylation (+42.01) and oxidation of methionine (+15.99) were selected as variable modifications and carbamidomethylation (+57.02) on cysteines as a fixed modification. The human reference proteome set (Uniprot, July 2017, 701567 entries) was used to identify peptides and proteins with a false discovery rate (FDR) less than 1%. Minimal ratio count for label-free quantification (LFQ) was 1. Reverse identifications and common contaminants were removed and the data-set was reduced to proteins that were identified in at least 5 of 7 samples in one experimental group. Missing LFQ or IBAQ values were replaced by random background values. Significant interacting proteins were determined by permutation-based false discovery rate (FDR) calculation and students T-Test. The mass spectrometry proteomics data have been deposited to the ProteomeXchange Consortium via the PRIDE [1] partner repository with the dataset identifier PXD044968.

Proximity ligation assay

PLA was carried out with Duolink® In Situ Red Starter Kit Mouse/Rabbit (Sigma-Aldrich, DUO92101-1KT) following manufacturer's protocol with minor modifications. Briefly, HeLa cells were fixed using 4% paraformaldehyde (Sigma-Aldrich, P6148) for 20 mins in room temperature and washed with PBS 3x with subsequent permeabilization with 0.15% Triton X-100 (Sigma-Aldrich, T8787-100ML) in room temperature for 15 mins followed by PBS wash. Permeabilized cells were blocked with blocking solution (provided in kit) for 1 hour in 37°C. Blocking solution was removed and primary antibodies with 1:100 dilution ratio was added to the samples and incubation was carried out at 37°C for 2 hours. Following primary antibodies were used: MIC10 (Abcam, 84969), MIC13 (custom made by Pineda (Berlin) against human MIC13 peptide CKAREYSKEGWYVKARTK), MIC19 (Proteintech, 25625-1-AP), MIC25 (Proteintech, 20639-1-AP), MIC26 (ThermoFisher Scientific, MA5-15493), MIC27 (Sigma-Aldrich, HPA000612-100UL), MIC60 (Abcam, ab110329), SLP2 (Abcam, ab102051), SLP2 (OriGene, TA808240), Mt-CO2 (Abcam, ab110258). Subsequent ligation of PLA probes and amplification of circular DNA probes was carried out following manufacturer's protocol. PLA signals were visualized in PerkinElmer spinning disc confocal microscope equipped with a 60× oil objective.

CRISPR-Cas9 knockout generation

CRISPR-Cas9 double nickase plasmid (Santa Cruz Biotechnology, SLP2: sc-403638-NIC, MIC26: sc-413137-NIC, MIC60: sc-403617-NIC, MIC25: sc-413621-NIC, MIC19: sc-408682-NIC, MIC10: sc-417564-NIC, MIC27: sc-414464-NIC) was transfected with GeneJuice (Sigma-

Aldrich, 70967-3) in Flp-In T-REx HEK293 WT, *MIC13* KO parental lines to generate KO and double KO cell lines. Briefly, cell lines were transfected at 60-70% confluency with 1 µg of double nickase plasmid and incubated for 48 hours followed by 2.5 µg/ml puromycin selection for 24 hours with subsequent single cell sorting based on green fluorescent protein (GFP) expression using flow cytometry in 96 well plate. Cells were incubated and upon visible colonies, cells were sub-cultured and KO screen was performed with western blotting. Cell lines showing no immune reactivity to respective antibodies were termed as KOs or double KOs.

Molecular cloning

Human SLP2-HA ORF (Sino Biologicals, HG16147-CY) was cloned into pMSCVpuro vector using Gibson assembly cloning kit (NEB, E2611L), following manufacturer's protocol. HA tag was replaced with MYC tag with Site Directed and Ligation Independent Mutagenesis (SLIM) (Chiu et al., 2008) to generate pMSCV-SLP2-MYC. Human *MIC13*-Flag from pMSCV puro *MIC13*-FLAG (Urbach et al., 2021) was cloned into pLIX403 (Addgene, 41395) with Gibson assembly following manufacturer's protocol. Primer sequences for Gibson assembly and SLIM are provided in Supplementary Table 3.

Generation of stable cell lines

For retroviral transduction, Plat-E cells were transfected with 1 µg of pMSCV-*MIC13*Flag or pMSCV-SLP2MYC and 1 µg of pVSV-G with 3.5 µL of GeneJuice per wells of 6-well plate. After 72 hours incubation, viral supernatant was added to the target cells. Media was replaced with puromycin containing media (2.5 µg/ml) 48 hours of transduction. Puromycin selection was carried out for 2 weeks and successful expression of exogenous protein was validated with western blot. For lentiviral transduction, HEK293FT cells were transfected with 1µg of pLIX403 EV or pLIX403-*MIC13*-Flag or pGIPZ-non-silencing-Control-shRNA (Horizon Discovery, RHS4346) or pGIPZ-YME1L-shRNA (Horizon Discovery, RHS4430-200157017, RHS4430-200215861, RHS4430-200221198, RHS4430-200268420, RHS4430-200273633, RHS4430-200280144) along with 1µg of psPAX2 (Addgene, 12260) and pMD2.G (Addgene, 12259) was transfected using GeneJuice. 72 hours post transfection, viral supernatant was collected and added on target cell lines. Media was replaced with puromycin (2.5 µg/ml) containing media and selection was carried out for about 2 weeks. Successful exogenous protein expression or knockdown was confirmed with western blotting.

SDS PAGE and Western blot

Cells were grown in 6-well dishes and harvested with cold PBS upon 70-90% confluency followed by protein extraction by RIPA lysis. Protein concentration was determined by Lowry method (Bio-Rad, 5000113, 5000114, 5000115) and samples were prepared using Laemmli loading buffer. Proteins were separated using 10% or 15% SDS-PAGE with subsequent transfer on nitrocellulose membrane (Amersham, 10600004) followed by 1 hour of blocking

using 5% skimmed milk (Carlroth, 68514-61-4). Membranes were incubated overnight in 4°C under shaking conditions in primary antibodies: MIC10 (Abcam, 84969), MIC13 (custom made by Pineda (Berlin) against human MIC13 peptide CKAREYSKEGWYVKARTK), MIC19 (Proteintech, 25625-1-AP), MIC25 (Proteintech, 20639-1-AP), MIC26 (ThermoFisher Scientific, MA5-15493), MIC27 (Sigma-Aldrich, HPA000612-100UL), MIC60 (Abcam, ab110329), SLP2 (Abcam, ab102051), beta-tubulin (Cell Signalling Technology, 2128S), HSP60 (sigma, SAB4501464), Mt-CO2 (Abcam, ab110258), YME1L (Proteintech, 11510-1-AP), MTX1 (Abcam, ab233205). Following primary antibody incubation, membranes were washed in TBST and probed with Goat anti-mouse IgG HRP-conjugated antibody (Abcam, ab97023) or goat anti-rabbit IgG HRP-conjugated antibody (Dianova, 111-035-144). Chemiluminescent signal was recorded with VILBER LOURMAT Fusion SL (Peqlab) and quantification was performed with ImageJ.

Mitochondria Isolation

Cells were grown in 15 cm dishes and scrapped in cold PBS and pelleted at 500g for 5 mins. Cell pellets were resuspended in isotonic buffer (220 mM mannitol, 70 mM sucrose, 1 mM EDTA, 20 mM HEPES (pH 7.5) and 1 × protease inhibitor cocktail (Sigma-Aldrich, 05056489001) with 0.1% bovine serum albumin (BSA) (Pan-Biotech, P06-1394100). Cells were mechanically homogenized using syringe with 26G cannula for 15 strokes. Cell homogenate was centrifuged at 1000g for 10 mins, supernatant was collected in fresh tube and further centrifuged at 10,000g for 10 mins at 4°C to obtain crude mitochondrial fractions. Crude mitochondrial pellets were resuspended in isotonic buffer and Lowry assay was performed to determine the concentration. Crude mitochondrial fractions were aliquoted, centrifuged at 10,000g for 5 mins and pellets were resuspended in freezing buffer (300 M trehalose, 10 mM KCl, 1 mM EDTA, 10 mM HEPES and 0.1% BSA) and stored in -80°C until further processing.

Co-immunoprecipitation

Mitochondrial aliquots of 500 µg were pelleted by centrifugation and re-suspended in isotonic buffer (150 mM NaCl, 10 mM Tris/HCl (pH 7.5), 5 mM EDTA, 1x protease inhibitor cocktail) with 10 µl of 10% Digitonin (2g/g of protein) and solubilized for 10 mins on ice. Solubilized proteins were centrifuged at 21,000g for 20 mins and 10% of the supernatant was separated as input fraction. Remaining supernatant were incubated with anti-Flag M2 affinity beads (Sigma) or MYC-Trap agarose beads (ChromTech) overnight in 4°C under rotation. For pulldown of MIC60, 1µg of MIC60 antibody (Abcam, ab110329) was conjugated with protein A Sepharose beads (Invitrogen, 101041). Excess antibodies from beads were washed out with PBS containing 1x protease inhibitor cocktail. Beads were centrifuged at 3700g for 1 min at 4°C. Beads were further washed (4x) with isotonic buffer with 0.01% digitonin. Proteins were eluted with Laemmli buffer without beta-mercaptoethanol at 65°C for 10 min with subsequent

addition of 1 μ l beta-mercaptoethanol and subjected to SDS-PAGE with subsequent western blotting.

Visualization of native protein complexes with blue native PAGE

Mitochondrial aliquots of 150 μ g were centrifuged and pellets were resuspended in 15 μ l of solubilization buffer (50 mM NaCl, 2 mM aminohexanoic acid, 50 mM imidazole/HCl pH 7, 1 mM EDTA, protease inhibitor cocktail) with 3 μ l of 10% digitonin (2g/g of protein) and incubated on ice for 10 mins. Samples were centrifuged at 21,000g for 10 mins at 4°C and supernatant was collected in fresh tube followed by addition of 50% glycerol and 1.5 μ l of 1% Coomassie brilliant blue G-250. Samples were loaded in 3-13% gradient gel and subsequently transferred on methanol activated PVDF membrane. Membranes were blocked in 5% skimmed milk for 1 hour and incubation was carried out overnight in 4°C under shaking conditions with primary antibodies: MIC10 (Abcam, 84969), MIC13 (custom made by Pineda (Berlin) against human MIC13 peptide CKAREYSKEGWYVKARTK), MIC19 (Proteintech, 25625-1-AP), MIC25 (Proteintech, 20639-1-AP), MIC26 (ThermoFisher Scientific, MIC27 (Sigma-Aldrich, HPA000612-100UL), MIC60 (Abcam, ab110329), SLP2 (Abcam, ab102051), MTX1 (Abcam, ab233205). Primary antibodies were washed 3x with TBST and incubated with Goat anti-mouse IgG HRP-conjugated antibody (Abcam, ab97023) or goat anti-rabbit IgG HRP-conjugated antibody (Dianova, 111-035-144) diluted to 1:10000 in 5% skimmed milk in TBST. Chemiluminescent signal was recorded with VILBER LOURMAT Fusion SL (Peqlab) and quantification was performed with ImageJ.

Mitochondria morphology analysis

Flp-In T-REX HEK293 cells were transfected with 1 μ g of mitochondrially targeted GFP (Mito-GFP) with along with 3.5 μ l of GeneJuice. 24 hours post transfection, cells were treated with 10 μ M cycloheximide and incubated for 2 hours at 37°C in CO₂ incubator. Media was removed following PBS washing three times. Cells were fixed using 4% paraformaldehyde (Sigma-Aldrich, P6148) for 20 mins in room temperature and washed with PBS 3 times. GFP signals were visualized in PerkinElmer spinning disc confocal microscope equipped with a 60 \times oil objective. Cells were classified as hypertubular, tubular, intermediate or fragmented based on the majority of mitochondrial population present in the particular cell. Cells classified as hypertubular contained large interconnected tubular mitochondrial networks. Cells classified as intermediate contained a comparable ratio of short tubes or fragmented mitochondria, while cells classified as tubular and fragmented contained mostly long tubular and very short mitochondria fragments, respectively.

Stimulated emission depletion (STED) super-resolution nanoscopy

Cells were fixed and permeabilized as described earlier (PLA assay). Permeabilized cells were blocked with 5% goat serum and primary antibody incubation was carried out with 1:100 rabbit anti-MIC60 antibody (custom-made, Pineda (Berlin)), which was generated using the peptide

CTDHPEIGEGKPTPALSEEAS against human MIC60, overnight at 4°C and 1:100 Aberrior STAR 635P goat-anti-rabbit (2-0012-007-2) secondary antibody incubated at room temperature for 1 h. STED imaging was performed with the Leica SP8 laser scanning confocal microscope coupled with a STED module. Initially, imaging of 80-nm gold particles (BBI Solutions) was carried out in reflection mode for correct alignment of excitation and depletion laser. A 93x glycerol (N.A = 1.3) objective was used with the pinhole set to 0.6 Airy units and a white light laser excitation wavelength of 633 nm was used for sample excitation. STED depletion was carried out with a pulsed STED depletion laser beam of 775 nm wavelength. A hybrid detector (HyD) was used for signal detection in the range from 643 to 699 nm. 13x magnification was used to acquire images covering a field of view of 9.62 x 9.62 µm. No image processing was performed except smoothing carried out with Fiji software.

Electron microscopy

Cells were cultured in petri dishes until about 80% confluency was reached and chemical fixation was carried out using 3% glutaraldehyde buffered with 0.1 M sodium cacodylate, pH 7.2, followed by cell scrapping and centrifugation. Cell pellets were washed with 0.1 M sodium cacodylate and embedded in 2% agarose. Cell staining was performed with 1% osmium tetroxide for 50 mins with subsequent incubation in 1% uranyl acetate/1% phosphotungstic acid for 1 hour. Samples were further dehydrated with graded acetone series and embedded in spur epoxy resin for polymerization at 65°C for 24 hours. Ultrathin sections of samples were prepared with microtome and images were captured with transmission electron microscope (Hitachi, H7100) at 75V equipped with Bioscan model 792 camera (Gatan) and analyzed with ImageJ software. The images were randomized and the data was analyzed in a double-blind manner by two scientists. Data analysis was carried out by GraphPad prism. Statistical analysis includes one-way Anova test, outlier test was performed with Grubb's test where indicated using GraphPad Prism.

Figures:

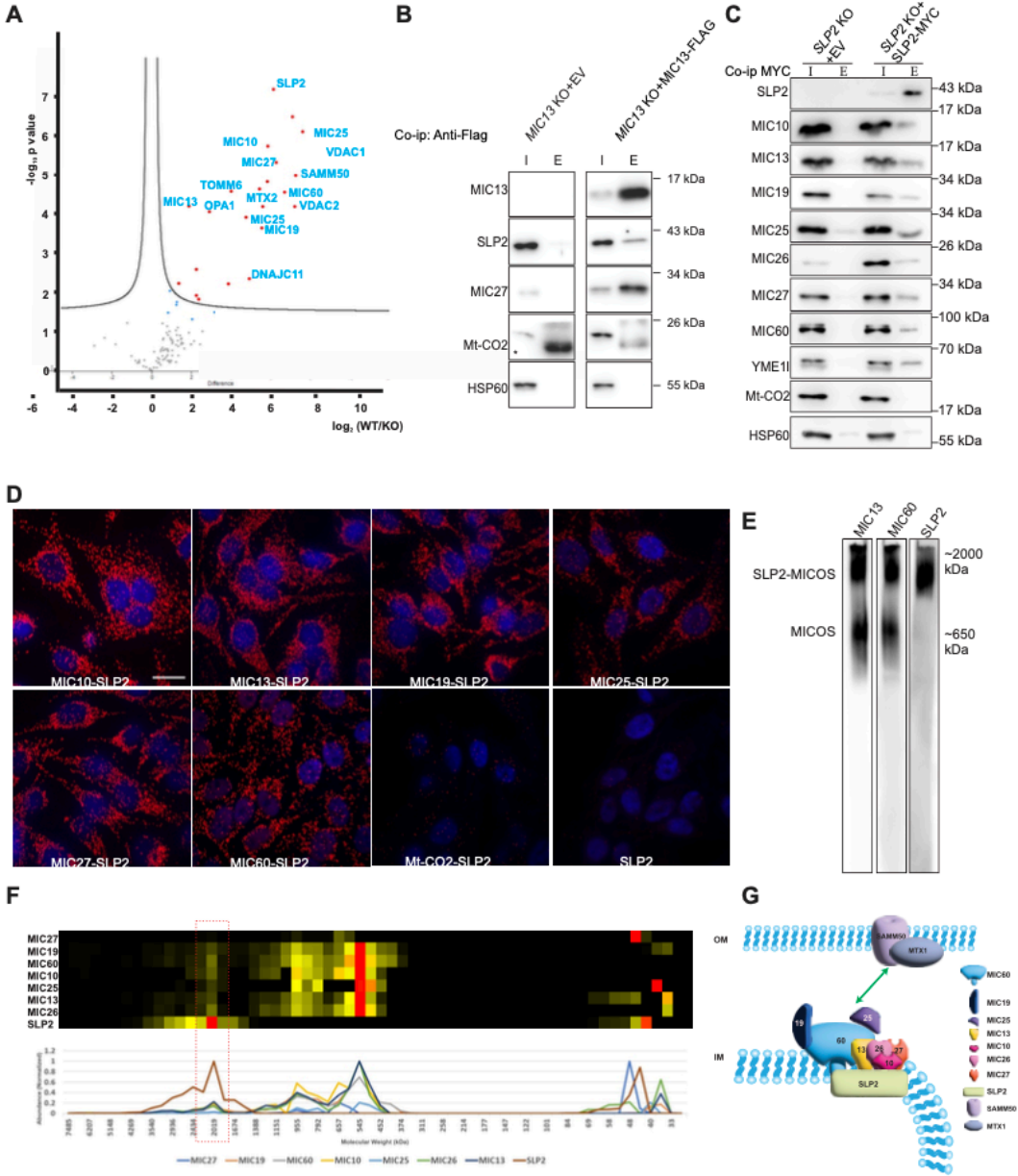


Figure 1

Figure 1. SLP2 is identified as a novel MIC13 interacting partner. **A**, Interactome of MIC13 with Co-IP (co-immunoprecipitation) coupled mass spectrometry revealed SLP2 as a novel interactor of MIC13. **B**, The interaction between SLP2 and MIC13 was validated by Co-IP using FLAG antibody in isolated mitochondria from *MIC13* KO cells stably expressing MIC13-FLAG or empty vector (EV) pMSCVpuro as background control. I: input lanes represent loading of 10% of total lysates, E: eluate represent proteins eluted from anti-Flag M2 beads, * non-specific IgG bands. **C**, Co-IP probed for SLP2-MICOS interaction with isolated mitochondria from *SLP2* KO stably expressing pMSCVpuro EV (background control) or SLP2-MYC. Co-IP was performed using MYC-Trap agarose beads. I: Input fraction (10% of total lysate), E: Eluate fraction. YME1L was used as a positive interactor of SLP2 whereas Mt-CO2 and HSP60 served as non-interactors. All the MICOS subunits were present in the elution fraction from SLP2-MYC co-ip. **D**, Proximity ligation assay (PLA) in HeLa cells with antibodies against MICOS subunits and SLP2. PLA signals are shown as red spots indicating respective protein interactions. SLP2 alone and Mt-CO2 & SLP2 antibodies were probed as negative controls. **E**. BN-PAGE with isolated mitochondria from WT cells revealed a co-migration pattern of SLP2 with higher molecular weight MICOS complex. **F**. A heatmap and graph represent the normalized occurrence of SLP2 and MICOS subunits in complexome profiling data obtained from Flp-In T-REx HEK293 cells studied previously (Anand et al., 2016). SLP2 co-clustered with high molecular weight MICOS complex around 2000 kDa. **G**. Scaffolding model depicting interaction of SLP2 as an auxiliary MICOS subunits shows that SLP2 provides a scaffold for interaction of MICOS subunits.

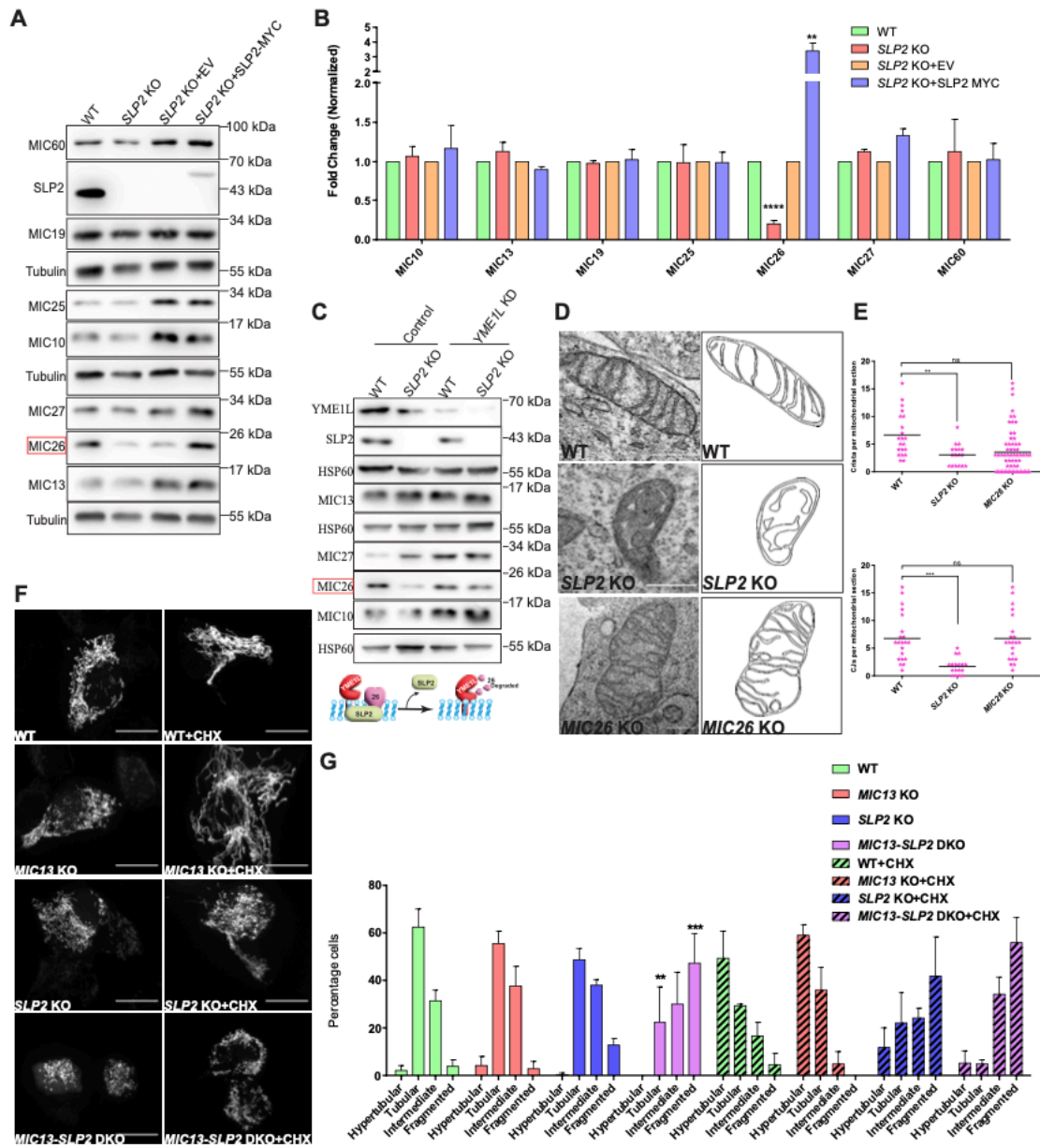


Figure 2

Figure 2. Loss of SLP2 leads to aberrant cristae structure and reduced MIC26 levels. **A**, Steady state levels of MICOS proteins with western blot analysis from WT, *SLP2* KO and *SLP2* KO cells stably expressing pMSCVpuro EV or *SLP2*-MYC. **B**, Western blot quantification depicting relative protein levels. *SLP2* KO was normalized to WT and *SLP2* KO+*SLP2* MYC was normalized to *SLP2* KO+EV samples. Data is represented as mean and standard error of mean. Statistical analysis was performed with one-way ANOVA. *P-value \leq 0.05, **P-value \leq 0.01, ***P-value \leq 0.001. **C**, Western blot analysis of steady state levels of MICOS proteins from WT and *SLP2* KO cells stably expressing pGIPZ-control shRNA or YME1L shRNA (knockdown represented as KD), depicted by a model illustrating the role of SLP2 in stabilizing MIC26 by regulating YME1L-mediated proteolysis. **D**, TEM images from WT, *SLP2* KO and *MIC26* KO cells. *SLP2* KO shows accumulation of swollen cristae, while *MIC26* KO shows interconnected cristae arranged in a honeycomb manner. **E**, Cristae number and CJs per mitochondrial section quantified from TEM images. Statistical analysis was performed with one-way ANOVA. *P-value \leq 0.05, **P-value \leq 0.01, ***P-value \leq 0.001. **F**, Assessment of mitochondrial morphologies from WT, *MIC13* KO, *SLP2* KO and *MIC13*-*SLP2* DKO cells untreated or post treatment with 10 μ M cycloheximide for 2 hours. **G**, Percentage of cells displaying tubular, intermediate, fragmented or hyperfused mitochondria (n= 3). *P-value \leq 0.05, **P-value \leq 0.01, ***P-value \leq 0.001. Data represented as mean with standard error of mean. Scale bar represented as 15 μ m.

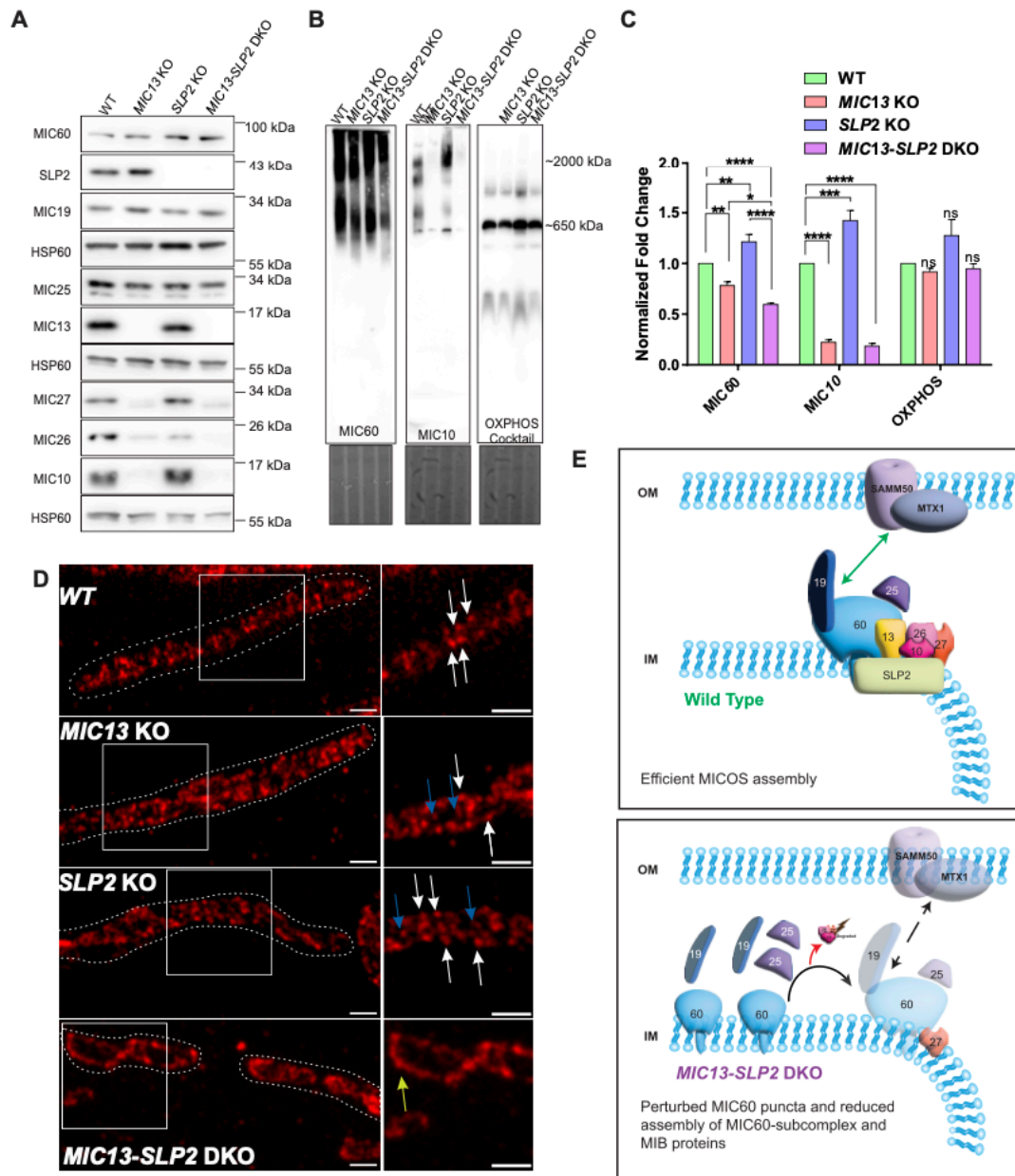


Figure 3

Figure 3. SLP2 and MIC13 synergistically contribute to the assembly and organization of the MIC60-subcomplex. **A**, Assessment of steady state levels of MICOS proteins with western blot from WT, *MIC13* KO, *SLP2* KO and *MIC13-SLP2* DKO cells. **B**, BN-PAGE of isolated mitochondria from WT, *MIC13* KO, *SLP2* KO and *MIC13-SLP2* DKO cells to assess MICOS assembly. *MIC13-SLP2* DKO showed reduced MIC60 assembly in MICOS complex compared to any single KO. **C**, BN-PAGE quantification depicting relative protein assembly levels normalized to Coomassie (MIC60 n=5, MIC10 n=4, OXPHOS n=3). Protein levels are normalized to WT and data is represented as mean and standard error of mean. Statistical analysis was performed with one-way ANOVA. *P-value ≤ 0.05 , **P-value ≤ 0.01 , ***P-value ≤ 0.001 . **D**, STED nanoscopy images from WT, *MIC13* KO, *SLP2* KO and *MIC13-SLP2* DKO cells displaying MIC60 punctae. White arrows indicate individual MIC60 punctae in a rail-like arrangement in WT cells. Arrow heads depict perturbed MIC60 puncta in *MIC13* KO and *SLP2* KO. Yellow arrow with curve depicts dispersed MIC60 puncta in *MIC13-SLP2* DKO cells. **E**, A model depicting that MIC60-subcomplex and MIB assembly is dependent on SLP2-MIC13.

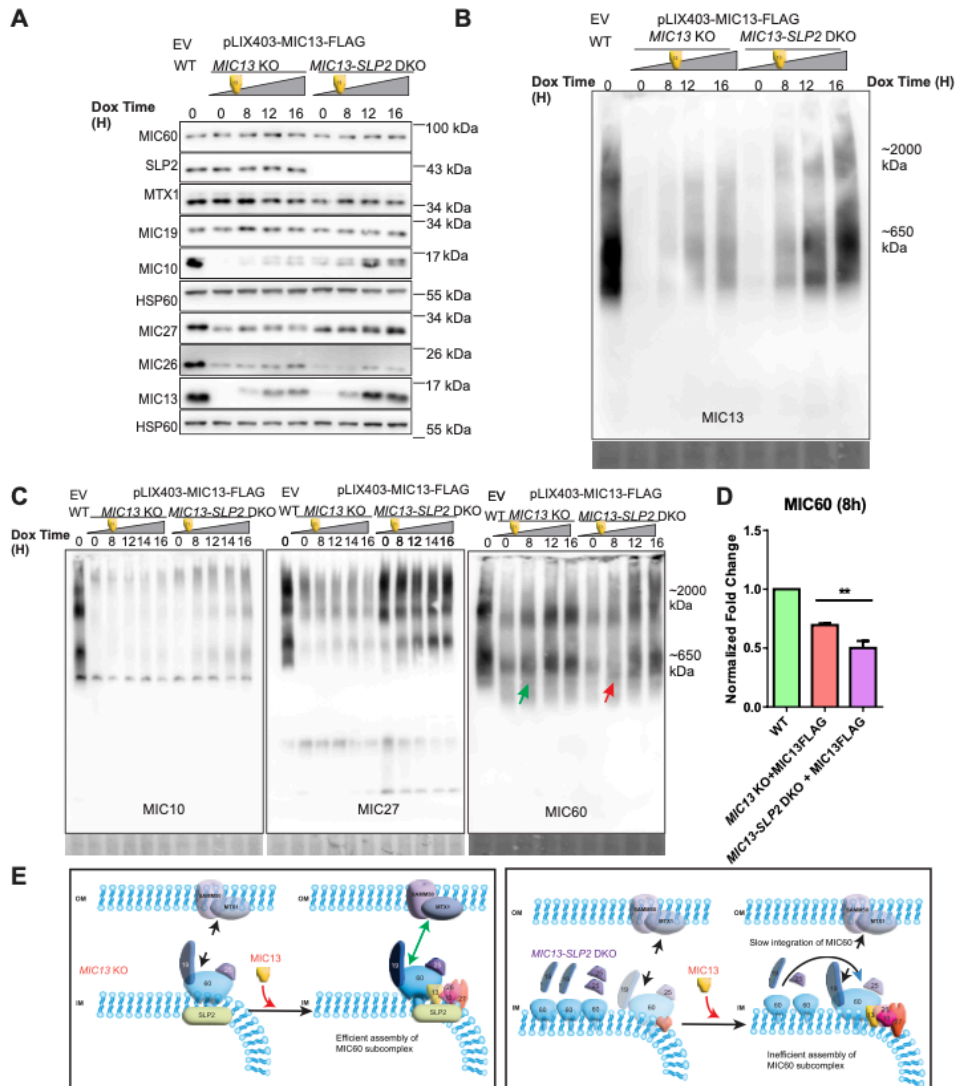


Figure 4

Figure 4. SLP2 specifically regulates assembly kinetics of MIC60. **A**, WT cells stably expressing pLIX403 EV and *MIC13* KO, *MIC13-SLP2* DKO cells stably expressing pLIX403-MIC13-FLAG were treated with 1 µg/ml of doxycycline (Dox) for indicated time points and western blot analysis depicting steady state levels of MICOS proteins upon induction of MIC13-FLAG are shown. **B**, BN-PAGE with isolated mitochondria from WT cells stably expressing pLIX403 EV, and *MIC13* KO and *MIC13-SLP2* DKO cells stably expressing pLIX403-MIC13-FLAG treated with 1 µg/ml of doxycycline (Dox) for indicated time points showing stable incorporation of MIC13-FLAG in MICOS complex. **C**, Blue native PAGE with isolated mitochondria from WT cells stably expressing pLIX403 EV, and *MIC13* KO and *MIC13-SLP2* DKO cells stably expressing pLIX403-MIC13-FLAG treated with 1 µg/ml of Dox for indicated time points was probed for MIC10, MIC27 and MIC60 antibody. It shows that kinetics of MIC60 assembly was dependent on SLP2. **D**. BN-PAGE quantification depicting relative protein assembly levels normalized to Coomassie for the 8 h time point (n= 4). Protein levels are normalized to WT and data is represented as mean and standard error of mean. Statistical analysis was performed with one-way ANOVA. *P-value ≤ 0.05, **P-value ≤ 0.01, ***P-value ≤ 0.001. **E**, A model depicting the assembly kinetics of MIC60 in MICOS complex depends on SLP2.

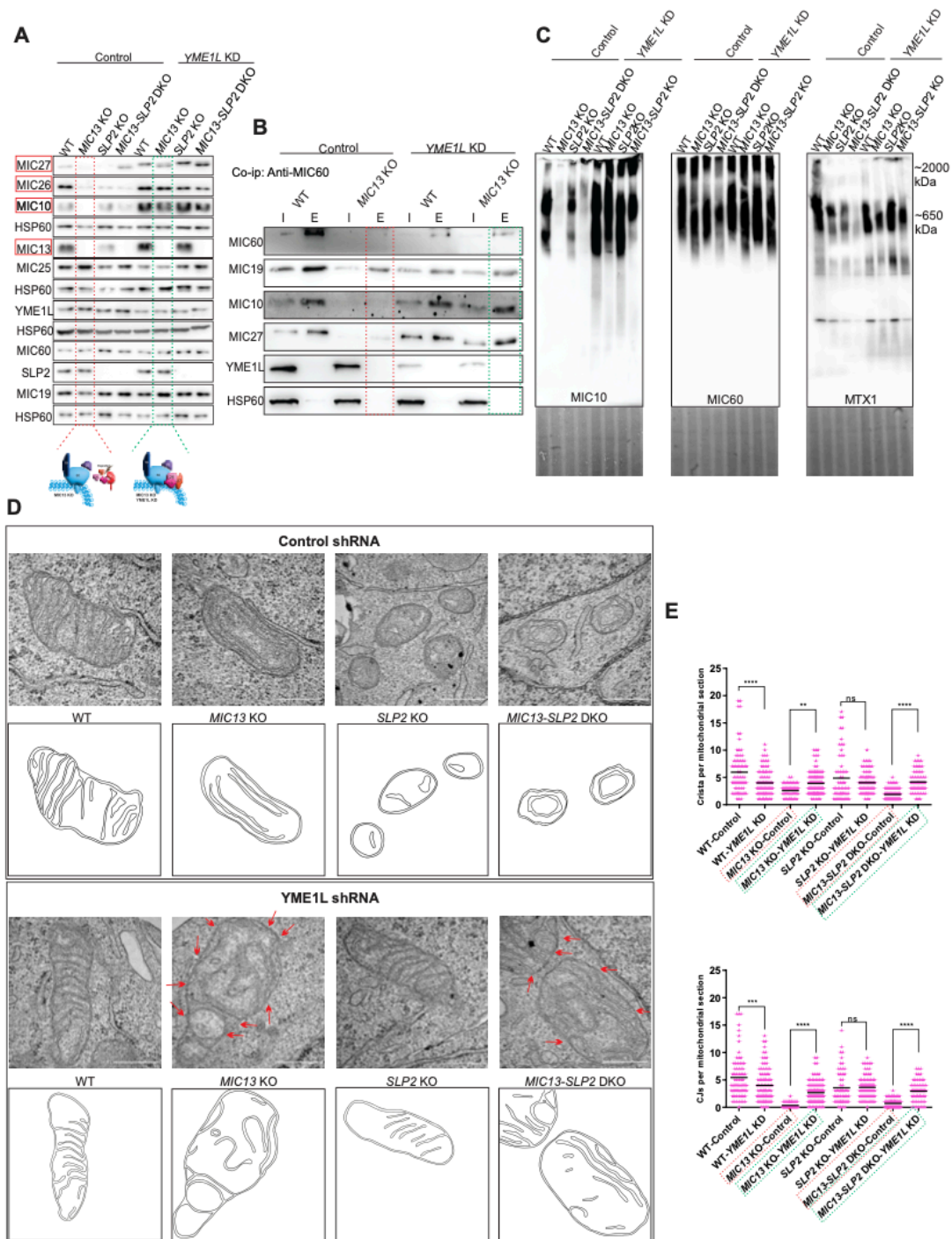


Figure 5

Figure 5. MIC13-YME1L and SLP2-YME1L stabilize MIC10- and MIC60-subcomplex assembly in a co-dependent manner. **A**, WT, *MIC13* KO, *SLP2* KO, *MIC13-SLP2* DKO stably expressing pGIPZ-Control shRNA or pGIPZ-YME1L shRNA (knockdown represented as KD) subjected to western blot to assess steady state levels of MICOS proteins. The levels of MIC10, MIC26 and MIC27 were dependent on YME1L-mediated proteolysis. **B**, The interaction between MIC60 and MIC10 was validated by Co-IP using MIC60 antibody conjugated Protein A sepharose beads in isolated mitochondria from WT, *MIC13* KO cells stably expressing pGIPZ YME1L shRNA or empty vector (EV) pGIPZ as background control. I: input lanes represent loading of 10% of total lysates, E: eluate represent proteins eluted from beads, * non-specific IgG bands. BN-PAGE with isolated mitochondria from WT, *MIC13* KO, *SLP2* KO, *MIC13-SLP2* DKO stably expressing pGIPZ-Control shRNA or pGIPZ- YME1L shRNA. Red arrow indicates downshift of MIC60 and green arrow indicates upshift of MIC60 in BN-PAGE. **C**, Mitochondrial cristae morphology accessed using TEM from WT, *MIC13* KO, *SLP2* KO, *MIC13-SLP2* DKO stably expressing pGIPZ-Control shRNA or pGIPZ-YME1L shRNA. Scale bar represents 0.5 μ m. Red arrows depict CJs in the mitochondrial section showing a partial beneficial effect on cristae morphology upon YME1L depletion. **D**, Quantification of crista and CJs per mitochondrial section. Outliers were removed with Grubbs' method and statistical significance was analysed by one-way ANOVA. *P-value \leq 0.05, **P-value \leq 0.01, ***P-value \leq 0.001.

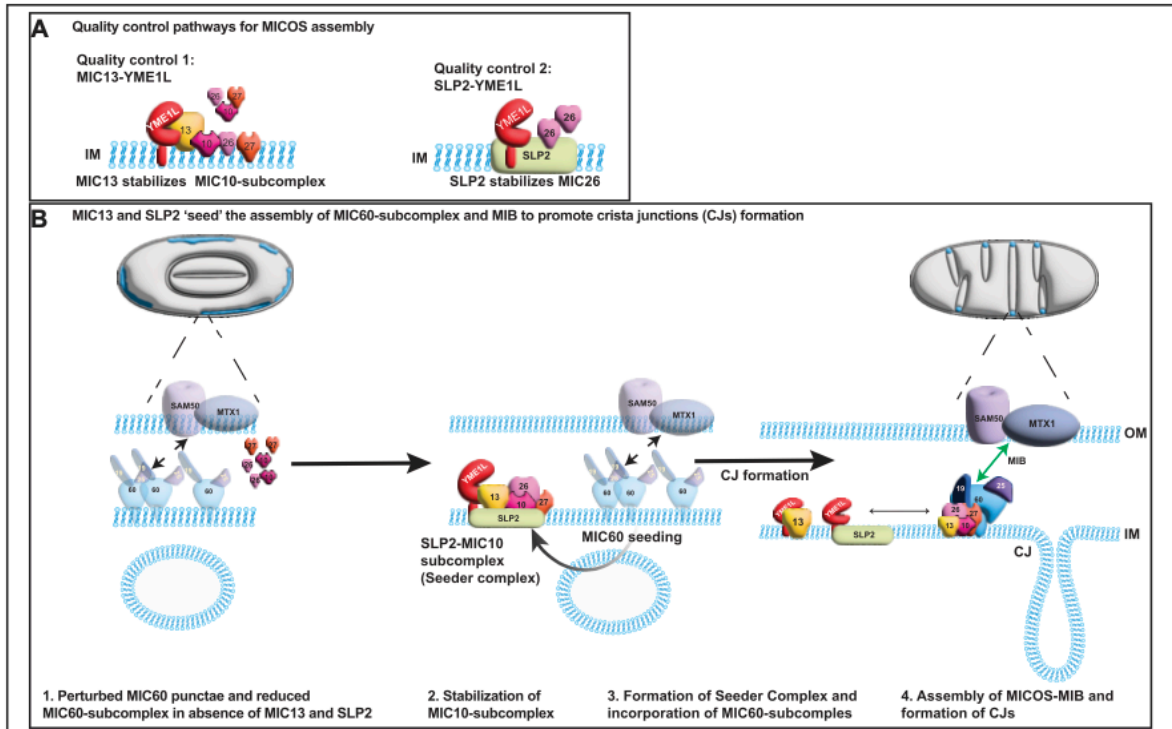
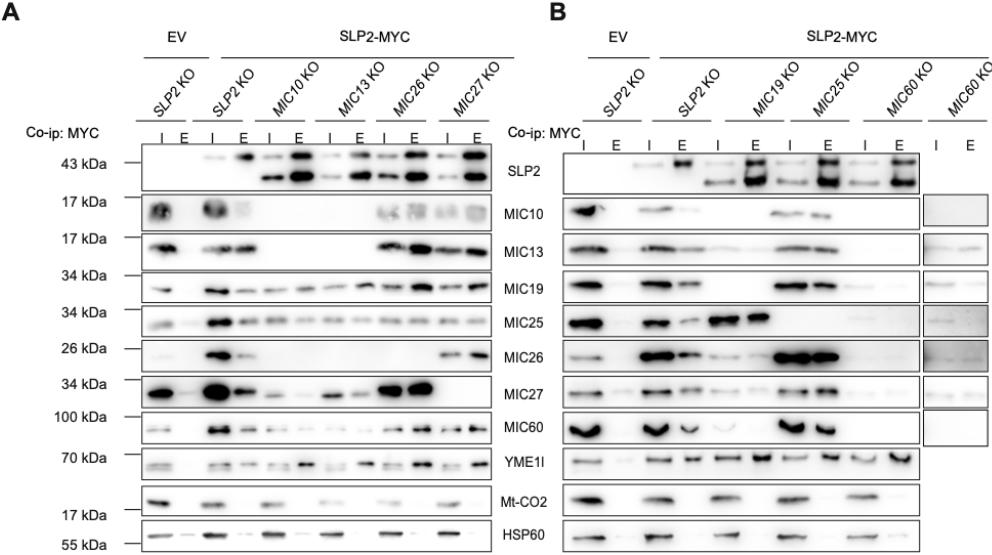


Figure 6

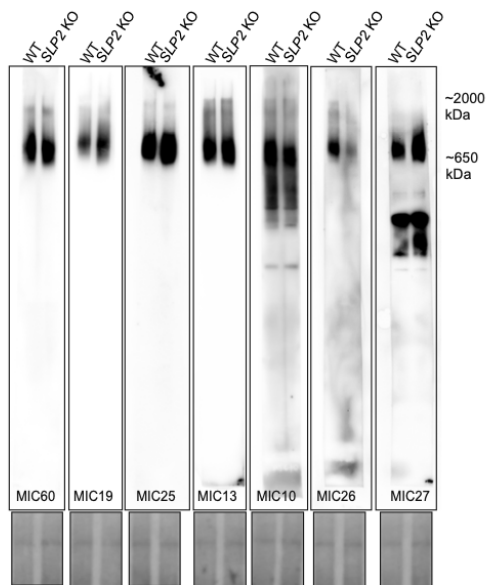
Figure 6. Model for MICOS assembly via 'seeder' complex. A comprehensive schematic model of CJ formation illustrating the novel quality control process orchestrated by the MIC13-YME1L and SLP2-YME1L axis, which facilitates the formation of the SLP2-MIC10-subcomplex, known as the 'seeder' complex. The 'seeder' complex promotes the 'seeding' or assembly of the MIC60-subcomplex and the essential MIB proteins SAMM50 and MTX1, consequently playing a crucial role in defining the formation of MIC60 puncta and the MICOS-MIB complex. This mechanistically promote the formation of CJ and contact between IM and OM.

Supplementary Figures:



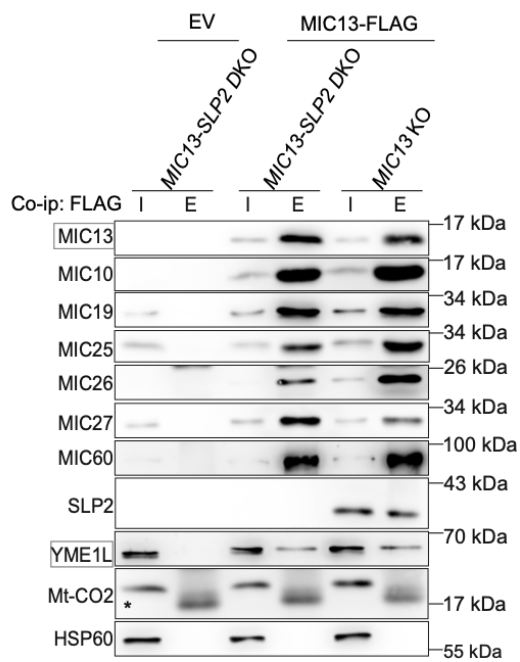
Supplementary Figure 1

Supplementary Figure 1. SLP2 interacts with all MICOS subunits. **A**, Co-ip-western blot analysis from *SLP2* KO or MIC10-subcomplex KO (left) and **B**, *SLP2* KO or MIC60-subcomplex KO (right) stably expressing pMSCVpuro EV or SLP2-MYC showed that SLP2 can stably interact with any remaining MICOS subunits even upon the loss of individual MICOS subunits. Due to low abundance of MICOS proteins in *MIC60* KO cells, overexposed blots were represented showing independent interaction of MIC13, MIC26, MIC27 and MIC19 with SLP2 in absence of MIC60. I: Input fraction (10% of total lysate), E: Eluate fraction.



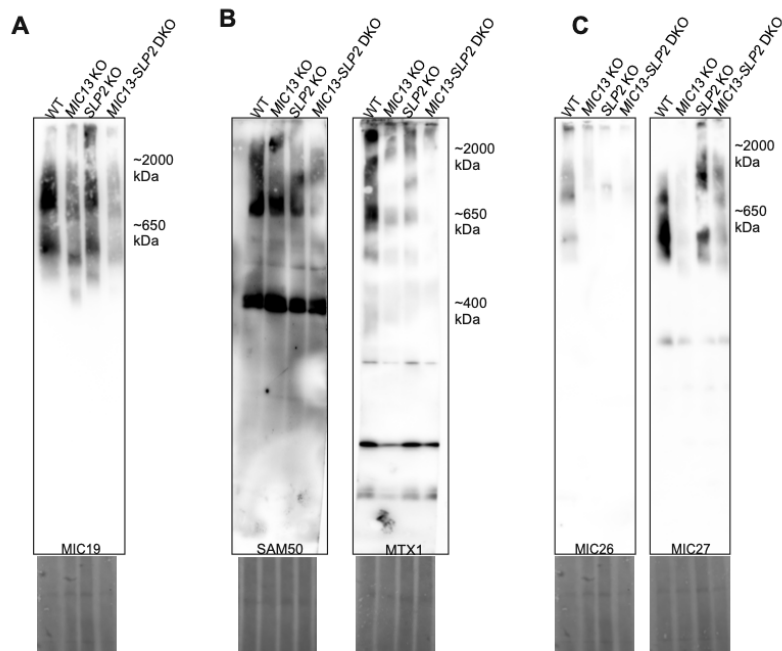
Supplementary Figure 2

Supplementary Figure 2. SLP2 stabilizes MIC26 and facilitates its assembly in MICOS complex. BN-PAGE of isolated mitochondria from WT and *SLP2* KO cells stained for MICOS subunits.



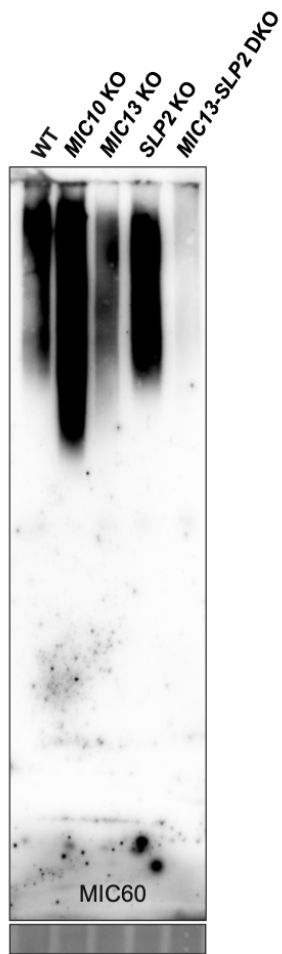
Supplementary Figure 3

Supplementary Figure 3. Co-IP of MIC13-Flag using anti-Flag M2 beads with isolated mitochondria from *MIC13* KO stably expressing pMSCVpuro EV (negative control) and MIC13-Flag expressing in *MIC13* KO and *MIC13-SLP2* DKO cells. The interaction of MIC13 with other MICOS subunits was unaffected upon loss of SLP2. YME1L was found as a novel interactor of MIC13. MIC13 -YME1L interaction is independent of SLP2.



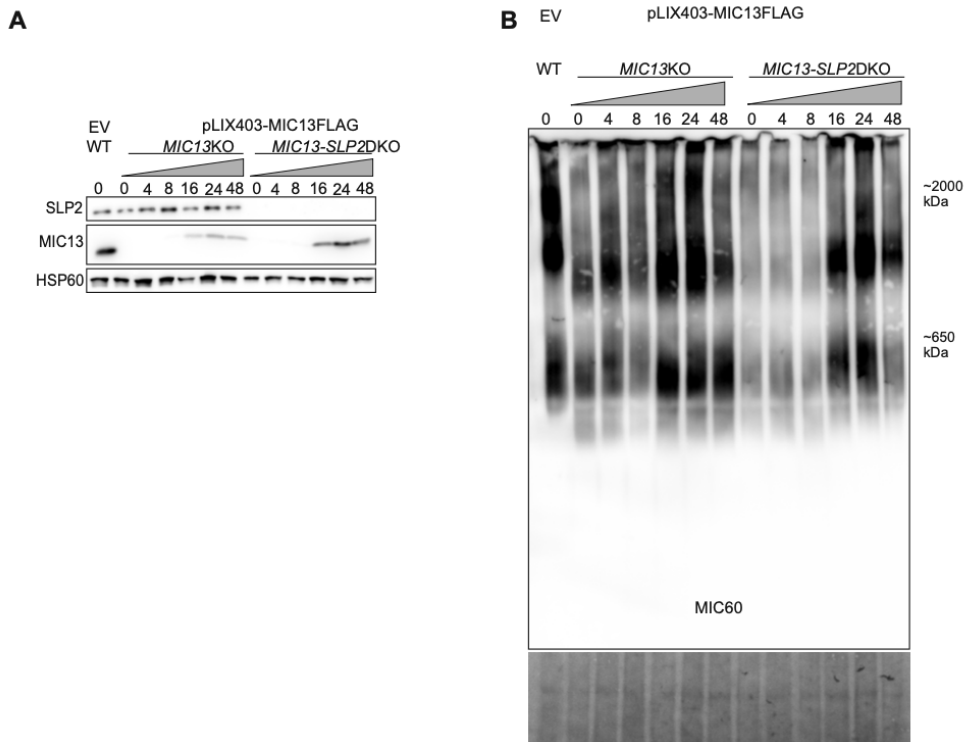
Supplementary Figure 4

Supplementary Figure 4. MIC13-SLP2 cooperatively mediates assembly of MICOS and MIB proteins. **A**, BN-PAGE of isolated mitochondria from WT, *MIC13* KO, *SLP2* KO and *MIC13-SLP2* DKO cells probed for MIC60-subcomplex protein MIC19. **B**, BN-PAGE of isolated mitochondria from WT, *MIC13* KO, *SLP2* KO and *MIC13-SLP2* DKO cells probed for MIC60-subcomplex protein MIC19. **C**, BN-PAGE of isolated mitochondria from WT, *MIC13* KO, *SLP2* KO and *MIC13-SLP2* DKO cells probed for MIB proteins SAMM50 and MTX1. **C**, BN-PAGE of isolated mitochondria from WT, *MIC13* KO, *SLP2* KO and *MIC13-SLP2* DKO cells probed for MIC10-subcomplex protein MIC27.



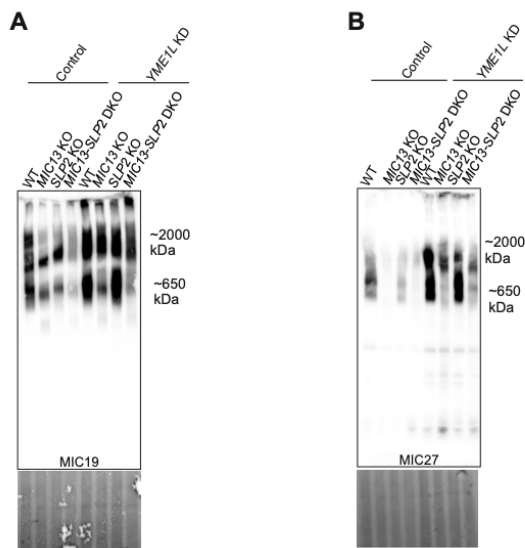
Supplementary Figure 5

Supplementary Figure 5. MIC60 assembly is reduced in *MIC13-SLP2* DKO and not in *MIC10* KO. BN-PAGE of isolated mitochondria from WT, *MIC10* KO, *MIC13* KO, *SLP2* KO and *MIC13-SLP2* DKO cells probed for MIC60.



Supplementary Figure 6

Supplementary Figure 6. SLP2 specifically regulates assembly kinetics of MIC60. A, WT cells stably expressing pLIX403 EV and *MIC13* KO, *MIC13-SLP2* DKO cells stably expressing pLIX403-MIC13-FLAG were treated with 1 µg/ml of doxycycline (Dox) for indicated time points. **B,** Blue native PAGE with isolated mitochondria from WT cells stably expressing pLIX403 EV, and *MIC13* KO and *MIC13-SLP2* DKO cells stably expressing pLIX403-MIC13-FLAG treated with 1 µg/ml of Dox for indicated time points was probed for MIC60 antibody. It shows that kinetics of MIC60 assembly was dependent on SLP2.



Supplementary Figure 7

Supplementary Figure 7. MIC13-YME1L and SLP2-YME1L stabilize MIC10- and MIC60-subcomplex assembly in a co-dependent manner. A, BN-PAGE of isolated mitochondria from WT, *MIC13* KO, *SLP2* KO and *MIC13-SLP2* DKO cells expressing pGIPZ YME1L shRNA or EV pGIPZ probed for MIC10-subcomplex protein MIC27. **B,** BN-PAGE of isolated mitochondria from WT, *MIC13* KO, *SLP2* KO and *MIC13-SLP2* DKO cells expressing pGIPZ YME1L shRNA or EV pGIPZ probed for MIC60-subcomplex protein MIC19.

AUTHOR CONTRIBUTIONS

Ritam Naha: Investigation, methodology, data curation, formal analysis, visualization, writing—original draft, writing—review and editing.

Rebecca Strohm: Investigation, methodology, data curation, formal analysis.

Jennifer Urbach: Investigation, methodology, formal analysis.

Ilka Wittig: investigation, methodology, formal analysis, data curation.

Arun Kumar Kondadi: formal analysis, supervision, validation, funding acquisition, writing—review and editing.

Andreas S. Reichert: supervision, funding acquisition, writing—review and editing.

Ruchika Anand: conceptualization, data curation, formal analysis, supervision, methodology, funding acquisition, project administration, writing—original draft, writing—review and editing.

Acknowledgements

Authors would like to thank Andrea Borchardt, Tanja Portugall for their technical assistance in cloning and electron microscopy. We further thank Anny Garces Palacio as student assistant for performing microscopy experiments. Electron microscopy was performed at the Core facility for electron microscopy (CFEM) at the medical faculty of the Heinrich Heine University Düsseldorf. The STED imaging experiments were performed at the Centre for Advanced Imaging (CAi) at Heinrich Heine University Düsseldorf.

The research was supported by funding from Medical faculty of Heinrich Heine University Düsseldorf, Foko-02/2015 (RA & ASR), FoKo-2020-71 (RA), FoKo 2022-11 (AKK) and Deutsche Forschungsgemeinschaft (DFG) grant, AN 1440/3-1 (RA), AN 1440/4-1 (RA), KO 6519/1-1 (AKK) and SFB 1208 project B12 (ID 267205415) to ASR.

Declaration of interests

The authors declare no competing interests.

References

- An, J., Shi, J., He, Q., Lui, K., Liu, Y., Huang, Y., & Sheikh, M. S. (2012). CHCM1/CHCHD6, novel mitochondrial protein linked to regulation of mitofilin and mitochondrial cristae morphology. *J Biol Chem*, 287(10), 7411-7426. <https://doi.org/10.1074/jbc.M111.277103>
- Anand, R., Kondadi, A. K., Meisterknecht, J., Golombek, M., Nortmann, O., Riedel, J., Peifer-Weiss, L., Brocke-Ahmadinejad, N., Schlutermann, D., Stork, B., Eichmann, T. O., Wittig, I., & Reichert, A. S. (2020). MIC26 and MIC27 cooperate to regulate cardiolipin levels and the landscape of OXPHOS complexes. *Life Sci Alliance*, 3(10). <https://doi.org/10.26508/lsa.202000711>
- Anand, R., Reichert, A. S., & Kondadi, A. K. (2021). Emerging Roles of the MICOS Complex in Cristae Dynamics and Biogenesis. *Biology (Basel)*, 10(7). <https://doi.org/10.3390/biology10070600>
- Anand, R., Strecker, V., Urbach, J., Wittig, I., & Reichert, A. S. (2016). Mic13 Is Essential for Formation of Crista Junctions in Mammalian Cells. *PLoS One*, 11(8), e0160258. <https://doi.org/10.1371/journal.pone.0160258>
- Barbot, M., Jans, D. C., Schulz, C., Denkert, N., Kroppen, B., Hoppert, M., Jakobs, S., & Meinecke, M. (2015). Mic10 oligomerizes to bend mitochondrial inner membranes at cristae junctions. *Cell Metab*, 21(5), 756-763. <https://doi.org/10.1016/j.cmet.2015.04.006>

- Beninca, C., Zanette, V., Brischiari, M., Johnson, M., Reyes, A., Valle, D. A. D., A, J. R., Degiorgi, A., Yeates, A., Telles, B. A., Prudent, J., Baruffini, E., ML, S. F. S., RL, R. d. S., Fernandez-Vizarra, E., A, J. W., & Zeviani, M. (2021). Mutation in the MICOS subunit gene APOO (MIC26) associated with an X-linked recessive mitochondrial myopathy, lactic acidosis, cognitive impairment and autistic features. *J Med Genet*, *58*(3), 155-167. <https://doi.org/10.1136/jmedgenet-2020-106861>
- Bock-Bierbaum, T., Funck, K., Wollweber, F., Lisicki, E., von der Malsburg, K., von der Malsburg, A., Laborenz, J., Noel, J. K., Hessenberger, M., Jungbluth, S., Bernert, C., Kunz, S., Riedel, D., Lilie, H., Jakobs, S., van der Laan, M., & Daumke, O. (2022). Structural insights into crista junction formation by the Mic60-Mic19 complex. *Sci Adv*, *8*(35), eabo4946. <https://doi.org/10.1126/sciadv.abo4946>
- Bohnert, M., Zerbes, R. M., Davies, K. M., Muhleip, A. W., Rampelt, H., Horvath, S. E., Boenke, T., Kram, A., Perschil, I., Veenhuis, M., Kuhlbrandt, W., van der Klei, I. J., Pfanner, N., & van der Laan, M. (2015). Central role of Mic10 in the mitochondrial contact site and cristae organizing system. *Cell Metab*, *21*(5), 747-755. <https://doi.org/10.1016/j.cmet.2015.04.007>
- Chiu, J., Tillett, D., Dawes, I. W., & March, P. E. (2008). Site-directed, Ligase-Independent Mutagenesis (SLIM) for highly efficient mutagenesis of plasmids greater than 8kb. *J Microbiol Methods*, *73*(2), 195-198. <https://doi.org/10.1016/j.mimet.2008.02.013>
- Christie, D. A., Lemke, C. D., Elias, I. M., Chau, L. A., Kirchhof, M. G., Li, B., Ball, E. H., Dunn, S. D., Hatch, G. M., & Madrenas, J. (2011). Stomatolipin 2 binds cardiolipin and regulates mitochondrial biogenesis and function. *Mol Cell Biol*, *31*(18), 3845-3856. <https://doi.org/10.1128/MCB.05393-11>
- Godiker, J., Gruneberg, M., DuChesne, I., Reunert, J., Rust, S., Westermann, C., Wada, Y., Classen, G., Langhans, C. D., Schlingmann, K. P., Rodenburg, R. J., Pohlmann, R., & Marquardt, T. (2018). QIL1-dependent assembly of MICOS complex-lethal mutation in C19ORF70 resulting in liver disease and severe neurological retardation. *J Hum Genet*, *63*(6), 707-716. <https://doi.org/10.1038/s10038-018-0442-y>
- Guarani, V., Jardel, C., Chretien, D., Lombes, A., Benit, P., Labasse, C., Lacene, E., Bourillon, A., Imbard, A., Benoist, J. F., Dorboz, I., Gilleron, M., Goetzman, E. S., Gaignard, P., Slama, A., Elmaleh-Berges, M., Romero, N. B., Rustin, P., Ogier de Baulny, H., . . . Schiff, M. (2016). QIL1 mutation causes MICOS disassembly and early onset fatal mitochondrial encephalopathy with liver disease. *Elife*, *5*. <https://doi.org/10.7554/eLife.17163>
- Guarani, V., McNeill, E. M., Paulo, J. A., Huttlin, E. L., Frohlich, F., Gygi, S. P., Van Vactor, D., & Harper, J. W. (2015). QIL1 is a novel mitochondrial protein required for MICOS complex stability and cristae morphology. *Elife*, *4*. <https://doi.org/10.7554/eLife.06265>
- Hessenberger, M., Zerbes, R. M., Rampelt, H., Kunz, S., Xavier, A. H., Purfurst, B., Lilie, H., Pfanner, N., van der Laan, M., & Daumke, O. (2017). Regulated membrane remodeling by Mic60 controls formation of mitochondrial crista junctions. *Nat Commun*, *8*, 15258. <https://doi.org/10.1038/ncomms15258>
- Huynen, M. A., Muhlmeister, M., Gotthardt, K., Guerrero-Castillo, S., & Brandt, U. (2016). Evolution and structural organization of the mitochondrial contact site (MICOS) complex and the mitochondrial intermembrane space bridging (MIB) complex. *Biochim Biophys Acta*, *1863*(1), 91-101. <https://doi.org/10.1016/j.bbamcr.2015.10.009>
- Jans, D. C., Wurm, C. A., Riedel, D., Wenzel, D., Stagge, F., Deckers, M., Rehling, P., & Jakobs, S. (2013). STED super-resolution microscopy reveals an array of MINOS clusters along human mitochondria. *Proc Natl Acad Sci U S A*, *110*(22), 8936-8941. <https://doi.org/10.1073/pnas.1301820110>
- Kondadi, A. K., Anand, R., Hansch, S., Urbach, J., Zobel, T., Wolf, D. M., Segawa, M., Liesa, M., Shirihai, O. S., Weidtkamp-Peters, S., & Reichert, A. S. (2020). Cristae undergo continuous cycles of membrane remodelling in a MICOS-dependent manner. *EMBO Rep*, *21*(3), e49776. <https://doi.org/10.15252/embr.201949776>
- Kondadi, A. K., Anand, R., & Reichert, A. S. (2020). Cristae Membrane Dynamics - A Paradigm Change. *Trends Cell Biol*, *30*(12), 923-936. <https://doi.org/10.1016/j.tcb.2020.08.008>

- Kondadi, A. K., & Reichert, A. S. (2024). Mitochondrial Dynamics at Different Levels: From Cristae Dynamics to Interorganellar Cross Talk. *Annu Rev Biophys*. <https://doi.org/10.1146/annurev-biophys-030822-020736>
- Kulak, N. A., Pichler, G., Paron, I., Nagaraj, N., & Mann, M. (2014). Minimal, encapsulated proteomic-sample processing applied to copy-number estimation in eukaryotic cells. *Nat Methods*, 11(3), 319-324. <https://doi.org/10.1038/nmeth.2834>
- Li, H., Ruan, Y., Zhang, K., Jian, F., Hu, C., Miao, L., Gong, L., Sun, L., Zhang, X., Chen, S., Chen, H., Liu, D., & Song, Z. (2016). Mic60/Mitofilin determines MICOS assembly essential for mitochondrial dynamics and mtDNA nucleoid organization. *Cell Death Differ*, 23(3), 380-392. <https://doi.org/10.1038/cdd.2015.102>
- Mannella, C. A., Lederer, W. J., & Jafri, M. S. (2013). The connection between inner membrane topology and mitochondrial function [Research Support, N.I.H., Extramural Research Support, Non-U.S. Gov't Review]. *J Mol Cell Cardiol*, 62, 51-57. <https://doi.org/10.1016/j.yjmcc.2013.05.001>
- Marco-Hernández, A. V., Tomás-Vila, M., Montoya-Filardi, A., Barranco-González, H., Vilchez Padilla, J. J., Azorín, I., Smeyers Dura, P., Monfort-Membrado, S., Pitarch-Castellano, I., & Martínez-Castellano, F. (2021). Mitochondrial developmental encephalopathy with bilateral optic neuropathy related to homozygous variants in IMMT gene. *Clin Genet*. <https://doi.org/10.1111/cge.14093>
- Monzel, A. S., Enríquez, J. A., & Picard, M. (2023). Multifaceted mitochondria: moving mitochondrial science beyond function and dysfunction. *Nat Metab*, 5(4), 546-562. <https://doi.org/10.1038/s42255-023-00783-1>
- Mukherjee, I., Ghosh, M., & Meinecke, M. (2021). MICOS and the mitochondrial inner membrane morphology - when things get out of shape. *FEBS Lett*, 595(8), 1159-1183. <https://doi.org/10.1002/1873-3468.14089>
- Olsen, V. J., Godoy, D. M. F. L., Li, G., Macek, B., Mortensen, P., Pesch, R., Makarov, A., Lange, O., Horning, S., & Mann, M. (2005). Parts per Million Mass Accuracy on an Orbitrap Mass Spectrometer via Lock Mass Injection into a C-trap. *Molecular & Cellular Proteomics*, 4(12), 2010-2021. <https://doi.org/10.1074/mcp.T500030-MCP200>
- Ott, C., Dorsch, E., Fraunholz, M., Straub, S., & Kozjak-Pavlovic, V. (2015). Detailed analysis of the human mitochondrial contact site complex indicate a hierarchy of subunits. *PLoS One*, 10(3), e0120213. <https://doi.org/10.1371/journal.pone.0120213>
- Peifer-Weiß, L., Kurban, M., David, C., Lubeck, M., Kondadi, A. K., Nemer, G., Reichert, A. S., & Anand, R. (2023). A X-linked nonsense APOO/MIC26 variant causes a lethal mitochondrial disease with progeria-like phenotypes. *Clin Genet*. <https://doi.org/10.1111/cge.14420>
- Perkins, G., Renken, C., Martone, M. E., Young, S. J., Ellisman, M., & Frey, T. (1997). Electron tomography of neuronal mitochondria: three-dimensional structure and organization of cristae and membrane contacts. *J Struct Biol*, 119(3), 260-272. <https://doi.org/10.1006/jsbi.1997.3885>
- Russell, B. E., Whaley, K. G., Bove, K. E., Labilloy, A., Lombardo, R. C., Hopkin, R. J., Leslie, N. D., Prada, C., Assouline, Z., Barcia, G., Bouchereau, J., Chomton, M., Debray, D., Dorboz, I., Durand, P., Gaignard, P., Habes, D., Jardel, C., Labarthe, F., . . . Schiff, M. (2019). Expanding and Underscoring the Hepato-Encephalopathic Phenotype of QIL1/MIC13. *Hepatology*, 70(3), 1066-1070. <https://doi.org/10.1002/hep.30627>
- Sakowska, P., Jans, D. C., Mohanraj, K., Riedel, D., Jakobs, S., & Chacinska, A. (2015). The Oxidation Status of Mic19 Regulates MICOS Assembly. *Mol Cell Biol*, 35(24), 4222-4237. <https://doi.org/10.1128/MCB.00578-15>
- Scorrano, L., Ashiya, M., Buttler, K., Weiler, S., Oakes, S. A., Mannella, C. A., & Korsmeyer, S. J. (2002). A distinct pathway remodels mitochondrial cristae and mobilizes cytochrome c during apoptosis. *Dev Cell*, 2(1), 55-67. [https://doi.org/10.1016/s1534-5807\(01\)00116-2](https://doi.org/10.1016/s1534-5807(01)00116-2)
- Stephan, T., Brüser, C., Deckers, M., Steyer, A. M., Balzarotti, F., Barbot, M., Behr, T. S., Heim, G., Hübner, W., Ilgen, P., Lange, F., Pacheu-Grau, D., Pape, J. K., Stoldt, S., Huser, T., Hell, S. W., Möbius, W., Rehling, P., Riedel, D., & Jakobs, S. (2020). MICOS assembly controls mitochondrial inner membrane remodeling and crista junction

- redistribution to mediate cristae formation. *EMBO J*, 39(14), e104105. <https://doi.org/10.15252/emboj.2019104105>
- Stoldt, S., Stephan, T., Jans, D. C., Bruser, C., Lange, F., Keller-Findeisen, J., Riedel, D., Hell, S. W., & Jakobs, S. (2019). Mic60 exhibits a coordinated clustered distribution along and across yeast and mammalian mitochondria. *Proc Natl Acad Sci U S A*, 116(20), 9853-9858. <https://doi.org/10.1073/pnas.1820364116>
- Tang, J., Zhang, K., Dong, J., Yan, C., Hu, C., Ji, H., Chen, L., Chen, S., Zhao, H., & Song, Z. (2020). Sam50-Mic19-Mic60 axis determines mitochondrial cristae architecture by mediating mitochondrial outer and inner membrane contact. *Cell Death Differ*, 27(1), 146-160. <https://doi.org/10.1038/s41418-019-0345-2>
- Tarasenko, D., Barbot, M., Jans, D. C., Kroppen, B., Sadowski, B., Heim, G., Mobius, W., Jakobs, S., & Meinecke, M. (2017). The MICOS component Mic60 displays a conserved membrane-bending activity that is necessary for normal cristae morphology. *J Cell Biol*, 216(4), 889-899. <https://doi.org/10.1083/jcb.201609046>
- Tondera, D., Grandemange, S., Jourdain, A., Karbowski, M., Mattenberger, Y., Herzig, S., Da Cruz, S., Clerc, P., Raschke, I., Merkwirth, C., Ehses, S., Krause, F., Chan, D. C., Alexander, C., Bauer, C., Youle, R., Langer, T., & Martinou, J. C. (2009). SLP-2 is required for stress-induced mitochondrial hyperfusion. *EMBO J*, 28(11), 1589-1600. <https://doi.org/10.1038/emboj.2009.89>
- Tsai, P. I., Lin, C. H., Hsieh, C. H., Papakyrikos, A. M., Kim, M. J., Napolioni, V., Schoor, C., Couthouis, J., Wu, R. M., Wszolek, Z. K., Winter, D., Greicius, M. D., Ross, O. A., & Wang, X. (2018). PINK1 Phosphorylates MIC60/Mitofilin to Control Structural Plasticity of Mitochondrial Crista Junctions. *Mol Cell*, 69(5), 744-756 e746. <https://doi.org/10.1016/j.molcel.2018.01.026>
- Urbach, J., Kondadi, A. K., David, C., Naha, R., Deinert, K., Reichert, A. S., & Anand, R. (2021). Conserved GxxxG and WN motifs of MIC13 are essential for bridging two MICOS subcomplexes. *Biochim Biophys Acta Biomembr*, 1863(12), 183683. <https://doi.org/10.1016/j.bbamem.2021.183683>
- van der Laan, M., Horvath, S. E., & Pfanner, N. (2016). Mitochondrial contact site and cristae organizing system. *Curr Opin Cell Biol*, 41, 33-42. <https://doi.org/10.1016/j.ceb.2016.03.013>
- Viana, M. P., Levytsky, R. M., Anand, R., Reichert, A. S., & Khalimonchuk, O. (2021). Protease OMA1 modulates mitochondrial bioenergetics and ultrastructure through dynamic association with MICOS complex. *iScience*, 24(2), 102119. <https://doi.org/10.1016/j.isci.2021.102119>
- Wai, T., Saita, S., Nolte, H., Muller, S., Konig, T., Richter-Dennerlein, R., Sprenger, H. G., Madrenas, J., Muhlmeister, M., Brandt, U., Kruger, M., & Langer, T. (2016). The membrane scaffold SLP2 anchors a proteolytic hub in mitochondria containing PARL and the i-AAA protease YME1L. *EMBO Rep*, 17(12), 1844-1856. <https://doi.org/10.15252/embr.201642698>
- Xie, J., Marusich, M. F., Souda, P., Whitelegge, J., & Capaldi, R. A. (2007). The mitochondrial inner membrane protein mitofilin exists as a complex with SAM50, metaxins 1 and 2, coiled-coil-helix coiled-coil-helix domain-containing protein 3 and 6 and DnaJC11. *FEBS Lett*, 581(18), 3545-3549. <https://doi.org/10.1016/j.febslet.2007.06.052>
- Zeharia, A., Friedman, J. R., Tobar, A., Saada, A., Konen, O., Fellig, Y., Shaag, A., Nunnari, J., & Elpeleg, O. (2016). Mitochondrial hepato-encephalopathy due to deficiency of QIL1/MIC13 (C19orf70), a MICOS complex subunit. *Eur J Hum Genet*, 24(12), 1778-1782. <https://doi.org/10.1038/ejhg.2016.83>
- Zerbes, R. M., Hoss, P., Pfanner, N., van der Laan, M., & Bohnert, M. (2016). Distinct Roles of Mic12 and Mic27 in the Mitochondrial Contact Site and Cristae Organizing System. *J Mol Biol*, 428(8), 1485-1492. <https://doi.org/10.1016/j.jmb.2016.02.031>
- Zerbes, R. M., van der Klei, I. J., Veenhuis, M., Pfanner, N., van der Laan, M., & Bohnert, M. (2012). Mitofilin complexes: conserved organizers of mitochondrial membrane architecture [Research Support, Non-U.S. Gov't Review]. *Biol Chem*, 393(11), 1247-1261. <https://doi.org/10.1515/hsz-2012-0239>

6 Discussion

MIC13 is an integral component of MICOS assembly, first identified in 2015 linking its mutations to fatal pathophysiological condition called mitochondrial hepato-encephalopathy. Patients with MIC13 deficiencies exhibit a range of metabolic and neurodevelopmental disorders (Guarani et al., 2015). Loss of MIC13 results in loss of MIC10 subcomplex consisting of two other proteins, MIC26 and MIC27, displaying aberrant cristae morphology lacking CJs. Assembly of MIC60 subcomplex, consisting of MIC19 and MIC25, remains conclusively unaffected at the protein levels, however, a shift in molecular weight in their migration pattern is observed upon analysis of the native protein complex (Anand et al., 2016; Guarani et al., 2015; Urbach et al., 2021). Our study provides a mechanistic overview of how MIC13 stabilizes the MIC10 subcomplex, and through an extensive exploration of the MIC13 interactome, we unveil SLP2 as a novel interaction partner of MIC13, offering crucial insights into the intricate processes governing MICOS assembly and cristae morphogenesis at distinct steps.

The cumulative findings of these studies present an elaborate depiction of mitochondrial IM organization, centered around the role of MIC13 in stabilizing the MIC10 subcomplex, with its WN and GxxxG motifs essential for the maintenance of mitochondrial cristae. MIC13 acts as a crucial modulator, protecting the MIC10 subcomplex from YME1L-mediated proteolytic degradation, thereby preserving the structural and functional integrity of mitochondria. Progressing further, SLP2 is introduced as a novel player in cristae morphogenesis, exerting a regulatory effect on the stability of MIC26, another MICOS component integral to mitochondrial morphology and the orchestration of metabolic responses to nutrient fluctuations.

Within the cellular metabolic context, MIC26 emerges as a pivotal regulator that adjusts mitochondrial function to meet cellular energy demands, especially under varying glucose conditions. It plays a crucial role in metabolic adaptation, influencing lipid metabolism, and affecting the oxidative phosphorylation system in response to the nutritional status of the cell. Integrating these insights, the 'seeder model' proposes that MIC10-subcomplex, stabilized by MIC13, and SLP2 are indispensable for the correct assembly of the MIC60 subcomplex and MIB complex, a key contributor to mitochondrial cristae structure. This model emphasizes their synergistic function in orchestrating the assembly of the MICOS complex, essential for mitochondrial morphology and the establishment of CJs, providing a sophisticated understanding of the molecular basis of mitochondrial architecture and its implications for mitochondrial-related pathologies.

6.1. MIC13 stabilizes MIC10 subcomplex with its conserved WN and GxxxG motif

In our study (Urbach et al., 2021), we elucidate the critical role of MIC13, a pivotal subunit of the MICOS complex implicated in infantile lethal mitochondrial hepato-encephalopathy, by systematically analyzing deletion variants across its sequence. We identify those specific regions, including the N-terminus and an area between amino acids 84 and 103, are crucial for MIC13's interaction with other MICOS subunits and the maintenance of normal cristae structure, crucial for mitochondrial function. Furthermore, through mutational analysis, we highlight the significance of two motifs in MIC13- the GxxxG motif in the N-terminus and the WN motif in the middle region. These motifs are vital for MIC13 stability, MIC10-subcomplex association, interactions with other MICOS components, and cristae morphology. The conserved WN motif, likely contributing to an amphipathic helix, and the GxxxG motif, a known dimerization element involved in protein-protein interactions within transmembrane domains, play crucial roles in the correct assembly of MICOS (Senes et al., 2000; Unterreitmeier et al., 2007). This GxxxG motif, recognized for its capacity to facilitate dimerization, may facilitate interactions not only within MIC13 itself but also potentially with other transmembrane proteins. Additionally, our study underscores that MIC13's crucial role, mediated by the conserved GxxxG and WN motifs, is highly conserved across species (Huynen et al., 2016), emphasizing their importance in facilitating interactions with other MICOS components and ensuring proper MICOS assembly. In summary, our findings shed light on the vital roles of these conserved motifs within MIC13, unveiling a model where MIC13 plays a pivotal role stabilizing MIC10-subcomplex, furthering our understanding of MICOS assembly and its implications for individuals with MIC13 deficiency.

6.2. MIC13 stabilizes MIC10 subcomplex from YME1L mediated proteolysis

MIC13, being an integral component of MICOS complex, significantly influences cristae morphology by stabilizing the MIC10 subcomplex (Anand et al., 2016; Guarani et al., 2015; Urbach et al., 2021). This stabilization is crucial as cristae are the sites of ATP synthesis, the energy currency of the cell. The absence of MIC13 leads to a cascade of structural mitochondrial defects, primarily due to the destabilization of the MIC10 subcomplex, which is otherwise protected from degradation by the protease YME1L, as evident from this study (Naha et al., 2023).

In *MIC13* KO cells, the MIC10 becomes vulnerable to the protease YME1L, resulting in its complete degradation and in the loss of cristae and CJs. MIC13's role is thus highlighted here as a regulator of YME1L, ensuring that the protease does not target the MIC10 subcomplex for degradation under normal conditions. When YME1L activity is suppressed in *MIC13* KO

cells, there is a notable increase in MIC10 levels, suggesting that YME1L directly mediates MIC10 degradation and that MIC13 acts as a checkpoint inhibitor of this process.

The restoration of MIC10 levels upon YME1L downregulation in MIC13KO cells leads not only to the assembly of MIC10 subcomplex but extended to the reformation of cristae and CJs. Consistent with previous findings where overexpression of MIC10 in MIC13 depleted cells could partially rescue CJs (Guarani et al., 2015). This demonstrates that MIC13's primary role is not "bridging" of the MIC10 and MIC60 subcomplexes per se, but in maintaining the stability of these structures by modulating the proteolytic activity of YME1L, as evident from the assembly of MIC10 subcomplex and interaction of MIC10 with MIC60 in *MIC13* KO cells upon YME1L depletion. The restoration also provides a mechanistic insight into how MIC13 affects mitochondrial ultrastructure and establishes a direct link between MIC13, YME1L-mediated proteolysis, and mitochondrial morphology.

The functional interplay between MIC13 and YME1L extends beyond mere stabilization; it points to a quality control mechanism within the mitochondria that is central to maintaining the integrity of mitochondrial architecture. This has therapeutic implications, as modulating YME1L activity could potentially counteract the mitochondrial defects caused by the absence of MIC13, offering a potential intervention strategy for mitochondrial pathologies linked to MIC13 deficiencies, mitochondrial hepato-encephalopathy.

In conclusion, MIC13 is more than a structural component; it is a key regulator of mitochondrial proteostasis, safeguarding the MIC10 subcomplex from proteolytic degradation, which is essential for the proper formation and maintenance of mitochondrial cristae. The understanding of MIC13's role in mitochondrial quality control is a vital step towards elucidating the complex regulation of mitochondrial architecture and could pave the way for novel therapeutic strategies in mitochondrial diseases.

6.3. SLP2 is a novel interactor of MIC13 regulating MIC26 stability and cristae architecture

The investigation of MIC13's interactome was a strategic approach to decipher its broader roles within the mitochondrial IM beyond its established function in stabilizing the MIC10 subcomplex and regulating YME1L-mediated proteolysis. By exploring the proteins that interact with MIC13, we aimed to uncover additional mechanisms by which MIC13 might influence mitochondrial architecture and function.

Detailed interactome analysis revealed a cascade of proteins residing in the mitochondrial membranes, of which most striking candidate being SLP2. This interaction has expanded our knowledge of mitochondrial dynamics, revealing that MIC13's role extends beyond stabilization of MIC10 subcomplex.

SLP2, traditionally recognized for its role in modulating mitochondrial morphology during cellular stress conditions by promoting stress induced hyperfusion (Tondera et al., 2009; Wai

et al., 2016), is now also considered a regulator within the MICOS complex, particularly in relation to MIC26. Depletion of SLP2 resulted in significant loss in MIC26 protein level. MIC26 level was rescued upon depletion of the protease YME1L from the *SLP2* KO cells, suggesting a modulation of proteolytic activity mediated by SLP2. This finding is in par with previous findings where SLP2 was suggested to form a large regulatory proteolytic hub together with YME1L and PARL in the IM, regulating the activity of these proteases (Wai et al., 2016). However, our findings provide the first proteolytic substrate of YME1L (i.e., MIC26) which is regulated by SLP2.

In single knockout models where either MIC13 or SLP2 was absent, the impact on mitochondrial structure was distinct and profound, underscoring the unique contributions of each protein. *MIC13* KO cells displayed onion-like cristae and loss of MIC10 subcomplex integrity, highlighting MIC13's crucial role in stabilizing MIC10 against YME1L-mediated degradation. This loss is detrimental to the structural integrity of the mitochondria, leading to the collapse of CJs.

In contrast, *SLP2* KO cells did not exhibit the same defects in the MIC10 subcomplex as seen in *MIC13* KOs, instead showing a direct impact on the stability of MIC26. The cells lacking SLP2 displayed a significantly reduced number of CJs with a characteristic cristae-swelling feature. To confirm if swollen cristae and reduced CJs were specifically contributed by loss of SLP2, we checked for the cristae architecture in *MIC26* KO cells. Loss of MIC26 displayed mostly normal cristae structures with a few interconnected cristae but no substantial swelling, concreating the finding that SLP2 has an alternate mode of contributing towards cristae morphology apart from MICOS proteins.

The interplay between SLP2 and YME1L regulating MIC26 is a new and important discovery, indicating that SLP2's role is not only structural but also regulatory, conserved among cell types (data not shown). By influencing the proteolytic landscape and interacting with several structural proteins, SLP2 indirectly affects the stability of mitochondrial structure (Da Cruz et al., 2008; Tondera et al., 2009; Wai et al., 2016). The findings from single KO studies emphasize that both MIC13 and SLP2 are crucial for the preservation of the MICOS complex and mitochondrial architecture. They do so by regulating YME1L's activity, which in turn stabilizes key structural proteins like MIC10 and MIC26.

6.4. SLP2 mediated MIC26 stabilization is crucial for maintaining cellular metabolic demands

Stabilization of MIC26 by SLP2 is a critical process towards integration of MIC26 in MICOS complex, whose function extends much beyond structural integrity of mitochondria and towards metabolic regulations in cells. MIC26 depletion has been implicated to alter mitochondrial morphology and functions consequently resulting in neurodegenerative and metabolic disorders (Benincá et al., 2020; Lamant et al., 2006; Peifer-Weiß et al., 2023).

MIC26, previously identified as a secreted protein, has been shown to be exclusively localized in mitochondria and contribute towards structural integrity (Lubeck et al., 2023). MIC26 functions as a key regulator in the mitochondria, orchestrating a complex interplay of metabolic processes that adapt to the cellular nutritional status (Lubeck et al., 2023). Under standard glucose conditions (normoglycemia), MIC26's absence is met with a cellular counter-response—an upregulation of glucose uptake, which is directed towards increased lipid anabolism via upregulation of G3P generation. At the same time fatty acid synthesis is also heightened by increased mitochondrial citrate export via an upregulation in citrate exporter SLC25A1 protein levels and an upregulation of lipid synthesis key enzymes, contributing to the expanding lipid storage. Interestingly, while the biosynthesis pathway for cholesterol is activated, the overall cholesterol level within the cell is maintained on WT level, suggesting a compensatory upregulation to meet cellular cholesterol demands. Furthermore, changes are observed in the OXPHOS energy generation and complex formation, possibly reflecting a change in the cell's energy allocation strategy. The glutamine metabolism too is altered, marked by an increase in glutamine accumulation, indicating an altered amino acid handling and usage.

In a hyperglycemic condition, loss of MIC26 imparts different metabolic outcomes. Here, without MIC26 to oversee the metabolic adjustments, the cell does not elevate glucose uptake despite an environment rich in glucose, however accumulates glucose. Consequently, the downstream pathways of lipid metabolism are affected, as evidenced by reduced G3P and a corresponding decrease in lipid droplet accumulation and decreased pyruvate level. Cholesterol biosynthesis follows this trend, with reduced activity leading to lower cellular cholesterol levels. In this glucose-rich condition, the TCA cycle also reflects the impact of MIC26's absence, with a reduction in citrate pointing towards a potential inefficiency in free fatty acids de novo synthesis. Furthermore, the downregulation of key transporters like SLC25A12 and SLC1A5 suggests a disruption in the shuttling of critical metabolites into the mitochondria, likely affecting the balance of fuel usage and energy output. This metabolic shift is an evidence to MIC26's integral role, which in normal physiological condition, stabilized by SLP2 mediated regulation of YME1L, in adapting mitochondrial function to the cellular energy state, with its absence leading to a significant reorganization of the cell's metabolic priorities. In conclusion, the study of MIC13's interactome has uncovered a complex network of protein interactions that are critical for maintaining mitochondrial integrity. The novel interaction between MIC13 and SLP2, and the subsequent regulation of YME1L, unveils a multi-layered regulatory mechanism that controls the stability of both MIC10 and MIC26. These findings not only enhance our understanding of the intricate processes governing mitochondrial architecture but also suggest new potential targets for therapeutic interventions in diseases associated with mitochondrial dysfunction.

6.5. MIC13-SLP2 synergistically regulate MIC60-subcomplex assembly

Building on the understanding of SLP2's role in stabilizing MIC26, we further investigated the scenario where both MIC13 and SLP2 are absent, exploring the implications of their synergistic functions. The DKO experiments reveal that MIC13 and SLP2 work in concert to facilitate the proper assembly of the MIC60 subcomplex, an essential component of the MICOS complex that is crucial for maintaining mitochondrial cristae structure (John et al., 2005). While the absence of SLP2 alone impairs the stability of MIC26 and thus affects the architecture of cristae, the simultaneous absence of MIC13 compounds this effect, disrupting the assembly of the MIC60 subcomplex. This disruption occurs despite the presence of normal protein levels of MIC60 subcomplex components, suggesting that MIC13 and SLP2 are not directly involved in the synthesis or stability of these proteins but are critical for their proper assembly into a functional complex. This failure is critical because the MIC60 subcomplex is central to the formation and maintenance of mitochondrial cristae and the inner-outer membrane contact sites by formation of the MIB complex (Darshi et al., 2011; Sastri et al., 2017; Tang et al., 2020). In addition to MIC60 subcomplex, the MIB proteins MTX1 and SAM50 also showed gross assembly defects in absence of MIC13 and SLP2. Extending the synergistic role of these proteins towards not only stabilizing the MICOS complex but also conferring stabilization effect on the inner-outer membrane contact sites via stable integration of MIB complex. Under normal conditions, MIC13 and SLP2 work synergistically to ensure the proper assembly and localization of the MIC60 subcomplex, which in turn dictates the structure of cristae.

The STED microscopy data from the *MIC13-SLP2* DKO cells provide a visual affirmation of this disruption. While wild type cells exhibit a punctate arrangement of MIC60, indicative of a properly organized MICOS complex (Stoldt et al., 2019), the *MIC13-SLP2* DKO cells show a dispersed arrangement of MIC60. This dispersal suggests that the absence of MIC13 and SLP2 leads to a failure in the spatial organization of the MIC60 subcomplex, disrupting the usual punctate distribution crucial for cristae integrity.

Although deletion of *SLP2* from *MIC13* KO background imparted a detrimental effect on MIC60-subcomplex and MIB complex proteins, a beneficial effect on the levels of MIC27 assembly was observed. An interesting phenomenon which further opens up an avenue to explore the independent assembly pattern of MIC27 despite the absence of MIC10 and MIC13. Independent assembly of MIC27 was previously reported (Tirrell et al., 2020), and together with the findings from this research, a novel assembly pathway for MICOS subunits could be deciphered in the future research. Additionally, a mild increase in CJs was also observed in the *MIC13-SLP2* DKO cell lines as compared to *MIC13* KO cells, indicating a beneficial effect towards deletion of SLP2, although detrimental to MIC60-subcomplex, but can still somehow promote assembly of MIC27 and mildly effect CJ formation. Exploring the detailed proteolytic

and quality control regulation mediated by SLP2 could further deepen our understanding towards assembly of MICOS subunits, such as MIC27, and formation of CJs.

The alteration in the MIC60 arrangement in the DKO cells underscores the roles of MIC13 and SLP2 in the higher-order assembly of MICOS complex. Without the stabilizing functions provided by these two proteins, the individual components of the MIC60 subcomplex cannot integrate into a functional MICOS complex. The STED data thus reinforce the idea that the assembly of the MICOS complex, particularly the integration of the MIC60 into this structure, is a highly coordinated process that depends on synergistic functions of MIC13 and SLP2.

4.4. SLP2 regulates assembly kinetics of MIC60 in presence of MIC10 subcomplex

Having established the synergistic relationship between MIC13 and SLP2 in the assembly of the MIC60 subcomplex, the focus now shifts to a more detailed exploration of this interplay. Utilizing the tetracycline inducible (Tet-On) system to control MIC13 expression, we delve into the specifics of how its time-dependent restoration impacts the assembly dynamics of the MIC60 and MIC10 subcomplexes, in presence and absence of SLP2. This approach allows for a precise dissection of the individual roles of MIC13 and SLP2, further illuminating their distinct yet interconnected contributions to the MICOS complex formation and mitochondrial cristae organization.

The observed kinetics of MIC60 subcomplex assembly upon MIC13 restoration in *MIC13-SLP2* DKO cells offer novel insights into the assembly of the MICOS complex. The reintroduction of MIC13, in absence of SLP2, led to a substantial slower assembly of the MIC60 subcomplex, underscoring the indispensable role of SLP2 in this process. This delay in assembly delineates the functional synergy between MIC13 and SLP2 in the MICOS complex. While MIC13 is crucial for the stability and presence of the MIC10 subcomplex, the efficient assembly kinetics of the MIC60 subcomplex is markedly dependent on SLP2 upon slow restoration of MIC13 (MIC10 subcomplex). This differential dependency indicates a specialized division of labor within the MICOS complex, where SLP2 appears to be integral to the assembly kinetics of the MIC60.

In contrast to the assembly dynamics of the MIC60 subcomplex, the assembly of the MIC10 subcomplex exhibits a distinct dependency solely on the presence of MIC13, irrespective of SLP2. This revelation is significant in the context of MICOS complex assembly, as it highlights the unique and indispensable role of MIC13 for the MIC10 subcomplex formation. Despite the slower kinetics observed in the MIC60 subcomplex assembly in *MIC13-SLP2* DKO cells, the restoration of MIC13 is sufficient to reestablish the MIC10 subcomplex, indicating that the presence of SLP2 does not influence this specific assembly pathway. This selective dependency underscores the critical and non-redundant role of MIC13 in maintaining the integrity of the MIC10 subcomplex, which is essential for the proper structural organization of

mitochondrial cristae. The distinct roles of MIC13 and SLP2 within the MICOS complex, as delineated by these observations, provide a novel understanding of how individual components contribute to the complex's overall assembly pattern.

Building upon the insights from the synergistic functions of MIC13 and SLP2 in the MIC60 subcomplex assembly, a compelling hypothesis emerges when examining the Tet-On system's results. We termed this the 'seeder hypothesis,' postulating a foundational role for the MIC10 subcomplex, in concert with SLP2, to facilitate the assembly of the MIC60 subcomplex. The time-dependent restoration of MIC13, particularly in the context of MIC13-SLP2 DKO cells, highlights not only the individual contributions of MIC13 and SLP2 but also suggests their collaborative role in priming the mitochondrial IM for the assembly of other MICOS components.

The 'seeder hypothesis' puts forward the idea that the MIC10 subcomplex, once stabilized by the presence of MIC13, acts in unison with SLP2 to facilitate the integration of the MIC60 subcomplex into the holo-MICOS complex. This hypothesis aligns well with the observed differences in assembly kinetics of the MIC60 subcomplex between *MIC13* KO and *MIC13-SLP2* DKO cells. It suggests that the coordinated action of the MIC10 subcomplex and SLP2 creates an optimal environment or 'seeding ground' for the efficient assembly and proper localization of MIC60, which is crucial for the maintenance of mitochondrial cristae structure and function.

6.6. 'Seeder Model' of MICOS assembly and cristae junction formation

In order to validate the 'seeder hypothesis', a critical step involved restoring the assembly of the MIC10 subcomplex in the *MIC13-SLP2* DKO cells. This was achieved through the strategic knockdown of YME1L, a mitochondrial protease whose regulation is dependent on MIC13. The rationale was that by mitigating the proteolytic activity of YME1L, we could facilitate the reassembly of the MIC10 subcomplex, even in the absence of MIC13 and SLP2, and subsequently facilitate the assembly of the MIC60 subcomplex.

YME1L effectively degrades MIC10-subcomplex in absence of MIC13, demonstrating a SLP2-independent role of MIC13 regulating YME1L activity. However, upon depletion of YME1L from WT cells, an increase in protein levels for MIC10-subcomplex is observed highlighting a fine-tuned proteostasis regulation within the MICOS complex. MIC10 was shown to oligomerize within the CJs (Bohnert et al., 2015), and constant degradation of excess MIC10 could be crucial towards hyper oligomerization leading to a vesicular crista formation, prompting further investigation towards quality control mechanism. Additionally, the constant degradation of MIC10-subcomplex by YME1L could be crucial for the fission-fusion of cristae membranes within mitochondria.

Following the YME1L knockdown in the *MIC13-SLP2* DKO cells, we observed that the protein levels of the MIC60 subcomplex did not change significantly. However, the assembly of the

MIC60 subcomplex was notably more efficient. This improvement in assembly can be linked to the reconstituted MIC10 subcomplex, made possible by the depletion in YME1L levels in the DKO cells. Essentially, the reassembled MIC10 subcomplex appears to function as a 'seeder' platform, enabling the MIC60 subcomplex to integrate into the MICOS complex more effectively. The role of MIC13, previously identified to have a bridging function between the two MICOS subcomplexes, transcends towards a more intricate function regulating a major mitochondrial protease YME1L. Further investigation MIC13 mediated regulation of YME1L, specifically identifying potential substrates under this regulation, could provide valuable knowledge towards a better understanding of intricate regulations of the structural proteins contributing towards mitochondrial functions.

This outcome strongly supports the seeder hypothesis. It demonstrates that an intact MIC10 subcomplex, even in the absence of MIC13 and SLP2, not only interacts with MIC60 but is crucial for the proper assembly of the MIC60 subcomplex and MIB complex. This finding highlights the role of the MIC10 subcomplex, stabilized against YME1L-mediated degradation, in guiding the overall assembly of the MICOS-MIB complex. YME1L has been implicated as a quality control protease within the mitochondrial IM, degrading unassembled or misfolded protein to maintain functional integrity of the organelle (Schreiner et al., 2012). We identify two-fold regulation of YME1L in this study, (1) its known regulation in SPY complex (Wai et al., 2016), where in SLP2 regulates its activity to stabilize MIC26 and (2) its regulation by MIC13 to stabilize the MIC10-subcomplex, thereby promoting its assembly. While YME1L could potentially degrade unassembled MIC10 and 'fine-tune' the amount of protein to be assembled as evident from the YME1L depletion in WT cells where MIC10 levels are drastically increased. We delve into the previously unexplored territory of MIC13-dependent regulation of YME1L, shedding light on a novel mechanism that influences MICOS assembly dynamics. Additionally, our study elucidates the collaborative role of SLP2 alongside MIC13 in modulating the assembly of MIC60 and MIB complexes, thereby extending far beyond the scope of the SPY complex, although the stabilization of MIC26 proteolysis by YME1L is conducted by SLP2, identifying a novel regulatory role of SPY complex on a vital CJ protein.

Crucially, the efficient assembly of the MIC60 subcomplex in the *MIC13-SLP2* DKO cells following YME1L depletion extends beyond just subunit assembly. It directly contributes to the reformation of nascent CJs, highlighting a functional restoration of mitochondrial architecture. This reformation is indicative of the crucial role played by the MIC10 subcomplex, now stabilized due to YME1L downregulation, in not only providing the 'seeding' ground for the assembly of the MIC60 subcomplex but also in driving the reconstruction of cristae morphology. SLP2 plays a substantial role in the assembly kinetics of MIC60 during the initial assembly of MIC10-subcomplex, however depletion of SLP2 does not drastically affect this process, indicating a rather supportive or accessory role of SLP2 in assembly of MIC60-

subcomplex. Together with the functional studies and the interaction data, it could be further concluded that SLP2 may not directly be a part of the MICOS complex, however it's role is crucial in supporting the MIC60-subcomplex and MIB complex assembly upon a pre-assembled MIC10-subcomplex

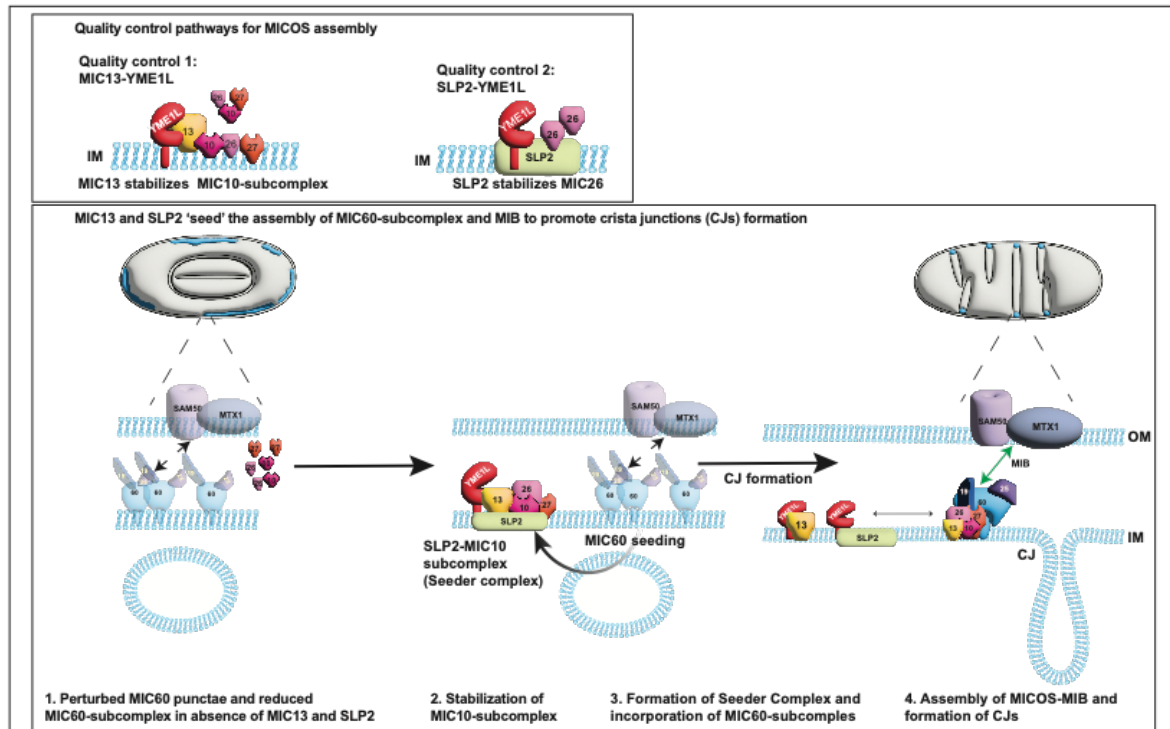


Figure 6: Model of MICOS-MIB assembly and CJ formation. MIC13 mediated stabilization of MIC10-subcomplex, together with SLP2, provides a 'seeding' ground for MIC60-subcomplex and MIB complex and facilitates CJ morphogenesis.

The emergence of these nascent CJs upon the restoration of the MIC10 subcomplex underscores the importance of the correct assembly and stabilization of MICOS components for the structural integrity of the mitochondria, with MIC13 and SLP2 playing a central role. The 'seeder' model thus encapsulates a vital mechanistic insight: the stabilization of the MIC10 subcomplex, together with SLP2, acts as a foundation, not only for the efficient assembly of the MIC60 subcomplex but also for the reestablishment of CJs, integral to mitochondrial function and health. This interplay between the MIC10 subcomplex and MIC60 subcomplex, modulated by MIC13 and SLP2 and the protease YME1L, paints a comprehensive picture of how mitochondrial ultrastructure is intricately regulated and maintained.

7 Outlook

The study has elucidated pivotal roles of MIC13, SLP2, and YME1L in the regulation of mitochondrial cristae architecture, emphasizing the intricate interplay between these proteins in maintaining mitochondrial integrity. Specifically, our findings highlight the stabilization of MIC10 imparted by MIC13 via regulation of YME1L, further diving deeper into the interactome of MIC13 where we identify SLP2 to be an accessory protein. We propose that SLP2, together with MIC10-subcomplex, promotes the assembly of MIC60-subcomplex and MIB proteins, although deletion of SLP2 from *MIC13* KO cells has beneficial effect on MIC27 assembly and mildly increases CJ formation.

From the major findings proposed in the previous section of this thesis, following future directions are proposed:

7.1. Deeper investigation into MIC13's regulatory mechanisms

Expanding our understanding of MIC13's role in the stabilization of the MIC10 subcomplex and its regulation by YME1L will be crucial. Future studies should focus on elucidating the precise molecular interactions and signaling pathways that underpin MIC13's protective effects against YME1L-mediated degradation, offering insights into mitochondrial quality control and disease mechanisms in both cell lines and mouse models. Notably, the rescue of the upper band of MIC27 upon depletion of YME1L from *MIC13* KO cells could provide vital evidence of potential post translational modifications with MICOS complex that could play crucial role in the assemblies of the subunits.

7.2. Therapeutic implications of MIC10 stabilization

The discovery that MIC13 regulates YME1L to stabilize MIC10, thereby facilitating the reformation of CJs, offers an exciting therapeutic opportunity, particularly for conditions like mitochondrial hepato-encephalopathy. The initial phase of this therapeutic development should prioritize the mapping of YME1L recognition sites on MIC10. A promising approach involves constructing a series of MIC10 variants with small, targeted deletions of amino acids. These constructs can be introduced into *MIC13* KO cells, followed by rigorous biochemical assays to identify which MIC10 mutants exhibit resistance to YME1L-mediated degradation. Armed with this molecular insight, the next step would be the strategic design and identification of small molecules, peptides, or aptamers. These therapeutic agents would be engineered to emulate MIC13's protective role, effectively shielding MIC10 from YME1L's proteolytic activity. The potential of these agents to selectively inhibit the degradation of MIC10 by YME1L holds substantial promise; however, it is imperative to conduct comprehensive validation studies. Such studies must ensure that these inhibitors are highly specific, mitigating any unintended off-target effects and confirming that the inhibition of YME1L's activity is strictly confined to the context of MIC10 proteolysis. The therapeutic implications of this strategy are profound, as it not only offers a novel method to counteract mitochondrial dysfunction in hepato-

encephalopathy but also paves the way for addressing a broader spectrum of mitochondrial pathologies with similar molecular mechanism of disease progression. This approach exemplifies the translational potential of basic mitochondrial research, turning biochemical pathways into targets for clinical intervention.

7.3. Investigating the role of SLP2 mediated YME1L regulation in crista swelling

SLP2 KO displayed about 50% reduction in CJs however it displayed a distinct crista swelling pattern which is discrete from any of the MICOS subunit KOs, indicating an alternate regulatory mechanism imparted by SLP2 on shaping cristae architecture. Upon knockdown of YME1L, this swelling pattern could be abolished, indicating a new “player” under control of SLP2-YME1L axis, which could prove to be a critical component in efficient formation of crista structure. Mass spectrometry approaches in *SLP2* KO cells and *SLP2* KO cells with YME1L depletion could identify this protein, which is involved in proper crista structure, substantially increasing our understanding of crista morphogenesis. To further investigate the role of this potential crista morphogenesis protein, depletion studies on this protein could be performed to further characterize its mechanistic functions.

7.4. Mechanistic insights into MIB complex regulation by MICOS Components

Unraveling the intricate molecular communication between the inner and outer mitochondrial membranes, especially the influence of the MICOS complex's integrity and assembly on the MIB complex, stands at the forefront of mitochondrial biology. Regulation of MICOS complex via SAMM50 is well established, however this is the first data which indicates a possibility of intricate regulation of MIB assembly mediated via the CJ shaping proteins. Our data reveal that the coordinated action of MIC13 and SLP2 significantly enhances the assembly of the MIC60 subcomplex, alongside crucial MIB proteins such as SAMM50 and MTX1. While the regulation of the MICOS complex by SAMM50 is well-documented, our study pioneers the identification of a potential sophisticated mechanism through which CJ shaping proteins might regulate MIB complex assembly.

This revelation opens up uncharted territories in mitochondrial research, suggesting a far-reaching role of the MICOS complex that transcends its known functions. To delve deeper into this novel regulatory axis, I propose a targeted approach: overexpressing SAMM50 and MTX1 in *MIC13-SLP2* DKO cells, a model strategically chosen for its impaired MIC60 assembly. This experiment is designed to probe whether the assembly of MIB proteins is still hindered in the absence of a functional MIC60 subcomplex. A compromised assembly of MIB proteins under these conditions would illuminate a previously unseen mechanism, indicating that OM components of the MIB complex are regulated by IM proteins, particularly through the actions of the MICOS complex.

This exploration not only promises to expand our understanding of mitochondrial dynamics but also posits the MICOS complex as a central orchestrator of mitochondrial architecture, influencing both OM and IM interactions. By bridging this crucial gap in knowledge, it could be aimed to illuminate the complex interdependencies that govern OM and IM regulation.

7.5. Mechanistic insights into MIB complex regulation by IM quality control pathways

An intriguing finding from this study highlights the decreased assembly in MIB proteins SAMM50 and MTX1 upon depletion of YME1L from the WT cells. YME1L, localized in IM, is a master protease involved in multiple quality control pathways. Though depletion of YME1L from *MIC13* KO and *MIC13-SLP2* DKO cells imparted a positive effect on MIC60-subcomplex and MIB assembly via restoration of MIC10 levels, it imparted a substantial detrimental effect on MIB assembly in the WT cells. This finding paves a novel pathway implicating the importance of IM quality control pathways which is essential for regulation of proper assembly of outer membrane proteins SAMM50 and MTX1.

Our study sheds light on a fascinating aspect of mitochondrial biology: the intricate regulation of the MIB complex by IM quality control pathways, particularly through the action of the protease YME1L. A key discovery is the observation that depleting YME1L from WT cells leads to a drastic decrease in the assembly of MIB proteins SAMM50 and MTX1. YME1L, a protease anchored in the IM, plays a pivotal role in mediating multiple quality control pathways within the mitochondria. Interestingly, while the depletion of YME1L from *MIC13* KO and *MIC13-SLP2* DKO cells is beneficial to the assembly of the MIC60 subcomplex and MIB components by restoring MIC10 levels, it conversely exerts a substantial negative impact on MIB assembly within WT cells.

This counterintuitive outcome uncovers a previously unrecognized pathway, underscoring the critical importance of IM quality control mechanisms in the regulation of OM proteins such as SAMM50 and MTX1. This revelation not only challenges our current understanding of mitochondrial protein regulation but also opens new avenues for exploring how mitochondrial quality control impacts the broader architectural integrity of the organelle.

Such insights have profound implications for our comprehension of mitochondrial dynamics, suggesting that the balance of proteolytic activity within the IM is crucial not only for the maintenance of IM components but also for the orchestration of complex assembly processes involving the OM. This discovery propels us into new research territories, necessitating a deeper investigation into how IM quality control pathways intricately govern the assembly and function of mitochondrial structures spanning both membranes.

Embarking on this research to decode the mechanistic underpinnings of MIB complex regulation by IM quality control pathways, it is poised to unravel the complex interdependencies that define mitochondrial integrity and function.

8 Conclusion

In conclusion, our comprehensive investigation underscores the pivotal role of MIC13 in safeguarding the stability and integrity of the MIC10-subcomplex through the suppression of YME1L-mediated proteolysis, highlighting a molecular mechanism in pathogenesis of mitochondrial hepato-encephalopathy. This finding led to the observation that CJs can be significantly rescued upon stabilization of MIC10, implicating that the loss in CJs in patient cells is due to the loss of MIC10 upon deleterious mutation in MIC13. Furthermore, we have identified SLP2 as a novel contributor to cristae morphogenesis, independent of its previous role in SPY complex. Our findings elucidate a distinct multistep process in which the MIC10-subcomplex and SLP2 serves as an essential 'seeding' platform, thereby enhancing the efficient assembly of the MIC60-subcomplex and the MIB complex. Crucially, SLP2 emerges as a key facilitator within this assembly mechanism, significantly augmenting the kinetics of MIC60-subcomplex formation. Expanding upon this multistep assembly narrative, we present initial evidence highlighting the reliance of the MIC60-subcomplex and the OM MIB complex on the IM proteins MIC10 and SLP2. This interdependence indicates a compelling avenue for further research, emphasizing the necessity to deepen our understanding of these molecular interactions and their implications for mitochondrial architecture and function.

9 References

- Abrams, A. J., Hufnagel, R. B., Rebelo, A., Zanna, C., Patel, N., Gonzalez, M. A., Campeanu, I. J., Griffin, L. B., Groenewald, S., Strickland, A. V., Tao, F., Speziani, F., Abreu, L., Schüle, R., Caporali, L., La Morgia, C., Maresca, A., Liguori, R., Lodi, R., ... Dallman, J. E. (2015). Mutations in SLC25A46, encoding a UGO1-like protein, cause an optic atrophy spectrum disorder. *Nature Genetics*, *47*(8), 926–932. <https://doi.org/10.1038/ng.3354>
- Adeva-Andany, M. M., Carneiro-Freire, N., Seco-Filgueira, M., Fernández-Fernández, C., & Mouriño-Bayolo, D. (2019). Mitochondrial β -oxidation of saturated fatty acids in humans. *Mitochondrion*, *46*, 73–90. <https://doi.org/10.1016/j.mito.2018.02.009>
- Ajrout-Driss, S., Fecto, F., Ajroud, K., Lalani, I., Calvo, S. E., Mootha, V. K., Deng, H.-X., Siddique, N., Tahmouh, A. J., Heiman-Patterson, T. D., & Siddique, T. (2015). Mutation in the novel nuclear-encoded mitochondrial protein CHCHD10 in a family with autosomal dominant mitochondrial myopathy. *Neurogenetics*, *16*(1), 1–9. <https://doi.org/10.1007/s10048-014-0421-1>
- Alexander, C., Votruba, M., Pesch, U. E. A., Thiselton, D. L., Mayer, S., Moore, A., Rodriguez, M., Kellner, U., Leo-Kottler, B., Auburger, G., Bhattacharya, S. S., & Wissinger, B. (2000). OPA1, encoding a dynamin-related GTPase, is mutated in autosomal dominant optic atrophy linked to chromosome 3q28. *Nature Genetics*, *26*(2), 211–215. <https://doi.org/10.1038/79944>
- Alkhaja, A. K., Jans, D. C., Nikolov, M., Vukotic, M., Lytovchenko, O., Ludewig, F., Schliebs, W., Riedel, D., Urlaub, H., Jakobs, S., & Deckers, M. (2012). MINOS1 is a conserved component of mitofilin complexes and required for mitochondrial function and cristae organization. *Molecular Biology of the Cell*, *23*(2), 247–257. <https://doi.org/10.1091/mbc.e11-09-0774>
- Anand, R., Kondadi, A. K., Meisterknecht, J., Golombek, M., Nortmann, O., Riedel, J., Peifer-Weiß, L., Brocke-Ahmadinejad, N., Schlütermann, D., Stork, B., Eichmann, T. O., Wittig, I., & Reichert, A. S. (2020). MIC26 and MIC27 cooperate to regulate cardiolipin levels and the landscape of OXPHOS complexes. *Life Science Alliance*, *3*(10), e202000711. <https://doi.org/10.26508/lsa.202000711>
- Anand, R., Strecker, V., Urbach, J., Wittig, I., & Reichert, A. S. (2016). Mic13 Is Essential for Formation of Crista Junctions in Mammalian Cells. *PLOS ONE*, *11*(8), e0160258. <https://doi.org/10.1371/journal.pone.0160258>
- Anand, R., Wai, T., Baker, M. J., Kladt, N., Schauss, A. C., Rugarli, E., & Langer, T. (2014). The i-AAA protease YME1L and OMA1 cleave OPA1 to balance mitochondrial fusion and fission. *The Journal of Cell Biology*, *204*(6), 919–929. <https://doi.org/10.1083/jcb.201308006>
- Anderson, S., Bankier, A. T., Barrell, B. G., de Bruijn, M. H., Coulson, A. R., Drouin, J., Eperon, I. C., Nierlich, D. P., Roe, B. A., Sanger, F., Schreier, P. H., Smith, A. J., Staden, R., & Young, I. G. (1981). Sequence and organization of the human mitochondrial genome. *Nature*, *290*(5806), 457–465. <https://doi.org/10.1038/290457a0>
- Andersson, S. G. E., Zomorodipour, A., Andersson, J. O., Sicheritz-Pontén, T., Alsmark, U. C. M., Podowski, R. M., Näslund, A. K., Eriksson, A.-S., Winkler, H. H., & Kurland, C. G. (1998). The genome sequence of *Rickettsia prowazekii* and the origin of mitochondria. *Nature*, *396*(6707), 133–140. <https://doi.org/10.1038/24094>
- Artal-Sanz, M., & Tavernarakis, N. (2009). Prohibitin couples diapause signalling to mitochondrial metabolism during ageing in *C. elegans*. *Nature*, *461*(7265), 793–797. <https://doi.org/10.1038/nature08466>
- Baker, M. J., Lampe, P. A., Stojanovski, D., Korwitz, A., Anand, R., Tatsuta, T., & Langer, T. (2014). Stress-induced OMA1 activation and autocatalytic turnover regulate OPA1-dependent mitochondrial dynamics. *The EMBO Journal*, *33*(6), 578–593. <https://doi.org/10.1002/embj.201386474>
- Bannwarth, S., Ait-El-Mkadem, S., Chaussenot, A., Genin, E. C., Lacas-Gervais, S., Fragaki, K., Berg-Alonso, L., Kageyama, Y., Serre, V., Moore, D. G., Verschuere, A., Rouzier, C., Le Ber, I., Augé, G., Cochaud, C., Lespinasse, F., N'Guyen, K., de Septenville, A., Brice, A., ... Paquis-Flucklinger, V. (2014). A mitochondrial origin for frontotemporal dementia

- and amyotrophic lateral sclerosis through CHCHD10 involvement. *Brain*, 137(8), 2329–2345. <https://doi.org/10.1093/brain/awu138>
- Baughman, J. M., Perocchi, F., Girgis, H. S., Plovanich, M., Belcher-Timme, C. A., Sancak, Y., Bao, X. R., Strittmatter, L., Goldberger, O., Bogorad, R. L., Koteliansky, V., & Mootha, V. K. (2011). Integrative genomics identifies MCU as an essential component of the mitochondrial calcium uniporter. *Nature*, 476(7360), 341–345. <https://doi.org/10.1038/nature10234>
- Benincá, C., Zanette, V., Brischigliaro, M., Johnson, M., Reyes, A., Valle, D. A. do, J. Robinson, A., Degiorgi, A., Yeates, A., Telles, B. A., Prudent, J., Baruffini, E., S. F. Santos, M. L., R. de Souza, R. L., Fernandez-Vizarra, E., J. Whitworth, A., & Zeviani, M. (2020). Mutation in the MICOS subunit gene APOO (MIC26) associated with an X-linked recessive mitochondrial myopathy, lactic acidosis, cognitive impairment and autistic features. *Journal of Medical Genetics*, jmedgenet-2020-106861. <https://doi.org/10.1136/jmedgenet-2020-106861>
- Birner, R., & Daum, G. (2003). *Biogenesis and cellular dynamics of aminoglycerophospholipids* (pp. 273–323). [https://doi.org/10.1016/S0074-7696\(05\)25007-6](https://doi.org/10.1016/S0074-7696(05)25007-6)
- Bohnert, M., Zerbes, R. M., Davies, K. M., Mühleip, A. W., Rampelt, H., Horvath, S. E., Boenke, T., Kram, A., Perschil, I., Veenhuis, M., Kühlbrandt, W., van der Klei, I. J., Pfanner, N., & van der Laan, M. (2015). Central Role of Mic10 in the Mitochondrial Contact Site and Cristae Organizing System. *Cell Metabolism*, 21(5), 747–755. <https://doi.org/10.1016/j.cmet.2015.04.007>
- Böttlinger, L., Horvath, S. E., Kleinschroth, T., Hunte, C., Daum, G., Pfanner, N., & Becker, T. (2012). Phosphatidylethanolamine and Cardiolipin Differentially Affect the Stability of Mitochondrial Respiratory Chain Supercomplexes. *Journal of Molecular Biology*, 423(5), 677–686. <https://doi.org/10.1016/j.jmb.2012.09.001>
- Chacinska, A., Koehler, C. M., Milenkovic, D., Lithgow, T., & Pfanner, N. (2009). Importing Mitochondrial Proteins: Machineries and Mechanisms. *Cell*, 138(4), 628–644. <https://doi.org/10.1016/j.cell.2009.08.005>
- Chakrabarty, S., Kabekkodu, S. P., Singh, R. P., Thangaraj, K., Singh, K. K., & Satyamoorthy, K. (2018). Mitochondria in health and disease. *Mitochondrion*, 43, 25–29. <https://doi.org/10.1016/j.mito.2018.06.006>
- Chan, D. C. (2012). Fusion and Fission: Interlinked Processes Critical for Mitochondrial Health. *Annual Review of Genetics*, 46(1), 265–287. <https://doi.org/10.1146/annurev-genet-110410-132529>
- Cipolat, S., de Brito, O. M., Dal Zilio, B., & Scorrano, L. (2004). OPA1 requires mitofusin 1 to promote mitochondrial fusion. *Proceedings of the National Academy of Sciences*, 101(45), 15927–15932. <https://doi.org/10.1073/pnas.0407043101>
- Cogliati, S., Enriquez, J. A., & Scorrano, L. (2016). Mitochondrial Cristae: Where Beauty Meets Functionality. *Trends in Biochemical Sciences*, 41(3), 261–273. <https://doi.org/10.1016/j.tibs.2016.01.001>
- Cogliati, S., Frezza, C., Soriano, M. E., Varanita, T., Quintana-Cabrera, R., Corrado, M., Cipolat, S., Costa, V., Casarin, A., Gomes, L. C., Perales-Clemente, E., Salvati, L., Fernandez-Silva, P., Enriquez, J. A., & Scorrano, L. (2013). Mitochondrial Cristae Shape Determines Respiratory Chain Supercomplexes Assembly and Respiratory Efficiency. *Cell*, 155(1), 160–171. <https://doi.org/10.1016/j.cell.2013.08.032>
- Cole, L. K., Kim, J. H., Amoscato, A. A., Tyurina, Y. Y., Bay R, H., Karimi, B., Siddiqui, T. J., Kagan, V. E., Hatch, G. M., & Kauppinen, T. M. (2018). Aberrant cardiolipin metabolism is associated with cognitive deficiency and hippocampal alteration in tafazzin knockdown mice. *Biochimica et Biophysica Acta. Molecular Basis of Disease*, 1864(10), 3353–3367. <https://doi.org/10.1016/j.bbadis.2018.07.022>
- Colombini, M. (1989). Voltage gating in the mitochondrial channel, VDAC. *The Journal of Membrane Biology*, 111(2), 103–111. <https://doi.org/10.1007/BF01871775>
- Csordás, G., Renken, C., Várnai, P., Walter, L., Weaver, D., Buttle, K. F., Balla, T., Mannella, C. A., & Hajnóczky, G. (2006). Structural and functional features and significance of the physical linkage between ER and mitochondria. *The Journal of Cell Biology*, 174(7), 915–921. <https://doi.org/10.1083/jcb.200604016>

- Czabotar, P. E., Lessene, G., Strasser, A., & Adams, J. M. (2014). Control of apoptosis by the BCL-2 protein family: implications for physiology and therapy. *Nature Reviews Molecular Cell Biology*, 15(1), 49–63. <https://doi.org/10.1038/nrm3722>
- Da Cruz, S., Parone, P. A., Gonzalo, P., Bienvenut, W. V., Tondera, D., Jourdain, A., Quadroni, M., & Martinou, J.-C. (2008). SLP-2 interacts with prohibitins in the mitochondrial inner membrane and contributes to their stability. *Biochimica et Biophysica Acta (BBA) - Molecular Cell Research*, 1783(5), 904–911. <https://doi.org/10.1016/j.bbamcr.2008.02.006>
- Darshi, M., Mendiola, V. L., Mackey, M. R., Murphy, A. N., Koller, A., Perkins, G. A., Ellisman, M. H., & Taylor, S. S. (2011). ChChd3, an Inner Mitochondrial Membrane Protein, Is Essential for Maintaining Crista Integrity and Mitochondrial Function*. *Journal of Biological Chemistry*, 286(4), 2918–2932. <https://doi.org/10.1074/jbc.M110.171975>
- Davies, K. M., Strauss, M., Daum, B., Kief, J. H., Osiewacz, H. D., Rycovska, A., Zickermann, V., & Kühlbrandt, W. (2011). Macromolecular organization of ATP synthase and complex I in whole mitochondria. *Proceedings of the National Academy of Sciences*, 108(34), 14121–14126. <https://doi.org/10.1073/pnas.1103621108>
- Del Dotto, V., Fogazza, M., Carelli, V., Rugolo, M., & Zanna, C. (2018). Eight human OPA1 isoforms, long and short: What are they for? *Biochimica et Biophysica Acta (BBA) - Bioenergetics*, 1859(4), 263–269. <https://doi.org/10.1016/j.bbabi.2018.01.005>
- Desmurs, M., Foti, M., Raemy, E., Vaz, F. M., Martinou, J.-C., Bairoch, A., & Lane, L. (2015). C11orf83, a Mitochondrial Cardiolipin-Binding Protein Involved in bc 1 Complex Assembly and Supercomplex Stabilization. *Molecular and Cellular Biology*, 35(7), 1139–1156. <https://doi.org/10.1128/MCB.01047-14>
- Ding, C., Wu, Z., Huang, L., Wang, Y., Xue, J., Chen, S., Deng, Z., Wang, L., Song, Z., & Chen, S. (2015). Mitofilin and CHCHD6 physically interact with Sam50 to sustain cristae structure. *Scientific Reports*, 5(1), 16064. <https://doi.org/10.1038/srep16064>
- Duvezin-Caubet, S., Jagasia, R., Wagener, J., Hofmann, S., Trifunovic, A., Hansson, A., Chomyn, A., Bauer, M. F., Attardi, G., Larsson, N.-G., Neupert, W., & Reichert, A. S. (2006). Proteolytic Processing of OPA1 Links Mitochondrial Dysfunction to Alterations in Mitochondrial Morphology. *Journal of Biological Chemistry*, 281(49), 37972–37979. <https://doi.org/10.1074/jbc.M606059200>
- Ehres, S., Raschke, I., Mancuso, G., Bernacchia, A., Geimer, S., Tondera, D., Martinou, J.-C., Westermann, B., Rugarli, E. I., & Langer, T. (2009). Regulation of OPA1 processing and mitochondrial fusion by m-AAA protease isoenzymes and OMA1. *Journal of Cell Biology*, 187(7), 1023–1036. <https://doi.org/10.1083/jcb.200906084>
- Ellis, C. E., Murphy, E. J., Mitchell, D. C., Golovko, M. Y., Scaglia, F., Barceló-Coblijn, G. C., & Nussbaum, R. L. (2005). Mitochondrial Lipid Abnormality and Electron Transport Chain Impairment in Mice Lacking α -Synuclein. *Molecular and Cellular Biology*, 25(22), 10190–10201. <https://doi.org/10.1128/MCB.25.22.10190-10201.2005>
- Eydt, K., Davies, K. M., Behrendt, C., Wittig, I., & Reichert, A. S. (2017). Cristae architecture is determined by an interplay of the MICOS complex and the F1FO ATP synthase via Mic27 and Mic10. *Microbial Cell (Graz, Austria)*, 4(8), 259–272. <https://doi.org/10.15698/mic2017.08.585>
- Flis, V. V., & Daum, G. (2013). Lipid Transport between the Endoplasmic Reticulum and Mitochondria. *Cold Spring Harbor Perspectives in Biology*, 5(6), a013235–a013235. <https://doi.org/10.1101/cshperspect.a013235>
- Frey, T. G., & Mannella, C. A. (2000). The internal structure of mitochondria. *Trends in Biochemical Sciences*, 25(7), 319–324. [https://doi.org/10.1016/S0968-0004\(00\)01609-1](https://doi.org/10.1016/S0968-0004(00)01609-1)
- Frezza, C., Cipolat, S., Martins de Brito, O., Micaroni, M., Beznoussenko, G. V., Rudka, T., Bartoli, D., Polishuck, R. S., Danial, N. N., De Strooper, B., & Scorrano, L. (2006). OPA1 Controls Apoptotic Cristae Remodeling Independently from Mitochondrial Fusion. *Cell*, 126(1), 177–189. <https://doi.org/10.1016/j.cell.2006.06.025>
- Friedman, J. R., Lackner, L. L., West, M., DiBenedetto, J. R., Nunnari, J., & Voeltz, G. K. (2011). ER Tubules Mark Sites of Mitochondrial Division. *Science*, 334(6054), 358–362. <https://doi.org/10.1126/science.1207385>

- Garlid, A. O., Schaffer, C. T., Kim, J., Bhatt, H., Guevara-Gonzalez, V., & Ping, P. (2020). TAZ encodes tafazzin, a transacylase essential for cardiolipin formation and central to the etiology of Barth syndrome. *Gene*, 726, 144148. <https://doi.org/10.1016/j.gene.2019.144148>
- Genin, E. C., Plutino, M., Bannwarth, S., Villa, E., Cisneros-Barroso, E., Roy, M., Ortega-Vila, B., Fragaki, K., Lespinasse, F., Pinero-Martos, E., Augé, G., Moore, D., Burté, F., Lacas-Gervais, S., Kageyama, Y., Itoh, K., Yu-Wai-Man, P., Sesaki, H., Ricci, J., ... Paquis-Flucklinger, V. (2016). CHCHD 10 mutations promote loss of mitochondrial cristae junctions with impaired mitochondrial genome maintenance and inhibition of apoptosis. *EMBO Molecular Medicine*, 8(1), 58–72. <https://doi.org/10.15252/emmm.201505496>
- Gieffers, C., Koriath, F., Heimann, P., Ungermann, C., & Frey, J. (1997). Mitofilin Is a Transmembrane Protein of the Inner Mitochondrial Membrane Expressed as Two Isoforms. *Experimental Cell Research*, 232(2), 395–399. <https://doi.org/10.1006/excr.1997.3539>
- Gödiker, J., Grüneberg, M., DuChesne, I., Reunert, J., Rust, S., Westermann, C., Wada, Y., Classen, G., Langhans, C. D., Schlingmann, K. P., Rodenburg, R. J., Pohlmann, R., & Marquardt, T. (2018). QIL1-dependent assembly of MICOS complex—lethal mutation in C19ORF70 resulting in liver disease and severe neurological retardation. *Journal of Human Genetics*, 63(6), 707–716. <https://doi.org/10.1038/s10038-018-0442-y>
- Green, D. R., & Kroemer, G. (2004). The Pathophysiology of Mitochondrial Cell Death. *Science*, 305(5684), 626–629. <https://doi.org/10.1126/science.1099320>
- Griparic, L., Kanazawa, T., & van der Bliek, A. M. (2007). Regulation of the mitochondrial dynamin-like protein Opa1 by proteolytic cleavage. *The Journal of Cell Biology*, 178(5), 757–764. <https://doi.org/10.1083/jcb.200704112>
- Guarani, V., McNeill, E. M., Paulo, J. A., Huttlin, E. L., Fröhlich, F., Gygi, S. P., Van Vactor, D., & Harper, J. W. (2015). QIL1 is a novel mitochondrial protein required for MICOS complex stability and cristae morphology. *ELife*, 4. <https://doi.org/10.7554/eLife.06265>
- Head, B., Griparic, L., Amiri, M., Gandre-Babbe, S., & van der Bliek, A. M. (2009). Inducible proteolytic inactivation of OPA1 mediated by the OMA1 protease in mammalian cells. *Journal of Cell Biology*, 187(7), 959–966. <https://doi.org/10.1083/jcb.200906083>
- Hell, K., Neupert, W., & Stuart, R. A. (2001). Oxa1p acts as a general membrane insertion machinery for proteins encoded by mitochondrial DNA. *The EMBO Journal*, 20(6), 1281–1288. <https://doi.org/10.1093/emboj/20.6.1281>
- Herzig, S., Raemy, E., Montessuit, S., Veuthey, J.-L., Zamboni, N., Westermann, B., Kunji, E. R. S., & Martinou, J.-C. (2012). Identification and Functional Expression of the Mitochondrial Pyruvate Carrier. *Science*, 337(6090), 93–96. <https://doi.org/10.1126/science.1218530>
- Hu, C., Shu, L., Huang, X., Yu, J., Li, liuju, Gong, L., Yang, M., Wu, Z., Gao, Z., Zhao, Y., Chen, L., & Song, Z. (2020). OPA1 and MICOS Regulate mitochondrial crista dynamics and formation. *Cell Death & Disease*, 11(10), 940. <https://doi.org/10.1038/s41419-020-03152-y>
- Huynen, M. A., Mühlmeister, M., Gotthardt, K., Guerrero-Castillo, S., & Brandt, U. (2016). Evolution and structural organization of the mitochondrial contact site (MICOS) complex and the mitochondrial intermembrane space bridging (MIB) complex. *Biochimica et Biophysica Acta (BBA) - Molecular Cell Research*, 1863(1), 91–101. <https://doi.org/10.1016/j.bbamcr.2015.10.009>
- Janer, A., Prudent, J., Paupe, V., Fahiminiya, S., Majewski, J., Sgarioto, N., Des Rosiers, C., Forest, A., Lin, Z., Gingras, A., Mitchell, G., McBride, H. M., & Shoubridge, E. A. (2016). SLC 25A46 is required for mitochondrial lipid homeostasis and cristae maintenance and is responsible for Leigh syndrome. *EMBO Molecular Medicine*, 8(9), 1019–1038. <https://doi.org/10.15252/emmm.201506159>
- John, G. B., Shang, Y., Li, L., Renken, C., Mannella, C. A., Selker, J. M. L., Rangell, L., Bennett, M. J., & Zha, J. (2005). The Mitochondrial Inner Membrane Protein Mitofilin Controls Cristae Morphology. *Molecular Biology of the Cell*, 16(3), 1543–1554. <https://doi.org/10.1091/mbc.e04-08-0697>

- Kazamel, M., Wong, L.-J., & Milone, M. (2014). Novel OPA1 mutation featuring spastic paraparesis and intestinal dysmotility. *Molecular Genetics and Metabolism Reports*, *1*, 443–445. <https://doi.org/10.1016/j.ymgmr.2014.09.006>
- Khosravi, S., & Harner, M. E. (2020). The MICOS complex, a structural element of mitochondria with versatile functions. *Biological Chemistry*, *401*(6–7), 765–778. <https://doi.org/10.1515/hsz-2020-0103>
- Kim, T.-H., Zhao, Y., Ding, W.-X., Shin, J. N., He, X., Seo, Y.-W., Chen, J., Rabinowich, H., Amoscato, A. A., & Yin, X.-M. (2004). Bid-Cardiolipin Interaction at Mitochondrial Contact Site Contributes to Mitochondrial Cristae Reorganization and Cytochrome c Release. *Molecular Biology of the Cell*, *15*(7), 3061–3072. <https://doi.org/10.1091/mbc.e03-12-0864>
- Kishita, Y., Shimura, M., Kohda, M., Akita, M., Imai-Okazaki, A., Yatsuka, Y., Nakajima, Y., Ito, T., Ohtake, A., Murayama, K., & Okazaki, Y. (2020). A novel homozygous variant in MICOS13 / QIL1 causes hepato-encephalopathy with mitochondrial DNA depletion syndrome. *Molecular Genetics & Genomic Medicine*, *8*(10). <https://doi.org/10.1002/mgg3.1427>
- Kitao, K., Mutai, H., Namba, K., Morimoto, N., Nakano, A., Arimoto, Y., Sugiuchi, T., Masuda, S., Okamoto, Y., Morita, N., Sakamoto, H., Shintani, T., Fukuda, S., Kaga, K., & Matsunaga, T. (2019). Deterioration in Distortion Product Otoacoustic Emissions in Auditory Neuropathy Patients With Distinct Clinical and Genetic Backgrounds. *Ear & Hearing*, *40*(1), 184–191. <https://doi.org/10.1097/AUD.0000000000000586>
- Klingenberg, M. (2008). The ADP and ATP transport in mitochondria and its carrier. *Biochimica et Biophysica Acta (BBA) - Biomembranes*, *1778*(10), 1978–2021. <https://doi.org/10.1016/j.bbamem.2008.04.011>
- Kondadi, A. K., Anand, R., & Reichert, A. S. (2020). Cristae Membrane Dynamics – A Paradigm Change. *Trends in Cell Biology*, *30*(12), 923–936. <https://doi.org/10.1016/j.tcb.2020.08.008>
- Koob, S., Barrera, M., Anand, R., & Reichert, A. S. (2015). The non-glycosylated isoform of MIC26 is a constituent of the mammalian MICOS complex and promotes formation of crista junctions. *Biochimica et Biophysica Acta*, *1853*(7), 1551–1563. <https://doi.org/10.1016/j.bbamcr.2015.03.004>
- Kornmann, B., Currie, E., Collins, S. R., Schuldiner, M., Nunnari, J., Weissman, J. S., & Walter, P. (2009). An ER-Mitochondria Tethering Complex Revealed by a Synthetic Biology Screen. *Science*, *325*(5939), 477–481. <https://doi.org/10.1126/science.1175088>
- Kozjak-Pavlovic, V. (2017). The MICOS complex of human mitochondria. *Cell and Tissue Research*, *367*(1), 83–93. <https://doi.org/10.1007/s00441-016-2433-7>
- Kunji, E. R. S., Aleksandrova, A., King, M. S., Majd, H., Ashton, V. L., Cerson, E., Springett, R., Kibalchenko, M., Tavoulari, S., Crichton, P. G., & Ruprecht, J. J. (2016). The transport mechanism of the mitochondrial ADP/ATP carrier. *Biochimica et Biophysica Acta (BBA) - Molecular Cell Research*, *1863*(10), 2379–2393. <https://doi.org/10.1016/j.bbamcr.2016.03.015>
- Lamant, M., Smih, F., Harmancey, R., Philip-Couderc, P., Pathak, A., Roncalli, J., Galinier, M., Collet, X., Massabuau, P., Senard, J.-M., & Rouet, P. (2006). ApoO, a novel apolipoprotein, is an original glycoprotein up-regulated by diabetes in human heart. *The Journal of Biological Chemistry*, *281*(47), 36289–36302. <https://doi.org/10.1074/jbc.M510861200>
- Lapatsina, L., Brand, J., Poole, K., Daumke, O., & Lewin, G. R. (2012). Stomatin-domain proteins. *European Journal of Cell Biology*, *91*(4), 240–245. <https://doi.org/10.1016/j.ejcb.2011.01.018>
- Leterme, S., & Michaud, M. (2023). Mitochondrial membrane biogenesis: A new pathway for lipid transport mediated by PERK/E-Syt1 complex. *Journal of Cell Biology*, *222*(3). <https://doi.org/10.1083/jcb.202301132>
- Li, H., Ruan, Y., Zhang, K., Jian, F., Hu, C., Miao, L., Gong, L., Sun, L., Zhang, X., Chen, S., Chen, H., Liu, D., & Song, Z. (2016). Mic60/Mitofilin determines MICOS assembly essential for mitochondrial dynamics and mtDNA nucleoid organization. *Cell Death & Differentiation*, *23*(3), 380–392. <https://doi.org/10.1038/cdd.2015.102>

- Liesa, M., & Shirihai, O. S. (2013). Mitochondrial Dynamics in the Regulation of Nutrient Utilization and Energy Expenditure. *Cell Metabolism*, 17(4), 491–506. <https://doi.org/10.1016/j.cmet.2013.03.002>
- Liu, Y.-T., Huang, X., Nguyen, D., Shammas, M. K., Wu, B. P., Dombi, E., Springer, D. A., Poulton, J., Sekine, S., & Narendra, D. P. (2020). Loss of CHCHD2 and CHCHD10 activates OMA1 peptidase to disrupt mitochondrial cristae phenocopying patient mutations. *Human Molecular Genetics*, 29(9), 1547–1567. <https://doi.org/10.1093/hmg/ddaa077>
- Lu, W., Karuppagounder, S. S., Springer, D. A., Allen, M. D., Zheng, L., Chao, B., Zhang, Y., Dawson, V. L., Dawson, T. M., & Lenardo, M. (2014). Genetic deficiency of the mitochondrial protein PGAM5 causes a Parkinson's-like movement disorder. *Nature Communications*, 5(1), 4930. <https://doi.org/10.1038/ncomms5930>
- Lubeck, M., Derkum, N. H., Naha, R., Strohm, R., Driessen, M. D., Belgardt, B.-F., Roden, M., Stühler, K., Anand, R., Reichert, A. S., & Kondadi, A. K. (2023). MIC26 and MIC27 are bona fide subunits of the MICOS complex in mitochondria and do not exist as glycosylated apolipoproteins. *PLOS ONE*, 18(6), e0286756. <https://doi.org/10.1371/journal.pone.0286756>
- Lubeck, M., Naha, R., Schaumkessel, Y., Westhoff, P., Stefanski, A., Petzsch, P., Stühler, K., Köhrer, K., Weber, A. P. M., Anand, R., Reichert, A., & Kondadi, A. K. (2023). Mitochondrial Apolipoprotein MIC26 is a metabolic rheostat regulating central cellular fuel pathways. *Biorxiv*.
- Lynn Margulis. (1970). *Origin of eukaryotic cells: evidence and research implications for a theory of the origin and evolution of microbial, plant, and animal cells on the Precambrian earth*. Yale University Press.
- MacVicar, T., Ohba, Y., Nolte, H., Mayer, F. C., Tatsuta, T., Sprenger, H.-G., Lindner, B., Zhao, Y., Li, J., Bruns, C., Krüger, M., Habich, M., Riemer, J., Schwarzer, R., Pasparakis, M., Henschke, S., Brüning, J. C., Zamboni, N., & Langer, T. (2019). Lipid signalling drives proteolytic rewiring of mitochondria by YME1L. *Nature*, 575(7782), 361–365. <https://doi.org/10.1038/s41586-019-1738-6>
- Mannella, C. A. (2006). Structure and dynamics of the mitochondrial inner membrane cristae. *Biochimica et Biophysica Acta (BBA) - Molecular Cell Research*, 1763(5–6), 542–548. <https://doi.org/10.1016/j.bbamcr.2006.04.006>
- Mannella, C. A., Marko, M., Penczek, P., Barnard, D., & Frank, J. (1994). The internal compartmentation of rat-liver mitochondria: Tomographic study using the high-voltage transmission electron microscope. *Microscopy Research and Technique*, 27(4), 278–283. <https://doi.org/10.1002/jemt.1070270403>
- Martínez-Reyes, I., & Chandel, N. S. (2020). Mitochondrial TCA cycle metabolites control physiology and disease. *Nature Communications*, 11(1), 102. <https://doi.org/10.1038/s41467-019-13668-3>
- Milenkovic, D., & Larsson, N.-G. (2015). Mic10 Oligomerization Pinches off Mitochondrial Cristae. *Cell Metabolism*, 21(5), 660–661. <https://doi.org/10.1016/j.cmet.2015.04.020>
- Mishra, P., & Chan, D. C. (2016). Metabolic regulation of mitochondrial dynamics. *Journal of Cell Biology*, 212(4), 379–387. <https://doi.org/10.1083/jcb.201511036>
- Mitsopoulos, P., Lapohos, O., Weraarpachai, W., Antonicka, H., Chang, Y.-H., & Madrenas, J. (2017). Stomatin-like protein 2 deficiency results in impaired mitochondrial translation. *PLOS ONE*, 12(6), e0179967. <https://doi.org/10.1371/journal.pone.0179967>
- Mukherjee, I., Ghosh, M., & Meinecke, M. (2021). MICOS and the mitochondrial inner membrane morphology – when things get out of shape. *FEBS Letters*, 595(8), 1159–1183. <https://doi.org/10.1002/1873-3468.14089>
- Murphy, M. P. (2009). How mitochondria produce reactive oxygen species. *Biochemical Journal*, 417(1), 1–13. <https://doi.org/10.1042/BJ20081386>
- Naha, R., Anees, A., Chakrabarty, S., Naik, P. S., Pandove, M., Pandey, D., & Satyamoorthy, K. (2020). Placental mitochondrial DNA mutations and copy numbers in intrauterine growth restricted (IUGR) pregnancy. *Mitochondrion*, 55. <https://doi.org/10.1016/j.mito.2020.08.008>

- Naha, R., Strohm, R., Urbach, J., Wittig, I., Reichert, A. S., Kondadi, A. K., & Anand, R. (2023). MIC13 and SLP2 seed the assembly of MIC60-subcomplex to facilitate crista junction formation. *Biorxiv*.
- Nasca, A., Rizza, T., Doimo, M., Legati, A., Ciolfi, A., Diodato, D., Calderan, C., Carrara, G., Lamantea, E., Aiello, C., Di Nottia, M., Niceta, M., Lamperti, C., Ardisson, A., Bianchi-Marzoli, S., Iarossi, G., Bertini, E., Moroni, I., Tartaglia, M., ... Ghezzi, D. (2017). Not only dominant, not only optic atrophy: expanding the clinical spectrum associated with OPA1 mutations. *Orphanet Journal of Rare Diseases*, *12*(1), 89. <https://doi.org/10.1186/s13023-017-0641-1>
- Neupane, P., Bhujju, S., Thapa, N., & Bhattarai, H. K. (2019). ATP Synthase: Structure, Function and Inhibition. *Biomolecular Concepts*, *10*(1), 1–10. <https://doi.org/10.1515/bmc-2019-0001>
- Neupert, W., & Herrmann, J. M. (2007). Translocation of Proteins into Mitochondria. *Annual Review of Biochemistry*, *76*(1), 723–749. <https://doi.org/10.1146/annurev.biochem.76.052705.163409>
- Olichon, A., Baricault, L., Gas, N., Guillou, E., Valette, A., Belenguer, P., & Lenaers, G. (2003). Loss of OPA1 perturbs the mitochondrial inner membrane structure and integrity, leading to cytochrome c release and apoptosis. *The Journal of Biological Chemistry*, *278*(10), 7743–7746. <https://doi.org/10.1074/jbc.C200677200>
- Osman, C., Haag, M., Potting, C., Rodenfels, J., Dip, P. V., Wieland, F. T., Brügger, B., Westermann, B., & Langer, T. (2009). The genetic interactome of prohibitins: coordinated control of cardiolipin and phosphatidylethanolamine by conserved regulators in mitochondria. *Journal of Cell Biology*, *184*(4), 583–596. <https://doi.org/10.1083/jcb.200810189>
- Ott, C., Dorsch, E., Fraunholz, M., Straub, S., & Kozjak-Pavlovic, V. (2015). Detailed Analysis of the Human Mitochondrial Contact Site Complex Indicate a Hierarchy of Subunits. *PLOS ONE*, *10*(3), e0120213. <https://doi.org/10.1371/journal.pone.0120213>
- Ott, C., Ross, K., Straub, S., Thiede, B., Gotz, M., Goosmann, C., Krischke, M., Mueller, M. J., Krohne, G., Rudel, T., & Kozjak-Pavlovic, V. (2012). Sam50 Functions in Mitochondrial Intermembrane Space Bridging and Biogenesis of Respiratory Complexes. *Molecular and Cellular Biology*, *32*(6), 1173–1188. <https://doi.org/10.1128/MCB.06388-11>
- Palmieri, F. (2013). The mitochondrial transporter family SLC25: Identification, properties and physiopathology. *Molecular Aspects of Medicine*, *34*(2–3), 465–484. <https://doi.org/10.1016/j.mam.2012.05.005>
- Palmieri, F., & Monné, M. (2016). Discoveries, metabolic roles and diseases of mitochondrial carriers: A review. *Biochimica et Biophysica Acta (BBA) - Molecular Cell Research*, *1863*(10), 2362–2378. <https://doi.org/10.1016/j.bbamcr.2016.03.007>
- Paradies, G., Petrosillo, G., Paradies, V., & Ruggiero, F. M. (2009). Role of cardiolipin peroxidation and Ca²⁺ in mitochondrial dysfunction and disease. *Cell Calcium*, *45*(6), 643–650. <https://doi.org/10.1016/j.ceca.2009.03.012>
- Peifer-Weiß, L., Kurban, M., David, C., Lubeck, M., Kondadi, A. K., Nemer, G., Reichert, A. S., & Anand, R. (2023). A X-linked nonsense *APOO/MIC26* variant causes a lethal mitochondrial disease with progeria-like phenotypes. *Clinical Genetics*, *104*(6), 659–668. <https://doi.org/10.1111/cge.14420>
- Pfanner, N., van der Laan, M., Amati, P., Capaldi, R. A., Caudy, A. A., Chacinska, A., Darshi, M., Deckers, M., Hoppins, S., Icho, T., Jakobs, S., Ji, J., Kozjak-Pavlovic, V., Meisinger, C., Odgren, P. R., Park, S. K., Rehling, P., Reichert, A. S., Sheikh, M. S., ... Nunnari, J. (2014). Uniform nomenclature for the mitochondrial contact site and cristae organizing system. *Journal of Cell Biology*, *204*(7), 1083–1086. <https://doi.org/10.1083/jcb.201401006>
- Pfeiffer, K., Gohil, V., Stuart, R. A., Hunte, C., Brandt, U., Greenberg, M. L., & Schägger, H. (2003). Cardiolipin Stabilizes Respiratory Chain Supercomplexes. *Journal of Biological Chemistry*, *278*(52), 52873–52880. <https://doi.org/10.1074/jbc.M308366200>
- Pickles, S., Vigié, P., & Youle, R. J. (2018). Mitophagy and Quality Control Mechanisms in Mitochondrial Maintenance. *Current Biology*, *28*(4), R170–R185. <https://doi.org/10.1016/j.cub.2018.01.004>

- Potting, C., Tatsuta, T., König, T., Haag, M., Wai, T., Aaltonen, M. J., & Langer, T. (2013). TRIAP1/PRELI Complexes Prevent Apoptosis by Mediating Intramitochondrial Transport of Phosphatidic Acid. *Cell Metabolism*, 18(2), 287–295. <https://doi.org/10.1016/j.cmet.2013.07.008>
- Rainbolt, T. K., Atanassova, N., Genereux, J. C., & Wiseman, R. L. (2013). Stress-Regulated Translational Attenuation Adapts Mitochondrial Protein Import through Tim17A Degradation. *Cell Metabolism*, 18(6), 908–919. <https://doi.org/10.1016/j.cmet.2013.11.006>
- Rampelt, H., & van der Laan, M. (2017). The Yin & Yang of Mitochondrial Architecture - Interplay of MICOS and F1Fo-ATP synthase in cristae formation. *Microbial Cell*, 4(8), 236–239. <https://doi.org/10.15698/mic2017.08.583>
- Rampelt, H., Wollweber, F., Gerke, C., de Boer, R., van der Klei, I. J., Bohnert, M., Pfanner, N., & van der Laan, M. (2018). Assembly of the Mitochondrial Cristae Organizer Mic10 Is Regulated by Mic26–Mic27 Antagonism and Cardiolipin. *Journal of Molecular Biology*, 430(13), 1883–1890. <https://doi.org/10.1016/j.jmb.2018.04.037>
- Raturi, A., & Simmen, T. (2013). Where the endoplasmic reticulum and the mitochondrion tie the knot: The mitochondria-associated membrane (MAM). *Biochimica et Biophysica Acta (BBA) - Molecular Cell Research*, 1833(1), 213–224. <https://doi.org/10.1016/j.bbamcr.2012.04.013>
- Richter, U., Ng, K. Y., Suomi, F., Marttinen, P., Turunen, T., Jackson, C., Suomalainen, A., Vihinen, H., Jokitalo, E., Nyman, T. A., Isokallio, M. A., Stewart, J. B., Mancini, C., Brusco, A., Seneca, S., Lombès, A., Taylor, R. W., & Battersby, B. J. (2019). Mitochondrial stress response triggered by defects in protein synthesis quality control. *Life Science Alliance*, 2(1), e201800219. <https://doi.org/10.26508/lsa.201800219>
- Rizzuto, R., De Stefani, D., Raffaello, A., & Mammucari, C. (2012). Mitochondria as sensors and regulators of calcium signalling. *Nature Reviews Molecular Cell Biology*, 13(9), 566–578. <https://doi.org/10.1038/nrm3412>
- Rostovtseva, T. K., & Bezrukov, S. M. (2008). VDAC regulation: role of cytosolic proteins and mitochondrial lipids. *Journal of Bioenergetics and Biomembranes*, 40(3), 163–170. <https://doi.org/10.1007/s10863-008-9145-y>
- Rowland, A. A., & Voeltz, G. K. (2012). Endoplasmic reticulum–mitochondria contacts: function of the junction. *Nature Reviews Molecular Cell Biology*, 13(10), 607–615. <https://doi.org/10.1038/nrm3440>
- Russell, O. M., Gorman, G. S., Lightowers, R. N., & Turnbull, D. M. (2020). Mitochondrial Diseases: Hope for the Future. *Cell*, 181(1), 168–188. <https://doi.org/10.1016/j.cell.2020.02.051>
- Sagan, L. (1967). On the origin of mitosing cells. *Journal of Theoretical Biology*, 14(3), 225–236. [https://doi.org/10.1016/0022-5193\(67\)90079-3](https://doi.org/10.1016/0022-5193(67)90079-3)
- Saita, S., Tatsuta, T., Lampe, P. A., König, T., Ohba, Y., & Langer, T. (2018). PARL partitions the lipid transfer protein STARD7 between the cytosol and mitochondria. *The EMBO Journal*, 37(4). <https://doi.org/10.15252/embj.201797909>
- Sakowska, P., Jans, D. C., Mohanraj, K., Riedel, D., Jakobs, S., & Chacinska, A. (2015). The Oxidation Status of Mic19 Regulates MICOS Assembly. *Molecular and Cellular Biology*, 35(24), 4222–4237. <https://doi.org/10.1128/MCB.00578-15>
- Sastri, M., Darshi, M., Mackey, M., Ramachandra, R., Ju, S., Phan, S., Adams, S., Stein, K., Douglas, C. R., Kim, J. J., Ellisman, M. H., Taylor, S. S., & Perkins, G. A. (2017). Sub-mitochondrial localization of genetic-tagged MIB interacting partners: Mic19, Mic60 and Sam50. *Journal of Cell Science*. <https://doi.org/10.1242/jcs.201400>
- Schon, E. A., & Przedborski, S. (2011). Mitochondria: The Next (Neurode)Generation. *Neuron*, 70(6), 1033–1053. <https://doi.org/10.1016/j.neuron.2011.06.003>
- Schreiner, B., Westerburg, H., Forné, I., Imhof, A., Neupert, W., & Mokranjac, D. (2012). Role of the AAA protease Yme1 in folding of proteins in the intermembrane space of mitochondria. *Molecular Biology of the Cell*, 23(22), 4335–4346. <https://doi.org/10.1091/mbc.e12-05-0420>

- Schuettpelez, J., Janer, A., Antonicka, H., & Shoubridge, E. A. (2023). The role of the mitochondrial outer membrane protein SLC25A46 in mitochondrial fission and fusion. *Life Science Alliance*, 6(6), e202301914. <https://doi.org/10.26508/lsa.202301914>
- Schug, Z. T., & Gottlieb, E. (2009). Cardiolipin acts as a mitochondrial signalling platform to launch apoptosis. *Biochimica et Biophysica Acta (BBA) - Biomembranes*, 1788(10), 2022–2031. <https://doi.org/10.1016/j.bbamem.2009.05.004>
- Scorrano, L., Ashiya, M., Buttle, K., Weiler, S., Oakes, S. A., Mannella, C. A., & Korsmeyer, S. J. (2002). A Distinct Pathway Remodels Mitochondrial Cristae and Mobilizes Cytochrome c during Apoptosis. *Developmental Cell*, 2(1), 55–67. [https://doi.org/10.1016/S1534-5807\(01\)00116-2](https://doi.org/10.1016/S1534-5807(01)00116-2)
- Senes, A., Gerstein, M., & Engelman, D. M. (2000). Statistical analysis of amino acid patterns in transmembrane helices: the GxxxG motif occurs frequently and in association with β -branched residues at neighboring positions. *Journal of Molecular Biology*, 296(3), 921–936. <https://doi.org/10.1006/jmbi.1999.3488>
- Shoshan-Barmatz, V., De Pinto, V., Zweckstetter, M., Raviv, Z., Keinan, N., & Arbel, N. (2010). VDAC, a multi-functional mitochondrial protein regulating cell life and death. *Molecular Aspects of Medicine*, 31(3), 227–285. <https://doi.org/10.1016/j.mam.2010.03.002>
- Siebert, V., Silber, M., Heuten, E., Muhle-Goll, C., & Lemberg, M. K. (2022). Cleavage of mitochondrial homeostasis regulator PGAM5 by the intramembrane protease PARL is governed by transmembrane helix dynamics and oligomeric state. *Journal of Biological Chemistry*, 298(9), 102321. <https://doi.org/10.1016/j.jbc.2022.102321>
- Siegmund, S. E., Grassucci, R., Carter, S. D., Barca, E., Farino, Z. J., Juanola-Falgarona, M., Zhang, P., Tanji, K., Hirano, M., Schon, E. A., Frank, J., & Freyberg, Z. (2018). Three-Dimensional Analysis of Mitochondrial Crista Ultrastructure in a Patient with Leigh Syndrome by In Situ Cryoelectron Tomography. *IScience*, 6, 83–91. <https://doi.org/10.1016/j.isci.2018.07.014>
- Sim, S. I., Chen, Y., Lynch, D. L., Gumbart, J. C., & Park, E. (2023). Structural basis of mitochondrial protein import by the TIM23 complex. *Nature*, 621(7979), 620–626. <https://doi.org/10.1038/s41586-023-06239-6>
- Spiegel, R., Saada, A., Flannery, P. J., Burté, F., Soiferman, D., Khayat, M., Eisner, V., Vladovski, E., Taylor, R. W., Bindoff, L. A., Shaag, A., Mandel, H., Schuler-Furman, O., Shalev, S. A., Elpeleg, O., & Yu-Wai-Man, P. (2016). Fatal infantile mitochondrial encephalomyopathy, hypertrophic cardiomyopathy and optic atrophy associated with a homozygous OPA1 mutation. *Journal of Medical Genetics*, 53(2), 127–131. <https://doi.org/10.1136/jmedgenet-2015-103361>
- Stephan, T., Brüser, C., Deckers, M., Steyer, A. M., Balzarotti, F., Barbot, M., Behr, T. S., Heim, G., Hübner, W., Ilgen, P., Lange, F., Pacheu-Grau, D., Pape, J. K., Stoldt, S., Huser, T., Hell, S. W., Möbius, W., Rehling, P., Riedel, D., & Jakobs, S. (2020). MICOS assembly controls mitochondrial inner membrane remodeling and crista junction redistribution to mediate cristae formation. *The EMBO Journal*, 39(14). <https://doi.org/10.15252/embj.2019104105>
- Stiburek, L., Cesnekova, J., Kostkova, O., Fornuskova, D., Vinsova, K., Wenchich, L., Houstek, J., & Zeman, J. (2012). YME1L controls the accumulation of respiratory chain subunits and is required for apoptotic resistance, cristae morphogenesis, and cell proliferation. *Molecular Biology of the Cell*, 23(6), 1010–1023. <https://doi.org/10.1091/mbc.e11-08-0674>
- Stoldt, S., Stephan, T., Jans, D. C., Brüser, C., Lange, F., Keller-Findeisen, J., Riedel, D., Hell, S. W., & Jakobs, S. (2019). Mic60 exhibits a coordinated clustered distribution along and across yeast and mammalian mitochondria. *Proceedings of the National Academy of Sciences*, 116(20), 9853–9858. <https://doi.org/10.1073/pnas.1820364116>
- Strauss, M., Hofhaus, G., Schröder, R. R., & Kühlbrandt, W. (2008). Dimer ribbons of ATP synthase shape the inner mitochondrial membrane. *The EMBO Journal*, 27(7), 1154–1160. <https://doi.org/10.1038/emboj.2008.35>
- Strauss, R. S. (2000). Adult functional outcome of those born small for gestational age: twenty-six-year follow-up of the 1970 British Birth Cohort. *JAMA*, 283(5), 625–632. <https://doi.org/10.1001/jama.283.5.625>

- Tang, J., Zhang, K., Dong, J., Yan, C., Hu, C., Ji, H., Chen, L., Chen, S., Zhao, H., & Song, Z. (2020). Sam50–Mic19–Mic60 axis determines mitochondrial cristae architecture by mediating mitochondrial outer and inner membrane contact. *Cell Death & Differentiation*, 27(1), 146–160. <https://doi.org/10.1038/s41418-019-0345-2>
- Tatsuta, T., Scharwey, M., & Langer, T. (2014). Mitochondrial lipid trafficking. *Trends in Cell Biology*, 24(1), 44–52. <https://doi.org/10.1016/j.tcb.2013.07.011>
- Tirrell, P. S., Nguyen, K. N., Luby-Phelps, K., & Friedman, J. R. (2020). MICOS subcomplexes assemble independently on the mitochondrial inner membrane in proximity to ER contact sites. *Journal of Cell Biology*, 219(11). <https://doi.org/10.1083/jcb.202003024>
- Tondera, D., Grandemange, S., Jourdain, A., Karbowski, M., Mattenberger, Y., Herzig, S., Da Cruz, S., Clerc, P., Raschke, I., Merkwirth, C., Ehses, S., Krause, F., Chan, D. C., Alexander, C., Bauer, C., Youle, R., Langer, T., & Martinou, J.-C. (2009). SLP-2 is required for stress-induced mitochondrial hyperfusion. *The EMBO Journal*, 28(11), 1589–1600. <https://doi.org/10.1038/emboj.2009.89>
- Tsai, P.-I., Lin, C.-H., Hsieh, C.-H., Papakyrikos, A. M., Kim, M. J., Napolioni, V., Schoor, C., Couthouis, J., Wu, R.-M., Wszolek, Z. K., Winter, D., Greicius, M. D., Ross, O. A., & Wang, X. (2018). PINK1 Phosphorylates MIC60/Mitofilin to Control Structural Plasticity of Mitochondrial Crista Junctions. *Molecular Cell*, 69(5), 744–756.e6. <https://doi.org/10.1016/j.molcel.2018.01.026>
- Unterreitmeier, S., Fuchs, A., Schäffler, T., Heym, R. G., Frishman, D., & Langosch, D. (2007). Phenylalanine Promotes Interaction of Transmembrane Domains via GxxxG Motifs. *Journal of Molecular Biology*, 374(3), 705–718. <https://doi.org/10.1016/j.jmb.2007.09.056>
- Urbach, J., Kondadi, A. K., David, C., Naha, R., Deinert, K., Reichert, A. S., & Anand, R. (2021). Conserved GxxxG and WN motifs of MIC13 are essential for bridging two MICOS subcomplexes. *Biochimica et Biophysica Acta (BBA) - Biomembranes*, 1863(12), 183683. <https://doi.org/10.1016/j.bbamem.2021.183683>
- van de Warrenburg, B. P., Schouten, M. I., de Bot, S. T., Vermeer, S., Meijer, R., Pennings, M., Gilissen, C., Willemsen, M. A., Scheffer, H., & Kamsteeg, E.-J. (2016). Clinical exome sequencing for cerebellar ataxia and spastic paraplegia uncovers novel gene–disease associations and unanticipated rare disorders. *European Journal of Human Genetics*, 24(10), 1460–1466. <https://doi.org/10.1038/ejhg.2016.42>
- Van Strien, J., Guerrero-Castillo, S., Chatzisprou, I. A., Houtkooper, R. H., Brandt, U., & Huynen, M. A. (2019). COmplexome Profiling ALignment (COPAL) reveals remodeling of mitochondrial protein complexes in Barth syndrome. *Bioinformatics*, 35(17), 3083–3091. <https://doi.org/10.1093/bioinformatics/btz025>
- Vance, J. E. (1991). Newly made phosphatidylserine and phosphatidylethanolamine are preferentially translocated between rat liver mitochondria and endoplasmic reticulum. *The Journal of Biological Chemistry*, 266(1), 89–97.
- Viana, M. P., Levytsky, R. M., Anand, R., Reichert, A. S., & Khalimonchuk, O. (2021). Protease OMA1 modulates mitochondrial bioenergetics and ultrastructure through dynamic association with MICOS complex. *iScience*, 24(2), 102119. <https://doi.org/10.1016/j.isci.2021.102119>
- Votruba, M., Moore, A. T., & Bhattacharya, S. S. (1998). Clinical features, molecular genetics, and pathophysiology of dominant optic atrophy. *Journal of Medical Genetics*, 35(10), 793–800. <https://doi.org/10.1136/jmg.35.10.793>
- Wai, T., Saita, S., Nolte, H., Müller, S., König, T., Richter-Dennerlein, R., Sprenger, H., Madrenas, J., Mühlmeister, M., Brandt, U., Krüger, M., & Langer, T. (2016). The membrane scaffold SLP2 anchors a proteolytic hub in mitochondria containing PARL and the *i*-AAA protease YME1L. *EMBO Reports*, 17(12), 1844–1856. <https://doi.org/10.15252/embr.201642698>
- Wallace, D. C. (2005). A Mitochondrial Paradigm of Metabolic and Degenerative Diseases, Aging, and Cancer: A Dawn for Evolutionary Medicine. *Annual Review of Genetics*, 39(1), 359–407. <https://doi.org/10.1146/annurev.genet.39.110304.095751>
- Wang, L., Hsu, T., Lin, H., & Fu, C. (2020). Drosophila MICOS knockdown impairs mitochondrial structure and function and promotes mitophagy in muscle tissue. *Biology Open*, 9(12), bio054262. <https://doi.org/10.1242/bio.054262>

- Weber, T. A., Koob, S., Heide, H., Wittig, I., Head, B., van der Bliek, A., Brandt, U., Mittelbronn, M., & Reichert, A. S. (2013). APOOL Is a Cardiolipin-Binding Constituent of the Mitofilin/MINOS Protein Complex Determining Cristae Morphology in Mammalian Mitochondria. *PLoS ONE*, *8*(5), e63683. <https://doi.org/10.1371/journal.pone.0063683>
- Wei, M. C., Zong, W.-X., Cheng, E. H.-Y., Lindsten, T., Panoutsakopoulou, V., Ross, A. J., Roth, K. A., MacGregor, G. R., Thompson, C. B., & Korsmeyer, S. J. (2001). Proapoptotic BAX and BAK: A Requisite Gateway to Mitochondrial Dysfunction and Death. *Science*, *292*(5517), 727–730. <https://doi.org/10.1126/science.1059108>
- Westermann, B. (2010). Mitochondrial fusion and fission in cell life and death. *Nature Reviews Molecular Cell Biology*, *11*(12), 872–884. <https://doi.org/10.1038/nrm3013>
- Westphal, D., Dewson, G., Czabotar, P. E., & Kluck, R. M. (2011). Molecular biology of Bax and Bak activation and action. *Biochimica et Biophysica Acta (BBA) - Molecular Cell Research*, *1813*(4), 521–531. <https://doi.org/10.1016/j.bbamcr.2010.12.019>
- Willsey, A. J., Fernandez, T. V., Yu, D., King, R. A., Dietrich, A., Xing, J., Sanders, S. J., Mandell, J. D., Huang, A. Y., Richer, P., Smith, L., Dong, S., Samochoa, K. E., Neale, B. M., Coppola, G., Mathews, C. A., Tischfield, J. A., Scharf, J. M., State, M. W., ... Yu, D. (2017). De Novo Coding Variants Are Strongly Associated with Tourette Disorder. *Neuron*, *94*(3), 486–499.e9. <https://doi.org/10.1016/j.neuron.2017.04.024>
- Xu, Y., Sutachan, J. J., Plesken, H., Kelley, R. I., & Schlame, M. (2005). Characterization of lymphoblast mitochondria from patients with Barth syndrome. *Laboratory Investigation*, *85*(6), 823–830. <https://doi.org/10.1038/labinvest.3700274>
- Youle, R. J., & van der Bliek, A. M. (2012). Mitochondrial Fission, Fusion, and Stress. *Science*, *337*(6098), 1062–1065. <https://doi.org/10.1126/science.1219855>
- Zeharia, A., Friedman, J. R., Tobar, A., Saada, A., Konen, O., Fellig, Y., Shaag, A., Nunnari, J., & Elpeleg, O. (2016). Mitochondrial hepato-encephalopathy due to deficiency of QIL1/MIC13 (C19orf70), a MICOS complex subunit. *European Journal of Human Genetics: EJHG*, *24*(12), 1778–1782. <https://doi.org/10.1038/ejhg.2016.83>
- Zerbes, R. M., Bohnert, M., Stroud, D. A., von der Malsburg, K., Kram, A., Oeljeklaus, S., Warscheid, B., Becker, T., Wiedemann, N., Veenhuis, M., van der Klei, I. J., Pfanner, N., & van der Laan, M. (2012). Role of MINOS in Mitochondrial Membrane Architecture: Cristae Morphology and Outer Membrane Interactions Differentially Depend on Mitofilin Domains. *Journal of Molecular Biology*, *422*(2), 183–191. <https://doi.org/10.1016/j.jmb.2012.05.004>
- Zerbes, R. M., Höß, P., Pfanner, N., van der Laan, M., & Bohnert, M. (2016). Distinct Roles of Mic12 and Mic27 in the Mitochondrial Contact Site and Cristae Organizing System. *Journal of Molecular Biology*, *428*(8), 1485–1492. <https://doi.org/10.1016/j.jmb.2016.02.031>
- Zhou, W., Ma, D., Sun, A. X., Tran, H.-D., Ma, D.-L., Singh, B. K., Zhou, J., Zhang, J., Wang, D., Zhao, Y., Yen, P. M., Goh, E., & Tan, E.-K. (2019). PD-linked CHCHD2 mutations impair CHCHD10 and MICOS complex leading to mitochondria dysfunction. *Human Molecular Genetics*, *28*(7), 1100–1116. <https://doi.org/10.1093/hmg/ddy413>

10 Publications

- **Naha,R.**, Strohm,R., Urbach,J., Wittig,I., Reichert,A.S., Kondadi,A.K., &Anand,R.(2023) MIC13 and SLP2 seed the Assembly of MIC60-subcomplex to facilitate Crista Junction Formation. bioRxiv. doi:10.1101/2023.09.04.556207
- Lubeck, M., **Naha, R.**, Schaumkessel, Y., Westhoff, P., Stefanski, A., Petzsch, P., Stühler, K., Köhrer, K., Weber, A. P. M., Anand, R., Reichert, A. S., & Kondadi, A. K. (2023, January 1). Mitochondrial apolipoprotein MIC26 is a metabolic rheostat regulating central cellular fuel pathways. bioRxiv. <https://doi.org/10.1101/2023.12.01.569567>
- Lubeck,M., Derkum,N.H., **Naha,R.**, Strohm,R., Driessen,M.D., Belgardt,B.-F., Roden,M., Stühler, K., Anand, R., Reichert, A. S., & Kondadi, A. K. (2023). MIC26 and MIC27 are bona de subunits of the Micos complex in mitochondria and do not exist as glycosylated apolipoproteins. PLOS ONE, 18(6). <https://doi.org/10.1371/journal.pone.0286756>
- Urbach, J., Kondadi, A. K., David, C., **Naha, R.**, Deinert, K., Reichert, A. S., & Anand, R. (2021). Conserved gxxxg and WN motifs of Mic13 are essential for bridging two Micos subcomplexes. Biochimica et Biophysica Acta (BBA) - Biomembranes, 1863(12), 183683. <https://doi.org/10.1016/j.bbamem.2021.183683>

11 Acknowledgements

First and foremost, I would like to thank and express my heartfelt indebtedness to the Almighty for all his blessings upon me. If not for his grace upon me I would not have been able to achieve what I have achieved.

I am particularly grateful for the support and insights of Prof. Dr. rer. nat. Andreas Reichert, his contributions have been invaluable. His involvement, particularly with his strategic and insightful contributions during meetings, has been a cornerstone of my development. Prof. Reichert has a unique ability to inspire, teaching me to dream about the possibilities within science beyond the confines of publishing. His approach to research, characterized by a deep passion for discovery and understanding, has shown me the true essence of being a scientist. Beyond his academic support, Prof. Reichert's kindness and readiness to provide personal support have been incredibly meaningful to me. I am profoundly grateful for his positive influence and the expansive view of science he has instilled, which will undoubtedly shape my future endeavors.

In my journey through research, I've been exposed to a diverse range of perspectives that have each contributed to my development, including the guidance of my supervisor, Dr. Ruchika Anand. Her distinctive approach and meticulous standards encouraged me to delve deeper into our field, providing a rich tapestry of challenges and insights. This engagement has been invaluable, pushing me to refine my analytical skills and broaden my understanding. Throughout this process, my dedication to maintaining high work ethics has been reinforced, further enriching the unique dynamics of our interactions, which have spurred both personal and academic growth.

I would also like to extend my gratitude to Dr. rer. nat. Arun Kondadi for his mentorship and for opening doors to several projects that have been instrumental in broadening my research skills and contributing to co-authored publications. His ability to recognize and nurture students has opened up invaluable opportunities for me, sparking a curiosity to challenge and expand upon existing knowledge within our research. Dr. Kondadi's guidance has been instrumental in navigating the intricate layers of our work, inspiring a drive towards uncovering new insights and perspectives. Moreover, his mentorship, while challenging, has provided valuable lessons in resilience and perseverance, subtly pushing me to overcome obstacles and doubts along the way. His confidence in my abilities encouraged me to not only meet but to transcend the conventional boundaries of our field.

I extend my gratitude to Prof. Dr. med. Felix Distelmaier, whose valuable insights during intensive discussions about mechanistic insights on clinical research have played a role in shaping and broadening my academic perspective and understanding during my PhD journey.

I extend my sincere gratitude to Prof. Dr. rer. nat. Peter Brenneisen for his valuable insights and guidance in the broader field of mitochondria, which significantly contributed to the success of this project.

My heartfelt thanks to Dr. rer. nat. Marcel Zimmerman, whose guidance and ingenuity in the lab turned pivotal challenges into opportunities for discovery. His willingness to share his vast knowledge (TWSS) and meticulous attention to detail have been instrumental in both my project's success and my growth as a scientist. Of all the scientific creativity you embarked on us, the “board of shame” was your ultimate creation in our office. For Dr. rer. nat.. Kai Völtzke, whose contributions to my project may have been limited in quantity but were significant in impact, I am truly grateful. Beyond offering valuable insights, his willingness to lend an ear during my moments of frustration and his humor brought much-needed lightness to the lab environment, helping me to navigate the emotional highs and lows of this journey.

Within the crucible of my PhD journey, the fellowships forged with colleagues-turned-friends has been nothing short of legendary.

Melissa, beyond our shared scientific quests across continents, and the promise of unconventional entertainment from my side at your bachelorette party, your resilience and spirit have been my anchor in the stormiest of times. Your ability to question established norms and pave new paths in our field has not only been inspiring but has also emboldened me to challenge and redefine my own research boundaries. Your readiness to share in both the mundane and the madness, to gossip, and strategize against the odds, has been a source of immeasurable strength and that fueled our collective courage to venture beyond the accepted. Yulia, from my first week in the lab, you've been the gravitational force that brought our constellation of misfits together. Your unwavering support, your knack for fostering unity among us, and your wisdom have been the glue of our group. Always there with a listening ear, a thoughtful word, or a rallying cry of a “Dragonborn Paladin”, you've helped transform this journey into one of discovery, not just of science but of friendship and solidarity that transcends the confines of our lab. Michelle, my co-conspirator in crafting jokes that would make sailors blush, our laughter has been a rebellious antidote to the seriousness of our scientific endeavors. As a true “Cleric of Rillifane Rallathil”, your healing words have provided solace and guidance, much like the divine light of your character. Your presence has been a constant reminder that even in our most challenging moments, we can find solace and strength in each other, infusing our lab with laughter and lightness even in the darkest of times. Your camaraderie has been a foundation of our solidarity, reminding us that no matter the challenges we face, we're stronger together. Alex, the “Dungeon Master” (not in a dirty way, or maybe idk), who navigates realms of fantasy with the same ease as complex data, your stories have added layers of imagination to our reality. Alongside our shared experiences on similar projects, we've weathered challenges together, finding solace and strength in our

shared camaraderie. Whether discussing data or unwinding with a drink and dhosa, your presence has been a grounding force, fostering friendship amid the whirlwind of our endeavors. Deepti, my sister from another mister, much like the disciplined “Monk”, your steadfast resolve and inner strength, despite every challenge, inspire us through the realms of academia. Our shared adventures in exploring Indian cuisine have been a delightful addition to our friendship. As we navigate the complexities of academia together, your presence in the lab and in our lives has added a touch of home, grounding us in familiarity amid the whirlwind. Rebecca, who wages war on proteins with the ferocity of a Strohm, your triumphs and challenges have fueled our collective resilience. Much like the ancient “Druids”, you bring a sense of harmony and balance to our scientific endeavors. Your presence in the lab has been a reminder that even amidst the chaos, there is always room for growth and transformation. And to Mathias and Andre, the dudes who’ve shared not just their insights but an endless supply of coffee, alcohol, and the resulting hangovers, you’ve made the lab feel like a home.

Our countless hours of discussion, drenched in alcohol and unfiltered humor, have been the undercurrent of my PhD life, teaching me that science is not just about discovery but also about the human connections that sustain us. This journey, acknowledged to every other person in the institute, peppered with moments of brilliance and debauchery, would have been insufferably dull without your friendship, insights, and the sanctuary of laughter we built together.

In every lab, the remarkable work and invaluable support provided by technicians are the unsung heroes behind every scientific breakthrough. Andrea, the wizard of electron microscopy, whose expertise has gifted us with amazing EM pictures that have enhanced our research beyond measure. Gilla, Tanja, and Sandra, your invaluable support in the lab work has been the bedrock of our scientific endeavors, ensuring smooth operations and progress at every turn.

I would like to extend my heartfelt gratitude to Petra Oprea for her constant support and taking care of “other scientific stuff” which fast-tracked the progression of my journey.

For my mentor and “ally” Dr. Shyamtanu Datta, whose unwavering mental support and wealth of scientific knowledge have been my guiding lights from afar. Your teachings on research principles and integrity have shaped not just my research, but my character.

Lastly, for my devoted parents, whose unwavering support, encouragement, and sacrifices have been the bedrock of my journey. Your resilience and belief in me have been my greatest source of strength and motivation throughout.

12 Eidesstattliche Versicherung

I certify under oath that the dissertation was written by me independently and without any unauthorized outside help, in compliance with the "Principles for Ensuring Good Scientific Practice at the Heinrich Heine University Düsseldorf". The ideas taken from external sources are identified as such. The dissertation has not yet been submitted to any other institution in the form presented or in a similar form. I have not yet made any unsuccessful attempts at a doctorate.